RANGE FINDING IN PASSIVE WIRELESS SENSOR NETWORKS USING POWER-OPTIMIZED WAVEFORMS

A Thesis
Presented to
The Academic Faculty

by

Matthew S. Trotter

In Partial Fulfillment
of the Requirements for the Degree
Doctor of Philosophy in the
School of Electrical and Computer Engineering

Georgia Institute of Technology
December 2011

RANGE FINDING IN PASSIVE WIRELESS SENSOR NETWORKS USING POWER-OPTIMIZED WAVEFORMS

Approved by:

Mark A. Richards, Committee Chair
School of Electrical and Computer Engineering
Georgia Institute of Technology

Gregory D. Durgin, Advisor
School of Electrical and Computer Engineering
Georgia Institute of Technology

Andrew F. Peterson
School of Electrical and Computer Engineering
Georgia Institute of Technology

Mary Ann Ingram
School of Electrical and Computer Engineering
Georgia Institute of Technology

Neal Patwari
School of Electrical and Computer Engineering
University of Utah

Date Approved: 11 November 2011

To Mom, Dad, B.C., and Mitch.

ACKNOWLEDGEMENTS

The Propagation Group at Georgia Tech is quite possibly one of the best learning environments in the world. I have learned so much about electromagnetics, communications, and of course propagation from my colleagues and my advisor. Joshua Griffin, Ryan Pirkl, and Lorne Liechty: I was merely a blob of incoherent naivety before you showed me what it took to perform good research. Yenpao Albert Lu: There is a creative side to research and engineering, which you consistently exemplify. Raj Bhattacharjea: The isolated world of pure mathematics has found a conduit to engineering, and you are it. Gregory Koo: You are an academic at heart but also a whiz at fabricating RF boards. Azhar Hasan: Thank you for all the fruitful discussions on direction and life. Christopher Valenta: Your engineering talents are widespread, and you have been an excellent collaborator. Marcin Morys, Bashir Akbar, and Blake Marshall: You are the future of the lab. I wish you the best of luck.

Professor Gregory Durgin has taught me many things over the years, but the most significant thing I have learned is how to focus on the aspects of research that make the problem interesting. I surely would have been a rambling wreck if it were not for your guidance.

Thank you to the committee - Dr. Mark Richards, Professor Andrew Peterson, Professor Mary Ann Ingram, Professor Neal Patwari, and Professor Gregory Durgin - for the valuable feedback and new viewpoints.

I give a special thank you to Professor Kevin Sowerby and Professor Michael Neve at the University of Auckland for their guidance in framing a Ph.D. dissertation and planning simulations and experiments. Thank you to Salim Namik, Ramin Vali, Liza Pujji, Andrew Austin, Rachita Dahama, Farrukh Bhatti, Hazim Namik, Rav Chandra, and Claudio Camasca for all the New Zealand adventures!

TABLE OF CONTENTS

LIST OF TABLES

LIST OF FIGURES

LIST OF SYMBOLS OR ABBREVIATIONS

α	attenuation constant that encapsulates link budget items like antenna gain and path loss.
$\tilde{b}(t-\tau)$	complex-valued tag-data signal reflected in two reflection states within the tag.
B_{3dB}	half-power bandwidth of the spectrum of a periodic POW.
$B_{\text{3dB,pls}}$	half-power bandwidth of the single-pulse spectrum of a POW.
B_{f}	total bandwidth of the ideal filter used for calculating the RMS bandwidth of a square POW.
B_{path}	path blockage.
B_{RMS}	root-mean-square bandwidth of the single-pulse spectrum of a POW.
C	stage capacitance of the charge pump.
D	duty cycle of a square POW.
ϵ_{r}	relative permittivity of a dielectric.
F	fade margin.
f_{c}	center frequency of the passband or carrier frequency.
$f_{\tilde{y}}(\tilde{y}\|\tau)$	probability distribution of the received signal given the roundtrip time delay τ.
$\tilde{\Gamma}_A$	complex reflection coefficient of tag reflection state "A".
$\text{I}_0(\cdot)$	modified Bessel function of the first kind with order zero.
K	K-factor of a frequency-flat Ricean fading channel.
λ_{POW}	length of space spanned by a POW according to its time period and the speed of light.
$L(\tau\|\tilde{y})$	likelihood function with respect to time delay τ given the received signal $\tilde{y}$ is observed.
M	number of cosine terms added together at baseband to form the M-POW. Also, modulation factor.
$\tilde{n}(t)$	complex-valued additive white Gaussian random noise process represented as a noise signal.
N	number of charge pump stages. Also, total number of samples taken for one range estimate.
N_{POW}	number of POW time periods sampled for one range estimation.

PAPR	peak-to-average power ratio.
$\text{pow}(t-\tau)$	periodic POW delayed in time by τ seconds.
$POW(f)$	frequency spectrum of a periodic POW.
$\text{pow}_{\text{pls}}(t)$	one POW pulse centered around $t=0$ with finite energy.
$\text{POW}_{\text{pls}}(f)$	frequency spectrum of one POW pulse centered around $t=0$.
$\prod_{0}^{T_{\text{POW}}}(\cdot)^{\,dt}$	product integral notation.
P_{S}	source power; power impinging on the charge pump.
P_{t}	signal power required to produce a maximum voltage equal to the threshold voltage of a diode.
Q_{L}	charge absorbed by the charge pump during time period of the carrier wave.
R_{L}	load resistance of a charge pump.
$R_{\text{pow}}(\tau-\tau_{\text{true}})$	real-valued autocorrelation of the transmitted POW evaluated at delay $\tau-\tau_{\text{true}}$.
$R''_{\text{pow}}(0)$	second derivative of the autocorrelation of a POW evaluated at zero delay.
$\text{Si}(\cdot)$	Sine integral function. $\text{Si}(x)=\int_{0}^{x}{}^{\sin(t)}\!/_{t}\;dt$.
σ_i	radar cross-section of the i^{th} object in the environment.
σ^2_{RMS}	root-mean-square delay spread of a one-way channel.
SNR	signal-to-noise ratio.
τ	roundtrip time delay of the targeted tag.
$\hat{\tau}$	estimate of the round trip time delay.
T_{ch}	charge time of the charge pump under a POW excitation.
T_{st}	starve time of the charge pump under a POW excitation.
T_{POW}	time period of a POW.
T_{RMS}	root-mean-square time width of one pulse of a POW.
T_{S}	sampling time period.
$\mathcal{U}(a,b)$	probability distribution of a uniform random variable with support between a and b.
V_{A}	antenna voltage source signal.

V_{clip}	amount of voltage that is clipped from the transmitted POW in the bias model.
$V^{-}(t)$	backward-propagating signal evaluated at the load terminals at time t.
v_p	velocity of propagation of electromagnetic waves in a medium.
$V^{+}(t)$	forward-propagating signal evaluated at the load terminals at time t.
V_{t}	threshold voltage of a diode.
$\tilde{X}_{\text{pow,y}}(\tau)$	complex-valued cross-correlation between the transmitted POW and the received signal $\tilde{y}$ evaluated at the tested delay τ.
$\tilde{y}(t)$	complex-valued received signal at baseband.
$\tilde{Z}_{\text{A}}$	complex-valued antenna impedance.
Z_{O}	characteristic impedance of a transmission line.
AC	alternating current.
ADC	analog-to-digital converter.
AM	amplitude modulation.
ASIC	application-specific integrated circuit.
AWGN	additive white Gaussian noise.
BPSK	binary phase-shift keying.
CDMA	code-division multiple access.
CMOS	complimentary metal-oxide-semiconductor.
CRLB	Cramér-Rao lower bound.
CW	continuous wave or carrier wave.
DAC	digital-to-analog converter.
DC	direct current.
EEPROM	electrically erasable programmable read-only memory.
EIRP	equivalent isotropically radiated power.
FM	frequency modulation.
FM0	biphase space encoding, a type of frequency modulation.
FPGA	field-programmable gate array.
FR4	glass-reinforced epoxy laminate used as a substrate for a circuit board.
GPS	global positioning system.

GSM	global system for mobile communications.
IEEE	institute of electrical and electronic engineers.
ISM	industrial, scientific, and medical.
ISO	international organization for standardization.
LO	local oscillator.
LOS	line of sight.
MAP	maximum a posteriori.
ML	maximum-likelihood.
PN	psuedo-random noise.
POW	power-optimized waveform.
PTFE	Polytetrafluoroethylene. Also known as Teflon.
RCS	radar cross section.
RF	radio-frequency.
RFID	radio-frequency identification.
RMS	root-mean square.
RSS	received signal strength.
RSSI	received signal strength indicator.
RX	receiver or receiver antenna.
SMA	sub-miniature version A.
ToA	time of arrival.
ToF	time of flight.
VCO	voltage-controlled oscillator.
VNA	vector network analyzer.
WiFi	wireless fidelity. Refers to wireless local area networks.
WISP	wireless identification and sensing platform.
WSN	wireless sensor network.

SUMMARY

Passive wireless sensor networks (WSNs) are quickly becoming popular for many applications such as article tracking, position location, temperature sensing, and passive data storage. Passive tags and sensors are unique in that they collect their electrical energy by harvesting it from the ambient environment. Tags with charge pumps collect their energy from the signal they receive from the transmitting source. The efficiency of converting the received signal to DC power is greatly enhanced using a power-optimized waveform (POW). Measurements in the first part of this dissertation show that a POW can provide efficiency gains of up to 12 dB compared to a sine-wave input.

Tracking the real-time location of these passive tags is a specialized feature used in some applications such as animal tracking. A passive WSN that uses POWs for the improvement of energy-harvesting may also estimate the range to a tag by measuring the time delay of propagation from the transmitter to the tag and back to the transmitter. The maximum-likelihood (ML) estimator is used for estimating this time delay, which simplifies to taking the cross-correlation of the received signal with the transmitted signal.

This research characterizes key aspects of performing range estimations in passive WSNs using POWs. The shape of the POW has a directly-measurable effect on ranging performance. Measurements and simulations show that the RMS bandwidth of the waveform has an inversely proportional relationship to the uncertainty of a range measurement. The clutter of an environment greatly affects the uncertainty and bias exhibited by a range estimator. Random frequency-selective environments with heavy clutter are shown to produce estimation uncertainties more than 20 dB higher than the theoretical lower bound. Estimation in random frequency-flat environments is well-behaved and fits the theory quite nicely. Nonlinear circuits such as the charge pump distort the POW during reflection, which biases the range estimations. This research derives an empirical model for predicting the estimation bias for Dickson charge pumps and verifies it with simulations and measurements.

CHAPTER I

INTRODUCTION

"Ubiquitous" or "pervasive" computing is a new model of human-computer interaction where computers and their computations are forced to enter the human world [4]. This is opposed to the current reality where humans enter the virtual world as with desktop computers. The data in a pervasive computing system is obtained from the real world in real time. For example, a pervasive-computing bridge-monitoring system senses the bridge stresses at the ends of the trusses with wireless stress sensors. This data can be used by the bridge supervisor at the local Department of Transportation office for monitoring. It can also be used for tightening or loosening cable forces in real time.

A wireless sensor network (WSN) is a key component of the pervasive computing model that extracts real-world data from the environment. The parallel device in the virtual world is the reading mechanism that loads data from a hard disk. In this way, the WSN is a tool used to monitor environmental variables that are deemed useful to a user. Some examples of data that WSNs can extract are:

1. Weather: ambient temperature, pressure, humidity, and wind speed;
2. Motion: gyroscopic, collision, and stress forces;
3. Electrical: current, voltage and power consumption; and
4. Informative: identification number and object presence.

This list is not exhaustive, but it shows the wide variety of data that an environment can contain and a WSN can extract. In addition to collecting the data from the environment, it is useful to know the precise location of the sensor (also called a "tag") at the time of measurement. The act of determining a tag's position in two- or three-dimensional space is called **localization**, and the tag's location can be measured in a number of ways including triangulation, trilateration, or multilateration.

1.1 Current Ranging Methods

This research will focus on measuring the range between a reader and a tag. A localization algorithm can then use a range-based localization technique. To this end, the current ranging methods in WSNs include received signal strength indication (RSSI) ranging, interferometric ranging, and time-of-flight (ToF) ranging. The current state of the art in WSN ranging involving these techniques is discussed in detail later in Chapter 4.

RSSI ranging systems measure the received signal strength of the tag's backscatter response [5]. Then, the range is estimated by backsolving the range from the link budget equation. As a simple example, consider a WSN in free space with isotropic antennas operating on a carrier frequency of 5.8 GHz. The reader transmits 1 W of signal power to the tag, and the RSSI reports a received signal strength of 10 pW at the reader after reflection from the tag. The backscatter link budget for this simple case is [1]

$$P_{\mathrm{r}} = P_{\mathrm{T}} G_{\mathrm{T}}^2 G_{\mathrm{t}}^2 \left(\frac{\lambda}{4\pi r} \right)^4 . \tag{1}$$

Substituting the values for received power $P_{\mathrm{r}} = 10$ pW, transmitted power $P_{\mathrm{T}} = 1$ W, isotropic reader antenna gain $G_{\mathrm{T}} = 1$, isotropic tag antenna gain $G_{\mathrm{t}} = 1$, and wavelength $\lambda \approx 5.17$ cm, the range is calculated as $r \approx 2.31$ m. This is a deterministic calculation in a free-space environment in the absence of noise. However, practical RSSI-ranging systems must *estimate* the range when interferers such as noise, multipath fading, and propagation effects such as edge diffraction and shadowing are present. Much research has been performed on improving RSSI-ranging performance, and many implementations have been developed [5] [6] [7]. RSSI ranging is a simple ranging method that is integrated into WSNs inexpensively since RSS indicators are ubiquitous in receiver architectures. Realistic ranging accuracies and precisions are generally poor compared to interferometric ranging and ToF ranging.

Interferometric ranging systems measure the phase delay of the backscattered signal compared to the transmitted signal at two or more frequencies. The range is calculated from measuring the change in phase delay versus frequency. The interferometric ranging

equation is [8]

$$r = \frac{c}{4\pi}\frac{d\theta(f)}{df} \tag{2}$$

where $\theta(f)$ is the phase delay at a measured frequency f. The phase delay is measured from the in-phase (I) and quadrature (Q) components of the received signal. The reader hops through different frequencies in the measurement set, and interferometric ranging becomes more precise as more frequencies are included in the calculation of $d\theta(f)/df$. There are many implementations of interferometric ranging (also called "phase-based" ranging) in WSNs as well [8] [9] [10]. Implementation is relatively inexpensive since I/Q demodulators are ubiquitous in receiver architectures. The advantages of interferometric ranging are ease of implementation and some resilience to multipath fading since multiple frequencies are measured. The main disadvantage is the long measurement time taken to step through multiple frequencies.

Time-of-flight (ToF) ranging is the intuitive approach to ranging where a pulse is transmitted to the tag and reflected from the tag back to the reader. The time delay between transmission and reception corresponds to twice the tag range. In addition, the time delay includes the propagation times of the reader and tag, but these can be calibrated out. Once calibrated, the range is found using

$$r = \frac{c\tau}{2} \tag{3}$$

where c is the speed of light and τ is the roundtrip time delay. The time delay is estimated by maximizing the cross-correlation of the received signal with a noiseless copy of the transmitted signal. This technique is derived from Maximum Likelihood (ML) estimation, which is the common method for ToF delay estimation [11]. The choice of pulse shape is a research topic on its own [12] [13] [14] that aims to maximize ranging performance, minimize occupied signal bandwidth, and minimize computation time. WSN implementations generally use spread-spectrum pseudo-random noise (PN) waveforms for their excellent autocorrelation properties, which approximate a delta function. The ranging accuracy of ToF ranging is not biased in the same way as RSSI ranging by small-scale fading, however severe fading reduces the ranging precision. Implementation requires dedicated hardware for spreading

and despreading the PN waveform and software algorithms for estimating the peak of the cross-correlation. The tradeoffs for this relatively expensive implementation (as compared to RSSI and interferometric ranging) are more precise and accurate range estimations.

1.2 Energy Harvesting in Passive Wireless Sensor Networks

"Passive" tags are unique in their need to harvest DC energy from the signal transmitted by the reader. "Semi-passive" tags and "active" tags both have local power sources available either as batteries or wall-connected power. The passive tag wakes up with harvested DC energy and reflects the reader-transmitted signal with modulation between two reflective states. It is important that the ranging method works efficiently with energy harvesting and preserves communications between the reader and the tag.

Power-optimized waveforms (POWs) are a new development that increases the energy-harvesting efficiency of passive tags. The waveform shape of a POW is the key characteristic that overcomes the diode threshold voltage limitations of energy harvesters within passive tags. POWs have been shown to increase the maximum range of passive RFID tags in the 915 MHz industrial, scientific, and medical (ISM) band [15] [16], which have energy harvesters based on the Dickson charge pump topology [17]. POW parameters such as time period, peak-to-average-power ratio (PAPR), and signal bandwidth can be designed to improve the maximum tag range on top of an existing passive WSN. For example, a passive tag that normally must stay within 7 m from the reader can be augmented by receiving a POW that is designed to extend the range to 10 m.

A passive WSN that has chosen a POW out of necessity to extend the maximum tag range can use the same POW as a ToF ranging waveform. This makes the POW a dual-purpose tool in a passive WSN: POWs extend maximum range and help estimate tag range. The range-improvement characteristics of POWs have been researched and are presented in Chapter 3.

1.3 Research Overview

This research seeks to answer the following question:

Assuming power-optimized waveforms are used for estimating range,
what are the effects of waveform shape, environmental clutter,
and nonlinear reflections on ranging performance?

Chapters 2 through 4 present the theoretical background for understanding passive WSNs, POWs, current ranging techniques, and POW ranging. Chapter 2 describes the typical passive tag architecture and common reader architectures that are used in passive WSNs. Chapter 3 formally presents the energy-harvesting improvement capabilites of POWs and presents a signal model for the backscattered waveform assuming a POW is transmitted by the reader. It also presents a methodology for designing POWs and charge pumps together. Chapter 4 presents the preferred methods for estimating range to a passive tag using POWs. The ranging performance of such a system is derived either empirically or theoretically for all three phenomena introduced in the research question.

Chapters 5 and 6 present simulated and experimental tests that confirm the ranging performance of the POW ranging technique based on the derived models. Chapter 5 contains simulations that cover all three phenomena discussed. Chapter 6 describes the test plan for testing ranging performance against different POW shapes and nonlinear reflections. It also contains the analysis and results of the tests.

CHAPTER II

LOW-ENERGY WIRELESS SENSOR NETWORKS

WSNs provide real environmental data to computers and users with a conglomeration of wireless sensor nodes and readers. Wireless sensor nodes, or **tags** for short, extract the environmental data and communicate it back to the readers. The **readers** of a WSN are the devices that request or "ping" the tags for environmental data. These definitions are very broad as there are many classifications of WSNs including single-hop, multi-hop, active, semi-passive, passive, near-field, far-field, and others. In addition, the frequency of operation differentiates WSNs even furthur. This research focuses on passive, far-field WSNs operating in the 5.8 GHz industrial, scientific, and medical (ISM) band, which can be used by unlicensed users (as deemed by the Federal Communications Commission [18]) at up to 30 dBm of transmitted power with an antenna that has gain up to 23 dBi. This essentially means that the end users of WSNs (e.g. warehouse inventory managers, bridge supervisors, nurses etc.) may operate a WSN that is designed to transmit up to 53 dBm EIRP without a radio license. Similar restrictions to these are imposed by governing agencies around the world [19].

This chapter explains in detail the components and operation of wireless sensor networks. Stockman formulated the modern mechanism of reflected (or backscattered) communications [20], which is the method by which passive tags communicate their sensor data back to the reader. A reader must first provide the communication carrier signal to the tag before the tag can reflect its data. The situation is the RF equivalent of a flashlight shining light upon a wiggling mirror that reflects the light back toward the flashlight according to a pattern of digital data. The mirror can only communicate data when the light is shone upon it.

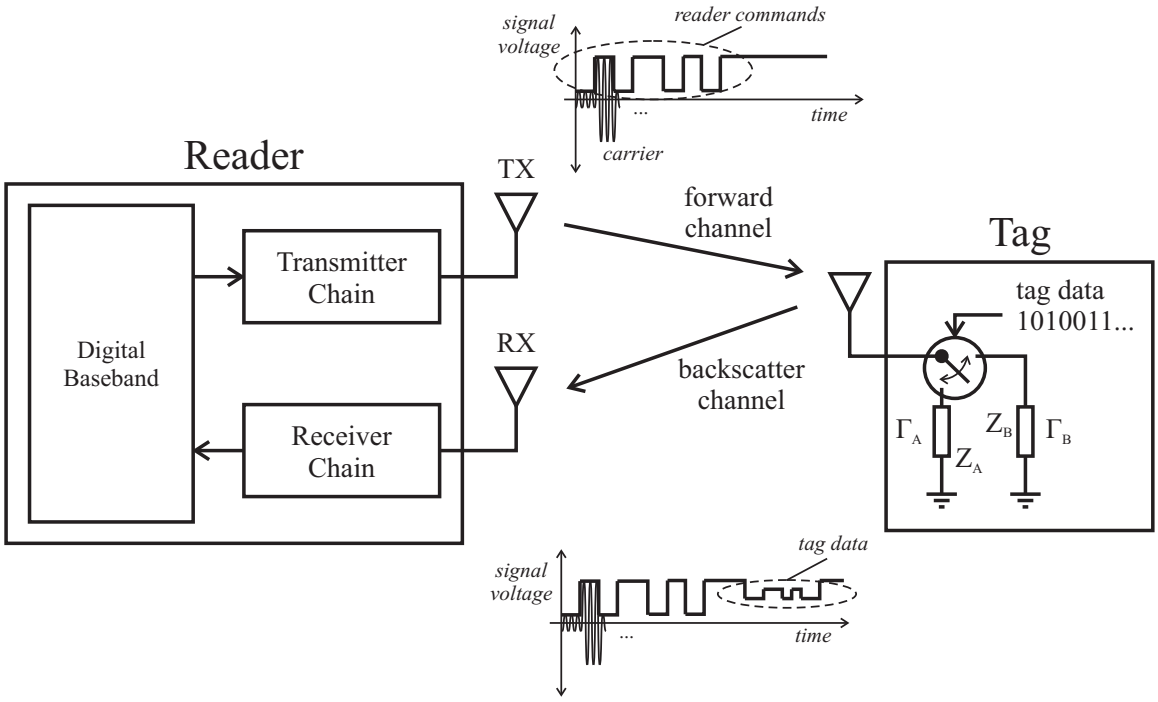

Figure 1: Readers initiate the half-duplex, reflected communication sequence with the tag. The tag reflects its sensor data on the unmodulated CW provided by the reader.

2.1 Basic Configuration and Terminology

Passive backscatter WSNs are typically half-duplex, reflected communications systems. The sequence of communications is initiated by the reader once the user requests data. Figure 1 shows this communication dynamic. The reader in a half-duplex WSN transmits an amplitude-modulated (AM) data-request signal to the tag immediately followed by an unmodulated continuous wave (CW) carrier. The tag receives and demodulates the data-request signal, and then reflects its own sensor data back to the reader on top of the unmodulated CW portion of scattered RF power in the form of reflective load modulation.

A passive tag differentiates itself from semi-passive or active tags by its need to rectify the reader-transmitted waveform into DC power for itself. DC power needs to be continuously provided during the tag's demodulation procedure, sensor data collection, and load-modulation procedure. Figure 1 shows the load modulation procedure switching a passive load impedance between two different reflection coefficients according to the tag's

sensor data. The reader subsequently receives this *backscattered* data (i.e. the signal reflected out of the tag directed toward the reader), and the process can repeat for the same tag or another tag in the environment.

Individually, passive tags are designed to be low-cost as most of their applications require up to thousands of tags to collect data at different locations in the environment. Conversely, only a few readers are desired to communicate with these tags to minimize cost and complexity. Passive tag circuitry consists of passive components such as diodes, capacitors, and transistors that can be scaled down into an Application-Specific Integrated Circuit (ASIC).

Most of the material cost of a passive WSN originates in the readers. The reader controls the communication medium in a passive WSN by indicating which tags are to activate and backscatter information. Readers transmit signals to the tags at the highest signal power point for the system (at the reader RX antenna as in Figure 1), and receive the backscattered signal at the lowest signal power point of the system (at the reader RX antenna). Therefore, readers are designed with a high dynamic range as compared to the tags. Low-noise amplifiers, analog-to-digital and digital-to-analog converters, and system oscillators are all located within readers.

2.2 Components of a Passive Tag

A passive tag is able to perform these functions:

1. Harvest DC energy from the received signal transmitted by the reader.
2. Detect the commands received from the reader.
3. Extract data from the environment using a sensor.
4. Backscatter the sensor data to the reader.

The block diagram shown in Figure 2 shows the components necessary for a tag to perform these functions. A detailed description of each block and its connection with the other blocks is given below.

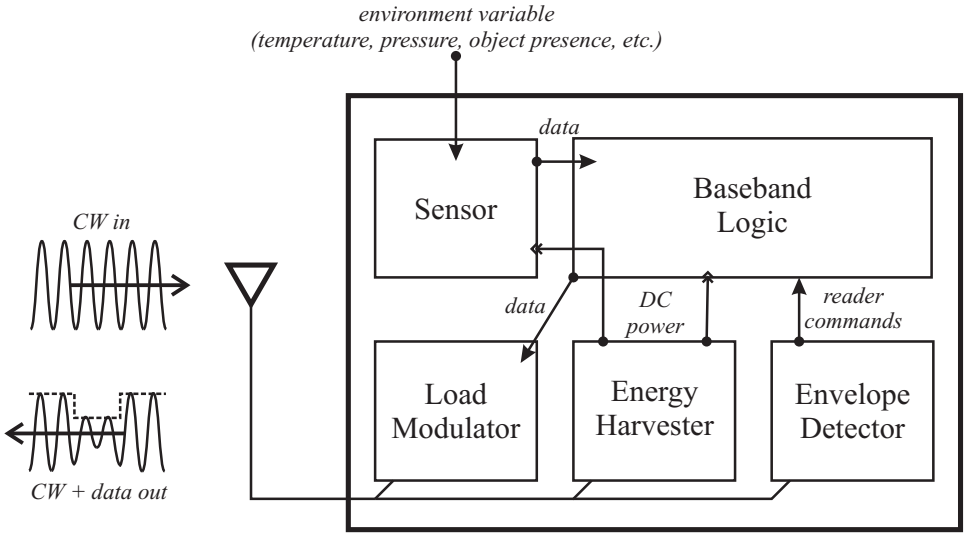

Figure 2: This block diagram of a passive tag shows the typical components used to take a sensor measurement, receive reader commands, reflect sensor data, and power itself.

2.2.1 Energy Harvester

A few charge pump topologies are used to convert RF power from the reader-transmitted signal into usable DC power for the tag's sensor and baseband logic. The Cockroft/Walton voltage multiplier was originally designed to generate high DC voltages ($>$ 100 kV) for atomic physics measurements [21]. The Villard voltage multiplier [22] is another example. The Dickson charge pump [17] is commonly used as well as modifications and improvements like pre-bias of diode-connected transisters [23]. All charge pumps use diodes or transistors as devices to control current flow. Thus, they all require input voltages large enough to forward-bias the threshold voltage.

The Dickson charge pump, originally designed for DC to DC conversion [17], also operates as an AC to DC rectifier and voltage booster. It can be produced inexpensively in CMOS taking up little area. Thus, the Dickson charge pump topology is commonly used for energy harvesting in passive wireless sensors and RFID tags [24]. It is a very power-efficient AC to DC converter when the input power is large enough to render the threshold voltage of the diodes insignificant. However, power efficiency suffers when the input is low-power, as is the case when a passive tag is taken to the outskirts of its read range. The diode threshold voltage then becomes the limiting obstacle, and the charge pump operates inefficiently. To

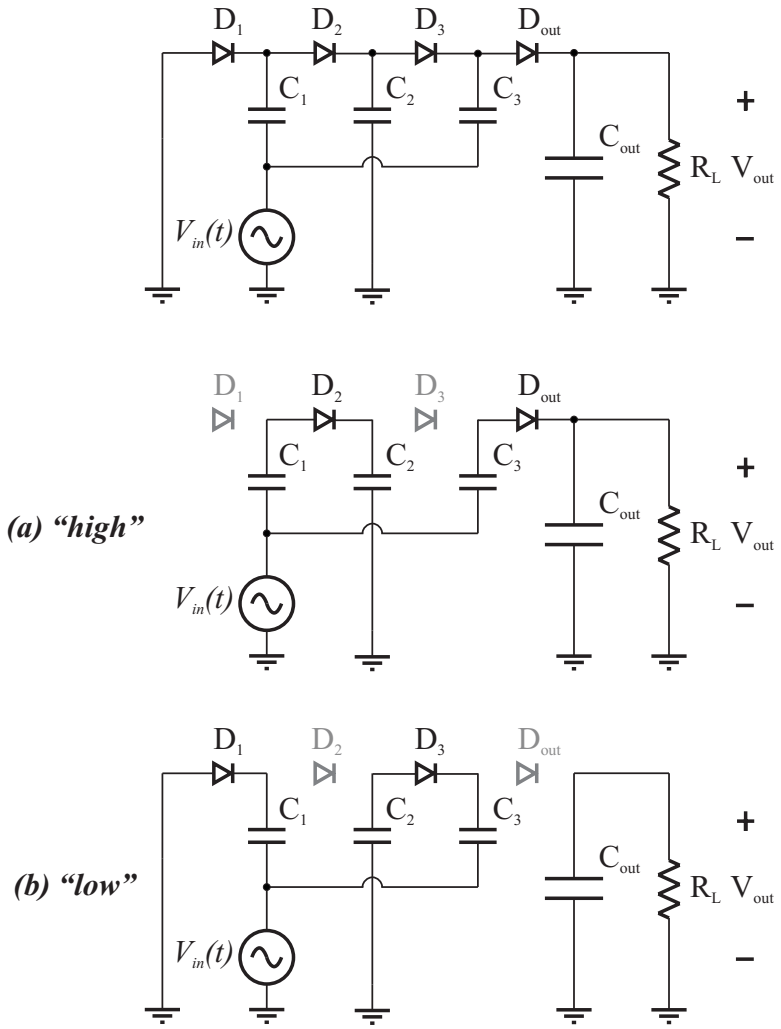

Figure 3: Dickson charge pump operation showing the different circuit states when the AC input voltage cycle is (a) high or (b) low.

see this effect, it is imperative to understand how the charge pump rectifies and boosts voltage.

The charge pumping operation is clearly described using the 4-stage Dickson charge pump shown in Figure 3 containing four capacitors, four diodes, and a load resistor, which represents the DC load of the passive tag. In Figure 3, the input voltage $V_{\text{in}}(t)$ represents the received signal from the tag antenna fed directly into the charge pump after impedance matching. The circuit takes on two distinct states that help to move charge from capacitor to capacitor: when the input voltage is (a) "high" ($V_{\text{in}}(t) > V_{\text{t}}$) and when the input voltage is (b) "low" ($V_{\text{in}}(t) < -V_{\text{t}}$) where V_{t} is the diode threshold voltage. Let V_{max} be the

maximum voltage of the input source.

In the "low" state, the input source pulls current from ground through diode D_1 into the first stage capacitor C_1 charging it up to $(V_{\max} - V_{\mathrm{t}})$. Capacitor C_1 holds its charge until the next "high" state when it helps charge capacitor C_2 to $2(V_{\max} - V_{\mathrm{t}})$. Notice here that the voltage presented to C_2 is the input voltage plus the voltage across C_1. During the next "low" state, the third stage capacitor, C_3 is charged to $3(V_{\max} - V_{\mathrm{t}})$ with the help of the second stage capacitor and input source. The output voltage across C_{out} then charges up to $4(V_{\max} - V_{\mathrm{t}})$ during the next "high" state.

The mechanism behind building a high output voltage is controlling charge transfer between stages with the diodes. However, overcoming the diode threshold is the largest obstacle for charge pump operation. The output voltage drops to zero when the maximum of the input voltage signal does not exceed the diode threshold, which makes the charge pump ineffective. This situation occurs when the input is low-power because the tag is at the edge of its read range. For example, suppose a passive tag's RF front end has a characteristic impedance of 300 Ω. This tag receiving a sinusoid with signal power of -10 dBm will reach a maximum voltage of 0.245 V, which is not high enough to meet the 0.7 V threshold voltage for standard silicon Schottky diodes. However, current passive RFID tags can operate with as little as -19.9 dBm of received power [25] with advanced RF matching and extremely low-threshold diodes.

2.2.2 Envelope Detector

The reader's AM signals are demodulated using a single diode-capacitor rectifying circuit that closely follows the envelope of the tag's received signal. The output of the envelope detector shown in Figure 4 is sent to a threshold detector, where the symbol decisions are made.

The capacitor size is designed to withstand a few periods of the CW so that symbol errors are less likely to occur. However, its time constant must be short enough to transition quickly between amplitude levels. The output of the threshold detector is fed to the baseband logic device for decoding.

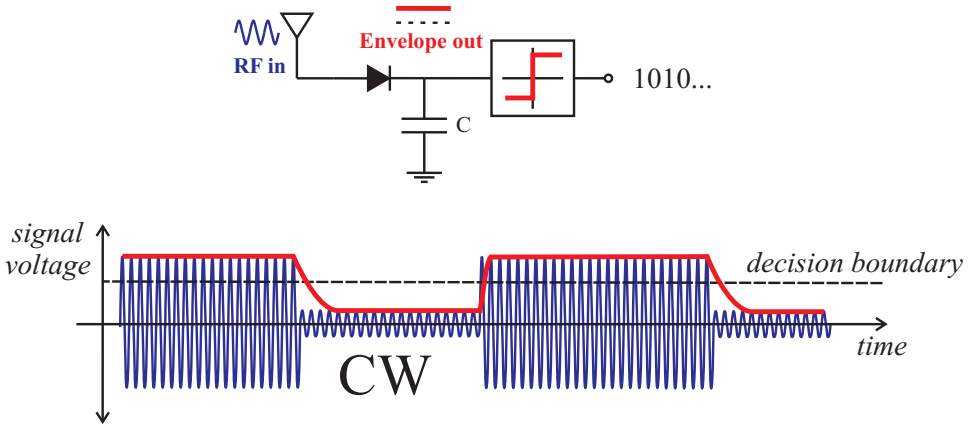

Figure 4: The envelope detector is a simple circuit for downconverting the received signal from the reader. The capacitor is designed to be large enough to withstand the time period between carrier peaks.

2.2.3 Baseband Logic Device

The baseband logic device takes the place of a central processor in a classical transceiver, which creates its own clock signal. Passive tags are designed to operate on as little DC power as possible, thus the received signal is used as a clock source for the logic device. Frequency division circuitry is then used to control the clock rate within the baseband logic. It is feasible for passive tags to use microcontrollers with local clocks such as the Texas Instruments MSP430 family of microcontrollers used in Intel Labs' wireless identification and sensing platform (WISP) tags [26]. The extra power needed to source the microcontroller's oscillator diminishes the tag's power sensitivity.

All other tag blocks interface with the baseband logic. The sensor is controlled and its data is read by baseband logic, which stores the data to temporary memory or static memory (e.g. EEPROM). The envelope detector provides data signals from the reader. The energy harvester provides DC power, which is used by the baseband logic to read and write to memory, detect received data, and control the sensor. Finally, the load modulator is switched between states according to the sensor data and communication protocol by the baseband logic.

2.2.4 Load Modulator

The signals entering the tag's antenna terminals reflect off the load impedance presented by the load modulator. The tag switches the effective load at the terminals by switching on and off a transistor switch, which connects and disconnects an extra load impedance. This switching process essentially creates an alternating reflection coefficient that modulates the impinging CW sent by the reader according to the tag data and communication protocol.

The reflected signal is partially attenuated due to the resistive part of the load states, yet it will be shown later in Section 2.3.2 that the complex Euclidian distance between reflection coefficients determines the received signal-to-noise ratio (SNR). The modulation factor M encapsulates the amount of backscattered signal power remaining after reflection in relation to the impinging signal power into the load modulator:

$$M = \frac{1}{4}\left|\tilde{\Gamma}_A - \tilde{\Gamma}_B\right|^2 \tag{4}$$

The difference between complex reflection coefficients $\tilde{\Gamma}_A$ and $\tilde{\Gamma}_B$ can be as high as 2 when one state is an open circuit ($\tilde{\Gamma}_A = 1$) and the other is an short circuit reflection ($\tilde{\Gamma}_B = -1$), which results in $M = 1$. This implies the reflected signal has the same signal power as the impinging signal. However, a passive tag needs to absorb power from the impinging signal to power itself through the energy harvester as well as reflect data. So, perfect short circuits and open circuits are very difficult to achieve.

The charge pump by itself can be used in lieu of one of the load impedance states devoted strictly to load modulation to save on component count. This has the added benefit of providing maximum available power to the charge pump rather than diverting some power to a separate load reflector. The downside is the charge pump's nonlinear reflective behavior, which comes from the diodes' characteristic curves. The effect of nonlinear reflections on the backscatter signal is addressed in detail in Section 4.5 where it will be shown that the reflected signal is a distorted version of the impinging waveform.

The tag modulator switches between states according to the sensor data and the signaling scheme. A frequency-modulation (FM) signaling scheme such as FM0 or Miller Modulation encoding is commonly used to convey data bits in the backscatter link. In FM0

encoding, the tag encodes two load state transitions to convey a "0" while encoding just one load state transition to convey a "1". Further background on FM0 and Miller Modulation is found in Dobkin's book [27].

2.2.5 Antenna

Tag orientation in the environment with respect to the reader is random. The tag may be flipped upside down or rotated around as the object to which it is attached moves or the environment changes, thus the antenna is designed for omni-directionality. This limits the maximum gain in any particular direction but does protect against loss of power due to a pattern null.

Inductive loops serve as the main matching technique as shown in Figure 5 (e.g. for Radio Frequency IDentification (RFID) tags). Tag antennas are conjugate matched to the ASIC, which is the conglomeration of impedances from the charge pump, envelope detector, baseband logic, and load modulator. It is typical of tag ASICs to have a negative reactance at the designed frequency due to the capacitive nature of CMOS diodes, capacitors, and transistors; hence the reason for the inductive loop. Discretized designs such as the Intel WISP use two-element matching networks to match to the charge pump [26]. The voltage magnitude presented to the ASIC (and thus the charge pump) is dependent on the magnitude of the reactance of the antenna and tag:

$$|V_{\text{in}}| = \frac{2\sqrt{R_{\text{tag}}^2 + X_{\text{tag}}^2} \cdot \sqrt{2R_{\text{A}}P_{\text{tag}}}}{\sqrt{(R_{\text{tag}}^2 + R_{\text{A}}^2) + (X_{\text{tag}}^2 + X_{\text{A}}^2)}} \tag{5}$$

The tag's total ASIC impedance is $\tilde{Z}_{\text{tag}} = R_{\text{tag}} + jX_{\text{tag}}\ \Omega$ and the antenna's impedance is $\tilde{Z}_{\text{A}} = R_{\text{A}} + jX_{\text{A}}\ \Omega$.

Beyond matching, there are two environmental factors that can diminish the amount of power received by the tag. In the first factor, antenna gain penalties arise when the tag is placed on or near a conductor or dielectric thereby changing the antenna impedance and distorting the gain pattern. The **on-object penalty** is defined as the ratio of free-space, load-matched gain to the gain of the tag antenna attached to an object:

$$\Theta = \frac{G_{\text{tag}}}{G_{\text{on-obj}}} \tag{6}$$

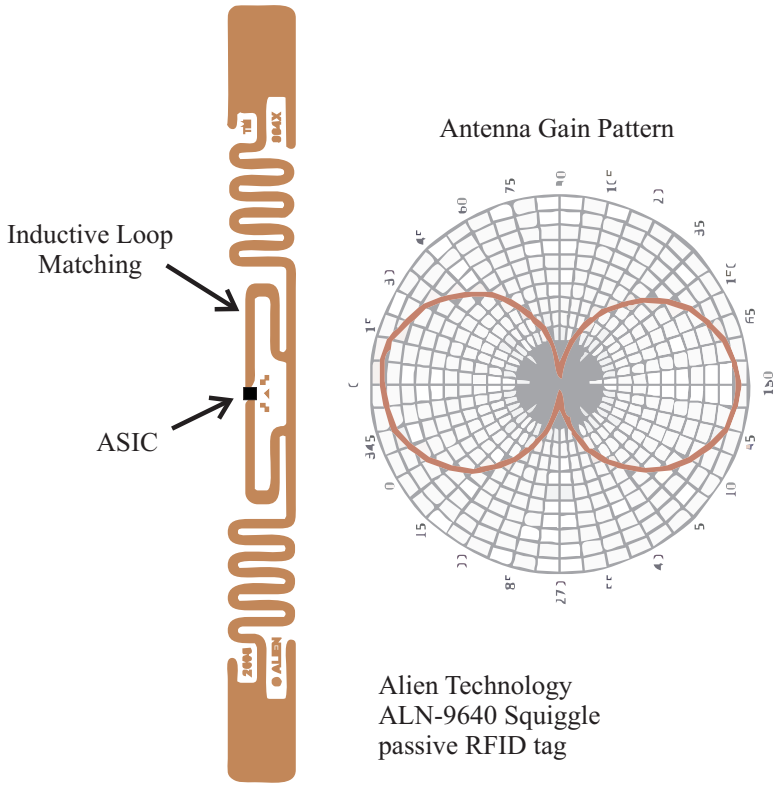

Figure 5: The typical passive RFID tag antenna consists of an omni-directional topology (dipole with meandering traces in this case) and an inductive loop to match to a net capacitive ASIC. (Image and pattern from data sheet [2])

Table 1: On-object gain penalties for various materials measured at 915 MHz with a dB scale [1]

Cardboard Sheet	Acrylic Slab	Pine Plywood	De-Ionized Water	Ethylene Glycol	Ground Beef	Aluminum Slab
0.9 dB	1.1 dB	4.7 dB	5.8 dB	7.6 dB	10.2 dB	10.4 dB

Some measured values obtained by Griffin. et. al. at 915 MHz are shown in Table 1 showing the effect of placing the tag antenna on various materials [1]. Placing tags on cardboard boxes, bottles of water, trees, or aluminum engine blocks can severely reduce the tag's antenna gain according to the table.

In the second factor, **polarization mismatch** (quanitifed as X in a link budget equation, not to be confused with reactance) between the reader antenna(s) and tag antenna can vary from zero to one in the linear scale. For example, a linearly polarized reader transmitter antenna oriented vertically transmitting to a linearly polarized tag antenna that has

been oriented horizontally by the environment would not be able to communicate. The polarization mismatch is zero in this case. When designing a WSN link budget, it is useful to assume an average polarization mismatch of 0.5 to account for the randomness of tag orientation relative to the reader antenna(s). Circularly polarized antennas used on the reader and tag can reduce the chance of mismatch due to random rotation but not pitch or yaw relative to the reader antenna.

2.2.6 Sensor

The sensor provides the link between the environment and the tag. It is provided with power from the baseband logic device via the charge pump and can be duty-cycled (periodically turned on and then turned off) to save power. Some sensors require a bias voltage to operate such as thermometers and accelerometers, and all analog sensors require analog to digital converters that provide the baseband logic with sensor data. Completely passive sensors such as Reflected ElectroMagnetic Signature (REMS) [28] and Surface Acoustic Wave (SAW) [29] tags are controlled from the reader instead of the tag logic, so no power needs to be provided.

2.3 Components of a Reader

The reader is able to perform the following functions:

1. Control each tag's access to the communication medium.
2. Provide power to the tags.
3. Demodulate the tags' backscatter data.
4. Interface with the user.

These tasks are accomplished with a transceiver architecture as shown in Figure 6. Readers may employ antenna structures in a monostatic (one transceiving antenna) or bistatic (one antenna for transmitting, one for receiving) mode. More detail about each reader component is given in the next few sections.

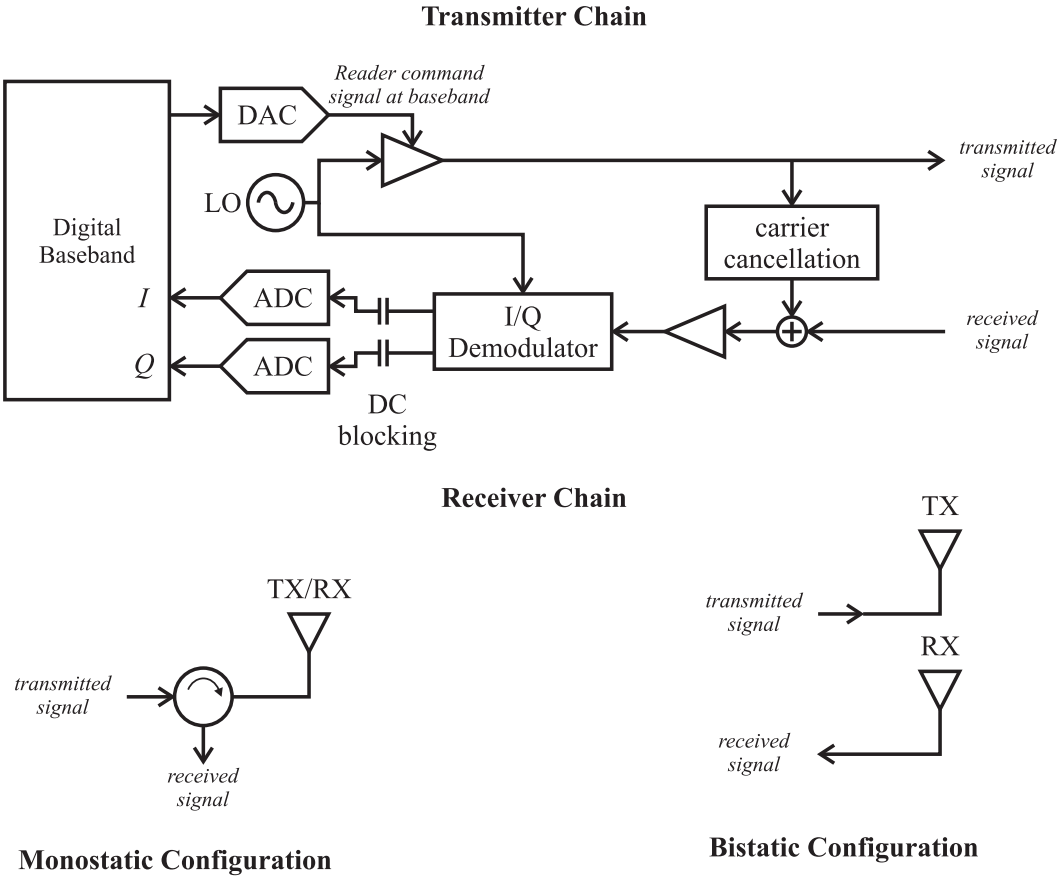

Figure 6: A reader is composed of a transmitter chain, receiver chain, and either a monostatic or bistatic configuration of antennas.

Some existing communication protocols used by wireless sensor networks to interface the readers with tags are listed here. The items in bold represent protocols for use with far-field, energy-harvesting, passive tags:

- ISO 18000-1: Generic parameters for air interfaces for globally accepted frequencies
- ISO 18000-2: Air interface standard for 135 kHz
- ISO 18000-3: Air interface standard for 13.56 MHz
- **ISO 18000-4: Air interface standard for 2.45 GHz**
- **ISO 18000-6: Air interface standard for 860 to 930 MHz**
- ISO 18000-7: Air interface standard for 433.92 MHz

- IEEE 802.15.1: "Bluetooth" standard for 2.4 GHz
- IEEE 802.15.2: WPANs coexisting with WLANs
- IEEE 802.15.3: High-rate WPANs greater than 11 $^{\text{Mbits}}/_{\text{s}}$
- **IEEE 802.15.4: Low-rate WPANs for semi-passive tags or long-battery life tags on which the Zigbee specification is based**
- EnOcean: passive tags that harvest energy from non-electromagnetic sources such as vibration or solar energy

This research will focus on protocols that are half-duplex, reader-talks-first protocols such as ISO 18000-6.

2.3.1 Transmitter Chain

In reader-talks-first protocols, the reader's command signal is amplitude modulated on to a carrier and transmitted to the tag. Figure 7 shows two configurations for upconverting and amplifying the signal. It can be accomplished classically by mixing the reader command signal with the carrier prior to amplification through an amplifier. However, mixers can produce intermodulation products and drive the amplifier into its nonlinear gain. To avoid this, a reader will power the amplifier with the reader command signal itself, which is common practice in passive RFID in the ISO 18000-6 protocol [27]. This keeps the amplifier within its linear range. Class A amplifiers are typically chosen for their high linearity when the power pin is supplied with the reader command signal. However, a power-conscious design would choose a class AB or class C amplifier where the signal is premixed and the amplifier is powered with a DC power supply.

The output of the amplifier, after any necessary filtering, is routed to the transmitting antenna in a bistatic configuration. Alternatively, the signal can be routed to the monostatic transceiving antenna via a circulator. Both configurations will produce self-interference. In the bistatic configuration, the receiver antenna will unintentionally receive the transmitted signal. And the reflected signal off the monostatic transceiving antenna will pass through the circulator to the receiver chain.

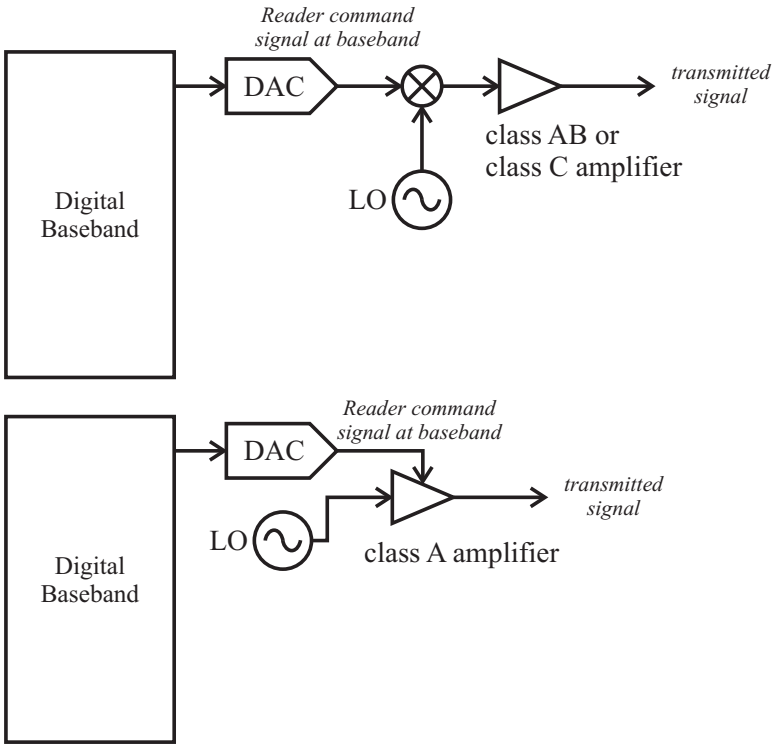

Figure 7: A classical technique mixes the reader commands with the carrier before amplification, but connecting the reader commands to the power pin of the amplifier itself maintains high linearity.

2.3.2 Receiver Chain

The signal received at the reader's receive antenna contains the tag's backscatter response, noise, multipath components and self-interference. Figure 8 helps visualize each of the signal components. Each of these signal components are contained in this signal model:

$$\tilde{y}(t) \quad = \quad \alpha\tilde{b}(t-\tau)r(t-\tau)e^{-j2\pi f_c(t-\tau)} + \sum_{l=1}^{L} \alpha_l r(t-\tau_l)e^{-j2\pi f_c(t-\tau_l)} + \tilde{n}(t) \qquad (7)$$

where $r(t-\tau)e^{-j\omega(t-\tau)}$ is the upconverted reader command signal delayed in time by τ s corresponding to the round-trip time delay of the signal propagating from the reader to the tag and back to the reader. The backscattered data signal $\tilde{b}(t-\tau)$ is the modulating reflection coefficient provided by the tag encoded with a FM signaling scheme. The received amplitude of each component is contained in the terms α and α_l, both of which account for link budget items such as path loss, antenna gain, and antenna polarization effects. The summation term $\sum_{l=1}^{L} \alpha_l r(t-\tau_l)e^{-j\omega(t-\tau_l)}$ consolidates all multipath bounces that are not

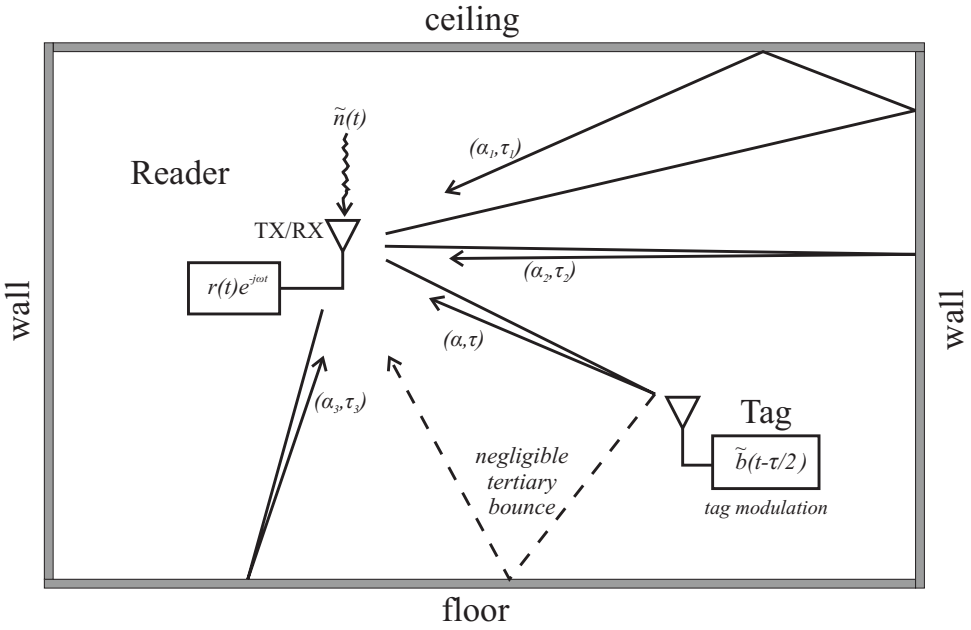

Figure 8: The received signal contains the time-delayed, amplitude-decayed versions of the transmitted signal. The environmental clutter provides unmodulated signal components while the tag modulates its data signal on the carrier. Tertiary bounces as shown are assumed negligible and do not contribute significantly to the signal model.

modulated by the tag on the backscatter link. This includes self-interference where the transmitted signal leaks into the receiver chain at a significantly high power level as compared to the tag's backscattered signal power. This model does not account for modulated tertiary bounces (e.g. when the signal propagates from the reader transmitter antenna to the tag, gets modulated by the tag, then to a wall, and back to the reader). It is assumed that the interference from these tertiary bounces are negligible. Lastly, $\tilde{n}(t)$ is a complex AWGN noise process with noise power $P_{\mathrm{N}} = kTB$.

The main function of the reader receiver chain is to demodulate the tag data, which is mired in interference and noise as shown in the received signal model of equation (7). A typical receiver is shown in Figure 9. A receiver first downconverts the received signal to the baseband either directly (as a homodyne receiver) or using an intermediate frequency (heterodyne receiver) to filter any near-band interferers. Once the signal is in the baseband, the DC block filters out the unmodulated self-interference and multipath components.

Carrier cancellation is necessary when the tag response is significantly lower power ($>$ 60 dB down) than the self-interference of the receiver. Reducing the self-interference

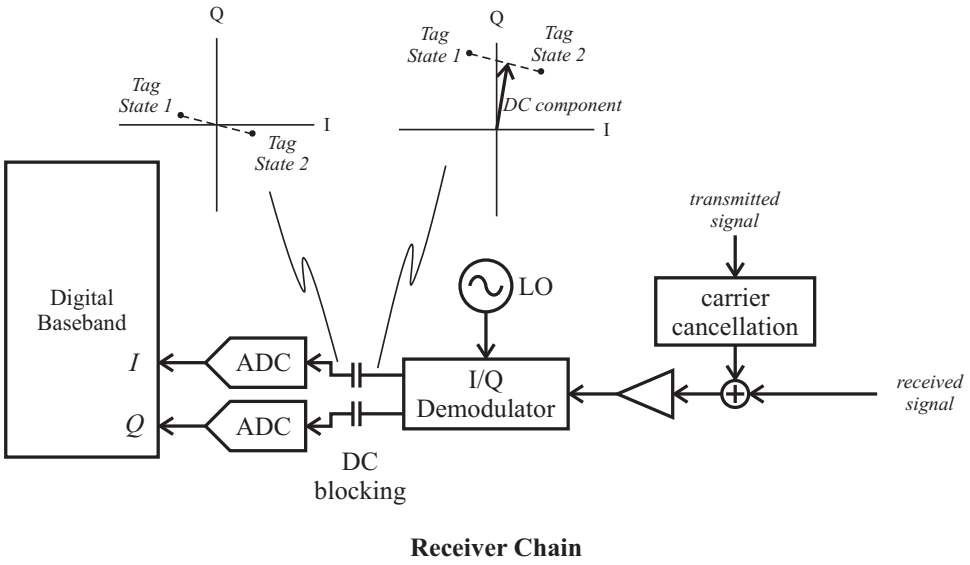

Figure 9: A homodyne I/Q reader receiver filters out multipath components and self-interference using active cancellation and a DC block in the baseband.

prior to passband amplification reduces the likelihood of voltage clipping within the passband amplifiers, which destroys the tag backscatter component in the received signal. A cost-effective method for carrier cancellation is fabricating a delay line from the transmitter chain to the receiver chain to coherently cancel the self-interference. The delay line must attenuate the carrier to the same power level as the self-interference signal. Lasser et. al. achieved a 40 dB reduction in self-interference in the receiver chain across an 82 MHz bandwidth in the UHF band 860 - 960 MHz [30]. A more robust, yet costlier method is to design a variable attenuator with a negative feedback loop that actively tries to completely cancel the self-interference. However, active cancellation is unnecessary when the amplifiers are designed to withstand the self-interference without clipping. In either case, the unmodulated multipath and self-interference signal components will downconvert straight to DC in the I and Q channels.

The DC blocking capacitors block out the DC component of the received signal leaving zero-centered I and Q signals as shown in Figure 9. The tag's backscatter signal represents a small portion of the received signal, but the DC-blocked signal filters out all interferers. The resulting SNR is found by performing a complete linear link budget covering all aspects of the signal channel. This list covers the monostatic case:

1. Reader TX antenna gain G_{TR}
2. Reader TX power P_{T}
3. Forward link path loss $(\lambda/4\pi R)^2$
4. Path blockage B_{path}
5. Tag antenna gain (G_{tag}^2 total; from forward and backscatter link)
6. Modulation factor M
7. Reader to tag antenna polarization mismatch (X^2 total; from forward and backscatter link)
8. Tag-on-object penalty Θ
9. Fade margin F
10. Path blockage B_{path}
11. Backscatter link path loss $(\lambda/4\pi R)^2$
12. Reader RX antenna gain $G_{\mathrm{TX/RX}}$

These items together make up the monostatic link budget, where the total received backscatter signal power at the output terminals of the reader transceiving antenna is found with:

$$\text{(linear)}\quad P_{\mathrm{R}} = \frac{P_{\mathrm{T}} G_{\mathrm{TR}}^2 G_{\mathrm{tag}}^2 \lambda^4 X^2 M}{(4\pi R)^4 \Theta^2 B_{\mathrm{path}}^2 F}\ \text{(W)} \tag{8}$$

$$\begin{aligned}\text{(log)}\quad P_{\mathrm{R}} &= P_{\mathrm{T}} + 2G_{\mathrm{TR}} + 2G_{\mathrm{tag}} + 2\cdot 20\log_{10}\left(\frac{\lambda}{4\pi R}\right) \\ &\quad +2X + M - 2\Theta - 2B_{\mathrm{path}} - F\ \text{(dB)}\end{aligned} \tag{9}$$

Path blockage quantifies the amount of signal power lost due to a line-of-sight (LOS) impediment such as a wall, a group of trees, or a person. The standard model in conventional one-way wireless sensors is the *log-normal* distribution, where the mean of the log-normal distribution is chosen for B_{path} in the link budget. The distribution is defined for the

logarithmic variable B_{path} (dB):

$$f_{\text{B}_{\text{path}}}(b_{\text{path}}\ (\text{dB})) = \frac{1}{\sigma_B\sqrt{2\pi}} e^{-(b_{\text{path}}-\mu_{\text{path}})^2/2\sigma_B^2}, \tag{10}$$

In very short-range (< 2 m) passive backscatter links, it can be safely assumed that path blockages are unlikely resulting in $B_{\text{path}} = 0$ dB.

The **fade margin** F quantifies the most likely value of received power at the reader receiver antenna, which is dependent on tag position in a cluttered environment that experiences small-scale fading. The net constructive and destructive interference of radio waves received by the tag from the reader have a Rician distribution for LOS channels and a Rayleigh distribution for non-LOS channels. However, the signal power at a monostatic reader receiver will experience a product-Rician or product-Rayleigh distribution due to the round-trip nature of the forward and backscatter links together. The linear fade margin value can be found once the fading distribution is known and the specification for outage probability is known using

$$F = \frac{F_R^{-1}(\text{ Outage prob. spec.})}{P_{\text{av}}}, \tag{11}$$

where F_R is the cumulative distribution function of the reader-received signal envelope and P_{av} is the average power in the channel (in units of envelope-squared).

The SNR at the reader receiver antenna output is $\text{SNR}_{\text{rec}} = P_{\text{R}} - 10\log_{10}(kTB)\ (dB)$. Finally, the SNR of the complex baseband I/Q signal used for symbol detection, assuming multipath components have been completely cancelled with DC blocking, is the received SNR degraded by the noise figures of the subsequent amplifiers within the receiver.

$$\text{SNR}_{\text{base}} = \text{SNR}_{\text{rec}} - \text{NF}_1 - \text{NF}_2 - \ldots - \text{NF}_{\text{K}}\ (\text{dB}) \tag{12}$$

where NF_{K} is the noise figure of the K^{th} receiver in the chain.

CHAPTER III

POWER-OPTIMIZED WAVEFORMS

Passive WSNs are comparatively less costly to maintain than semi-passive or active WSNs that accomplish the same sensing task. Passive tags are generally fabricated inexpensively, and they do not require battery replacement. Thus, passive WSNs are preferred in many sensing applications that sense in hazardous environments or demand autonomy. One such hazardous environment and autonomous application is the monitoring of current in high-voltage power lines within power substations [31]. Here, passive WSNs are ideal for monitoring current since there are no batteries that need to be replaced.

The autonomy of passive WSNs motivates the need for achieving a highly reliable response rate of each tag. Passive tags are expected to work "reliably" (definitions vary, but this means approximately 100% of the time) without human adjustments. Reliability is greatly improved when the tags are close to the reader thus capturing a large amount of radiated power. However, this means many tags and readers are necessary to cover a large space such as a warehouse, which increases total system cost. Thus, cost motivates the need for increasing the maximum range of each tag from the reader.

Research on range and reliability improvement is split into two categories: on-tag and off-tag research. On-tag research focuses on reducing tag power consumption in the tag's physical structure. For instance, investigating low-parasitic components, low-power circuit design, duty-cycling algorithms, impedance matching networks, and tag antenna designs are all considered on-tag research. Off-tag research focuses on reducing tag power consumption without changing the tag. Two specific examples include intermittent continuous wave (CW) transmission [32] and auxiliary CW transmission [33]. The intermittent CW transmission provides a low-average power yet high-peak power waveform into the charge pump. This method improves the energy harvesting efficiency of the passive tag and is essentially the same method as the "Square POW" discussed in later in Section 3.1.2. The

auxiliary CW transmission uses a secondary reader-transmitter to transmit the same CW frequency as the primary reader-transceiver. This method reduces the probability of a deep fade from the destructive interference imposed by random environmental clutter.

Power-optimized waveforms (POWs) are an off-tag method for improving the reliability and maximum range of a tag. POWs are defined next in Section 3.1. A model for expected gains using POWs and demonstrations of POWs operating on passive RFID tags are presented in Section 3.2. The necessary architecture changes to the reader to accomodate the transmission and reception of POWs are discussed in Section 3.4.2. Lastly, the signal model for the complete backscattered signal received at the reader under a POW transmission is presented in Section 3.3.

3.1 Power-Optimized Waveforms Defined

A **power-optimized waveform** (POW) is a multiple-tone carrier that is designed to improve the energy-harvesting efficiency of charge pump-based tags while preserving the ability to exchange information between tag and reader. All POWs have a passband peak-to-average power ratio (PAPR) greater than two, which is the PAPR of a CW. This simply means a POW has a nonconstant envelope as opposed to the CW, which has a constant envelope.

The choice of POW shape, bandwidth, time period, and PAPR in a WSN are dependent on the design specifications for available spectrum, tag quality factor, ranging performance (seen later in Chapter 4), and maximum tag range. An infinite number of POW shapes are possible that provide a nonconstant passband envelope with a PAPR greater than two. Three possible POW shapes are analyzed here: the M-POW, Gaussian-POW, and Square-POW.

In the following sections, the shape-specific parameters of each of these POWs are defined along with their time-domain representation, frequency spectrum, 3-dB bandwidth, PAPR, and RMS time width. RMS bandwidth is derived as well since it characterizes ranging performance (explained in Chapter 4). The POW spectrum is defined as the Fourier transform of the periodic pulse train of POW pulses. 3-dB bandwidth is defined on the POW

spectrum as the minimum frequency band such that all spectral content outside of the band is attenuated more than 3 dB from the peak.

RMS bandwidth and RMS time width are defined on a single POW pulse as opposed to the POW pulse train. RMS bandwidth is another measure of the spectral width and is defined as

$$B_{\text{RMS}} = \sqrt{\frac{\int_{-\infty}^{\infty} f^2 \text{POW}_{\text{pls}}^2(f) df}{\int_{-\infty}^{\infty} \text{POW}_{\text{pls}}^2(f) df}}. \tag{13}$$

The numerator is the 2$^{\text{nd}}$ centered moment of the single-pulse spectrum $\text{POW}_{\text{pls}}(f)$ of the POW, and the denominator is the energy of the single-pulse. Similarly, the RMS time width is defined in the time domain as

$$T_{\text{RMS}} = \sqrt{\frac{\int_{-\infty}^{\infty} t^2 \text{pow}_{\text{pls}}^2(t) dt}{\int_{-\infty}^{\infty} \text{pow}_{\text{pls}}^2(t) dt}}. \tag{14}$$

Again, this integral is taken across one POW pulse. The denominator is the signal energy, which is equivalent to the denominator in the RMS bandwidth definition by Parseval's Theorem. The uncertainty principle links these two RMS measures together [34]:

$$B_{\text{RMS}}^2 T_{\text{RMS}}^2 \geq \frac{1}{16\pi^2} \tag{15}$$

The only function that satisfies the equality is the Gaussian function, which is presented as a POW shape in the next section. All other waveform shapes have the product of the RMS bandwidth and RMS time width greater than $1/16\pi^2$.

PAPR is defined as

$$\text{PAPR} = \frac{\max(\text{pow}_{\text{pls}}^2(t))}{P_{\text{avg}}}, \tag{16}$$

where the numerator is the peak signal power (in V^2), and the denominator is the average signal power (in V^2) across one POW time period. The POW time period T_{POW} is the length of time between the peaks of consecutive POW pulses.

3.1.1 Gaussian-POW

The Gaussian function satisfies the equality in the uncertainty principle from equation (15). The time-domain definition of the Gaussian POW is the square-root of the Gaussian function. The square-root is taken because the formulas for the RMS widths and PAPR are

simpler. The periodic POW with time period T_{POW} is defined as

$$\mathrm{pow}(t) = \sqrt{\frac{P_{\mathrm{avg}} T_{\mathrm{POW}}}{\sigma}} \frac{1}{\sqrt[4]{2\pi}} \sum_{k=\infty}^{\infty} e^{\frac{-(t-kT_{\mathrm{POW}})^2}{4\sigma^2}}. \tag{17}$$

The signal power function ($\mathrm{pow}^2(t)$) of this Gaussian POW definition is an infinite train of pulses where each pulse is the well-known Normal distribution definition from probability theory. The "standard deviation" σ is a measure of the length of time the Gaussian POW signal power rises to a high voltage. Figures 10 through 12 show three realizations of the Gaussian POW spanning multiple "standard deviations". The peak signal power of the Gaussian POW is ${}^{P_{\mathrm{avg}} T_{\mathrm{POW}}}/_{\sigma\sqrt{2\pi}}$. The average power is P_{avg} in the baseband and ${}^{P_{\mathrm{avg}}}/_{2}$ in the passband. Therefore, the passband PAPR is

$$\mathrm{PAPR} = \sqrt{\frac{2}{\pi}} \cdot \frac{T_{\mathrm{POW}}}{\sigma} \approx 0.7979 \frac{T_{\mathrm{POW}}}{\sigma} \tag{18}$$

This PAPR equation and the equations below assume the small tail approximation where the Gaussian function is assumed to decay to exactly zero at the beginning and end of the POW time period.

The envelope of the frequency spectrum is also Gaussian:

$$\mathrm{POW}(f) = \sqrt{\sigma P_{\mathrm{avg}} T_{\mathrm{POW}}} \sqrt[4]{8\pi} e^{-4\pi^2\sigma^2 f^2} \sum_{k=-\infty}^{\infty} \delta(f + \frac{k}{T_{\mathrm{POW}}}) \tag{19}$$

This spectrum as written is the spectrum of the Gaussian pulse train in equation (17). The 3-dB bandwidth of the Gaussian-POW is found by equating the spectrum envelope (i.e. the spectrum of a single Gaussian POW pulse) to the half-power point of its spectrum, which has maximum power at zero frequency. The 3-dB bandwidth of the periodic POW pulse train is computed from this 3-dB envelope calculation. The 3-dB bandwidth of the single-pulse function and the periodic function is

$$B_{\mathrm{3dB,pls}} = \frac{\sqrt{-\ln(\frac{1}{2})}}{\sqrt{2}\pi\sigma} \approx \frac{0.1874}{\sigma}, \tag{20}$$

$$B_{\mathrm{3dB}} = \max\left(\frac{2k}{T_{\mathrm{POW}}} : k < \frac{T_{\mathrm{POW}} B_{\mathrm{3dB,pls}}}{4} \text{ and } k \in \mathbb{N}\right) \tag{21}$$

where $\mathbb{N}$ is the set of natural numbers (1, 2, 3, ...). The Gaussian-POW spectrum is combed with the Dirac comb function, and the Gaussian-POW 3-dB bandwidth is twice the frequency of the maximum-frequency subcarrier that lies at a frequency less than $B_{\mathrm{3dB,pls}}/2$.

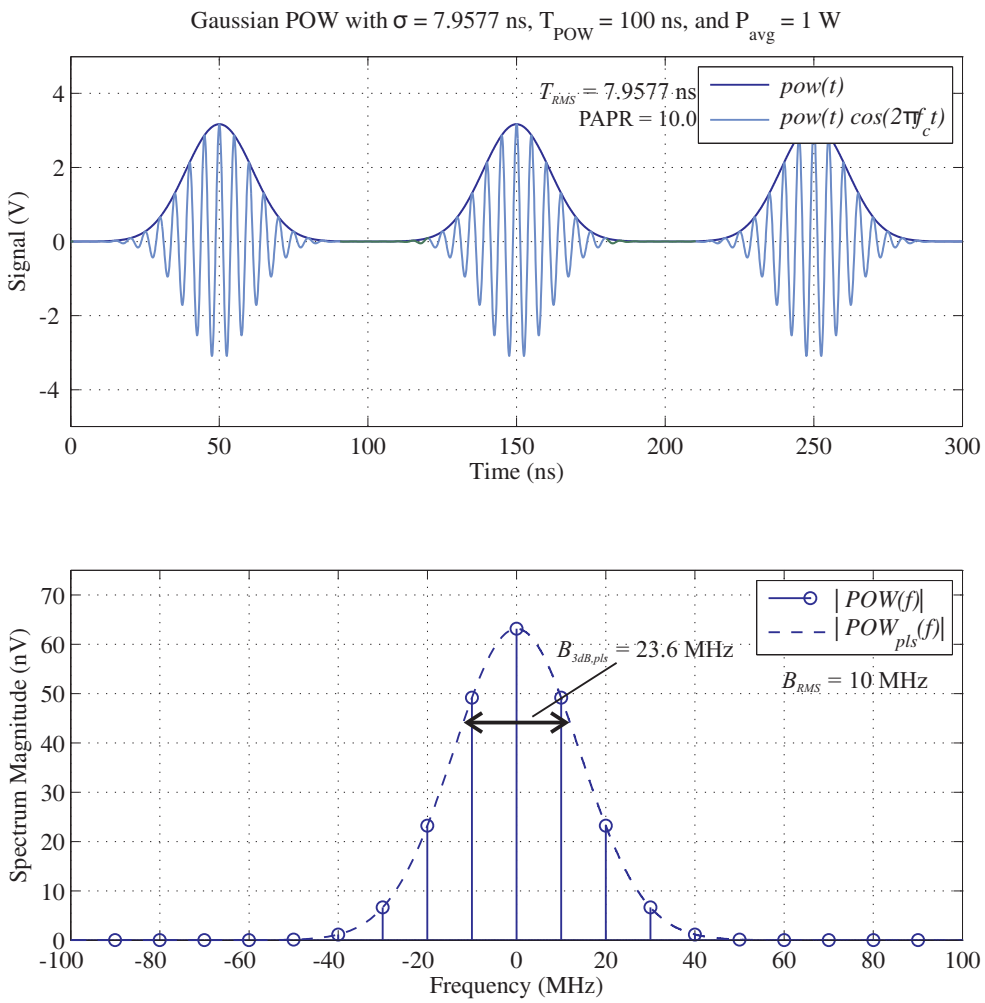

Figure 10: A Gaussian-POW with parameter $\sigma = 7.9577$ ns, which corresponds to a RMS bandwidth $B_{\text{RMS}} = 10$ MHz. The time-domain plot shows the baseband envelope and the passband signal assuming a center frequency of 200 MHz for figure clarity. The spectrums shown are the single-pulse spectrum $POW_{\text{pls}}(f)$ and periodic spectrum $POW(f)$ from equation (19) where the POW time period $T_{\text{POW}} = 100$ ns.

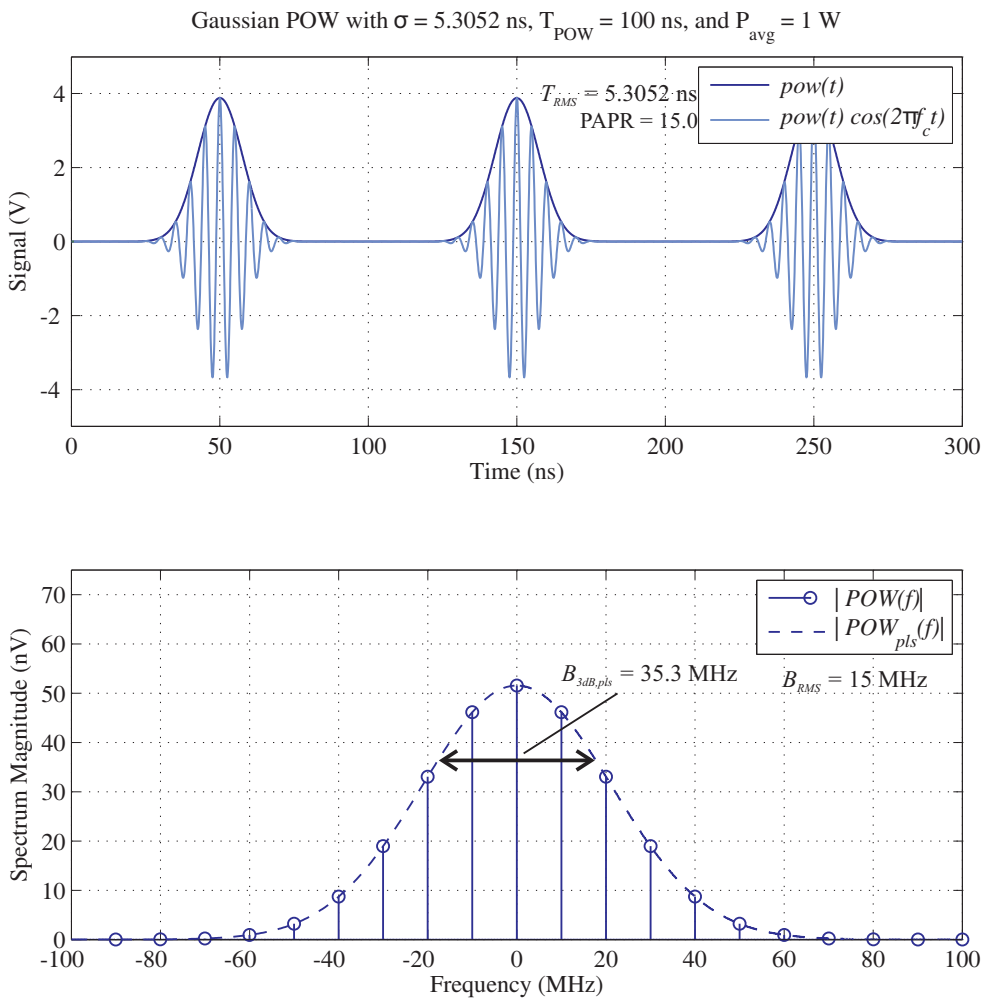

Figure 11: A Gaussian-POW with parameter $\sigma = 5.3052$ ns, which corresponds to a RMS bandwidth $B_{\text{RMS}} = 15$ MHz. The time-domain plot shows the baseband envelope and the passband signal assuming a center frequency of 200 MHz for figure clarity. The spectrums shown are the single-pulse spectrum $POW_{\text{pls}}(f)$ and periodic spectrum $POW(f)$ from equation (19) where the POW time period $T_{\text{POW}} = 100$ ns.

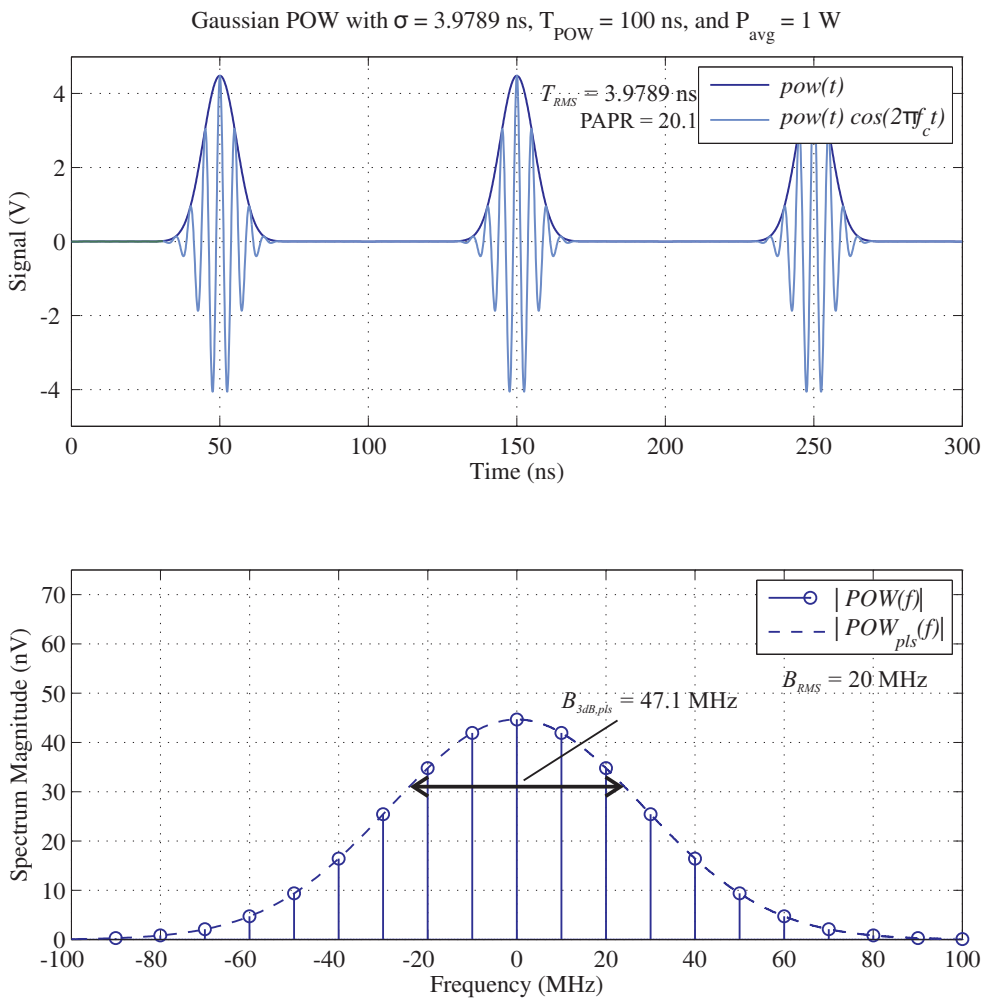

Figure 12: A Gaussian-POW with parameter $\sigma = 3.9789$ ns, which corresponds to a RMS bandwidth $B_{\text{RMS}} = 20$ MHz.The time-domain plot shows the baseband envelope and the passband signal assuming a center frequency of 200 MHz for figure clarity. The spectrums shown are the single-pulse spectrum $POW_{\text{pls}}(f)$ and periodic spectrum $POW(f)$ from equation (19) where the POW time period $T_{\text{POW}} = 100$ ns.

The RMS bandwidth and RMS time width are calculated in the baseband with respect to a single Gaussian pulse as opposed to the periodic function. These definitions are pertinent to ranging performance equations presented in the next chapter. The analysis is identical to wavelet analysis where the waveforms have finite duration and bandlimited spectrums [35]. The RMS time width and RMS bandwidth are

$$T_{\mathrm{RMS}} = \sigma \tag{22}$$

$$B_{\mathrm{RMS}} = \frac{1}{4\pi\sigma} \tag{23}$$

These RMS widths are related to the PAPR by

$$T_{\mathrm{RMS}} = \sqrt{\frac{2}{\pi}} \cdot \frac{T_{\mathrm{POW}}}{\mathrm{PAPR}} \tag{24}$$

$$B_{\mathrm{RMS}} = \frac{\mathrm{PAPR}}{4\sqrt{2\pi}T_{\mathrm{POW}}}. \tag{25}$$

The uncertainty principle shows that the Gaussian POW spectrum has the narrowest RMS bandwidth of any possible POW shape with identical RMS time widths. This suggests that the Gaussian POW is a very spectrally-efficient POW. Spectral mask requirements are most easily met with a Gaussian POW.

A slowly changing, low-PAPR Gaussian POW affords a charge pump plenty of time to charge and discharge the stage capacitors. Conversely, a quickly changing, high-PAPR Gaussian POW presents large voltage swings to a charge pump, which induces large current spikes from the transient charging and discharging of the stage capacitors. It will be shown later in Section 4.5 that a large transient current spike produces a large distortion on the waveform reflected from a charge pump.

3.1.2 Square-POW

The square-POW is the familiar rectangular pulse train with duty cycle D, low-voltage level B, and high-voltage level A. The time-domain representation of a Square-POW is

$$\mathrm{pow}(t) = B + \sum_{k=-\infty}^{\infty} (A-B)\mathrm{rect}\left(\frac{t - kT_{\mathrm{POW}}}{DT_{\mathrm{POW}}}\right), \tag{26}$$

$$\text{where rect}\left(\frac{t - kT_{\mathrm{POW}}}{DT_{\mathrm{POW}}}\right) = \begin{cases} 1 & \frac{DT_{\mathrm{POW}}}{2} \le t - kT_{\mathrm{POW}} < \frac{DT_{\mathrm{POW}}}{2} \\ 0 & \text{otherwise} \end{cases} \tag{27}$$

The PAPR for the Square-POW in the passband is twice the baseband PAPR with the multiplication of a cosine carrier. The passband PAPR for the square-POW is

$$\text{PAPR} = \frac{2}{D + (B^2/A^2)(1-D)}. \tag{28}$$

In the special case where the low level voltage $B = 0$, PAPR reduces to the simple result $2/D$.

The duty cycle D, which ranges between 0 and 1, controls the width of the rectangle pulse and the spacing of the subcarriers in the square-POW spectrum:

$$\text{POW}(f) = B\delta(f) + (A-B)DT_{\text{POW}} \cdot \text{sinc}(\pi DT_{\text{POW}} f) \sum_{k=-\infty}^{\infty} \delta\left(f - \frac{k}{T_{\text{POW}}}\right), \tag{29}$$

$$\text{where} \quad \text{sinc}(x) \quad = \quad \frac{\sin(x)}{x}. \tag{30}$$

The 3-dB bandwidth of the square-POW is found by equating the single-pulse spectrum envelope to the half-power point of the spectrum, which has maximum power at zero frequency. The 3-dB bandwidth of the spectrum envelope is

$$B_{\text{3dB,pls}} \quad = \quad \frac{2}{\pi DT_{\text{POW}}} \text{sinc}^{-1}\left(\frac{1}{\sqrt{2}}\left(\frac{B}{(A-B)DT_{\text{POW}}} + 1\right)\right) \tag{31}$$

$$\approx \quad \frac{0.8859}{DT_{\text{POW}}} \quad \text{when} \quad B = 0. \tag{32}$$

where the inverse sinc function produces multiple positive and negative solutions. Only the solution $0 < x < \pi$ is valid for the 3-dB envelope calculation. The periodic Square-POW 3-dB bandwidth is twice the frequency of the maximum-frequency subcarrier that lies at a frequency less than $B_{\text{3dB,pls}}/2$:

$$B_{\text{3dB}} \quad = \quad \max\left(\frac{2k}{T_{\text{POW}}} : k < \frac{T_{\text{POW}} B_{\text{3dB,pls}}}{4} \text{ and } k \in \mathbb{N}\right) \tag{33}$$

where $\mathbb{N}$ is the set of natural numbers (1, 2, 3, ...). The RMS bandwidth of the square-POW is infinite when the integral in equation (13) is evaluated (i.e. the square-POW has sharp corners). However, in the special case where the square-POW spectrum is bandlimited to B_{f} Hz and the low-level voltage $B = 0$, the RMS bandwidth becomes

$$B_{\text{RMS}} = \sqrt{\left(\frac{1}{4\pi DT_{\text{POW}}}\right)\left(\frac{\pi DT_{\text{POW}} B_{\text{f}} - \sin(\pi DT_{\text{POW}} B_{\text{f}})}{\pi DT_{\text{POW}} \text{Si}(\pi DT_{\text{POW}} B_{\text{f}}) + 1/B_{\text{f}}(\cos(\pi DT_{\text{POW}} B_{\text{f}}) - 1)}\right)}. \tag{34}$$

where Si$(\cdot)$ is the sine integral function. Ideal square-POWs with perfect rectangular corners in the time domain waveform (i.e. $B_{\mathrm{f}} \to \infty$) have spectral content that is far away from its center frequency. Thus, the RF chains of the reader and tag will naturally band-limit the square-POW. The RMS bandwidth of the reader-received signal after backscattering from the tag is dependent on the filter bandwidth. Figures 13 through 15 show waveform examples and their frequency spectrums when the filtered bandwidth is 150 MHz. The RMS time width is finite when including the entire spectrum:

$$T_{\mathrm{RMS}} = \frac{T_{\mathrm{POW}}}{2\sqrt{3}} \sqrt{\frac{A^2 D^3 + B^2(1 - D^3)}{A^2 D + B^2(1 - D)}} \tag{35}$$

This equation reduces to $DT_{\mathrm{POW}}/2\sqrt{3}$ when the low-level voltage $B = 0$.

The band-limited square-POWs in Figures 13 through 15 exhibit quick transitions from low to high voltage. This large voltage swing can induce large transient current spikes in the charge pump, which increases the distortion of the reflected waveform. The peak of the square-POW is long-lasting as opposed to the Gaussian POW and M-POw, which both have singular peaks. This gives the charge pump more time to reach the peak output voltage if there is significant ripple.

3.1.3 M-POW

Figures 16 through 19 show the time domain signal and frequency spectrum of the 1-POW, 2-POW, 3-POW, and 4-POW which are four realizations of the M-POW. This POW consists of M equally powered and equally spaced subcarriers. Its baseband time-domain representation is

$$\mathrm{pow}(t) = \sqrt{\frac{2P_{\mathrm{avg}}}{M}} \sum_{k=1}^{M} \cos(2\pi \frac{k}{T_{\mathrm{POW}}} t), \tag{36}$$

where M is the number of cosine terms summed together, and T_{POW} is the POW time period. The baseband envelope of the 1-POW in the time-domain plot of Figure 16 is a single cosine at 10 MHz (i.e. the frequency corresponding to a 100 ns POW time period). The baseband envelope of the 2-POW is the summation of two cosines: One cosine has a 10 MHz frequency, and the other cosine has a 20 MHz frequency. The 3-POW contains

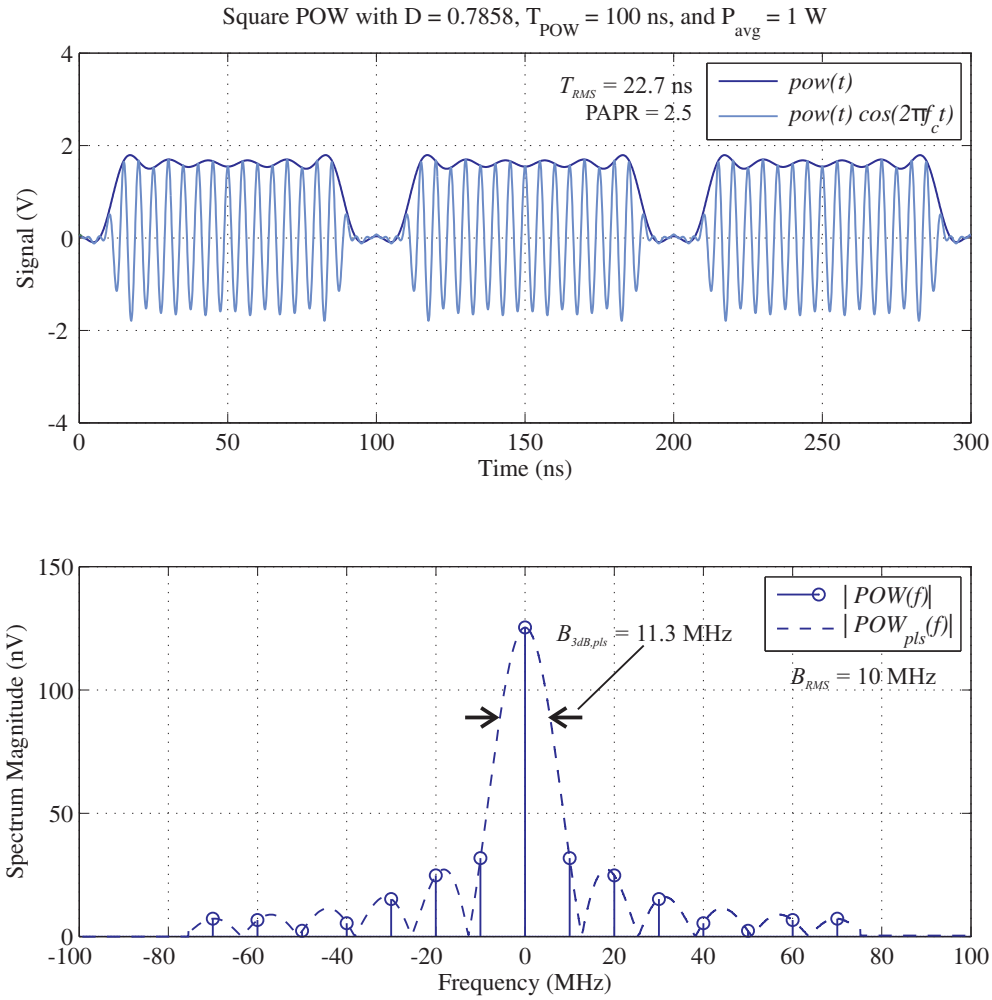

Figure 13: A square-POW with duty cycle D = 0.7858, which corresponds to a RMS bandwidth $B_{\text{RMS}} = 10$ MHz. The spectra shown are the single-pulse spectrum $POW_{\text{pls}}(f)$ and periodic spectrum $POW(f)$ from equation (29) where the POW time period $T_{\text{POW}} = 100$ ns. The filtered bandwidth is $B_{\text{f}} = 150$ MHz, and $f_{\text{c}} = 200$ MHz.

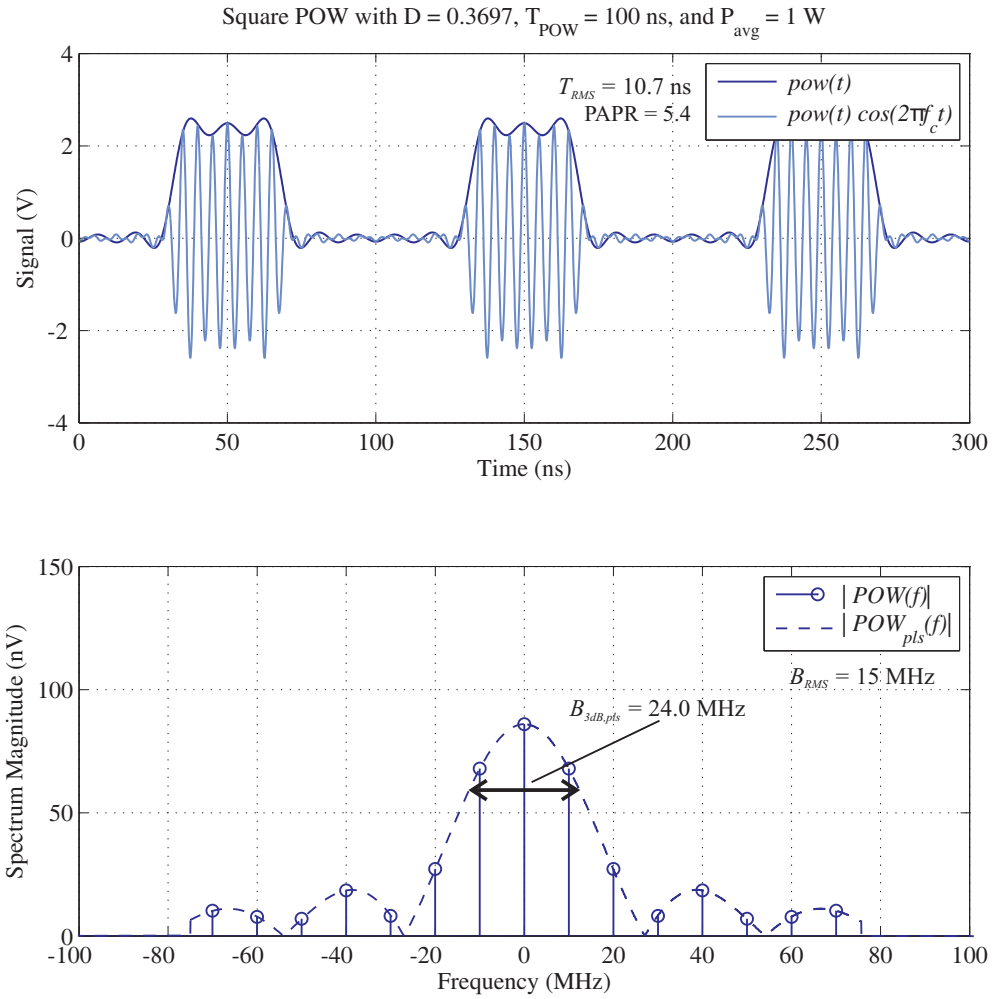

Figure 14: A square-POW with duty cycle D = 0.3697, which corresponds to a RMS bandwidth $B_{\text{RMS}} = 15$ MHz. The spectra shown are the single-pulse spectrum $POW_{\text{pls}}(f)$ and periodic spectrum $POW(f)$ from equation (29) where the POW time period $T_{\text{POW}} = 100$ ns. The filtered bandwidth is $B_{\text{f}} = 150$ MHz, and $f_{\text{c}} = 200$ MHz.

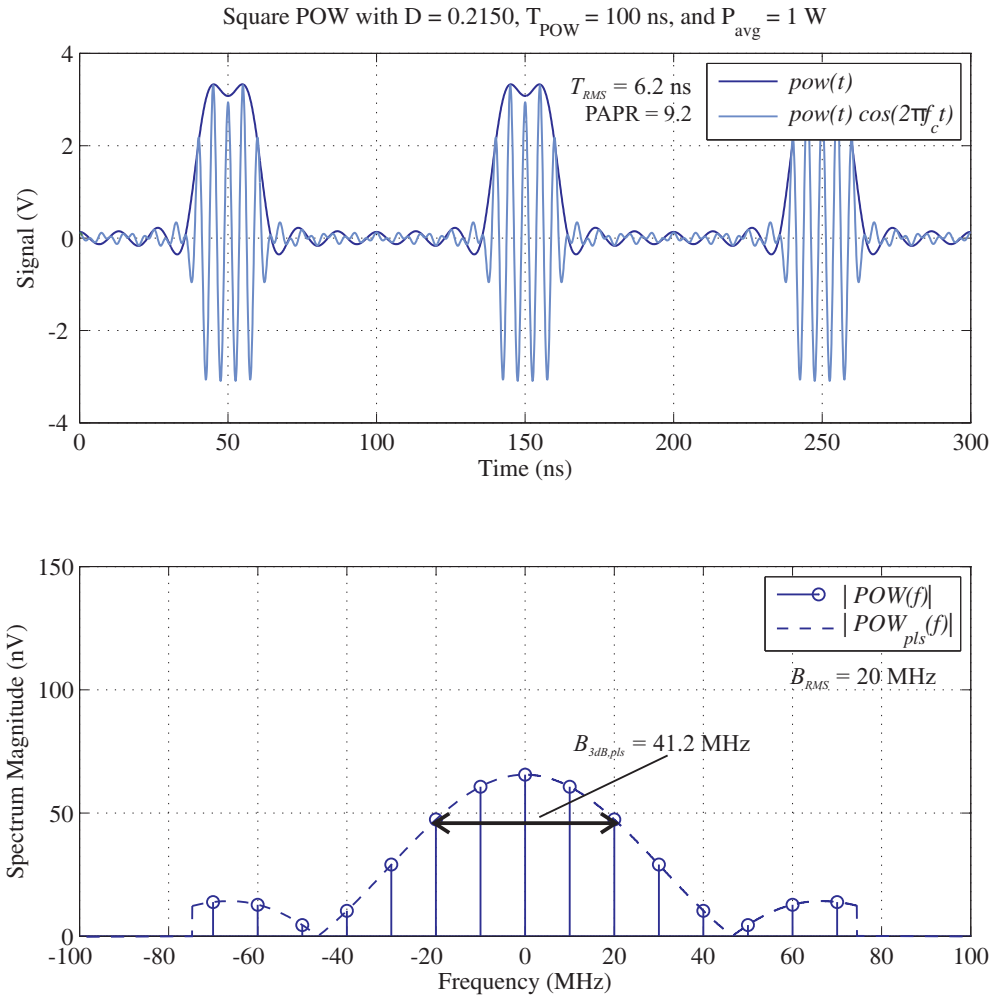

Figure 15: A square-POW with duty cycle D = 0.2150, which corresponds to a RMS bandwidth $B_{\text{RMS}} = 20$ MHz. The spectra shown are the single-pulse spectrum $POW_{\text{pls}}(f)$ and periodic spectrum $POW(f)$ from equation (29) where the POW time period $T_{\text{POW}} = 100$ ns. The filtered bandwidth is $B_{\text{f}} = 150$ MHz, and $f_{\text{c}} = 200$ MHz.

the summation of 3 cosines with frequencies of 10 MHz, 20 MHz, and 30 MHz. Lastly, the 4-POW contains 4 cosines at 10 MHz, 20 MHz, 30 MHz, and 40 MHz.

PAPR is simply calculated as

$$\text{PAPR} = 4M. \tag{37}$$

The peak of the M-POW occurs when all cosines add coherently in phase, which makes the peak signal power $2P_{\text{avg}}M$ V^2. The time-domain definition includes a constant $\sqrt{2P_{\text{avg}}/M}$ that normalizes the baseband signal power to P_{avg} V^2. Upconverting to the passband as depicted in the figure halves the signal power to $P_{\text{avg}}/2$ V^2. Thus, the passband PAPR is $4M$ while the baseband PAPR is $2M$.

The baseband spectrum for the periodic M-POW is

$$\text{POW}(f) = \sqrt{\frac{P_{\text{avg}}}{2M}} \sum_{k=1}^{M} \left[\delta\left(f - \frac{k}{T_{\text{POW}}} \right) + \delta\left(f + \frac{k}{T_{\text{POW}}} \right) \right]. \tag{38}$$

The POW time period determines the subcarrier spacing while the number of subcarriers M normalizes the energy of each subcarrier. The spectrum of the single-pulse POW could not be derived analytically. However, the spectrum can be found numerically as in the example figures. The 3-dB bandwidth of the periodic M-POW is

$$B_{\text{3dB}} \quad = \quad \frac{2M}{T_{\text{POW}}}. \tag{39}$$

The subcarriers in the periodic spectrum have the same signal energy $\frac{P_{\text{avg}}}{2M}$ V^2. Thus, the 3-dB bandwidth contains the entire spectrum. The RMS bandwidth and RMS time width of the single-pulse M-POW do not exist in closed form. Both of these width parameters can be numerically found by using formulas (13) and (14).

Note that the RMS bandwidth calculation does not converge for the single-pulse 1-POW and 3-POW in Figures 16 and 18. This is true for all M-POWs with odd M tested numerically since the integral in the numerator of the RMS bandwidth definition (13) contains an f^2 in the integrand. The M-POWs with even M have spectra that decay quickly enough to zero as $f \to \infty$ that the numerator of equation (13) is finite. For example, compare the spectrum of the 4-POW in Figure 19 to the spectrum of the 3-POW in Figure 18. Notice that the 4-POW spectrum decays to zero quicker than does the 3-POW spectrum. Table 2

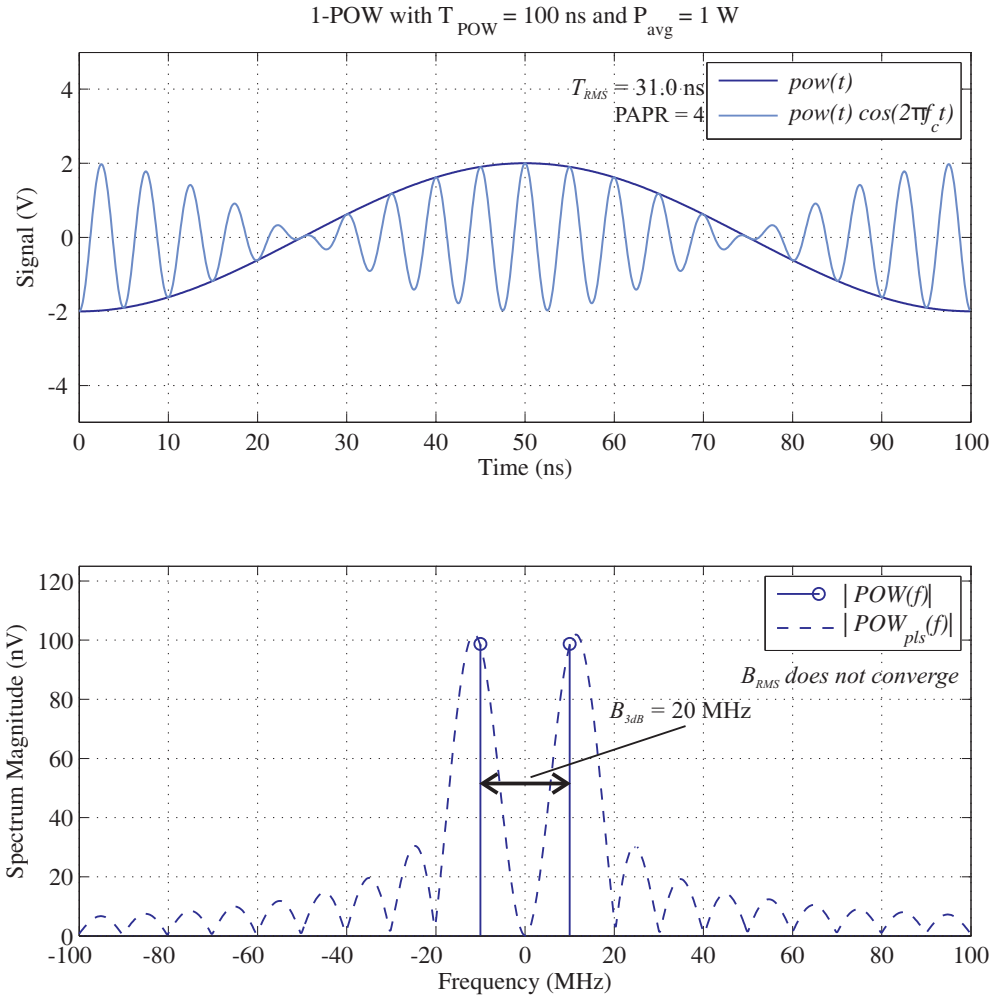

Figure 16: A 1-POW with time period $T_{\mathrm{POW}} = 100$ ns has a trivial spectrum $POW(f)$ given by equation (38). However, the single-pulse spectrum $POW_{\mathrm{pls}}(f)$ is numerically found here. The passband center frequency $f_{\mathrm{c}} = 200$ MHz for figure clarity.

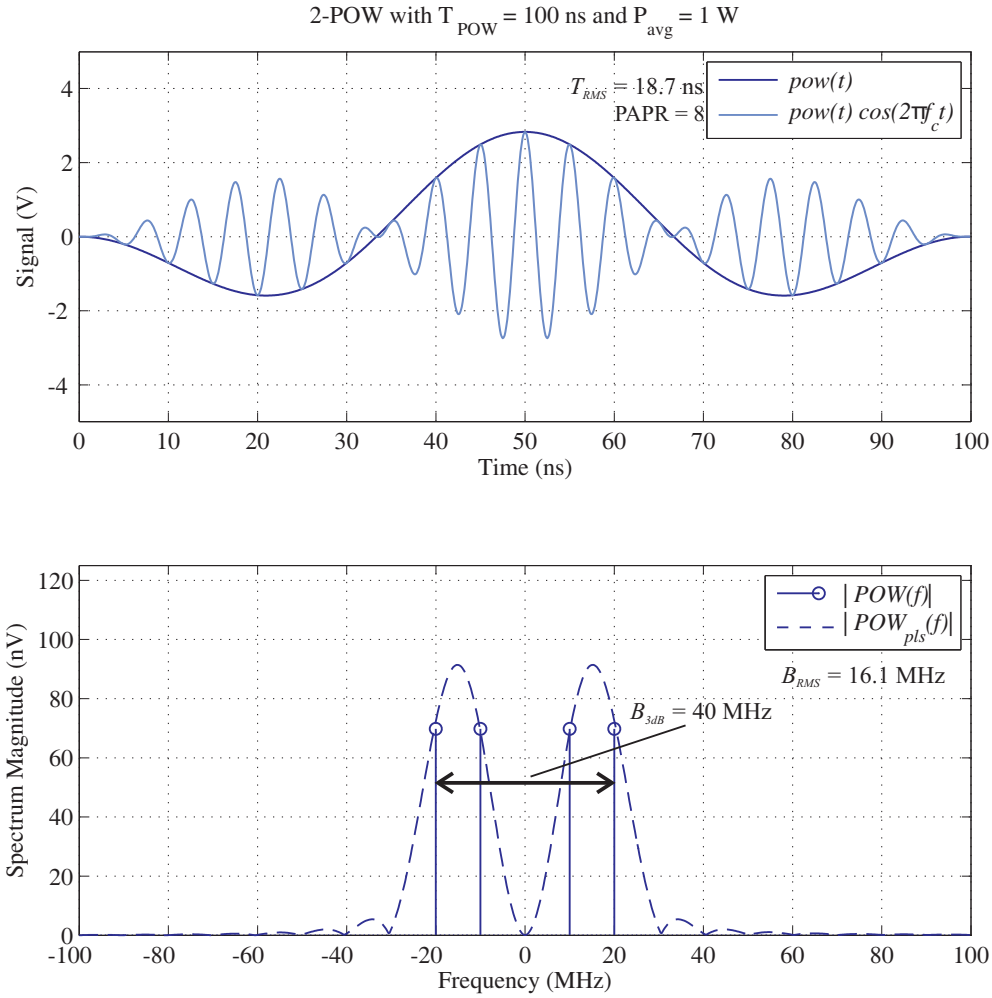

Figure 17: A 2-POW with time period $T_{\mathrm{POW}} = 100$ ns has a trivial spectrum $POW(f)$ given by equation (38). However, the single-pulse spectrum $POW_{\mathrm{pls}}(f)$ is numerically found here. The passband center frequency $f_{\mathrm{c}} = 200$ MHz for figure clarity.

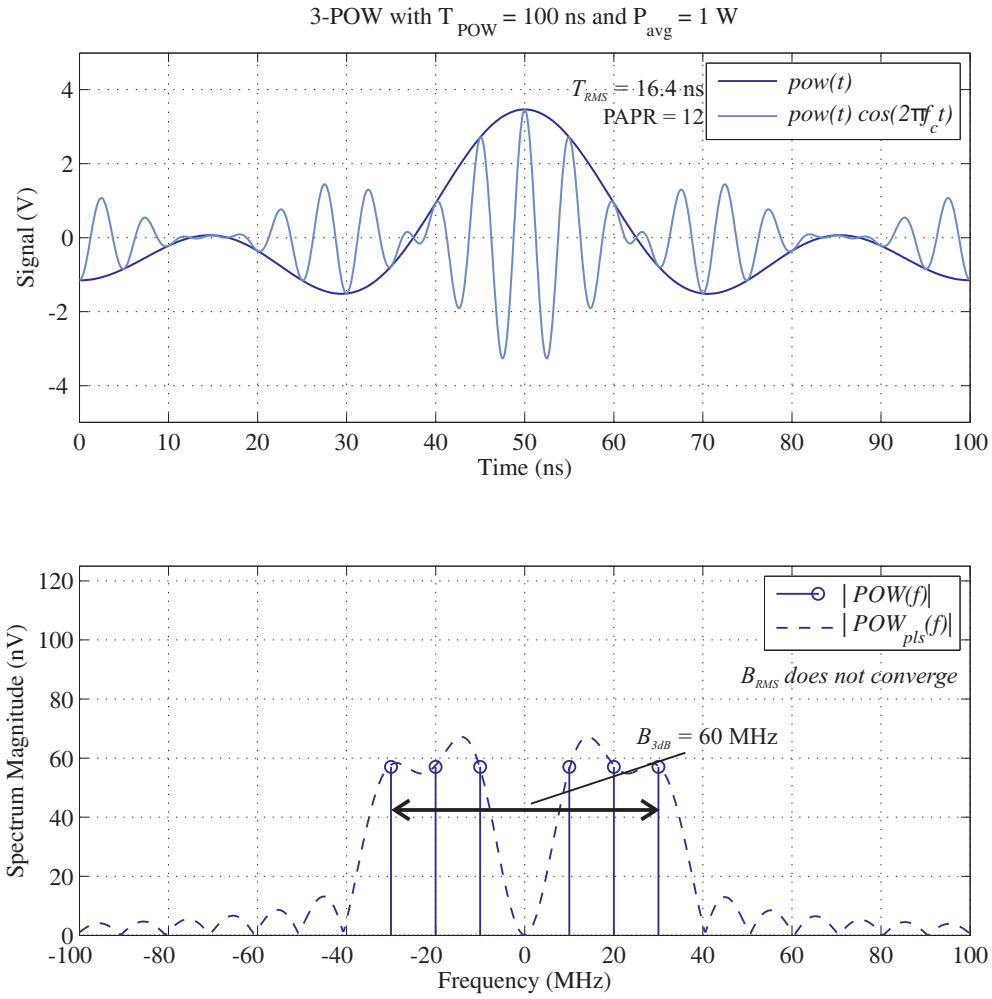

Figure 18: A 3-POW with time period $T_{\text{POW}} = 100$ ns has a trivial spectrum $POW(f)$ given by equation (38). However, the single-pulse spectrum $POW_{\text{pls}}(f)$ is numerically found here. The passband center frequency $f_{\text{c}} = 200$ MHz for figure clarity.

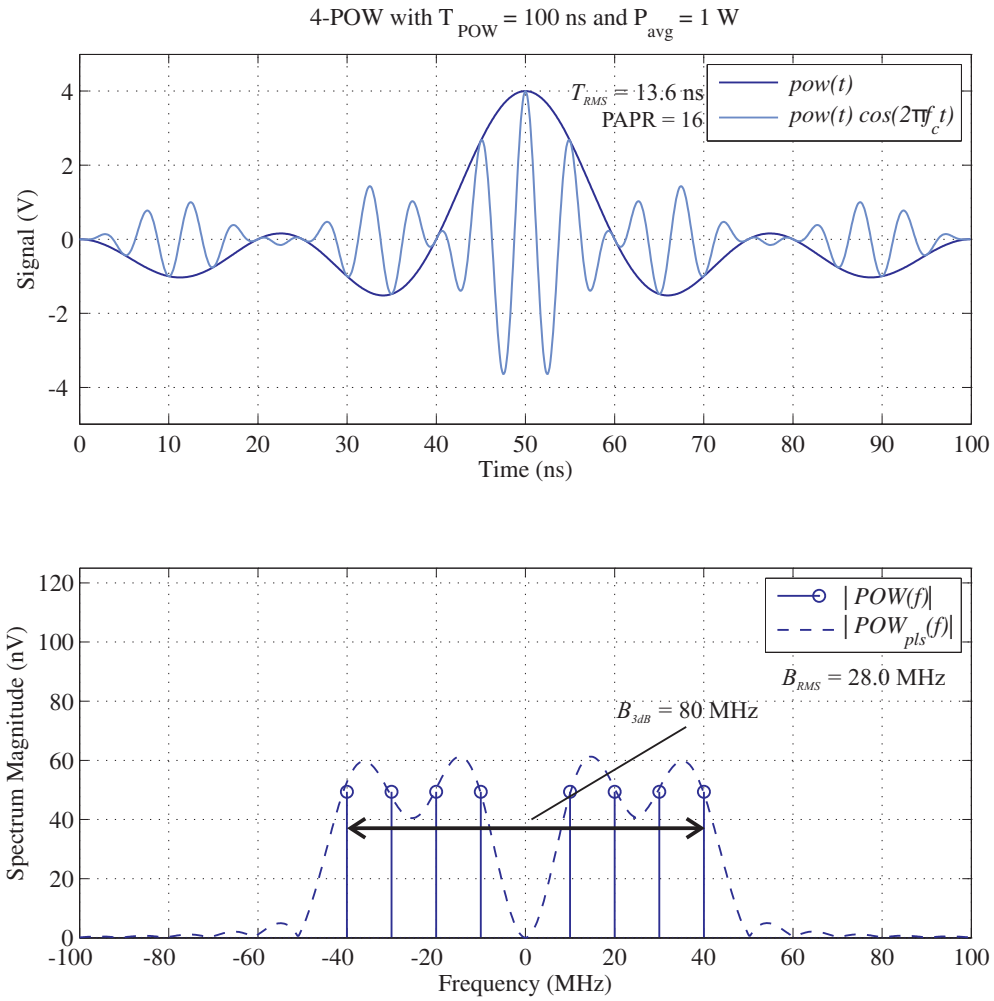

Figure 19: A 4-POW with time period $T_{\mathrm{POW}} = 100$ ns has a trivial spectrum $POW(f)$ given by equation (38). However, the single-pulse spectrum $POW_{\mathrm{pls}}(f)$ is numerically found here. The passband center frequency $f_{\mathrm{c}} = 200$ MHz for figure clarity.

Table 2: RMS bandwidths for M-POWs with even M.

	$T_{\text{POW}} = 50$ ns	$T_{\text{POW}} = 75$ ns	$T_{\text{POW}} = 100$ ns	$T_{\text{POW}} = 125$ ns
2-POW	32.2 MHz	21.5 MHz	16.1 MHz	12.9 MHz
4-POW	55.9 MHz	37.3 MHz	28.0 MHz	22.4 MHz
6-POW	79.6 MHz	53.1 MHz	39.8 MHz	31.8 MHz
8-POW	103.2 MHz	68.8 MHz	51.6 MHz	41.3 MHz
10-POW	126.9 MHz	84.6 MHz	63.5 MHz	50.8 MHz

shows the values of RMS bandwidth for even order POWs with various POW time periods. In general, RMS bandwidth increases as POW time period shortens and the number of subcarriers increases.

M-POWs are useful for back-of-the-envelope designs of energy harvesting systems. The design procedure presented in Section 3.2.2 shows that a POW is used when a 10-stage charge pump operating with a CW input cannot produce the required DC voltage. The necessary PAPR is then computed to reach the required DC voltage, and a POW shape is selected. The designer can deduce the necessary number of baseband subcarriers M to produce the necessary PAPR from equation (37). The selection of M automatically tells the designer how much bandwidth is required for an M-POW using the 3-dB bandwidth equation (39). This back-of-the-envelope design gives the designer a point of reference to formally design a customized POW of another shape to use in the energy harvesting system.

The equal-power subcarriers of the M-POW in the passband are typically difficult to fit within a spectral mask defined in terms of dBc (i.e. decibals relative to the center frequency). The center frequency of the passband is the strongest transmission while the surrounding subcarriers are required to be lower power. Such a spectral mask is described in the "Generation 2" UHF passive RFID standard published by EPCglobal [36]. A POw with a strong central subcarrier and low-power surrounding subcarriers such as a Gaussian POW or Square POW is better suited for meeting this type of spectral mask requirement.

3.2 Improvement of Energy Harvesting Efficiency

Charge pumps are nonlinear devices that have efficiencies dependent on signal amplitude. Also, the output voltage equations derived in the literature [17] [37] [38] assume either

a square-wave clock signal or a sinusoidal CW input. These large-signal output voltage equations would not consistently predict the output voltage of a charge pump under POW excitation for all POW shapes and parameters. From the literature, the DC output voltage of a Dickson charge pump under CW excitation is [17]:

$$V_{\mathrm{DC}} = \frac{N\left(\max\left(V_{\mathrm{in}}\right) - V_{\mathrm{t}}\right)}{1 + \frac{N}{fR_{\mathrm{L}}C}} \tag{40}$$

Here, the output voltage is dependent on the maximum voltage of the input. The denominator terms are charge pump parameters: N is the number of charge pump stages. R_{L} is the load resistance. C is the stage capacitance. f is the input source frequency, and V_{t} is the diode threshold voltage. This output voltage equation is accurate for POW excitations where the POW envelope changes very slowly compared to the charging and discharging transients of the capacitors in the charge pump. A charge pump excited with a 1-POW may produce an output voltage according to equation (40) due to the slow-changing 1-POW envelope. However, the same charge pump excited with a 10-POW may not produce the predicted voltage from the Dickson equation due to the rapid fluctuations of the envelope.

Hence, the output voltage predicted by equation (40) is sometimes inaccurate for a POW input. An energy-delivery approach to predicting the output voltage is used here to get around this issue of transient innaccuracy. The end result of this derivation is an analytical model of the DC power gain from using a POW over using a CW as the input waveform. This **POW gain** is defined as the ratio of DC power delivered by a POW to DC power delivered by CW:

$$G_{\mathrm{POW}} = \frac{P_{\mathrm{DC,POW}}}{P_{\mathrm{DC,CW}}} \quad \text{(unitless)} \tag{41}$$

The POW gain can be used in a link budget analysis to determine maximum range or the necessary transmit power from a reader-transmitter to accomplish a specified range.

Compare two equal-power signals at the input to a charge pump:

$$\mathrm{cw}(t) = \sqrt{2P_{\mathrm{avg}}}\cos\left(2\pi f_{\mathrm{c}}t\right) \tag{42}$$

$$\mathrm{pow}(t) = \sqrt{2P_{\mathrm{avg}}}\sum_{k=-\infty}^{\infty}\mathrm{pow}_{\mathrm{pls}}\left(t - kT_{\mathrm{POW}}\right)\cos\left(2\pi f_{\mathrm{c}}t\right) \tag{43}$$

where f_c is the center frequency of the passband. Both signals have average signal power P_{avg} V^2 and a RMS voltage $V_{RMS} = \sqrt{P_{avg}}$ V. The finite-energy baseband POW pulse $pow_{pls}(t)$ has RMS time width T_{RMS} and RMS bandwidth B_{RMS}. The average input power absorbed by the charge pump for the signal in equation (43) is

$$P_{in} = \frac{R_{in}}{|Z_{in}|^2}\left[\frac{1}{T_{POW}}\int_{-T_{POW}/2}^{T_{POW}/2} pow^2(t)dt\right] = \frac{R_{in}}{|Z_{in}|^2}P_{avg} \text{ (W)} \tag{44}$$

where R_{in} is the time-averaged input resistance to the charge pump, and Z_{in} is the time-averaged input impedance. In the special case where the charge pump is assumed to be matched to a characteristic impedance Z_O, the input power equation reduces to P_{avg}/Z_O W.

Figure 20 approximates $pow_{pls}(t)$ as a narrow square pulse. The voltage V_P is an approximation to the average voltage level of the actual pulse during the energizing portion of the waveform; outside this interval, the POW's low energy levels are considered ineffective at producing energy at the charge pump output. The voltage level is

$$V_P = \sqrt{\frac{P_{avg}T_{POW}}{T_{RMS}}} \tag{45}$$

This square-interval approximation has the added benefit of being constant over the interval T_{RMS}, thus we can use the CW charge pump output voltage equation (40) to represent the energizing portion of the waveform. Any $p(t)$ that is already a square-POW pulse is already band-limited by the reader filter bandwidth just as the RMS bandwidth calculation assumed in equation (34). This band-limited square-POW is then approximated as an unfiltered square pulse. A delta function cannot be created in the limit by taking the square-POW duty cycle to zero since the filtering process prevents such high frequency content in the spectrum.

For diodes with threshold voltage V_t, the energy delivered to the charge pump load

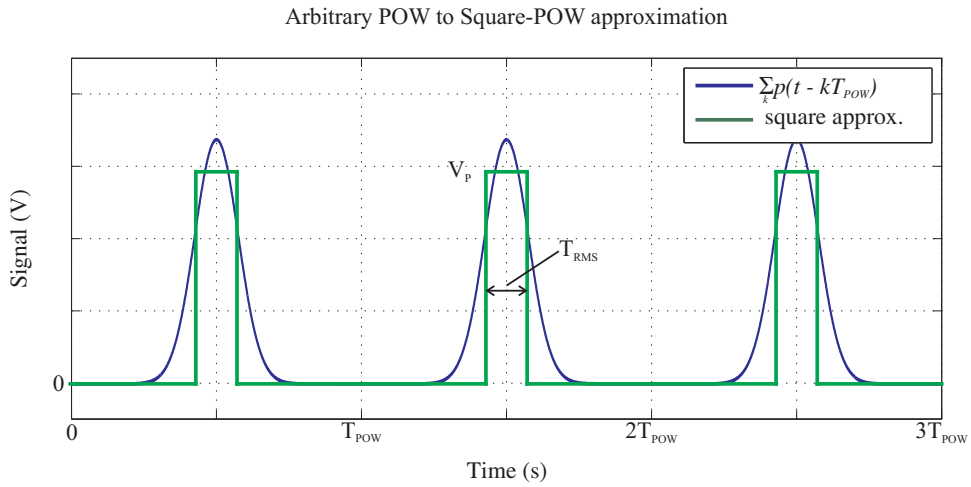

Figure 20: Approximating an arbitrary POW pulse as a square pulse with equal signal energy.

during one POW period T_{POW} is

$$\begin{aligned} E_{\mathrm{CW}} &= \frac{V_{\mathrm{DC,CW}}^2}{R_{\mathrm{L}}} T_{\mathrm{POW}} \\ &= \frac{N^2 \left(2\sqrt{2P_{\mathrm{in}}Z_{\mathrm{O}}} - V_{\mathrm{t}}\right)^2 \mathrm{u}\left(2\sqrt{2P_{\mathrm{in}}Z_{\mathrm{O}}} - V_{\mathrm{t}}\right)}{R_{\mathrm{L}}\left(1 + \frac{N}{f_{\mathrm{c}}R_{\mathrm{L}}C}\right)^2} T_{\mathrm{POW}} \end{aligned} \tag{46}$$

$$\begin{aligned} E_{\mathrm{POW}} &= \frac{V_{\mathrm{DC,POW}}^2}{R_{\mathrm{L}}} \left(2T_{\mathrm{RMS}}\right) \\ &\approx \frac{N^2 \left(2\sqrt{\frac{P_{\mathrm{in}}Z_{\mathrm{O}}T_{\mathrm{POW}}}{T_{\mathrm{RMS}}}} - V_{\mathrm{t}}\right)^2 \mathrm{u}\left(2\sqrt{\frac{P_{\mathrm{in}}Z_{\mathrm{O}}T_{\mathrm{POW}}}{T_{\mathrm{RMS}}}} - V_{\mathrm{t}}\right)}{R_{\mathrm{L}}\left(1 + \frac{N}{f_{\mathrm{c}}R_{\mathrm{L}}C}\right)^2} \left(T_{\mathrm{RMS}}\right). \end{aligned} \tag{47}$$

The unit step function, $\mathrm{u}(\cdot)$ is used to describe the on/off behavior of the output when the input voltage is larger/smaller than the the diode threshold voltage. Energy is constantly delivered for the CW transmission because the input is always on. However, the POW delivers a large amount of energy for the short amount of time T_{RMS}.

The POW Gain can equivalently be expressed by the ratio of energy delivered by a POW to energy delivered by CW. After simplification, this yields

$$\begin{aligned} G_{\mathrm{POW}} &= \frac{E_{\mathrm{POW}}}{E_{\mathrm{CW}}} \\ &\approx \frac{\left(2\sqrt{P_{\mathrm{in}}} - \sqrt{2P_{\mathrm{t}}\frac{T_{\mathrm{RMS}}}{T_{\mathrm{POW}}}}\right)^2 \mathrm{u}\left(2P_{\mathrm{in}} - P_{\mathrm{t}}\frac{T_{\mathrm{RMS}}}{T_{\mathrm{POW}}}\right)}{\sqrt{2}\left(2\sqrt{P_{\mathrm{in}}} - \sqrt{P_{\mathrm{t}}}\right)^2 \mathrm{u}\left(2P_{\mathrm{in}} - P_{\mathrm{t}}\right)} \end{aligned} \tag{48}$$

P_{t} is the sinusoidal signal power required to achieve a maximum signal voltage equal to the

diode threshold V_{t}:

$$P_{\mathrm{t}} \quad = \quad \frac{V_{\mathrm{t}}^2}{2Z_{\mathrm{O}}} \tag{49}$$

Equation. (48) illustrates four regions of POW Gain vs. input power as shown in Figure 21:

- Region I, *"Below Threshold region"*: Neither POW nor CW can forward-bias the diodes since there is not enough input power. The device remains unpowered for both POW and CW.

- Region II, *"Max Gain region"*: The POW forward-biases the diodes, but CW does not. POW Gain is theoretically infinite in this region for ideal diodes.

- Region III, *"Common region"*: POW Gain approaches $1/\sqrt{2}$ as the POW and CW both efficiently operate the charge pump when input power reaches very high power.

- Region IV, *"Reverse Breakdown region"*: Reverse-breakdown diode behavior begins to limit the effectiveness of the POW but not the CW. Note that a very large PAPR with a correspondingly small RMS time width can completely collapse region III. Equation (48) does not model this behavior as the equation assumes ideal diodes without a breakdown voltage.

Equation (48) also shows that, for fixed RMS bandwidth, POW Gain is maximized if and only if $\mathrm{pow}_{\mathrm{pls}}(t)$ is a Gaussian POW. The Fourier uncertainty principle shows the Gaussian pulse has the smallest combination of RMS bandwidth and RMS time width (assuming both widths are finite) of any time-varying signals [34].

3.2.1 Precisely Measured POW Gains on a Dickson Charge Pump

Measurements were run to verify the validity of the POW gain model derived in equation (48) and depicted in Figure 21. The testbed system diagram is shown in Figure 22. The testbed was constructed using 50 Ω components and cables with standard SMA connectors. All power splitters, filters, and amplifiers were acquired from Mini-Circuits.

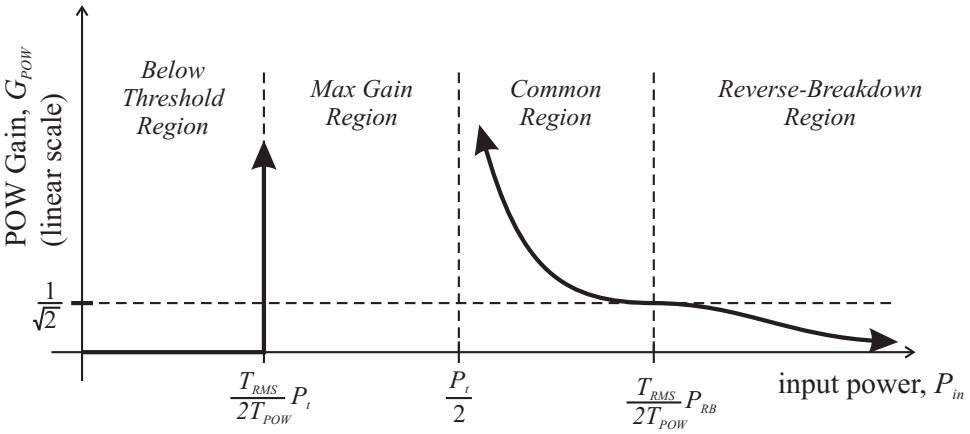

Figure 21: POW Gain across four regions of input power: The boundary between the Below Threshold region and the Max Gain region is determined by the POW signal power necessary to turn on a diode while the upper boundary of the Max Gain region is determined by the CW signal power necessary to turn on the same diode.

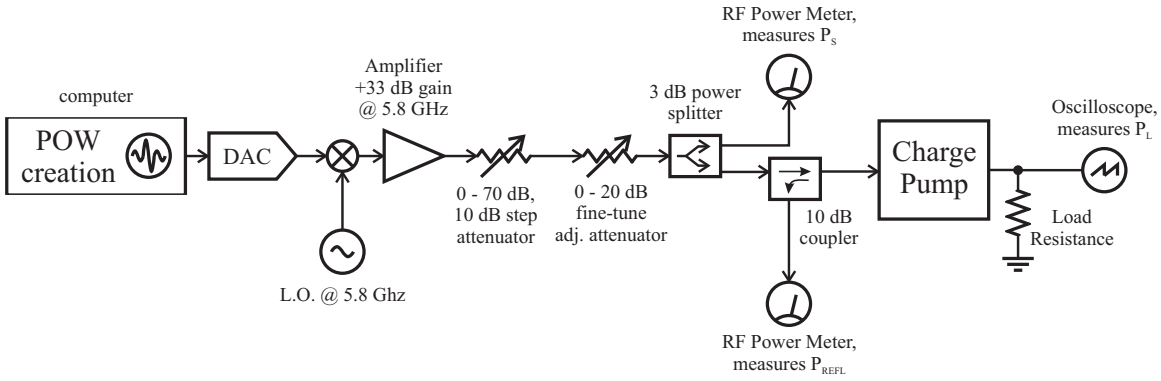

Figure 22: POW Gain and charge pump efficiency are calculated from measurements of source power P_{S}, reflected power P_{REFL}, and DC load power, P_{L} in this test system diagram.

The charge pump used in the test shown in Figure 23 is a six-stage Dickson charge pump with 4.7 pF stage capacitors. Six Schottky diodes from Avago Technologies were used as the stage diodes, each with a 0.35 V threshold voltage [39]. The circuit board substrate is FR4 with SMA connectors mounted on the edge of the board.

The system is configured so that the source power impinging on the charge pump is controlled with two adjustable attenuators at the output of the amplifier in the figure; the first attenuator is a discrete 10-dB step attenuator, and the second is a continuous-adjustable attenuator with a 0 to 20 dB range. For a CW excitation, a maximum incident power on the charge pump of 23 dBm was measured by the RF power meter measuring

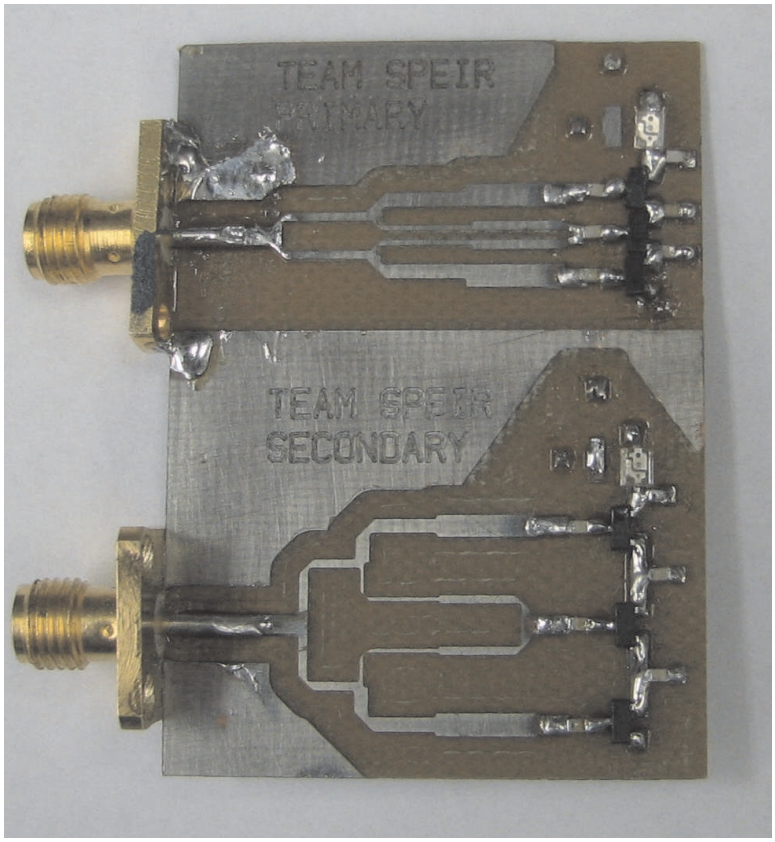

Figure 23: The circuit in the upper portion of the board is the charge pump used in the POW gain measurements. It is a six-stage Dickson charge pump with 4.7 pF capacitors and diodes with a low threshold voltage of 0.35 V to drive a variable load resistance (10 kΩ and 100 kΩ).

source power P_{S} after taking into account the cable and coupler insertion losses leading to the charge pump. For a POW excitation, the maximum incident source power was 17 dBm for 1-POW and 2-POW and 15 dBm for 3-POW.

The charge pump output power was measured for each excitation type (CW, 1-POW, 2-POW, or 3-POW) across a wide domain of source power from -10 dBm to the maximum possible source power in 1 dB steps. Each excitation type produced a time-varying output voltage on the charge pump. An oscilloscope was used to measure the RMS voltage across the load resistance in order to simply calculate average load power. Once the load power was measured for each excitation type across the domain of source power (P_{S}), POW Gain was computed as a function of source power using the formula

$$G_{\mathrm{POW}}(P_{\mathrm{S}}) = 10\log_{10}\left(\frac{P_{\mathrm{L,POW}}(P_{\mathrm{S}})}{P_{\mathrm{L,CW}}(P_{\mathrm{S}})}\right) \text{ (dB)} \tag{50}$$

where $P_{\mathrm{L,POW}}(P_{\mathrm{S}})$ is the DC load power under POW excitation at source power (P_{S}), and $P_{\mathrm{L,CW}}(P_{\mathrm{S}})$ is the DC load power under CW excitation at the same source power. A positive POW gain represents an increase in load power under a POW excitation at the same source power, whereas a negative POW Gain represents a decrease in DC load power.

The reflected power P_{REFL} was also measured in order to ascertain whether the charge pump efficiency changed under POW excitation from the CW excitation at the same source power. This measurement shed light on the possibility that positive POW gain may occur because of an increase in the power absorbed by the charge pump. The results show that the converse is true; POW gain is the result of an increase in charge pump efficiency rather than an increase in absorbed power. The charge pump power efficiency is calculated for every excitation type at every source power level as

$$\eta(P_{\mathrm{S}}) = \frac{P_{\mathrm{L}}}{P_{\mathrm{S}} - P_{\mathrm{REFL}}} \tag{51}$$

The denominator represents the charge pump's absorbed input power, which is the difference between source power and reflected power in the linear scale. Power efficiency is unitless and is first calculated in the linear scale before converting to the log scale.

Figure 24 shows the measured POW gains on the vertical axis for the 10 kΩ load resistance vs. source power, and Figure 25 shows the same measurements for the 100 kΩ load resistance. The 100 kΩ load resistance graph shows larger POW gains overall than the 10 kΩ load resistance graph. These observations show that POWs provide the largest power gains at the output of the charge pump when signal power is low and when load resistance is high (or equivalently when ripple voltage is minimized). The model predicts the decreasing trend of POW gain in the Common region but does not conform well with the measured results. The model is more accurate for the 10 kΩ measurements than the 100 kΩ measurements.

The two possible reasons for the increase in load power when using a POW excitation are the increase of power efficiency and the increase in power absorbed by the charge pump. Return loss is measured throughout these measurements using the 10-dB coupler from Figure 22 in order to find how much power the charge pump absorbed at its input. There

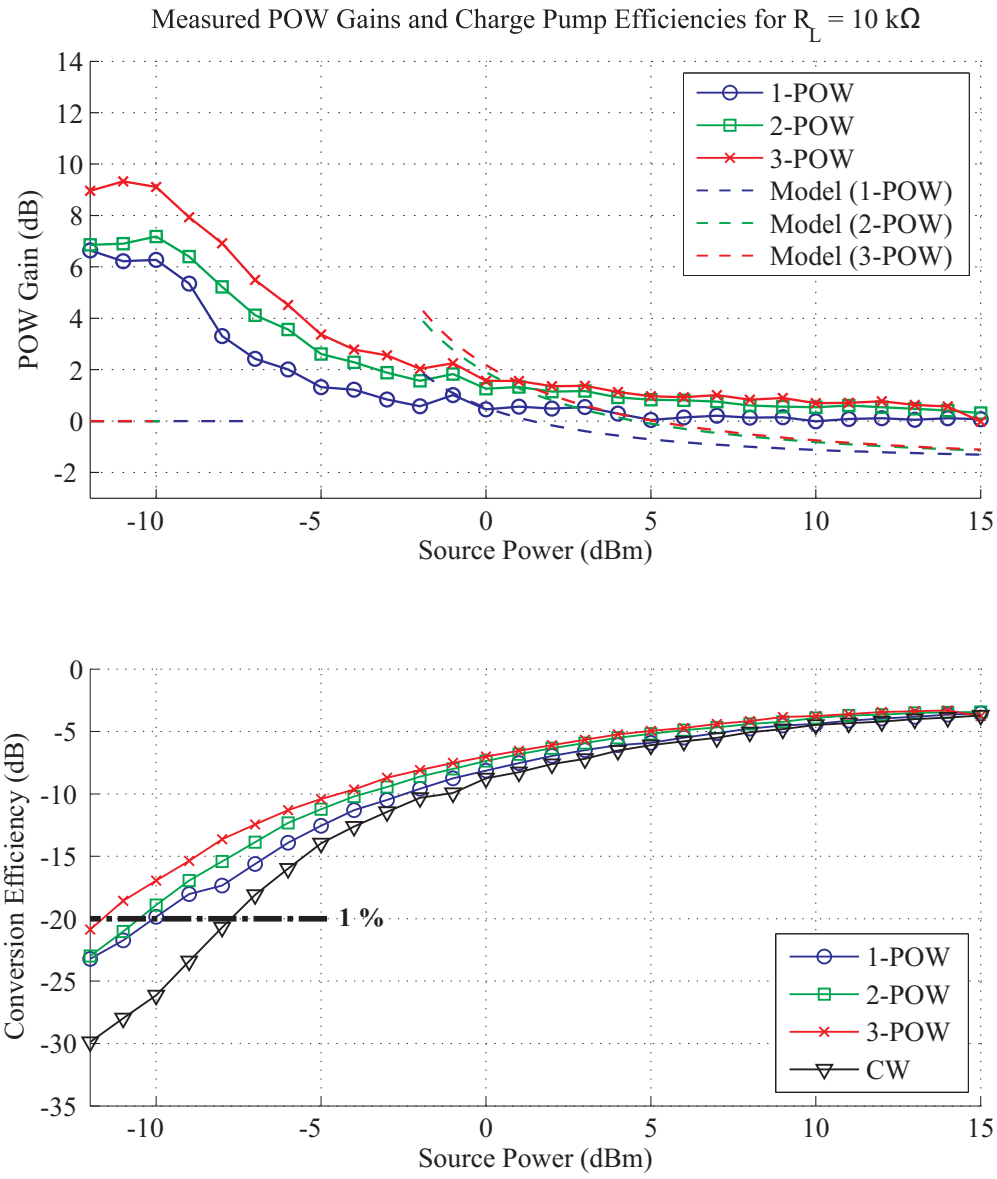

Figure 24: Above, the measurement results show that 1-POW, 2-POW, and 3-POW provide extra power to the 10 kΩ load resistance of a Dickson charge pump over a CW excitation. The bottom graph shows power efficiency (in dB) vs. input power for the $R_{\mathrm{L}} = 10$ kΩ measurements.

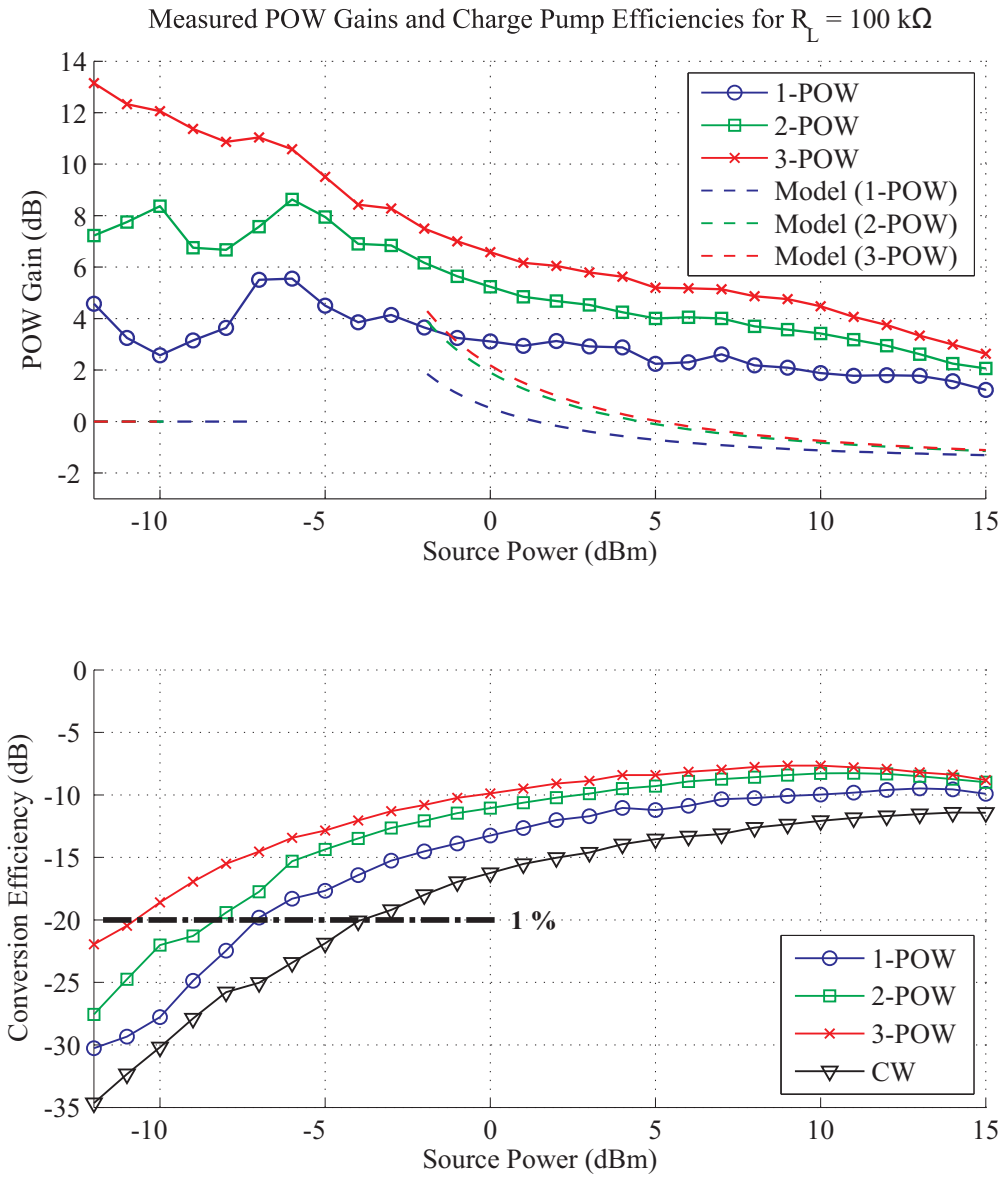

Figure 25: Above, the measurement results show that 1-POW, 2-POW, and 3-POW provide significant extra power to the 100 kΩ load resistance than they did to the 10 kΩ load resistance. The bottom graph shows power efficiency (in dB) vs. input power for the $R_{\mathrm{L}} =$ 100 kΩ measurements.

are a few slight discrepancies (< 0.5 dB) between the input power using a POW excitation and the input power using a CW excitation when the source power was held constant. The main reason for this is imprecise human error when setting the appropriate variable attenuation to attain a specified source power. This error is insignificant when compared to the charge pump power efficiency gains in the bottom graphs of Figures 24 and 25. Charge pump power efficiency changed dramatically between CW and POW excitation and is the main component of POW gain. In fact, the measured POW gains can be accurately recalculated by taking the dB-difference in measured power efficiency between a POW and CW excitation at any source power level.

The POW gain model predicts the boundary between the Max Gain region and the Common region is P_S = -2.1 dBm assuming a diode threshold of 0.35 V and source impedance of 50 Ω. The measured POW gains in the Common region shows the same decreasing trend as predicted by the model in Figure 22. The Max gain region shows large POW gains in excess of 2 dB for both sets of measurements. The model predicts infinite POW gain in this region, but the measured POW gain is finite. The POW gain is largest in this region, and this is an expected result; Real diodes do not behave as ideal diodes (i.e. perfect open and short behavior). Some energy harvesting of CW occurs, albeit very little, when its voltage magnitude is below the threshold voltage.

The model predicts the Below-Threshold region lies at source power less than -7.4 dBm for the 1-POW, -9.5 dBm for the 2-POW, and -10.1 dBm for the 3-POW. The behavior of the measured POW gain curves do not show any indication that these predicted boundaries for the Below-Threshold region are correct. As source power decreases to -5 dBm, POW gain gets larger for all POWs tested in both Figures 24 and 25. In Figure 24, the 10 kΩ measured results show a slight dip in POW gain at -11 dBm, which could indicate the beginning of the measured Below-Treshold region. However, more measurements are needed to confirm this. In Figure 25, a noticeable dip in measured POW gain occurs at -8 dBm. After this dip, the POW gain displays erratic behavior. Overall, the Below-Threshold cannot be confirmed in the measured results.

The Reverse-Breakdown region could not be measured completely due to the limitations

of the hardware used in the experiment. Assuming $V_{\mathrm{RB}} = 5$ V, the model predicts the boundary line between the Common region and the Reverse-Breakdown region is 15.9 dBm for the 1-POW, 13.7 dBm for the 2-POW, and 13.1 dBm for the 3-POW. The POW gain for the 3-POW begins to fall below 0 dB at a source power of 15 dBm for the 10 kΩ measurements in Figure 24. The 100 kΩ measurements in Figure 25 show that the POW gains for all three POWs fall rapidly around a source power of 15 dBm, but no conclusive evidence was measured to verify the theoretical boundary.

3.2.2 Energy Harvesting System Design

This section provides a basic procedure for designing a suitable POW and Dickson charge pump circuit to meet DC power and meximum range requirements. The typical design process follows the steps outlined in Table 3. The first step is determining whether a CW excitation can provide enough voltage to turn on the diodes and provide enough DC output voltage. If so, a charge pump with the minimum number of stages necessary to create the specified DC voltage is designed. Charge pumps with more than 10 stages are typically discarded since they take up an enormous amount of space within an RFIC. A POW is needed if the CW charge pump is too big. Last, a charge pump is designed to produce the specified DC voltage with the POW input.

Assume a passive wireless tag has the specifications given in Table 4. The reader antenna, tag antenna, and other link budget items are already designed such that the tag's received power is P_{in} = -10 dBm. Assume the tag's antenna is a dipole with an antenna impedance $Z_{\mathrm{A}} = 77\ \Omega$. The tag's DC load requires -20 dBm. The task is to design the charge pump's number of stages N, stage capacitances C, and output capacitance C_{out}. Furthermore, a POW should be designed in case the CW does not provide enough DC power to the tag.

The DC output power required is -24 dBm, and the DC voltage specified is 2 V. This implies the load resistance is $R_{\mathrm{L}} = V_{\mathrm{DC}}^2/P_{\mathrm{DC}} = 1$ MΩ. The magnitude of the input signal into the charge pump under a tag-received power of -10 dBm is just $2\sqrt{2 \cdot 100\mu\mathrm{W} \cdot 77\Omega} = 0.2482$ V, which is not enough to crest the diode threshold voltage of 0.35 V (Avago Schottky diodes [39]).

Table 3: Design procedure of a POW and charge pump energy-harvesting system.

1. Compute the maximum tag voltage $|V_{\text{tag,CW}}(t)|$ from a link budget at maximum range assuming a CW excitation.
2. Design a charge pump to meet the DC power specification with an input voltage of $|V_{\text{tag,CW}}(t)|$:
   a. Design a POW if $|V_{\text{tag,CW}}(t)| < V_{\text{t}}$.
   b. Design a POW if $|V_{\text{tag,CW}}(t)| > V_{\text{t}}$, but the necessary charge pump has more than 10 stages.
   c. Skip POW design if $|V_{\text{tag,CW}}(t)| > V_{\text{t}}$, and the necessary charge pump has 10 or fewer stages.
3. Pick a suitable PAPR such that:
   a. the DC power requirements can be met,
   b. and the number of necessary charge pump stages is 10 or fewer.
4. Pick a POW shape and design the parameters such that the POW has:
   a. the necessary PAPR.
   b. a smooth transition to its peak
   c. a narrower 3-dB bandwidth than the tag RF front-end.
5. Design a charge pump to meet the DC power specification with an input voltage of $|V_{\text{tag,POW}}(t)|$.

A POW is needed to increase the maximum input voltage into the charge pump.

A POW with PAPR ≥ 4 should produce enough extra voltage to turn on the diodes. However, the critical design requirement is meeting the 2 V DC specification. Assuming the stage capacitors are able to charge up completely during each POW cycle, the output voltage under a POW excitation is

$$V_{\text{DC,POW}} = \frac{N\left(2\sqrt{\text{PAPR}\cdot P_{\text{in}} Z_{\text{A}}} - V_{\text{t}}\right)}{1+\frac{NT_{\text{POW}}}{CR_{\text{L}}}} \text{ V} \tag{52}$$

Pick a PAPR of 16 and a charge pump with 9 stages. Assuming these values, the numerator of the output voltage equation is 3.17 V, which exceeds the specification. The denominator cannot be evaluated at this point since the POW time period and stage capacitance have not been chosen. The 3.17 V numerator provides plenty of room for the denominator to reduce the voltage in case T_{POW} or C are limited in any way.

The POW shape is chosen based on the smoothness of the shape and the tag's bandwidth

Table 4: Specifications for the charge pump design example.

Wireless Sensor Parameters:	Specified Value:
Maximum Range	10 m
DC Output Voltage V_{DC}	2 V
DC Output Power P_{DC}	-24 dBm
Tag-received power at max. range P_{in}	-10 dBm
Tag front-end 3-dB bandwidth	100 MHz
Carrier frequency f_{c}	5.8 GHz

requirements. A POW with a smooth transition from zero to its peak provides the charge pump plenty of time to charge up from a prior starvation of voltage. For instance, a square-POW has a quick transition from zero to its peak, which limits the amount of time the charge pump has to completely charge up. A Gaussian POW or an M-POW, on the other hand, allows for a longer charging time. Also, the tag must be able to receive a majority of the spectrum of the POW in order to benefit from peak voltage of the POW. For this design, a Gaussian POW is chosen because it has an excellent combination of PAPR, smoothness, and 3-dB bandwidth.

A Gaussian POW with a PAPR of 16 is chosen as the POW shape. The POW period is chosen to be 50 ns (i.e. a short time period) to minimize the denominator in equation (52). The standard-deviation parameter $\sigma = 2.49$ ns, and the 3-dB bandwidth is 75.2 MHz, which is within the tag's 3-dB bandwidth.

The stage capacitors must be designed to charge up quickly within one time period of a sine wave at the carrier frequency. Numerically, this means the charging time constant must be less than one-half the carrier wave time period. The time period of a 5.8 GHz sine wave is 172.4 ps. Conversely, the size of the capacitor must be large enough such that the DC output voltage in equation (52) is greater than the specification.

$$CR_{\text{A}} < \frac{T_{\text{c}}}{2} = 86.2 \text{ ps} \tag{53}$$

$$V_{\text{DC,POW}} = \frac{9\left(2\sqrt{16 \cdot 100\ \mu\text{W} \cdot 77\ \Omega} - 0.35\ \text{V}\right)}{1 + \frac{950\ \text{ns}}{C \cdot 1\ \text{M}\Omega}} \tag{54}$$

Table 5: Designed parameters for the charge pump design example.

Charge Pump Parameters:	Designed Value:
Number of Stages N	9 stages
Stage Capacitance C	1 pF
Output Capacitance C_{out}	1 pF
POW Parameters:	**Designed Value:**
Shape	Gaussian
PAPR	16
σ	2.49 ns
B_{3dB}	75.2 MHz

The time constant constraint limits the stage capacitance to a maximum of 1.1 pF. Choosing a value of 1 pF to allow for tolerance error makes the output voltage 2.18 V, which satisfies the specification.

The output voltage will decay with the RC time constant between the output capacitor and load resistor at the output of the charge pump between successive POW peaks. Thus, the output capacitor must be sized to ensure the voltage does not decay below 2 V. The voltage after a decay lasting for the 50 ns time period of the POW is

$$V_{\text{DC,POW}}(50 \text{ ns}) \quad = \quad 2.18e^{\frac{50\text{ns}}{1\text{M}\Omega \cdot C_{\text{out}}}} \quad \text{V}$$

A 1 pF output capacitor produces a decayed voltage after 50 ns of 2.07 V. A somewhat larger output capacitor may be used to provide a larger cushion above 2 V. The design is completed, and the results are displayed in Table 5.

3.3 Power-Optimized Waveforms in the Backscatter Link

The signal received at the reader-receiver antenna is modeled in this section. A POW serves as the carrier for the backscattered data. The tag may add nonlinear distortion to the signal, which alters the POW shape. Nonlinear distortion of POWs is explained in detail later in Section 4.5. Beyond nonlinear distortion, the channel adds multipath components, which can interfere with signal detection. The resulting signal that the reader receives consists of:

- an attenuated, delayed signal from the line-of-sight path to the tag,

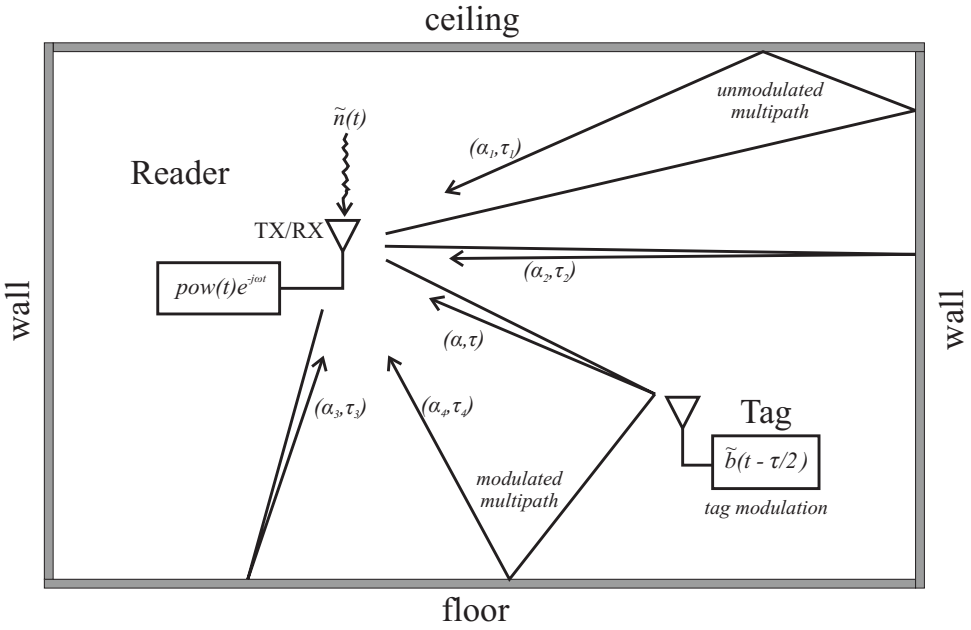

Figure 26: The signal components that comprise the complete signal model within a POW-based passive WSN.

- unmodulated multipath reflections,
- tag-modulated multipath reflections, and
- noise.

Figure 26 shows each of these signal components. This figure differs from previous signal models in passive WSNs by including tag-modulated multipath components and additive nonlinear distortion. Previous works either ignored these two signal components or assumed them negligible.

The complete signal model for the reader-received signal is

$$\begin{aligned}\tilde{y}(t) &= \overbrace{\alpha\tilde{b}(t-\tau)\mathrm{pow}(t-\tau)e^{-j\omega(t-\tau)}}^{\text{LOS component}} + \tilde{n}(t) \\ &\quad + \underbrace{\sum_{l=1}^{L}\alpha_l \mathrm{pow}(t-\tau_l)e^{-j\omega(t-\tau_l)}}_{\text{unmodulated multipath}} + \underbrace{\sum_{m=L+1}^{M+L}\alpha_m\tilde{b}(t-\tau_m)\mathrm{pow}(t-\tau_m)e^{-j\omega(t-\tau_m)}}_{\text{modulated multipath}}.\end{aligned} \tag{55}$$

The line-of-sight, delayed tag signal is the first term in this signal model and contains the round-trip time delay τ. The ranging system estimates the range by performing operations to extract the true time delay τ from the received signal. All other signal components are

interferers to the estimation of delay. Here is a list of terms in the received signal model with descriptions:

- α is the attenuation constant consolidating all deterministic aspects of the link budget equation including antenna gain, path loss, antenna polarization mismatch, etc. The magnitude of α depends on the forward and backscatter links together. All of these propagation effects were explained in Section 2.3.2.

- $\tilde{b}(t-\tau)$ is the complex backscattered data waveform that switches between two impedance states corresponding to the two reflective load modulators as explained in Section 2.2.4. This waveform is delayed in time by τ seconds with respect to the signal transmited from the antenna of the reader-transmitter.

- $\text{pow}(t-\tau)e^{-j\omega(t-\tau)}$ is the upconverted POW in the passband delayed in time by τ seconds corresponding to the round-trip time from reader to tag and back to reader. The POW itself, $\text{pow}(t)$, is a continuous pulse train of baseband POW pulses, which can be chosen to be M-POW, Gaussian-POW, Square-POW, etc. As written, the signal model assumes a linear tag reflection from each of the two tag modulations states. The subscript "NL" is included if one or both of these modulation states includes a nonlinear reflection from a charge pump. Thus, the term $\text{pow}_{\text{NL}}(t-\tau)$ is used in lieu of $\text{pow}(t-\tau)$ under a nonlinear reflection. A nonlinear reflection only affects the POW shape. All other components of the received signal model remain the same as the linear reflection case.

- $\sum_{l=1}^{L}\alpha_l \text{pow}(t-\tau_l)e^{-j\omega(t-\tau_l)}$ is the sum total of all unmodulated multipath components from the environment including self-interference from the reader itself. Readers with monostatic configurations experience significant leakage of the transmitted signal from its transmit chain to its receive chain. Bistatic configurations similarly suffer from cross-talk between the transmitter and receive antennas. The l^{th} umodulated multipath component is multiplied by its path gain α_l and has path delay τ_l seconds. These components of the received signal are unmodulated by tag data, so they can be

filtered out using active cancellation (in the case of self-interference), DC blocking, or comb filtering after down-conversion.

- $\sum_{m=L+1}^{M+L} \alpha_m \tilde{b}(t-\tau_m)\text{pow}(t-\tau_m)e^{-j\omega(t-\tau_m)}$ is the sum total of all *modulated* multipath components, which include a reflection off the tag. These signal components travel from the reader-transmit antenna to the tag and back to the reader-receive antenna while including at least one reflection from an object in the environment. Each of these multipath components has a path gain α_m and path delay τ_m by geometry. The tag's line-of-sight path delay is shorter than the modulated multipath delays ($\tau < \tau_m$).

- $\tilde{n}(t)$ is the complex AWGN process with noise power $P_{\text{N}} = kTB$ dependent on Boltzmann's constant, receiver effective temperature, and bandwidth of the reader receiver.

This received signal has an SNR related to the nominal SNR of an equal-power CW system. Much like a spread-spectrum reception, the signal power of the received POW remains the same while the noise power increases with the extra bandwidth occupied by the POW. The received SNR using a POW as a data carrier is

$$\text{SNR}_{\text{rec,POW}} = \frac{B_{\text{tag}}}{B_{\text{POW}} + B_{\text{tag}}}\text{SNR}_{\text{rec,CW}}, \tag{56}$$

where B_{tag} is the signal bandwidth of the tag backscatter signal and B_{POW} is the bandwidth of the POW. This formula assumes the reader's receiver bandwidth is exactly $B_{\text{POW}} + B_{\text{tag}}$ Hz. The receiver bandwidth of a CW system is assumed to be B_{tag} Hz.

3.4 Necessary Changes to The Reader

A reader designed for POW transmission and reception needs to amplify POWs without voltage clipping the peaks. The high PAPR of a POW necessitates more robust power-handling on both the reader transmitter and reader receiver just as required by OFDM transmitters and receivers [40]. The power amplifiers in the reader are designed with higher peak-power handling capability to preserve the peaks of the POW without voltage clipping. Furthermore, the reader should be able to detect the tag backscatter response. The tag backscatter signal detection methods are either POW-subcarrier filtering or comb-filtering.

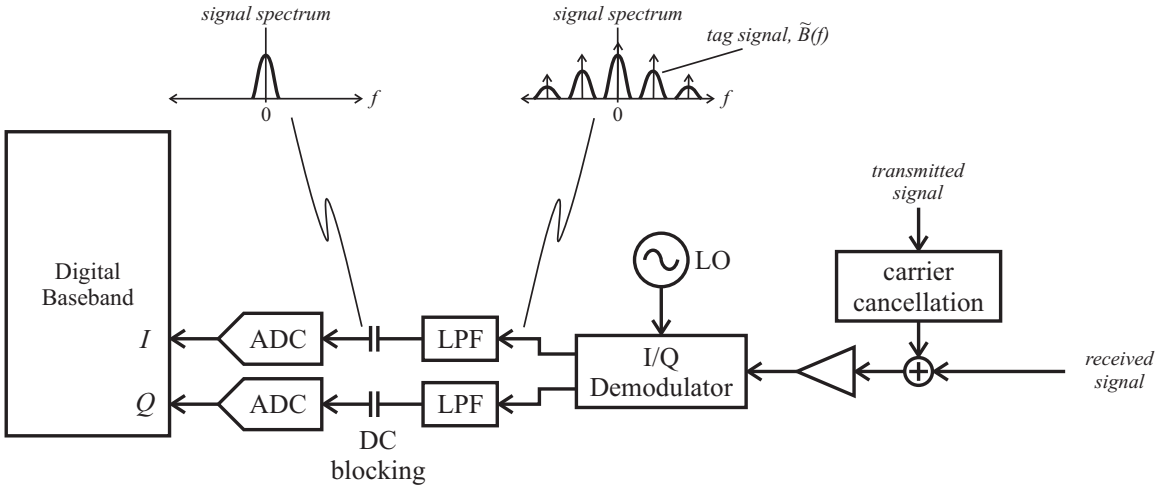

Figure 27: The reader applies a low-pass filter to the downconverted received signal to remove the POW subcarriers. Then, the filtered signal is DC-blocked to remove any unmodulated multipath components.

3.4.1 Changes to Reader Receiver

There are two methods for demodulating tag data from the POW carrier in equation (55). The first method filters out all POW sidebands in the baseband as shown in Figure 27. The strongest POW subcarrier available is downconverted to 0 Hz in the baseband using a heterodyne receiver architecture, and the remaining subcarriers are filtered out. The signal is then DC-blocked to remove all unmodulated multipath components.

The modulated multipath components exist only if the backscatter channel is "frequency selective" across the bandwidth of the tag backscatter signal. Section 4.4 explains "frequency-selective" and also "frequency-flat" channels in more detail. It is sufficient to say in this section that the frequency response of a frequency-flat channel is approximately constant across the bandwidth of the tag backscattered signal. This implies the channel impulse response is represented by a single time-delayed impulse. On the other hand, the frequency response of a frequency-selective channel varies across the bandwidth of the tag backscattered signal, which means its channel impulse response is approximated by multiple impulses. The extraneous impulses beyond the line-of-sight impulse produce the modulated multipath components on the backscatter link that cannot be filtered out. In the receiver in

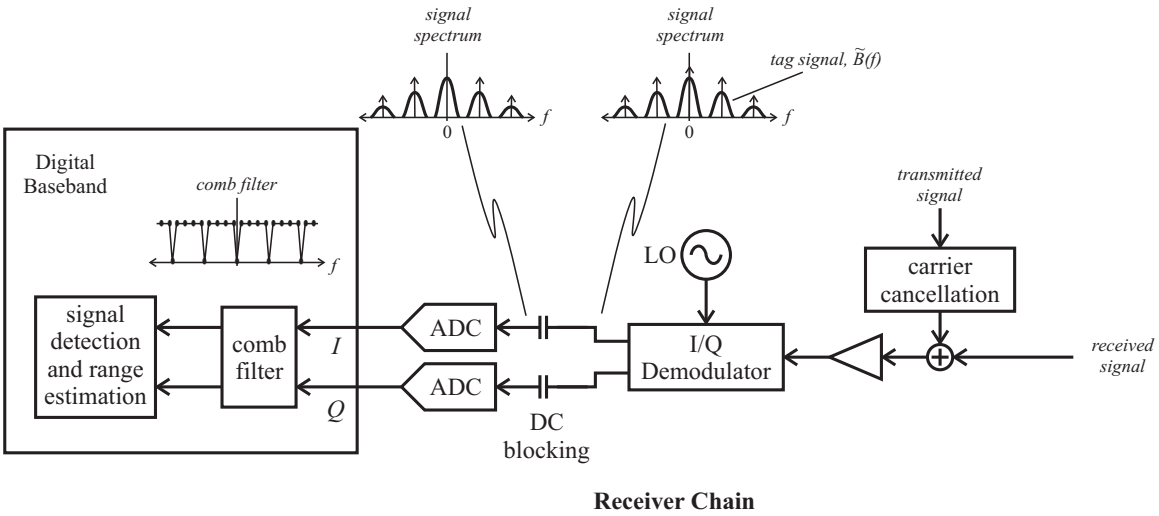

Figure 28: The reader samples the downconverted received waveform at above Nyquist for the POW and applies a comb filter with notches at each POW subcarrier frequency. This preserves the POW carrier for range estimation.

Figure 27, the signal is sampled faster than the Nyquist rate for the tag backscatter signal and detected as a binary phase-shift-keyed (BPSK) signal just as the reader based on a CW carrier in Section 2.3.2.

Figure 28 shows that the second method maintains the POW in the signal. This method uses a digital comb filter with notches at each POW subcarrier frequency to remove the unmodulated multipath components while preserving the POW carrier. The tradeoff is the need for sampling rates faster than the Nyquist rate of the POW rather than the tag backscattered signal. Conventional readers only sample faster than the Nyquist rate of the tag backscattered signal. Modulated multipath components depend on the frequency selectivity of the channel at the POW signal bandwidth.

The high PAPRs of POWs are likely to drive the passband LNAs and amplifiers into clipping distortion. The passband amplifiers in a POW system are designed to handle the peak-power levels of $P_{\text{out,CW}} + PAPR_{\text{dB}}$ dBm where $P_{\text{out,CW}}$ is the output power into the amplifier in a CW system in dBm. This augmented amplifier power-handling specification may be undesirable if it entails increased cost. Active cancellation of self-interference alleviates clipping in the initial passband LNAs.

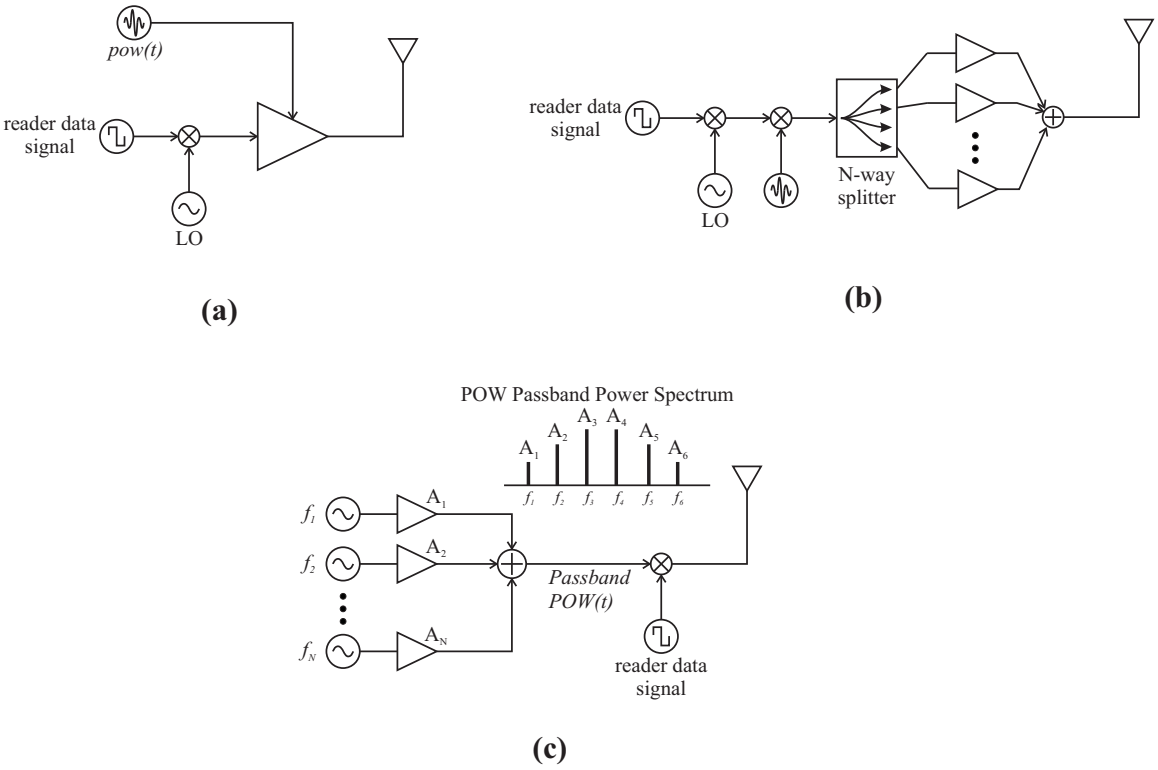

Figure 29: The reader transmit signal consisting of data and POW can be mixed and amplified by either (a) a class A amplifier with POW providing the power supply or (b) distributed amplification of N equally-power signals into class AB or class C amplifiers. Alternatively, the POW can be (c) sourced and amplified at passband with class AB or class C amplifiers.

3.4.2 Changes to Reader Transmitter

The most cost-effective, simple, and efficient way of creating a POW source at baseband is to store the POW digitally and output it with a digital-to-analog converter (DAC). The output is repeated continuously every T_{POW} seconds and low-pass filtered to remove quantization noise. Then the POW is amplified and upconverted to passband.

Figure 29a shows how a POW can be modulated onto a local oscillator (LO) at the passband center frequency premixed with reader data. There is one class A amplifier that takes the passband reader data as an input and amplifies it with a gain linearly proportional to the POW voltage. The amplifier uses the POW as its power input rather than its signal input. This way, there is no voltage clipping at the amplifier output due to the POW's voltage peaks. Another modification to this method is premixing the reader commands

with the POW instead of with the LO, ensuring minimal distortion at the amplifier output. A Class A amplifier is used here to avoid any distortion of the output signal. This method has the least number of necessary components to fully implement POW. However, Class A amplifiers only operate with up to 25% power efficiency and are typically more expensive than other classes of amplifiers [41].

Figure 29b shows the distributed amplification method. The reader signal, consisting of POW mixed with the passband centery frequency and reader data is split into N equally powered signals amplified in parallel and then combined to form the transmitted signal. This method avoids voltage clipping since the signal voltage input into each amplifier is smaller than the pre-split voltage. This method may use Class AB or Class C amplifiers to get power efficiencies up to 78.5% or 90%, respectively [41].

In Figure 29c, discrete frequency subcarrier sources and amplifiers are combined to form a POW at passband. The frequency sources are individually tuned to the frequencies of the desired POW passband spectrum, and the amplifiers' gains are individually tuned to fit the POW passband spectrum as in the figure. Class AB or class C amplifiers are used in this configuration since they operate with higher power efficiency than Class A amplifiers. This method works best for POWs with many subcarriers since there is no need for upconversion, which adds intermodulation distortion. Its disadvantage is the large cost and space requirements of implementing so many components.

CHAPTER IV

RANGING IN PASSIVE WIRELESS SENSOR NETWORKS

The last chapter showed that the reader-received waveform contains information about the round-trip time delay of a propagating radio wave backscattered from the tag. There also exists nonlinear reflection interference, two types of multipath interference, and noise, which are the obstacles that a POW ranging system must overcome to measure range. This chapter presents the current state of the art in passive WSN ranging and discusses how to implement a POW ranging system. Theory for characterizing the ranging performance of a POW-based range estimator covers the effects of POW shape, cluttered environments, and nonlinear reflections.

The "performance" of a range estimation system is typically broken down into the qualitative descriptors accuracy and precision. **Accuracy** is a qualitative descriptor that describes the degree of closeness of the range estimates to the true range. The amount that the mean of a large, statistically significant set of range estimates deviates from the true range quantifies the bias of the estimator. Mathematically, the bias is

$$\text{Bias} \equiv r_{\text{true}} - E\left[\hat{r}\right] \tag{57}$$

$$\hat{\text{Bias}} = r_{\text{true}} - \frac{1}{N}\sum_{n=1}^{N}\hat{r}_n \tag{58}$$

Here, equation (57) is the formal definition where the expected value of the range estimate $\hat{r}$ is used. Equation (58) is the estimated bias of a set of N range estimates. An unbiased estimator has perfect accuracy, which means it displays zero deviation from the true range as the number of range estimations goes to infinity. Biased estimators display a nonzero deviation from the true range. A positively biased estimator that predicts positive deviations on average is said to "predict the range farther than normal". Conversely, a negatively biased estimator that predicts negative deviations is said to "predict the range closer than normal". Positive and negative bias can be calibrated out of the estimator once the bias is

measured.

Precision is the degree to which the estimator produces the same results when the tag range remains fixed. Precision is the inverse of uncertainty; An estimator which is highly uncertain is very imprecise and vice versa. The standard deviation of a large, statistically significant set of estimates quantifies the uncertainty of the estimator. Estimator uncertainty is mathematically defined as

$$\text{Uncertainty} \equiv \sqrt{E\left[\hat{r}^2\right] - \left(E\left[\hat{r}\right]\right)^2} \tag{59}$$

$$\text{Uncertainty} = \sqrt{\frac{1}{N}\sum_{n=1}^{N}\hat{r}_n^2 - \left(\frac{1}{N}\sum_{n=1}^{N}\hat{r}_n\right)^2} \tag{60}$$

Here, equation (59) is the formal definition of the uncertainty of the estimator, and equation (60) is the estimate of the uncertainty for a set of N range estimates. Uncertainty has physical meaning of the expected deviation from the mean of any given range estimate. It has the same units as the range variable (m).

Classical estimation theory is extremely useful in explaining the bias and uncertainty of a POW-based range estimation system. The Crámer-Rao lower bound (CRLB) [42] and Ziv-Zakai lower bound [43] both serve as tight lower bounds to the actual estimation uncertainty. The Ziv-Zakai lower bound is tighter in general than the CRLB, and it accounts for many types of environmental and practical phenomena such as small-scale fading and edge-correlation errors. However, the conciseness and simplicity of the CRLB makes it the preferred model for practical design work over the Ziv-Zakai lower bound.

Existing theory of nonlinear reflections is not adequate for predicting the effects of a charge pump reflection on POW ranging. A new empircal model is presented that allows for different charge pump parameters and POW shapes. The validity of this proposed model is evaluated in the next chapter.

4.1 Current Ranging Methods in Wireless Sensor Networks

Ranging systems for WSNs require estimating a parameter of the reader-received waveform and deducing the estimated range. The current state-of-the-art of ranging in WSNs is shown here. There are numerous scientific studies and commercial implementations summarized

in this section. The methods for ranging are received signal strength indication (RSSI), interferometry, and time-of-flight (ToF).

4.1.1 Received Signal Strength Systems

According to the backscatter radio link budget equation (8), the reader-received signal power falls off $1/r^4$ in a free space environment. The reader can measure its received signal power using a received signal strength indicator (RSSI) and backsolve the link budget equation to determine range. For a free-space environment, there is one unique value of range that fulfills the link budget equation, and a contour map of equi-power lines can be drawn to characterize the environment.

The path-loss exponent (4.0 in the backscatter radio case) varies depending on the type of environment present. Sparse environments such as outdoor or low-clutter indoor backscatter radio environments have low backscatter (i.e. two-way) path-loss exponents typically between 4.4 and 4.8 [44]. Densely-cluttered environments such as indoor office environments with hard partitions have backscatter path-loss exponents up to 6.0 [44]. These values are purely statistical and can only be practically measured rather than derived for any given environment. Every environment is different, and clutter perturbs the equi-power contours of the free-space model. Moving clutter around within the environment changes the equi-power contous as well. For these reasons, RSSI ranging is considered unreliable in environments that do not approximate free space.

RSS ranging has several advantages over other range-finding methods. Its primary advantage is low-cost implementation. RSS ranging does not require cross-correlations, upsampling, or synchronization of any kind. All that is needed is to measure received signal strength, which is simply done with a software routine in any receiver with an ADC that performs signal processing at baseband. Secondly, RSS ranging can be implemented with minor hardware change in analog receivers. One final advantage is that modulation schemes and data rates do not significantly affect the RSS ranging algorithm.

A common drawback for RSS ranging is its poor accuracy due to small-scale fading. A range measurement that would be accurate in one particular environment would be thrown

off due to the presence of an extra reflector in the environment such as a person, a puddle of water, or a moving forklift. One study uses loss and scattering features to enhance their ranging algorithm [45]. For accurate RSS ranging, a database of RSSI values versus location on a map can be created and indexed to provide more accurate ranging rather than just assuming a constant path-loss exponent [46]. Many studies and suggested improvements of accuracy and precision have been performed for RSS ranging in WSNs [6] [5] [7]. However, the prevailing issue of inflexibility to a changing multipath environment remains the biggest drawback.

4.1.2 Interferometry Systems

A ranging system can measure the phase difference at a single-frequency tone between transmission and reception to ascertain the distance to the tag. Two independent phase measurements at different frequencies eliminate the ambiguity and resolve the distance to the tag. The distance to the tag can be expressed in terms of frequency and phase delay as

$$\begin{aligned} \hat{r} &= \frac{c}{2f_1}\left(\frac{\theta_1}{2\pi} + n_{\text{amb},1}\right) \\ \hat{r} &= \frac{c}{2f_2}\left(\frac{\theta_2}{2\pi} + n_{\text{amb},2}\right), \end{aligned} \tag{61}$$

at two measurement frequencies f_1 and f_2. The ambiguity factors $n_{\text{amb},1}$ and $n_{\text{amb},2}$ express the fact that the distance may be integer multiples of half-wavelengths away from the transmitter. However, this ambiguity is factored out after some rearranging and subtraction to obtain [8]

$$\hat{r} = \frac{c}{4\pi}\frac{\theta_2 - \theta_1}{f_2 - f_1}. \tag{62}$$

The distance is dependent on how phase difference changes with frequency. This equation can be extended to N measurements by generalizing to a partial derivative that represents slope of phase difference versus frequency:

$$\hat{r} = \frac{c}{4\pi}\frac{\partial\theta}{\partial f} \tag{63}$$

The partial derivative measures the slope of a linear least-squares fit as shown in Figure 30.

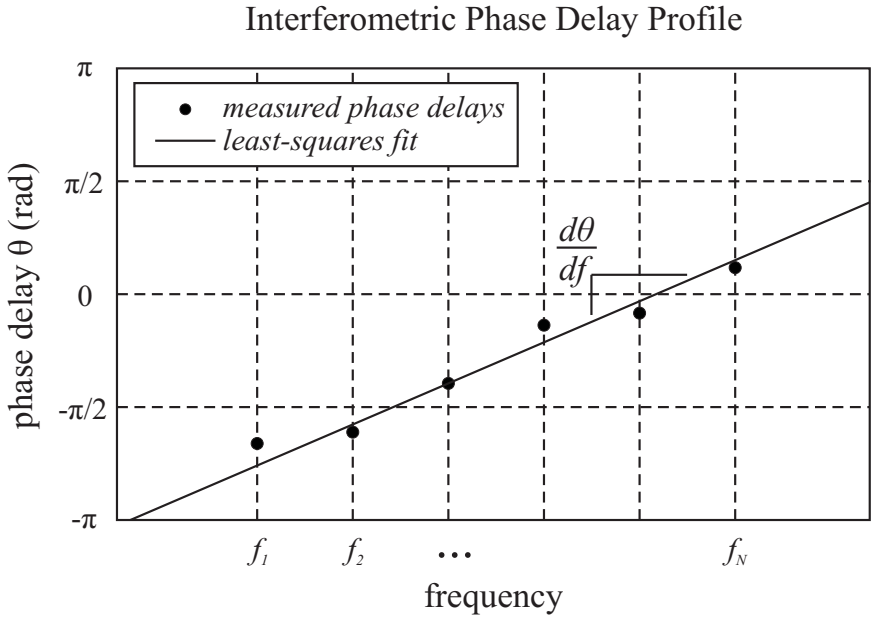

Figure 30: An interferometry system measures the phase difference between transmitted and received signals at N separate frequencies. Noise and interference can perturb the measured points. The slope of a linear least-squares fit is used to estimate the tag range as in equation (63).

A typical coherent receiver consists of an I/Q downconverter and a voltage-controlled oscillator (VCO) that changes the measurement frequency. The phase difference is estimated with I and Q signals as

$$\theta_e = \begin{cases} \tan^{-1}\left(\frac{Q}{I}\right) & \text{if } \mathrm{I} > 0 \\ \pi + \tan^{-1}\left(\frac{Q}{I}\right) & \text{if } \mathrm{I} < 0 \end{cases} \tag{64}$$

The tag's reflection states can add extra phase delay, but this can be accounted for within the ranging system if the tag's reflection states are known a-priori.

The uncertainty of an interferometric range estimator depends on the SNR, number of measured frequencies N, and frequency separation between measured frequencies Δf. In general, the variance of a range estimation measurement is estimated as [44]:

$$\sigma_r^2 = \left(\frac{c}{4\pi}\right)\left(\frac{\sigma_{\theta_e}^2}{\Delta f^2}\right)\left[\frac{\sum_{k=0}^{N-1} k^2}{\left[\sum_{k=0}^{N-1} k^2 - \frac{1}{N}\left(\sum_{k=0}^{N-1} k\right)^2\right]}\right] \tag{65}$$

Here, $\sigma_{\theta_e}^2$ is the estimate of the variance of the phase estimator from equation 64. A useful approximation is used when SNR > 8 dB [44]: $\sigma_{\theta_e}^2 \approx 1/2 \cdot SNR$. The variance for distance

then simplifies to

$$\sigma_r^2 \approx \left(\frac{c}{4\pi}\right)\left(\frac{1}{2\cdot \mathrm{SNR}\cdot \Delta f^2}\right)\left[\frac{\sum_{k=0}^{N-1} k^2}{\left[\sum_{k=0}^{N-1} k^2 - \frac{1}{N}\left(\sum_{k=0}^{N-1} k\right)^2\right]}\right] \tag{66}$$

This equation shows that uncertainty of interferometric ranging decreases as SNR and frequency spacing increase. It is not obvious from the equation, but uncertainty decreases with the number of frequency measurements N taken as well. These observations are validated by Li et. al. with their work with ranging in passive UHF RFID tags [47].

Interferometry systems are simple to implement in backscatter radio since the reader contains the system's oscillator, which enables coherent detection of the received waveform without needing timestamps or other clock synchronization between transmitter and receiver. Nikitin et. al. showed that the only necessary augmentation to passive UHF RFID systems is a dedicated software algorithm to compute the phase differences according to equation (64) after the signals have been sampled digitally [8]. This method works on existing passive UHF RFID readers that already employ a coherent receiver to communicate with passive tags.

Two drawbacks of interferometry are the time of measurement and bandwidth limitations. It takes more time to hop through multiple frequencies and to sample waveforms at each frequency before deducing range than to read an RSSI or sample one period of a time-of-flight waveform before deducing range. This is a limitation in WSNs that require very fast location update rates. Also, the frequency hopping sequence must confine itself to within the allotted spectrum. This limits the frequency spacing and number of frequency measurements that can be taken, which limits the uncertainty in equation (66).

4.1.3 Time-Of-Flight Systems

The most intuitive method of measuring distance to a tag is measuring the propagation time of a waveform originating from the reader transmitter, reflecting off the tag, and arriving back at the reader receiver. The range is then found using

$$\hat{r} = \frac{c\hat{\tau}}{2}, \tag{67}$$

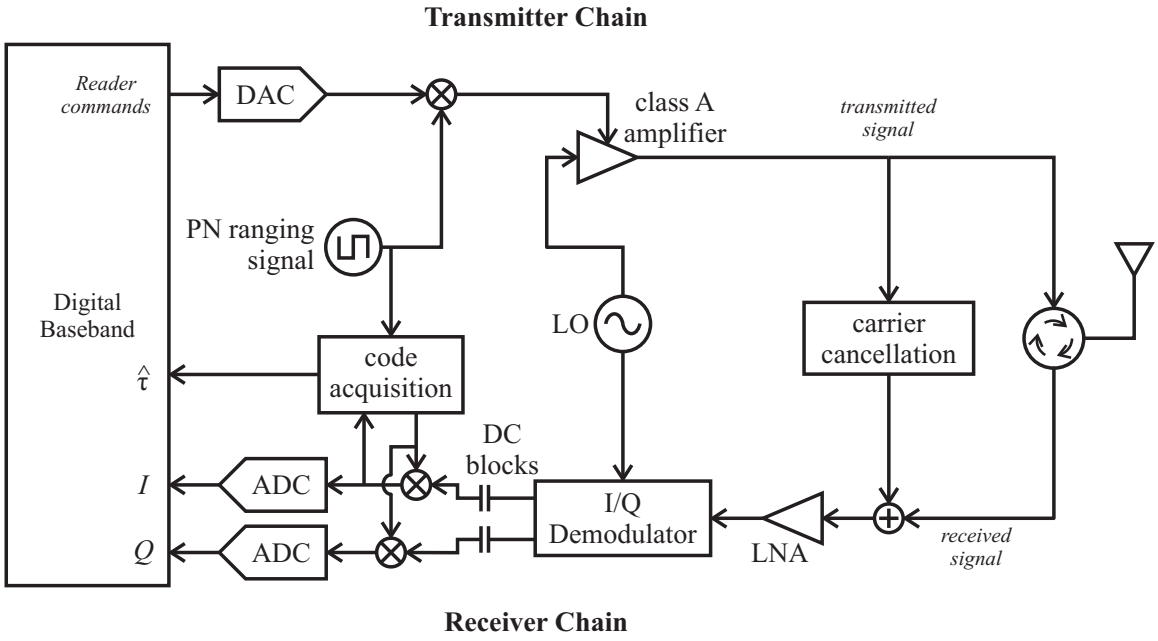

Figure 31: A conventional reader architecture is augmented with a PN code that spreads the transmitted waveform and despreads the received waveform. The code acquisition and tracking loop outputs a relative time delay between the transmitted and received waveform, which is converted to a range estimate.

where $\hat{\tau}$ is the estimated propagation delay and c is the speed of light. This method is called either "Time of Flight" (ToF) or "Time of Arrival" (ToA) in the literature, which spans applications such as radar, global positioning system (GPS), and WSNs.

ToF ranging systems in passive WSNs typically use spread-spectrum signals that are binary phase-shift keyed (BPSK) between values of +1 and -1 to obtain fine precision of range measurements while maintaining the signal envelope to allow energy harvesting to occur in the tag. A possible reader architecture that is slightly modified from the conventional CW reader from Figure 6 is shown in Figure 31. The backscatter detection section of the receiver is largely unchanged, but extra hardware is added to implement the psuedorandom noise (PN) sequence. The acquisition/tracking block actively tracks the delay of the PN sequence with respect to the transmitted PN sequence. The relative time delay output is then converted into range using the distance equation (67).

The maximum unambiguous range of a spread-spectrum ToF ranging system depends

on the time period of the PN waveform:

$$d_{\max} = \frac{cT_{\mathrm{PN}}}{2}, \tag{68}$$

Therefore, this period is chosen to produce a maximum unambiguous range slightly greater than the maximum range of the passive tags. A PN sequence is composed of a unique sequence of digital bits, which are refered to as "chips" when represented as an analog waveform in the time domain. The number of chips transmitted per second is called the chipping rate. The time period of the PN sequence T_{PN} is the length of time required to transmit the unique sequence of chips.

The uncertainty of the ranging estimate depends on the "sharpness" of the PN waveform's autocorrelation function. A detailed explanation of this trait is given in section 4.2.1, but it is safe to point out here that a faster chipping rate produces more precise ranging measurements than a slower chipping rate (holding PN time period constant). This dependency is pointed out by Bensky [44] as well. The tradeoff of increasing the chipping rate is the requirement of faster system clocks and faster digital signal processing.

Multipath interference is inherently reduced in a spread-spectrum system, which is a unique advantage [11]. Consider a reader-received waveform that contains the reader-transmitted upconverted PN waveform carrier, the backscattered waveform, L multipath reflections, and complex noise:

$$\tilde{y}(t) \quad = \quad \alpha\tilde{b}(t-\tau)\mathrm{PN}(t-\tau)e^{-j2\pi f_{\mathrm{c}}(t-\tau)} + \sum_{l=1}^{L} \alpha_l \mathrm{PN}(t-\tau_l)e^{-j2\pi f_{\mathrm{c}}(t-\tau_l)} + \tilde{n}(t). \tag{69}$$

Refer to section 3.3 for descriptions of the variables in this equation. When this received signal is downconverted into I and Q and subsequently despread by the PN sequence at delay τ, the resulting complex waveform (constructed from I and Q) is:

$$\tilde{y}(t) \quad = \quad \alpha\tilde{b}(t-\tau)e^{-j2\pi f_{\mathrm{c}}(t-\tau)} + \sum_{l=1}^{L} \alpha_l \mathrm{PN}(t-\tau)\mathrm{PN}(t-\tau_l)e^{-j2\pi f_{\mathrm{c}}(t-\tau_l)} + \tilde{n}(t). \tag{70}$$

Here, the tag signal has been despread, and the multipath components are still mired in PN waveforms. the multipath components can be partially filtered out after the despreading process since the despread tag signal has smaller bandwidth than the spread multipath

components. This waveform is then used as the feedback for the acquisition/tracking block in Figure 31. The tag signal can be viewed as the target user in a code-division multiple access (CDMA) system while the multipath components are the other users. The key difference is that the multipath components actually have the same code as the desired backscattered waveform, but they are delayed by random delays and are unmodulated. The tag signal is despread while the multipath components remain spread.

In general, rake receivers, which combine the target direct-path signal with multipath-delayed components to improve the SNR [11], are not used in range estimation systems since only the direct-path delay is measured. However, the tag signal demodulator can use a rake receiver to improve the bit-error rate. Typically, rake receivers are not needed for applications with comparitively high received SNR as is the case with passive WSNs.

A potential drawback to spread-spectrum ToF ranging is the need for a wideband front end on the tag. The chipping rate required to achieve a specified measurement uncertainty produces a transmit spectrum with bandwidth $B \approx 2f_{\text{ch}}$ where f_{ch} is the chipping rate. The tag's front end must pass the entire band with approximately equal amplitude so as to not distort the PN waveform. It is problematic since increasing the bandwidth of the tag's front end necessarily decreases the quality of the match within the band. A lower-quality match will produce lower-amplitude input waveforms into the charge pump, reducing the energy harvesting efficiency.

4.2 Range Estimation With Power-Optimized Waveforms

A passive WSN that uses POWs for energy harvesting may estimate the range to the tag by cross-correlating the reader-received signal with the reader-transmitted signal. This process is the same as maximum-likelihood (ML) estimation of range. The ML estimator assumes noise as the only AWGN interferer to estimation. A channel equalizer can be used to reduce the effects of symbol distortion if any exists [48]. The theory presented in this section section 4.3 is existing theory on range estimation modified to accomodate POWs. The theory presented here is then compared to the simulations in Chapter 5 and the measurements in Chapter 6.

A POW-ranging system tests for the presence of tag data first and estimates range second if tag data is determined to be present. This is the basic sequence of operations within a general time-of-flight ranging system. **Detection** is the test a ranging system performs on the received signal to determine whether a target is present. The target (i.e. the tag) in a passive WSN differentiates itself from the surrounding clutter by modulating the incoming waveform in two different reflective states as discussed in Section 2.2.4. Therefore, the reader detects the presence of a tag by testing for the presence of tag data. The methods for tag data detection with a POW carrier already exist as explained in Section 3.4.1. The user requirements dictate whether the detected tag needs to have its range measured once a tag is detected.

Estimation is the calculated approximation of range based on the reader-received waveform. It will be explained in the next section that maximum likelihood estimation is the optimal estimator for signal delay estimation. The ML estimation process simplifies to the calculation of the maximum of a cross-correlation of the reader-received waveform with a copy of the transmitted POW. The delay at which the cross-correlation produces a maximum becomes the estimated delay and is then converted to estimated tag range using the distance formula. The data will be sampled digitally, and estimation will occur in software. A *coarse* estimation finds the maximum across one POW period at the sampling rate, while a *fine* estimation finds the maximum at an upsampled rate (assuming the data was sampled faster than Nyquist).

Figure 32 shows the coarse estimation is quick to perform. The upsampling procedure takes extra computation time to perform, which slows the update rate of the range estimations. Both coarse and fine estimates are only as precise as their sampling rates allow. Digital range estimates like these locate the tag within a **range bin**, which has length in space determined by the sampling time period:

$$r_{\text{bin}} = \frac{cT_{\text{s}}}{2} \quad \text{(m)} \tag{71}$$

A fine estimation upsamples the data, which shortens the sampling period effectively making the range bins much shorter in space.

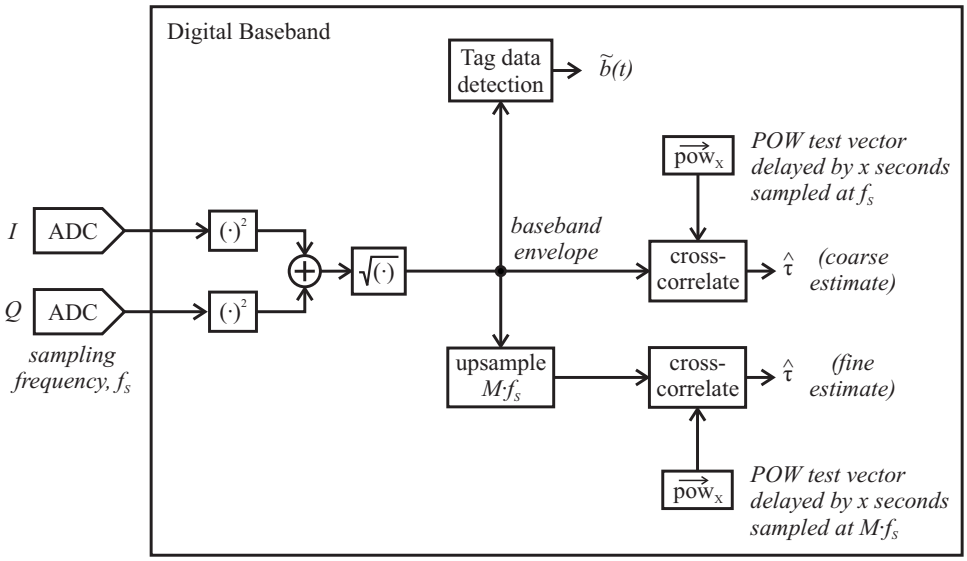

Figure 32: The sampled reader-received waveform is cross-correlated digitally with the transmitted POW to obtain the coarse estimation. The data can be upsampled to calculate the fine estimation in order to meet an uncertainty specification.

Implementing a ranging system in an existing reader is straightforward. There are a number of architectures for designing the reader receiver to detect tags and estimate tag range. Figure 33 shows an architecture that accomplishes both tasks. It is a coherent receiver as shown but can be converted to a noncoherent receiver by combining I and Q signals together to obtain the magnitude of the downconverted signal before detection or estimation occurs. Another simpler method is implementing an envelope detector. It is well known that noncoherent detectors are more error-prone than coherent detectors [49], so the cost savings of using one ADC rather than two ADCs is the primary motivator here. A matched filter receiver [49] that has an impulse response of a time-reversed POW is the classical receiver design. A field-programmable gate array (FPGA) can implement the matched filter and ranging algorithm as well. Building a new FPGA design incurs high development costs, thus they are not favorably compared to an existing system that already uses an ADC and computer to perform the range estimation.

The receiver in Figure 33 is optimized for high sensitivity of tag detection and range estimation at the cost of computation time. The I and Q signals are DC-blocked to partially attenuate the multipath interference as discussed in Section 3.4.1 and reduce the required

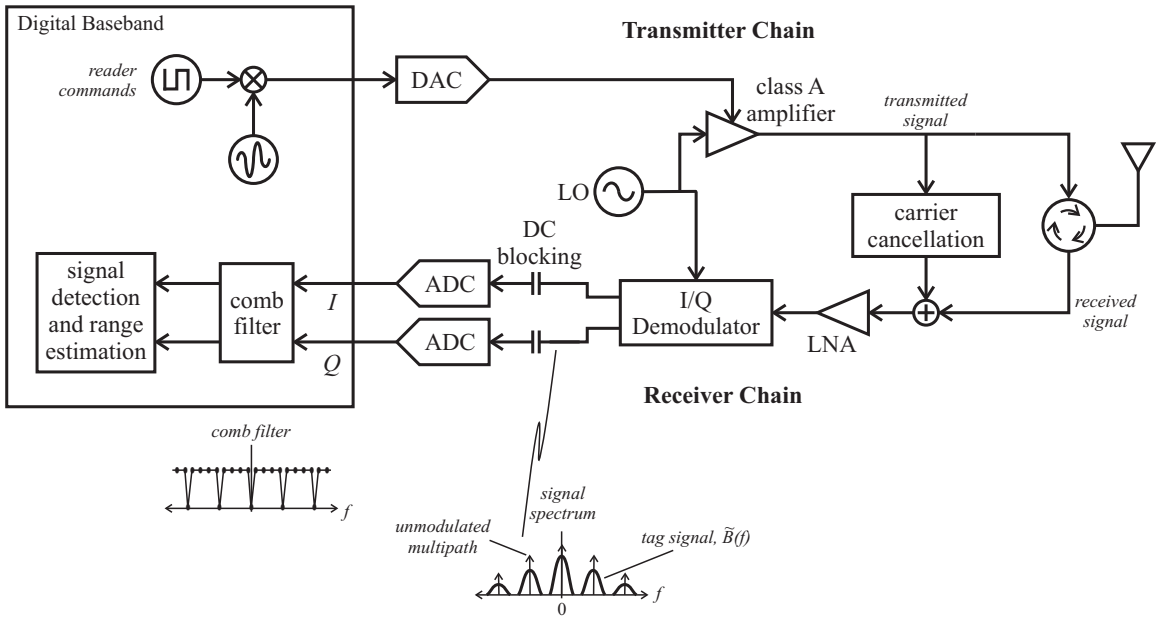

Figure 33: A possible receiver architecture that estimates range with a cross-correlation after analog-to-digital conversion.

dynamic range of the ADCs. The comb filter after the ADCs attenuates the unmodulated multipath components completely, but this operation requires upsampling and either a cross-correlation operation or a pair of Fourier transforms to perform. After comb filtering, the tag data is detected and fine-ranging is performed. Coarse ranging is redundant after the upsampling of the comb filtering operation.

This receiver uses active POW carrier cancellation to attenuate the self-interference of the reader. The comb-filtering receiver is highly sensitive to tag data since it eliminates any unmodulated multipath interferers. The testbed constructed for this research uses the architecture of Figure 33. However, the experiments test phenomena that have no bearing on the type of receiver used.

4.2.1 Estimation of Delay

Detection of the presence of a tag is a separate problem from tag range estimation. The only dependency between the two problems is that a positive detection initiates a range estimation. However, the estimation method is independent of the detection method, and the optimality of the estimator depends on the known probability distributions of delay and

input data.

The optimal estimator for ranging in a noisy line-of-sight channel assuming uniform random tag position is the maximum likelihood (ML) estimator [50]. A maximum a-posteriori (MAP) estimator reduces to the ML estimator since the probability distribution of the delay is assumed to be uniform between 0 and T_{POW} s. The software portion of the receiver upsamples the complex baseband waveform in the reader to a suitable rate for sufficient range-bin uncertainty according to the specifications. This sampled waveform spanning one or more POW time periods has a joint pdf conditioned on a particular round-trip time delay τ. The ML estimator equates the **likelihood function** to the joint pdf of the sampled waveform:

$$L(\tau|\tilde{y}) = f_{\tilde{y}}(\tilde{y}|\tau) \tag{72}$$

where $L(\tau|\tilde{y})$ is the likelihood function of delay τ given the received waveform $\tilde{y}$ is observed. The ML Estimator finds the maximum of the likelihood function L over all possible values of τ, which results in a delay estimate. Mathematically, the ML estimator solves

$$\hat{\tau} = \arg\max_{\tau} \left(L(\tau|\tilde{y})\right) \tag{73}$$

for τ, which results in the estimate $\hat{\tau}$. It will be seen later in Section 4.3 that the logarithm of the likelihood function reduces to the cross-correlation function of the received sample set and a copy of the transmitted POW. Then, the receiver simply finds the maximum value of the cross-correlation across one POW period, which serves as the delay estimate. The distance equation is used to convert the time delay estimate into a range estimate.

The variance of a noncoherent ML estimator has a minimum defined by the Cramer-Rao lower bound (CRLB). Ipatov [11] and Urkowitz [42] present the CRLB in two equivalent forms:

$$\mathrm{Var}(\hat{\tau}) \geq \frac{1}{-R''_{\mathrm{pow}}(0) \cdot \mathrm{SNR}} \tag{74}$$

$$\mathrm{Var}(\hat{\tau}) \geq \frac{1}{4\pi^2 B_{\mathrm{RMS}}^2 \cdot \mathrm{SNR}} \tag{75}$$

The RMS bandwidth B_{RMS} is the same as that defined in the previous chapter in equation (13). It is in terms of temporal frequency f instead of angular frequency ω. The CRLB

depends on the second derivative of the POW's normalized autocorrelation function evaluated at zero lag $R''_{\text{pow}}(0)$ and SNR. The normalized autocorrelation is defined in two ways: First, the time domain definition correlates the POW with itself as a function of time delay divided by POW signal power. Second, the autocorrelation is the inverse Fourier transform of the POW power spectral density normalized to POW signal power. Mathematically, these definitions are

$$R_{\text{pow}}(\tau) = \frac{1}{E_{\text{pow}}} \int_{-\infty}^{\infty} \text{pow}(t-\tau) \cdot \text{pow}(t)\ dt \tag{76}$$

$$R_{\text{pow}}(\tau) = \frac{1}{E_{\text{pow}}} \int_{-\infty}^{\infty} |\text{POW}(f)|^2 e^{j2\pi f\tau} df \tag{77}$$

$$\text{where } E_{\text{pow}} \equiv \int_{-\infty}^{\infty} |\text{POW}(f)|^2 df = \int_{-\infty}^{\infty} \text{pow}^2(t) dt \tag{78}$$

The second derivative of the POW's autocorrelation is a measure of the "sharpness" of the POW; a sharper autocorrelation function is less prone to perturbations from noise. Therefore, it is more precise in estimating the delay.

The ML estimator is asymptotically unbiased in the presence of noise as the number of estimations goes to infinity, which implies the estimator becomes more accurate as more range estimations are consolidated. It will be shown in Section 4.5 that nonlinear reflections distort the POW on the backward link to the reader, which adds bias to the ML estimator.

The CRLB presented by Ipatov [11] and Urkowitz [42] assume analog estimation methods. The received signal is not sampled through an ADC. Instead, an analog matched filter or an analog sample-and-hold correlator outputs the log-likelihood function. An analog estimator such as these operating over a single POW time period results in an estimator variance of equations (74) and (75). Extending these analog CRLBs to the discrete domain results in a reduction of the estimator variance by a factor of the number of points sampled N per delay estimate:

$$\text{Var}(\hat{\tau}) \geq \frac{1}{-N R''_{\text{pow}}(0) \cdot \text{SNR}} \tag{79}$$

$$\text{Var}(\hat{\tau}) \geq \frac{1}{N 4\pi^2 B_{\text{RMS}}^2 \cdot \text{SNR}} \tag{80}$$

The uncertainty imposed by the received noise is reduced by sampling more and more points on the received signal. The estimator may also span more than one POW time period, which

reduces the uncertainty even further. A more convenient formulation of the CRLB is found by substituting $N = N_{\mathrm{POW}} f_{\mathrm{s}} T_{\mathrm{POW}}$:

$$\mathrm{Var}(\hat{\tau}) \geq \frac{1}{-(N_{\mathrm{POW}} f_{\mathrm{s}} T_{\mathrm{POW}}) R''_{\mathrm{pow}}(0) \cdot \mathrm{SNR}} \tag{81}$$

$$\mathrm{Var}(\hat{\tau}) \geq \frac{1}{(N_{\mathrm{POW}} f_{\mathrm{s}} T_{\mathrm{POW}}) 4\pi^2 B^2_{\mathrm{RMS}} \cdot \mathrm{SNR}} \tag{82}$$

where the product of sampling frequency and POW time period $f_{\mathrm{s}} T_{\mathrm{POW}}$ is equal to the number of sampled points per POW time period. The parameter N_{POW} is the number of POW time periods used by the estimator. This may be a single POW time period, an integer multiple, or any positive rational number (e.g. 1, 2, 3, 3.25 and 4.6 are all valid) such that N is an integer.

4.2.2 Power-Optimized Waveform Shapes

The ranging uncertainty largely depends on the autocorrelation sharpness, RMS bandwidth, and the estimator's efficiency. The ML estimator for time delay is well-studied to be asymptotically efficient, which means the variance of a ML estimated delay approaches the variance predicted by the CRLB for large SNR as the number of estimations goes to infinity. Therefore, the CRLB equations (81) and (82) serve as the analytical model for ranging uncertainty.

Both CRLB expressions illuminate how the RMS bandwidth, SNR, and sharpness of the POW autocorrelation function affect uncertainty of a delay estimate. POWs with sharp autocorrelation functions at zero delay are more precise than POWs with blunt autocorrelation functions. Likewise, measurements performed on high SNR received waveforms are very precise. RMS bandwidth and autocorrelation sharpness are directly related as

$$R''_{\mathrm{pow}}(0) = \frac{\partial^2}{\partial \tau^2} \left[\frac{1}{E} \int_{-\infty}^{\infty} |\mathrm{POW}(f)|^2 e^{j2\pi f \tau} df \right]_{\tau=0} \tag{83}$$

$$= \frac{-4\pi^2}{E} \int_{-\infty}^{\infty} f^2 |\mathrm{POW}(f)|^2 df \tag{84}$$

$$= -4\pi^2 B^2_{\mathrm{RMS}} \tag{85}$$

A wideband POW exhibits a sharp autocorrelation and produces precise delay estimates.

The bias of the ML estimator is independent of POW shape because ML estimation of delay is itself unbiased [44]. Section 5.1 in the next chapter presents simulations that confirm the CRLB uncertainty model and the unbiased nature of ML estimated delay.

4.3 Noisy Free-Space Backscatter Channel

Analysis of ML estimation in a noisy free-space environment presents the basic principles of range estimation. A reader transmits a POW-pulse train into a free-space environment. A tag modeled as a modulating linear reflector then backscatters the signal back to the reader, where the reader receives it as a power-decayed and time-delayed version of the original pulse plus additive white Gaussian noise (AWGN):

$$\tilde{y}_{\mathrm{RX}}(t) = \alpha\tilde{b}(t-\tau)\mathrm{pow}(t-\tau)e^{j2\pi f_{\mathrm{c}}(t-\tau)} + \tilde{n}(t) \tag{86}$$

There are no multipath components to account for since there are no other reflectors in the environment. The true round-trip time delay τ spans the time the pulse departs the reader TX antenna to the time the reader RX antenna receives the signal after backscattering from the tag.

The reader receiver downconverts the received signal into in-phase $y_{\mathrm{I}}(t)$ and quadrature components $y_{\mathrm{Q}}(t)$ of the baseband signal as in Figure 33. DC blocks are not needed in the free-space environment since there are no unmodulated interferers. These real-valued signals I and Q can be used to construct the complex signal (magnitude and phase w.r.t. the transmitted carrier frequency) used for coherent estimation or just the magnitude for noncoherent estimation. The tag's backscatter signal is assumed to be binary phase shift keying (BPSK) switching between open and short-circuit reflection states. This signaling scheme has a modulation factor of 1, and it does not add or subtract energy during the tag's reflection (refer to Section 2.2.4).

The phase reversals of the BPSK backscattered signal do not affect estimation, even though detection of the tag backscatter signal relies on the presence and detection of these same phase reversals. This can be explained in two ways: First, the ML estimator can be designed to find the maximum of the *magnitude* of the likelihood function rather than simply the raw maximum. This accounts for the $\tilde{b}(t-\tau)$ phase reversals that negate the

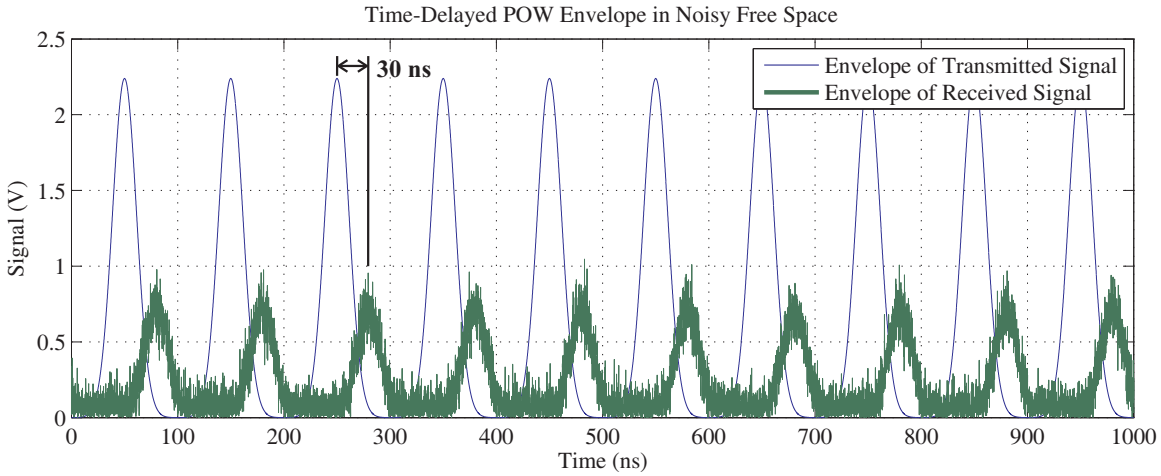

Figure 34: A simulated example illustration of a Gaussian POW transmitted and received in a passive WSN in a noisy free-space environment. The roundtrip delay $\tau = 30$ ns, the attenuation coefficient $\alpha = \sqrt{0.1}$, and the SNR is 10 dB.

POW carrier. Second, the detector can be designed to remove the $\tilde{b}(t-\tau)$ phase reversals prior to delay estimation such that the estimator operates on the received, delayed POW carrier alone plue noise. Thus, the complex baseband signal input into the estimator is

$$\begin{aligned} \tilde{y}(t) &= \alpha \text{pow}(t-\tau) e^{j2\pi f_c \tau} + \tilde{n}(t) \\ &= [\alpha \text{pow}(t-\tau)\cos(2\pi f_c \tau) + n_{\text{I}}(t)] \\ &\quad + j\left[\alpha \text{pow}(t-\tau)\sin(2\pi f_c \tau) + n_{\text{Q}}(t)\right]. \end{aligned} \tag{87}$$

Here, $\tilde{y}(t)$ denotes the baseband waveform used for estimation. The term $n_{\text{I}}(t)$ is the real-valued I-channel noise, and $n_{\text{Q}}(t)$ is the real-valued Q-channel noise each with thermal noise power $P_{\text{N,I}} = {}^{kTB}/_{2}$ W.

Figure 34 shows a transmitted POW and received POW in a noisy free-space channel. The magnitude of the received I and Q signals are taken, which discards the backscatter data waveform $\tilde{b}(t-\tau)$. Notice the peak of the received signal looks 30 ns delayed from the tranmission to the naked eye. The random vertical perturbations of the noise component add uncertainty to the ML estimator.

4.3.1 Coherent Estimator Test

This section derives the coherent estimator for the continuous-time receiver. The discrete estimator used in the digital receiver in Figure 33 uses the same test in discrete form.

In coherent estimation, both I and Q signals are combined to form the complex signal $\tilde{y}(t) = y_{\mathrm{I}}(t) + jy_{\mathrm{Q}}(t)$. This is a complex Gaussian random process with the distribution

$$f_{\tilde{y}(t)}(\tilde{y}(t)|\tau) = \frac{1}{\pi P_{\mathrm{N}}} e^{-\frac{1}{P_{\mathrm{N}}}|\tilde{y}(t) - \alpha \mathrm{p\tilde{o}w}(t-\tau))|^2} \tag{88}$$

The mean is simply the delayed POW at the received signal strength $\alpha \mathrm{p\tilde{o}w}(t-\tau)$, and the variance is the noise power P_{N}. The complex notation for the POW delayed by true time delay τ refers to the coherent phase provided during the I/Q downconversion:

$$\mathrm{p\tilde{o}w}(t-\tau) = \mathrm{pow}(t-\tau)e^{j2\pi f_{\mathrm{c}}\tau}. \tag{89}$$

The continuous-time estimator operates on an integer multiple of POW time periods. It is assumed that the data set spans one POW period for this analysis. The resulting likelihood function is the joint pdf of the random process over the span of one time period:

$$L(\tau|\tilde{y}) = f_{\tilde{y}}(\tilde{y}|\tau) = \prod_{0}^{T_{\mathrm{POW}}} \left(\frac{1}{\pi P_{\mathrm{N}}} e^{-\frac{1}{P_{\mathrm{N}}}|\tilde{y}(t) - \alpha \mathrm{p\tilde{o}w}(t-\tau)|^2} \right)^{dt} \tag{90}$$

A product integral $\prod_{0}^{T_{\mathrm{POW}}} (\cdot)^{\,dt}$ is the multiplicative equivalent to the standard, additive integral $\int_0^{T_{\mathrm{POW}}} (\cdot)\, dt$ [51]. This distribution assumes an independent and identically distributed noise process. The distribution for $f_{\tilde{y}}(\tilde{y}|\tau)$ uses the POW delayed by the true time delay τ as the mean of the signal vector and τ is a given constant.

The coherent ML estimator takes the natural logarithm of the likelihood function and finds its maximum by taking the partial derivative w.r.t. τ. Taking the natural logarithm and expanding the exponent results in:

$$\begin{aligned} \ln L(\tau|\tilde{y}) &= \int_0^{T_{\mathrm{POW}}} \left[\ln\left(\frac{1}{\pi P_{\mathrm{N}}}\right) \right. \\ &\quad \left. -\frac{1}{P_{\mathrm{N}}}\left(|\tilde{y}(t)|^2 - 2\alpha \mathrm{p\tilde{o}w}^*(t-\tau)\tilde{y}(t) + \alpha^2 \left|\mathrm{p\tilde{o}w}(t-\tau)\right|^2 \right) \right] dt \\ &= T_{\mathrm{POW}} \ln\left(\frac{1}{\pi P_{\mathrm{N}}}\right) - \frac{1}{P_{\mathrm{N}}} \int_0^{T_{\mathrm{POW}}} |\tilde{y}(t)|^2\, dt \\ &\quad + \frac{2\alpha}{P_{\mathrm{N}}} \int_0^{T_{\mathrm{POW}}} \mathrm{p\tilde{o}w}^*(t-\tau)\tilde{y}(t) dt - \frac{\alpha^2}{P_{\mathrm{N}}} \int_0^{T_{\mathrm{POW}}} \left|\mathrm{p\tilde{o}w}(t-\tau)\right|^2 dt \end{aligned} \tag{91}$$

The mathematical step in going from equation (90) to (91) is the property of the product integral: $\ln \prod_0^{T_{\mathrm{POW}}} f(t)^{\,dt} = \int_0^{T_{\mathrm{POW}}} \ln f(t) dt$ [51]. It is important at this point to understand

the variable for the likelihood function is roundtrip time delay τ. To make the analysis clearer, the true time delay will be denoted by τ_{true} and is considered a fixed constant. The observed waveform $\tilde{y}$ is a *given function* within the context of this likelihood function, and the POW waveform $\tilde{\text{pow}}(t-\tau)$ is now treated as a comparison function that depends on the tested delay τ. Simplifying the log-likelihood function further,

$$\begin{aligned} \ln L(\tau|\tilde{y}) &= T_{\text{POW}} \ln\left(\frac{1}{\pi P_{\text{N}}}\right) - \frac{E_{\text{RX}}}{P_{\text{N}}} + \frac{2\alpha}{P_{\text{N}}}\tilde{X}_{\text{pow,y}}(\tau) + \frac{\alpha^2 E_{\text{POW}}}{P_{\text{N}}} \qquad (92) \\ \text{where } \tilde{X}_{\text{pow,y}}(\tau) &= \int_0^{T_{\text{POW}}} \tilde{\text{pow}}^*(t-\tau)\tilde{y}(t)dt \\ E_{\text{RX}} &= \int_0^{T_{\text{POW}}} |\tilde{y}(t)|^2\, dt \\ E_{\text{POW}} &= \int_0^{T_{\text{POW}}} |\tilde{\text{pow}}(t-\tau)|^2\, dt \end{aligned}$$

The continuous-time, complex-valued cross-correlation function $\tilde{X}_{\text{pow,y}}(\tau)$ between the received signal $\tilde{y}$ and the test POW signal $\tilde{\text{pow}}^*(t-\tau)$ is substituted. Signal energies of the received signal E_{RX} and POW E_{POW} are substituted as well even though these terms have no specific bearing on the estimation.

The roundtrip delay is estimated by finding the maximum of $\ln L(\tau|\tilde{y})$ across the domain of tested time delays $\tau \in (0, T_{\text{POW}}]$. Many of the terms in equation (92) are independent of the tested delay such as noise power P_{N} and the signal energies E_{RX} and E_{POW}. The cross-correlation between the data vector and the conjugated POW is the only term that is dependent on tested delay τ. Thus, performing a search for the maximum value of the cross-correlation by changing the tested delay τ reduces to:

$$\hat{\tau} = \arg\max_{\tau}\left(\tilde{X}_{\text{pow,y}}(\tau)\right) \qquad (93)$$

This same cross-correlation test is used in the digital receiver from Figure 33. The sampled signal from the ADC consists of $N = N_{\text{POW}} f_{\text{s}} T_{\text{POW}}$ points. The cross-correlation then consists of $2N$ points. The maximum of this discrete-time cross correlation is simply found by running a maximum-finding routine without computing a discrete derivative. The delay that corresponds to the maximum is chosen for the coarse estimate if no upsampling was performed following quantization of the analog I and Q channels. The fine estimate is found by upsampling the sampled I and Q signals prior to cross-correlation.

4.3.2 Coherent Estimator Performance

ML estimators are unbiased. Therefore, the coherent ML estimator is perfectly accurate since its average range estimation tends to the true range as the number of estimations goes to infinity. The uncertainty of the coherent ML estimator tends to three bounds. The CRLB is the only bound that depends on the SNR. The other two bounds are called the information bounds:

$$\text{Upper Information Bound, } \sigma_{\text{up}} = \sqrt{\text{Var}\left(\mathcal{U}\left(0, \frac{T_{\text{POW}}}{2}\right)\right)} = \frac{T_{\text{POW}}}{2\sqrt{12}} \tag{94}$$

$$\text{Lower Information Bound, } \sigma_{\text{low}} = \sqrt{\text{Var}\left(\mathcal{U}\left(0, \frac{T_{\text{s}}}{2}\right)\right)} = \frac{T_{\text{s}}}{2\sqrt{12}} \tag{95}$$

Here, $\mathcal{U}(a, b)$ is the uniform probability distribution with limits a and b. These bounds are essentially determined by how much information is available to the estimator. The upper information limit caps the uncertainty since the estimator assumes the tag is closer than a roundtrip delay of T_{POW}. The lower information limit represents the situation where the estimator receives the most information in the received signal about the tag's delay.

The estimator's uncertainty fits within the information bounds according to these regions:

1. Uncertainty $= \sigma_{\text{up}}$ for SNR $\leq X_1$.
2. $\sqrt{\text{CRLB}} <$ Uncertainty $< \sigma_{\text{up}}$ for $X_1 <$ SNR $< X_2$.
3. Uncertainty $= \sqrt{\text{CRLB}}$ (efficient estimator) for $X_2 \geq$ SNR $< X_3$.
4. Uncertainty $\geq \sigma_{\text{low}}$ for SNR $> X_3$.

The first region covers SNR values where the noise significantly overpowers the received signal. Here, the estimator receives no useful information corresponding to the true time delay τ. Any maximum in the cross-correlation function of the POW with the received signal is caused almost exclusively by noise. This effectively makes the coherent estimator choose a random value between 0 and $T_{\text{POW}}/2$ s as the time delay estimate. The second region occurs when the received SNR is high enough to provide useful information to the estimator

about the true time delay but not enough to warrant efficient estimation. This second region is a transition region from random time delay estimation to efficient estimation. In the third region, the estimator's uncertainty is efficiently predicted by the CRLB. The fourth region is the minimum uncertainty possible for an estimator that samples at a rate of $f_{\mathrm{s}} = {}^{1}/_{T_{\mathrm{s}}}$ Hz. Here, the estimator effectively guesses randomly within the sampling period. The simulation graphs in Figures 45 through 47 in the next chapter (Section 5.1) show the four regions graphically.

The CRLB is defined for a single-parameter estimator as [11] [42]

$$\mathrm{Var}(\hat{\tau}) \geq \frac{1}{-E\left[\frac{d^2}{d\tau^2} \ln L(\tau|\tilde{y})|_{\tau=\tau_{\mathrm{true}}}\right]} \tag{96}$$

The expected value of the second derivative of the log-likelihood function evaluated at the true delay τ_{true} is called the *Fisher information*. Estimation becomes more precise when there is greater information in the log-likelihood function. The SNR, POW autocorrelation sharpness (or equivalently $4\pi^2 B_{\mathrm{RMS}}^2$), and passband frequency are the "information" to be used in estimation. The notation in equation (96) means the second derivative of the log-likelihood function is derived w.r.t. tested delay τ and evaluated at the true delay τ_{true}. The Fisher information can be evaluated for the continuous-time coherent estimator as

$$\begin{aligned} & -E\left[\frac{d^2}{d\tau^2} \ln L(\tau|\tilde{y})|_{\tau=\tau_{\mathrm{true}}}\right] \\ &= -E\left\{\frac{d^2}{d\tau^2}\frac{1}{P_{\mathrm{N}}}\left(2\alpha\tilde{X}_{\mathrm{pow,y}}(\tau) - E_{\mathrm{RX}} - \alpha^2 E_{\mathrm{POW}}\right)\right\} \\ &= \frac{2\alpha}{P_{\mathrm{N}}}\frac{d^2}{d\tau^2}\tilde{X}_{\mathrm{pow,y}}(\tau). \end{aligned} \tag{97}$$

The second derivative eliminates the signal energies, which are independent of tested delay τ and reduces to the second derivative of the complex-valued, continuous-time cross-correlation test. Expanding the cross-correlation function results in:

$$\begin{aligned}
&\frac{d^2}{d\tau^2}\tilde{X}_{\mathrm{pow,y}}(\tau) \qquad (98)\\
&= \frac{d^2}{d\tau^2}\int_0^{T_{\mathrm{POW}}} \tilde{\mathrm{pow}}^*(t-\tau)\tilde{y}(t)dt\\
&= \frac{d^2}{d\tau^2}\int_0^{T_{\mathrm{POW}}} \mathrm{pow}(t-\tau)e^{-j2\pi f_c\tau}\cdot\left[\alpha\mathrm{pow}(t-\tau_{\mathrm{true}})e^{j2\pi f_c\tau_{\mathrm{true}}}+\tilde{n}(t)\right]dt\\
&= \alpha\frac{d^2}{d\tau^2}\int_0^{T_{\mathrm{POW}}} \mathrm{pow}(t)\mathrm{pow}(t-(\tau-\tau_{\mathrm{true}}))e^{-j2\pi f_c(\tau-\tau_{\mathrm{true}})}dt\\
&\quad +\frac{d^2}{d\tau^2}\int_0^{T_{\mathrm{POW}}} \tilde{n}(t)\mathrm{pow}(t-\tau)e^{-j2\pi f_c\tau}dt
\end{aligned}$$

The simplification shows that the tested complex cross-correlation $\tilde{X}_{\mathrm{pow,y}}(\tau)$ is composed of the real-valued autocorrelation of the POW evaluated at $\tau-\tau_{\mathrm{true}}$ (i.e. $R_{\mathrm{pow}}(\tau-\tau_{\mathrm{true}})$) multiplied by a complex exponential and a cross-correlation of the tested POW with noise. Substituting these correlation functions and taking two derivatives results,

$$\begin{aligned}
&\frac{d^2}{d\tau^2}\tilde{X}_{\mathrm{pow,y}}(\tau) \qquad (99)\\
&= \frac{d^2}{d\tau^2}\left[\alpha R_{\mathrm{pow}}(\tau-\tau_{\mathrm{true}})e^{-j2\pi f_c(\tau-\tau_{\mathrm{true}})}+\tilde{X}_{\mathrm{pow,n}}(\tau)\right]\\
&= \frac{d}{d\tau}\left\{\alpha\left[R'_{\mathrm{pow}}(\tau-\tau_{\mathrm{true}})-j2\pi f_c R_{\mathrm{pow}}(\tau-\tau_{\mathrm{true}})\right]e^{-j2\pi f_c(\tau-\tau_{\mathrm{true}})}+\tilde{X}'_{\mathrm{pow,n}}(\tau)\right\}\\
&= \alpha\left[R''_{\mathrm{pow}}(\tau-\tau_{\mathrm{true}})-j4\pi f_c R'_{\mathrm{pow}}(\tau-\tau_{\mathrm{true}})-4\pi^2 f_c^2 R_{\mathrm{pow}}(\tau-\tau_{\mathrm{true}})\right]e^{-j2\pi f_c(\tau-\tau_{\mathrm{true}})}\\
&\quad +\tilde{X}''_{\mathrm{pow,n}}(\tau).
\end{aligned}$$

This is the fully-simplified form of the second derivative of the estimator cross-correlation. This second derivative is evaluated at $\tau=\tau_{\mathrm{true}}$ and substituted into the Fisher information. The POW autocorrelation evaluated at zero delay is 1.0 since this analysis assumed normalized autocorrelations. Evaluating equation (99) at $\tau=\tau_{\mathrm{true}}$ results in

$$\begin{aligned}
&-E\left[\frac{d^2}{d\tau^2}\ln L(\tau|\tilde{y})|_{\tau=\tau_{\mathrm{true}}}\right] \qquad (100)\\
&= -E\left\{\frac{2\alpha^2}{P_{\mathrm{N}}}\left[R''_{\mathrm{pow}}(0)-4\pi^2 f_c^2\right]+\tilde{X}''_{\mathrm{pow,n}}(\tau_{\mathrm{true}})\right\}\\
&= \left[-R''_{\mathrm{pow}}(0)+4\pi^2 f_c^2\right]\mathrm{SNR}.
\end{aligned}$$

The term $2\alpha^2/P_{\mathrm{N}}$ is substituted with SNR, and the expected value of the noise cross-correlation second derivative is zero. Finally, the CRLB for the ML estimator of time delay (and hence the ML estimator of range) for the coherent receiver is

$$\mathrm{Var}(\hat{\tau}) \geq \frac{1}{\left[-R''_{\mathrm{pow}}(0) + 4\pi^2 f_{\mathrm{c}}^2\right] \mathrm{SNR}} \tag{101}$$

$$\mathrm{Var}(\hat{r}) \geq \frac{c^2}{4\left[-R''_{\mathrm{pow}}(0) + 4\pi^2 f_{\mathrm{c}}^2\right] \mathrm{SNR}}. \tag{102}$$

The conversion $\hat{r} = c\hat{\tau}/2$ was used for the ranging CRLB. The discrete versions of these two CRLB equations assuming $N_{\mathrm{POW}} f_{\mathrm{s}} T_{\mathrm{POW}}$ total points sampled are

$$\mathrm{Var}(\hat{\tau}) \geq \frac{1}{N_{\mathrm{POW}} f_{\mathrm{s}} T_{\mathrm{POW}} \left[-R''_{\mathrm{pow}}(0) + 4\pi^2 f_{\mathrm{c}}^2\right] \mathrm{SNR}} \tag{103}$$

$$\mathrm{Var}(\hat{r}) \geq \frac{c^2}{4N_{\mathrm{POW}} f_{\mathrm{s}} T_{\mathrm{POW}} \left[-R''_{\mathrm{pow}}(0) + 4\pi^2 f_{\mathrm{c}}^2\right] \mathrm{SNR}} \tag{104}$$

The RMS bandwidth may be substituted as well since $-R''_{\mathrm{pow}}(0) = 4\pi^2 B_{\mathrm{RMS}}^2$.

4.3.3 Noncoherent Estimator Test

Noncoherent *detection* is typically less reliable than coherent detection assuming a constant false alarm rate due to the lack of phase information relative to the carrier frequency f_{c} [52]. Noncoherent *estimation* also experiences a detriment since no phase information is used even though the same cross-correlation maximum-finding routine is used. In noncoherent estimation, the analog I and Q signals are combined to form the envelope prior to estimation. This analysis assumes the estimator operates on a single POW time period just the same as in the coherent case.

The magnitude of a complex-valued AWGN process is well-known to be Rician distributed. The Rician distribution with noise power P_{N} is

$$f_{|\tilde{y}(t)|}(|\tilde{y}(t)|\,|\tau) = \frac{2\,|\tilde{y}(t)|}{P_{\mathrm{N}}} e^{-\frac{1}{P_{\mathrm{N}}}(|\tilde{y}(t)|^2 + \alpha^2 \mathrm{pow}(t-\tau)^2)} \mathrm{I}_0\left(\frac{2\alpha \mathrm{pow}(t-\tau)\,|\tilde{y}(t)|}{P_{\mathrm{N}}}\right). \tag{105}$$

The distribution contains the modified Bessel function of the first kind with order zero $\mathrm{I}_0(\cdot)$, which has an argument with the cross-multiplication of the POW and the received signal. The POW used in this distribution is the real-valued POW delayed in time by the time

delay τ. Then, the likelihood function is the joint pdf of the process over one POW time period. Taking the natural logarithm of the noncoherent likelihood function results in

$$\begin{aligned} \ln L(\tau|\,|\tilde{y}|) &= \int_0^{T_{\mathrm{POW}}} \ln f_{|\tilde{y}(t)|}(|\tilde{y}(t)|\,|\tau) dt \\ &= \int_0^{T_{\mathrm{POW}}} \ln\left(\frac{2\,|\tilde{y}(t)|}{P_{\mathrm{N}}}\right) + |\tilde{y}(t)|^2 + \alpha^2 \mathrm{pow}(t-\tau)^2 dt \\ &\quad + \int_0^{T_{\mathrm{POW}}} \ln \mathrm{I}_0\left(\frac{2\alpha \mathrm{pow}(t-\tau)\,|\tilde{y}(t)|}{P_{\mathrm{N}}}\right) dt. \end{aligned} \tag{106}$$

The same product integral property that was used in the coherent derivation in equation (91) is used here. The first two integrals do not have cross-multiplication terms of the POW and received signal. These integrals are independent of delay τ. The first integral is a scaled integration of the received data signal over T_{POW}. The second integral reduces to the signal energies of the received signal E_{RX} and the POW E_{POW}. A large-argument simplification $\ln \mathrm{I}_0(z) \approx z$ for $z >> 1$ can be used to simplify the log-likelihood function even further when the SNR is high. Also, the true delay is denoted by τ_{true} as in the coherent estimator derivation. With these simplifications, the noncoherent log-likelihood function is

$$\begin{aligned} \ln L(\tau|\,|\tilde{y}|) &= \int_0^{T_{\mathrm{POW}}} \ln\left(\frac{2\,|\tilde{y}(t)|}{P_{\mathrm{N}}}\right) dt + \frac{E_{\mathrm{RX}}}{P_{\mathrm{N}}} + \frac{\alpha^2 E_{\mathrm{POW}}}{P_{\mathrm{N}}} \\ &\quad + \frac{2\alpha}{P_{\mathrm{N}}} \int_0^{T_{\mathrm{POW}}} \mathrm{pow}(t-\tau)\,|\tilde{y}(t)|\, dt. \end{aligned} \tag{107}$$

The log-likelihood function depends on tested delay τ while τ_{true} is a given, fixed constant. The first integral and the signal energies are independent of time delay, but the last integral evaluates to the cross-correlation of the received signal with a test POW evaluated at delay τ and scaled by $2\alpha/P_{\mathrm{N}}$:

$$\frac{2\alpha}{P_{\mathrm{N}}} \int_0^{T_{\mathrm{POW}}} \mathrm{pow}(t-\tau)\,|\tilde{y}(t)|\, dt = \frac{2\alpha}{P_{\mathrm{N}}} X_{\mathrm{pow,y}}(\tau). \tag{108}$$

Searching for the maximum of this real-valued log-likelihood function results in a similar cross-correlation test as in the coherent esimation case:

$$\hat{\tau} = \arg\max_{\tau} \left(X_{\mathrm{pow,y}}(\tau)\right) \tag{109}$$

The noncoherent ML estimator performs a real-valued cross correlation and searches for the peak value at which the delay estimate is chosen.

This same cross-correlation test is used in the digital receiver from Figure 33. The sampled signal from the ADC consists of $N = N_{\text{POW}} f_{\text{s}} T_{\text{POW}}$ real-valued points. The cross-correlation then consists of $2N$ points. The maximum of this discrete-time cross correlation is simply found by running a maximum-finding routine over these $2N$ points.

4.3.4 Noncoherent Estimator Performance

The ML estimator is accurate since it is unbiased. The noncoherent estimator uncertainty follows four regions similar to the coherent estimator. The information bounds are exactly the same:

$$\text{Upper Information Bound, } \sigma_{\text{up}} = \sqrt{\text{Var}\left(\mathcal{U}\left(0, \frac{T_{\text{POW}}}{2}\right)\right)} = \frac{T_{\text{POW}}}{2\sqrt{12}} \tag{110}$$

$$\text{Lower Information Bound, } \sigma_{\text{low}} = \sqrt{\text{Var}\left(\mathcal{U}\left(0, \frac{T_{\text{s}}}{2}\right)\right)} = \frac{T_{\text{s}}}{2\sqrt{12}} \tag{111}$$

However, the CRLB is different for the noncoherent estimator compared to the coherent estimator. The noncoherent estimator's uncertainty fits within the information bounds according to these regions:

1. Uncertainty $= \sigma_{\text{up}}$ for SNR $\leq X_1$.
2. $\sqrt{\text{CRLB}_{\text{NC}}} <$ Uncertainty $< \sigma_{\text{up}}$ for $X_1 <$ SNR $< X_2$.
3. Uncertainty $= \sqrt{\text{CRLB}_{\text{NC}}}$ (efficient estimator) for $X_2 \geq$ SNR $< X_3$.
4. Uncertainty $\geq \sigma_{\text{low}}$ for SNR $> X_3$.

The meaning of the boundaries are the same as in the coherent case. The derivation of CRLB_{NC} starts by evaluating the Fisher information:

$$\begin{aligned} & -E\left[\frac{d^2}{d\tau^2} \ln L(\tau | \, |\tilde{y}|)|_{\tau=\tau_{\text{true}}}\right] \\ &= -E\left\{\frac{d^2}{d\tau^2}\left[\int_0^{T_{\text{POW}}} \ln\left(\frac{2\,|\tilde{y}(t)|}{P_{\text{N}}}\right) dt + \frac{E_{\text{RX}}}{P_{\text{N}}} + \frac{\alpha^2 E_{\text{POW}}}{P_{\text{N}}} + \frac{2\alpha}{P_N} X_{\text{pow,y}}(\tau)\right]\right\} \\ &= \frac{2\alpha}{P_{\text{N}}} \frac{d^2}{d\tau^2} X_{\text{pow,y}}(\tau). \end{aligned} \tag{112}$$

The derivatives of the constant terms w.r.t. τ disappear. Substituting for $X_{\mathrm{pow,y}}$, the Fisher information becomes

$$
\begin{aligned}
&-E\left[\frac{d^2}{d\tau^2}\ln L(\tau|\,|\tilde{y}|)|_{\tau=\tau_{\mathrm{true}}}\right] \qquad (113)\\
&= \frac{-2\alpha}{P_{\mathrm{N}}}\frac{d^2}{d\tau^2}E\left[\int_0^{T_{\mathrm{POW}}}\mathrm{pow}(t-\tau)\cdot\left|\alpha\mathrm{pow}(t-\tau_{\mathrm{true}})e^{-j2\pi f_{\mathrm{c}}\tau_{\mathrm{true}}}+\tilde{n}(t)\right|dt\right]\\
&= \frac{-2\alpha}{P_{\mathrm{N}}}\frac{d^2}{d\tau^2}E\left[\int_0^{T_{\mathrm{POW}}}\left|\alpha\mathrm{pow}(t-\tau)\mathrm{pow}(t-\tau_{\mathrm{true}})e^{-j2\pi f_{\mathrm{c}}\tau_{\mathrm{true}}}\right.\right.\\
&\quad\left.\left.+\,\mathrm{pow}(t-\tau)\tilde{n}(t)\right|\right]dt\\
&= \frac{-2\alpha}{P_{\mathrm{N}}}\frac{d^2}{d\tau^2}E\left[\left|\alpha R_{\mathrm{pow}}(\tau-\tau_{\mathrm{true}})e^{-j2\pi f_{\mathrm{c}}\tau_{\mathrm{true}}}+\tilde{X}_{\mathrm{pow,n}}(\tau)\right|\right]
\end{aligned}
$$

The autocorrelation of a POW is substituted as well as the cross-correlation of the POW with the received noise signal. It is tedious to take the second derivative in the equation above. Instead, the expectation is taken first followed by the second derivative. The expected value of the cross-correlation of the POW with noise is zero since AWGN has zero mean. Also, taking the absolute value eliminates the exponential phase information:

$$
\begin{aligned}
-E\left[\frac{d^2}{d\tau^2}\ln L(\tau|\,|\tilde{y}|)|_{\tau=\tau_{\mathrm{true}}}\right] &= -\frac{d^2}{d\tau^2}E\left[\ln L(\tau|\,|\tilde{y}|)\right]|_{\tau=\tau_{\mathrm{true}}} \qquad (114)\\
&= -\frac{d^2}{d\tau^2}\left[\frac{2\alpha^2}{P_{\mathrm{N}}T_{\mathrm{S}}}R_{\mathrm{pow}}(\tau-\tau_{\mathrm{true}})\right]\\
&= -R''_{\mathrm{pow}}(\tau-\tau_{\mathrm{true}})\mathrm{SNR}
\end{aligned}
$$

The lack of the exponential phase information causes the difference in uncertainty between the noncoherent case and the coherent case. Finally, the noncoherent CRLB for time delay and range are

$$
\begin{aligned}
\mathrm{Var}(\hat{\tau}_{\mathrm{NC}}) &\geq \frac{1}{-R''_{\mathrm{pow}}(0)\mathrm{SNR}} \qquad (115)\\
\mathrm{Var}(\hat{r}_{\mathrm{NC}}) &\geq \frac{c^2}{-4R''_{\mathrm{pow}}(0)\mathrm{SNR}}. \qquad (116)
\end{aligned}
$$

Clearly, the coherent ML estimator is more precise than the noncoherent ML estimator due to the $4\pi^2 f_{\mathrm{c}}^2$ denominator term in equation (101). However, the trade-off is the need for two ADCs for the coherent estimator versus one ADC for the noncoherent estimator. The noncoherent estimator is chosen if the ranging uncertainty specification can be met with only one ADC.

The CRLB of a noncoherent ML range estimator in the digital receiver in Figure 33 is reduced by the number of points sampled:

$$\mathrm{Var}(\hat{\tau}_{\mathrm{NC}}) \geq \frac{1}{-N_{\mathrm{POW}} f_{\mathrm{s}} T_{\mathrm{POW}} R''_{\mathrm{pow}}(0)\mathrm{SNR}} \tag{117}$$

$$\mathrm{Var}(\hat{r}_{\mathrm{NC}}) \geq \frac{c^2}{-4N_{\mathrm{POW}} f_{\mathrm{s}} T_{\mathrm{POW}} R''_{\mathrm{pow}}(0)\mathrm{SNR}} \tag{118}$$

Simulations and measurements in the next two chapters show a close adherence of the estimator's uncertainty to this formulation of the CRLB for range estimation.

4.4 Cluttered Environment Channel

Efforts to characterize and model real channels across a signal bandwidth such as the POW's 3 dB bandwidth have produced two distinct classifications of the channel spectrum for cluttered environments: frequency-flat and frequency-selective fading environments [53] [54] [55]. The distinction between the two fading environments is the comparison of signal bandwidth to coherence bandwidth at the input to the channel. A frequency-flat channel has a coherence bandwidth greater than the 3-dB signal bandwidth. Conversely, a frequency-selective channel occurs when the coherence bandwidth is less than the 3-dB signal bandwidth. Considering the signal input into the forward channel to the tag is a POW, the definition of coherence bandwidth and the two channel types are [56]

$$B_{\mathrm{coh}} \approx \frac{1}{5\sigma_{\mathrm{RMS}}}\,, \tag{119}$$

$$B_{\mathrm{3dB}} > B_{\mathrm{coh}} \Rightarrow \text{Frequency-Selective Channel,} \tag{120}$$

$$B_{\mathrm{3dB}} < B_{\mathrm{coh}} \Rightarrow \text{Frequency-Flat Channel,} \tag{121}$$

where σ^2_{RMS} is the RMS delay spread of the forward channel. The statistically based coherence bandwidth definition ensures the channel frequency response at any frequency has a correlation with the frequency response at other frequencies within the band greater than 0.9. This defines a high level of "flatness" that can be approximated by a single complex number for frequency-flat channels.

4.4.1 Frequency-Flat Fading Environments

Frequency-flat fading environments have impulse responses that can be effectively modeled by a single, delayed, complex impulse with a random path gain and random phase [56]. The typical impulse response is

$$h_{\text{flat}}(t) = \alpha\delta(t-\tau)e^{j\phi}. \tag{122}$$

The path gain α is commonly modeled as either a Rician, Rayleigh, Nakagami, or Weibull distribution. The path delay corresponds to the propagation time from the channel input to channel output. This is analogous to half of the roundtrip propagation delay from reader to tag. The random phase is commonly modeled as a uniform random variable $\phi \sim \mathcal{U}[-\pi, \pi)$ rad, which is a result of the coherent sum of multipath signal components at the output of the channel.

This work will assume Rician and Rayleigh distributions for path gains because of the ubiquitousness of these distributions in radar [52] and propagation literature [57]. Two studies modeling the backscatter channel in indoor office environments show the presence of product-Rician channels [1] [58]. The Rician parameter K (or K-factor) describes the ratio of the amount of direct-path power to the amount of indirect-path power impinging on the channel output from a single propagation path. For frequency-flat channels, a high K-factor quantitatively describes a low amount of clutter. In fact, as $K \to \infty$, the channel approximates a free-space channel. A low K-factor quantitatively describes a high amount of surrounding clutter. As $K \to 0$, the channel approximates one of three scenarios. First, the direct path is blocked leaving only indirect-path power to arrive at the channel output. Second, a high amount of reflective clutter is present near the channel output that trumps the direct-path power. Third, a combination of path blockage and high clutter is present.

The lower bound for ranging uncertainty in a one-way frequency-flat fading environment is the same CRLB as in equations (101) for the coherent ML estimator and (115) for the noncoherent ML estimator. However, the ensemble average of SNR is used in lieu of the deterministic SNR used in the case of a noisy free-space environment [59].

The ranging estimator is unbiased in a frequency-flat environment. The random fading

envelope is independent of the time delay. Therefore, the Rayleigh or Rician distributed envelope does not add or subtract delay from the estimate. The uniform random phase does alter coherent estimates, but the mean of multiple coherent range estimates remains unbiased in the asymptotic sense; the uniform random phase has zero mean.

4.4.2 Frequency-Selective Fading Environments

A typical reader is built with cost in mind. Thus, channel estimation capabilities are not designed into the reader. The distorting interference of a frequency-selective channel can be filtered out if the channel can be measured. A typical reader in passive WSNs must be designed to withstand the unfilterable distortions caused by a random frequency-selective environment if the reader has no channel-measurement capabilities. This part of the research aims to showcase the typical ranging performance degradations of frequency-selective environments.

The level of clutter defines how interfering the environment is when the tag is moved over the entire space of the environment. Simple statistics such as coherence bandwidth cannot fully describe the interference levels. It is possible that a frequency-selective environment with two major reflections (e.g. floor bounce and wall bounce) has the same coherence bandwidth as an environment with 20 major reflections (e.g. floor, wall, metal shelf, person, speaker, ceiling fan, etc.). The environment with 20 major reflections is likely to have a greater impact on the ranging performance than the two-reflection environment.

A stronger characterization of the interference due to a frequency-selective environment uses

1. the number of clutter objects,
2. the strength of each object's reflectivity, and
3. the size of the environment space

In this research, frequency-selective fading environments are modeled with a channel response with 10 randomly located scatterers each with a random radar cross section (RCS),

random path gain, and random phase. This channel impulse response is defined as

$$h_{\text{sel}}(t) = \alpha_{\text{tag}}\delta\left(t - \frac{r_{\text{tag}}}{c}\right)e^{-jkr_{\text{tag}}} + \sum_{i=1}^{10}\sqrt{\sigma_i}\alpha_i\delta(t-\tau_i)e^{j\phi_i}. \tag{123}$$

Here, the LOS path and the 10 paths of the random scatterers are modeled each with random radar cross sections σ_i, path gains α_i, path delays τ_i, and random phases $\phi_i \in [-\pi, \pi)$. Figure 35 shows a two-dimensional random environment with 10 scatterers that are uniform-randomly located in two dimensional space. The i^{th} scatterer's x- and y-coordinates are defined as

$$\begin{aligned} x_i &\sim \mathcal{U}(0, \lambda_{\text{POW}}) \\ y_i &\sim \mathcal{U}\left(\frac{-\lambda_{\text{POW}}}{2}, \frac{\lambda_{\text{POW}}}{2}\right). \end{aligned} \tag{124}$$

Each of the 10 scatterers represents a reflective object of random size and orientation in the environment. For example, a person standing in the environment may walk to a different location in between range measurements. The person may also turn around, sit down, raise an arm, or do any number of actions to change the propagation environment. The person's real-time RCS changes according to the angle of incidence of radiation for each of the person's permutations. A log-normal distribution with a mean RCS of 0 dB(m^2) (i.e. 1 m^2) [60] is used in the simulations of the next chapter to represent the radar cross section of a person when the person's orientation is considered random. Furthermore, a log-normal distribution is chosen to represent the RCS of an arbitrary object because it is chosen as the empirical fit to many measured clutter distributions [52].

The reader is located at the origin and the tag is located at a uniform-random range away from the reader along the x-axis:

$$\begin{aligned} (x_{\text{r}}, y_{\text{r}}) &= (0, 0) \\ (x_{\text{t}}, y_{\text{t}}) &\sim \left(\mathcal{U}\left(0, \frac{T_{\text{POW}}}{2}\right), 0\right) \end{aligned} \tag{125}$$

The one-way channel impulse response is constructed by computing the distances from the reader to the scatterers and the distances from the scatterers to the tag. The i^{th} path gain α_i is computed with

$$\alpha_i = \frac{\sqrt{G_r G_t}\lambda_{\text{c}}}{4\pi r_{ri} r_{ti}} \tag{126}$$

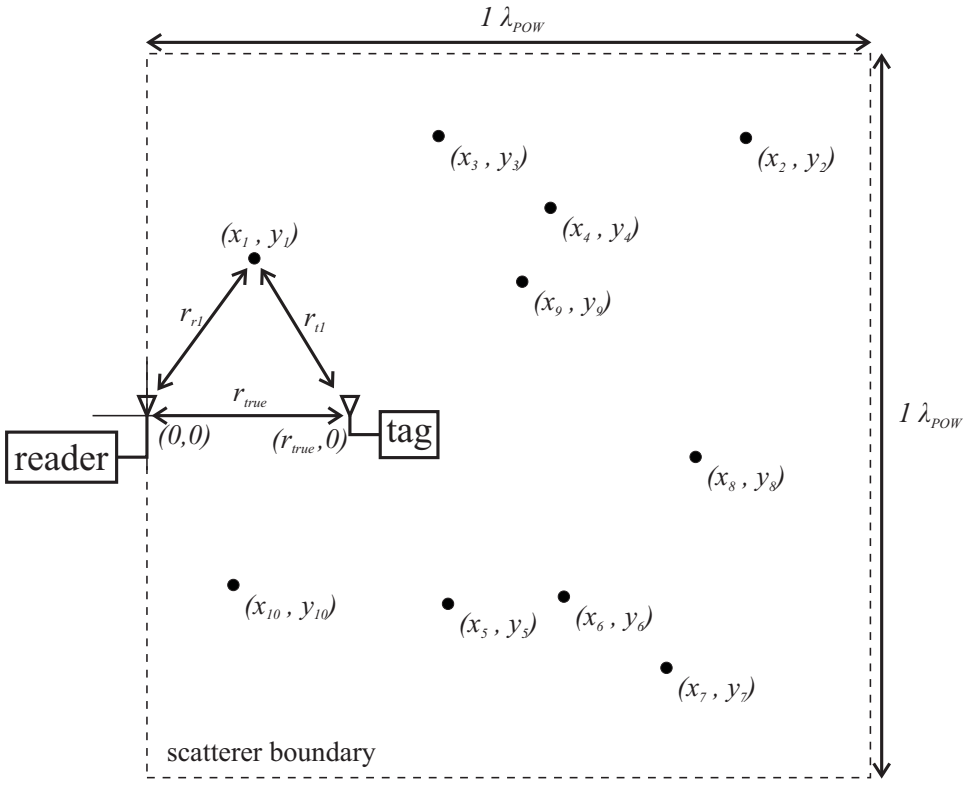

Figure 35: Ten random scatterers each with uniform-random positions in two-dimensional space and log-normal radar cross-sections represent a frequency-selective cluttered environment.

where r_{ri} is the euclidian distance from the reader to the i^{th} scatterer, and r_{ti} is the euclidian distance from the i^{th} scatterer to the tag. Only the primary paths (i.e. paths involving only one scatterer) are included in the model. Any secondary, tertiary, or higher order paths are considered negligible (i.e. paths involving two or more scatterers). The path delays are computed using the distance formula for each primary path. The i^{th} path has a total path delay

$$\tau_i = \frac{r_{ri} + r_{ti}}{c} \tag{127}$$

Then, the path phase is modeled as a uniform random variable:

$$\phi_i \sim \mathcal{U}(-\pi, \pi) \tag{128}$$

This model provides the flexibility to model many different levels of clutter and frequency selectivity. 10 objects were chosen because it is a typical number of objects within a 20 m radius of a typical reader in a passive wireless sensor network. Environments that have

fewer than 10 objects can be appoximated by a smaller mean RCS, and environments with more than 10 objects can be approximated by a larger mean RCS.

The strength of the clutter reflectivity is represented by the mean RCS of the 10 random scatterers in the environment. Three classifications based on common objects are:

1. "Light" clutter environments contain 10 scatterers each with a mean RCS of -20 dB(m^2). This models items such as small birds, paper clips, and baseballs. An animal pasture or a baseball field can be considered to contain light clutter.

2. "Medium" clutter environments contain 10 scatterers with a mean RCS of 0 dB(m^2). People, copy machines, and televisions are modeled; An office environment would contain these types of items.

3. "Heavy" clutter environments contain 10 scatterers with a mean RCS of 10 dB(m^2). Forklifts, metal shelves, and automobiles have very large values of RCS. A full warehouse can be considered a heavy-clutter environment.

The simulation results in Section 5.3 show the precision degradation and biasing effect of clutter on range estimation performance.

The ML estimator is not the ideal estimator for use with a frequency-selective channel that introduces signal distortion. Channel equalization is used for flattening the channel response in the frequency domain [61] if the channel is known a-priori. Adaptive equalizers actively adjust to a changing environment [48]. These improvements can reduce the symbol interference induced by the frequency-selective channel.

4.5 Nonlinear Reflections

It is rare that a ranging system estimates the range to a nonlinear reflector. Radar systems typically model all significant reflectors in an environment by their radar cross section [52]. It has been proposed that certain environmental objects like wire fencing or rusted metal objects can behave like nonlinear reflectors if there is enough incident radiated power on the object [62]. The electric fields scattered by a linear reflector and nonlinear reflector are

modeled by

$$\text{(linear)} \quad E_{\text{refl}}(r,t) = \frac{\sqrt{\sigma}}{r} E_{\text{inc}}(r,t) \tag{129}$$

$$\text{(nonlinear)} \quad E_{\text{refl}}(r,t) = \frac{\sqrt{\sigma}}{r} E_{\text{inc}}(r,t) + \alpha E_{\text{inc}}^2(r,t) + \beta E_{\text{inc}}^3(r,t) \tag{130}$$

where α and β are proportionality constants that are object-specific much like radar cross section σ. An equivalent nonlinear scatter model proposes harmonic radar cross sections $\sigma_1(f_1),\ \sigma_2(f_1,f_2),\ \ldots,\ \sigma_n(f_1,\ldots,f_n)$, which model the linear, quadratic, cubic, etc. features of the object [63] [64]. In realistic radar systems, it was found that metallic objects are poor reflectors of second-harmonic radiation [62].

Passive wireless sensors employing charge pumps as one of the reflective states for backscatter communications alter the performance of the range estimator. Generally speaking, bias is added to the ranging estimates, which primarily depends on received power and charge pump parameters. Ranging uncertainty grows over the short-circuit reflector case since the received SNR is reduced by the energy absorbed by the charge pump, and the reflected harmonics of the carrier frequency are filtered out by the reader receive chain bandpass filters. The amount that uncertainty grows is proportional to the ratio of SNR from the short-circuit case to the charge pump reflector case.

Efforts to model the reflection of a nonlinear circuit have been proposed in literature. For example, the "Describing Function" method effectively *linearizes* the nonlinear circuit by approximating the reflected signal as a linear function of the impinging signal [65]. Other methods model the input current as a function of the input voltage as shown in Figure 36. The Thévenin source models the antenna and transmission line feeding the nonlinear circuit. The reflection coefficient of this nonlinear system is derived as

$$\Gamma(t) = 1 - Z_{\text{O}} \frac{I\left(V(t)\right)}{V^+(t)} \tag{131}$$

where Z_{O} is the characteristic as seen by the nonlinear circuit. For this analysis, the equivalent characteristic impedance is assumed to be real-valued. The impinging signal $V^+(t)$ is known a-priori from evaluating the tag-received signal from the link budget. The nonlinear circuit's input voltage $V(t)$ is the sum of the impinging signal and reflected signal,

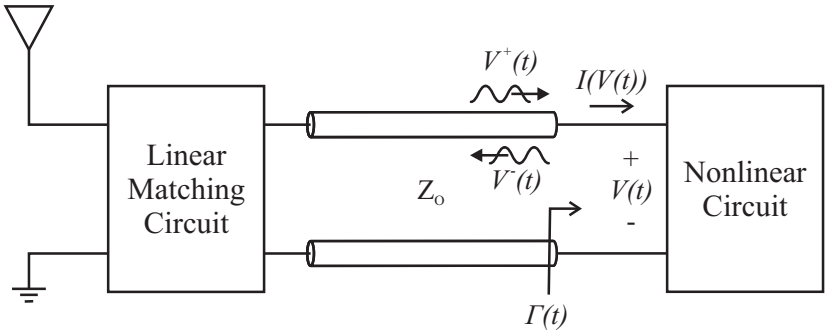

Figure 36: A nonlinear circuit as the load reflector of a passive tag. The tag antenna, matching network, and transmission line are modeled as an equivalent source from the perspective of the nonlinear circuit. The reflection coefficient changes with the instantaneous voltage and current through the nonlinear circuit.

which means $V(t)$ is dependent on the reflection coefficient. A linear circuit's reflection coefficient is constant and can be evaluated a-priori, after which the reflected signal $V^{-}(t)$ is evaluated. The nonlinear circuit's reflection coefficient varies with time and impinging signal amplitude. Numerical techniques such as the Newton-Raphson method are used to evaluate the nonlinear reflection coefficient, which varies with time according to the system properties of the nonlinear circuit [66]. A nonlinear circuit consisting of a single diode has a reflection coefficient which is nonlinear, causal, memoryless, and time-invariant with respect to the impinging wave input signal. Adding capacitors to the nonlinear circuit adds memory to the system.

A practical, empirical model for estimating the ranging bias is presented here. It seems it is feasible to derive a theoretical model for ranging bias, but the resulting model may be too complex or tedious for practical design work. Evaluation of this model is performed with simulations and measurements on a two-stage charge pump in Chapters 5, 6, and 7.

An exemplary simulation of an ideal two-stage charge pump with a Gaussian POW input is shown in Figure 37 with an RMS bandwidth of 15 MHz. The signal power of the impinging signal is 0 dBm. The diodes are ideal with threshold voltage $V_{\mathrm{t}} = 0.7$ V. The simulation graphs show the impinging signal, reflected signal, and charge pump output voltage across 10 POW time periods. The charge pump reaches steady state after the first POW time period as evidenced by the output voltage rising and falling to the same maximum and minimum levels. During steady state, the output capacitor is absorbing and

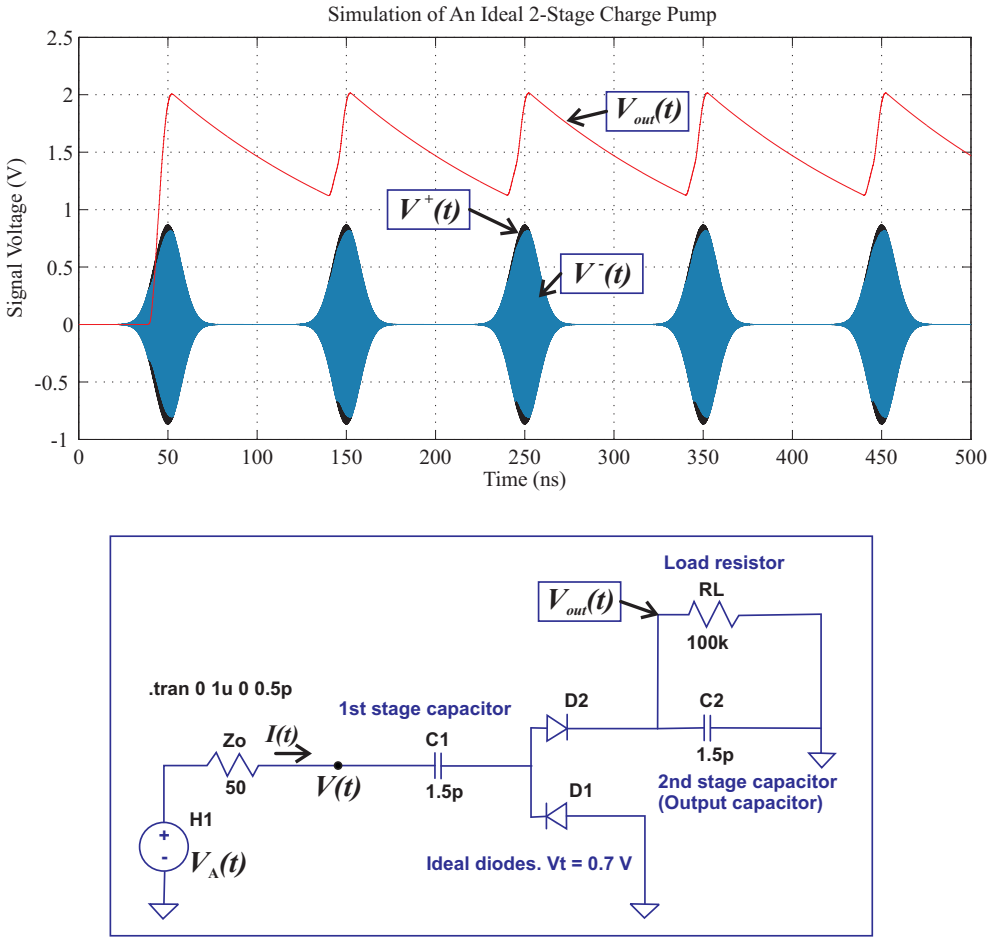

Figure 37: Simulation in LTspice of an ideal 2-stage charge pump. The charge pump reaches steady state quickly after 1 POW time period.

supplying the same amount of charge, which results in a net change of zero charge after each POW time period. It is assumed that ranging takes place on reflected signals during the steady-state of the charge pump since the tag's baseband logic does not power on (and hence no backscatter communications occur) until sufficient output voltage is reached.

The equations for the impinging and reflected signals are

$$V^+(t) = \frac{1}{2}\left(V(t) + Z_O I(t)\right) = \frac{1}{2}V_A(t) \tag{132}$$

$$V^-(t) = \frac{1}{2}\left(V(t) - Z_O I(t)\right). \tag{133}$$

The input voltage $V(t)$ is simulated at node at the output of the equivalent source and the input to the charge pump. The input current $I(t)$ is the current leaving the top node of the voltage source and flowing to the right through the source resistor into the charge pump.

The output voltage is the node voltage at the top of the output resistor.

The amount of charge absorbed by the charge pump (and then supplied to the load resistor) during one time period of the carrier in steady state is

$$Q_{\mathrm{L}} = CV_{\mathrm{out}}\left(1 - e^{\frac{-T_{\mathrm{st}}}{R_{\mathrm{L}}C}}\right) \quad \text{Coulombs} \tag{134}$$

which depends on the output capacitance C (assumed equal to the capacitance of each stage capacitor), the load resistor R_{L}, the starve time T_{st}, and the maximum output voltage of the charge pump V_{out}. **Starve time** is defined as the duration of time during which the output capacitor is discharging after the peak input voltage is reached and before the charge time begins. The **charge time** T_{ch} is the time period during which the output capacitor is being charged. The charge time and starve time are related by

$$T_{\mathrm{POW}} = T_{\mathrm{ch}} + T_{\mathrm{st}} \tag{135}$$

The charge time begins once the input signal rises above the diode threshold voltage. This time occurs when the impinging signal reaches half the diode treshold. The charge pump absorbs the steady-state value of charge Q_{L} during the charge time T_{ch}. Therefore, the average current input into the charge pump during the charge time is $Q_{\mathrm{L}}/T_{\mathrm{ch}}$ A.

The Dickson equation gives the value of maximum output voltage:

$$V_{\mathrm{out}} = \frac{N\left(2\sqrt{\mathrm{PAPR}\cdot Z_{\mathrm{O}}\cdot P_{\mathrm{tag}}} - V_{\mathrm{t}}\right)}{1 + \frac{N}{fR_{\mathrm{L}}C}} \quad \text{V.} \tag{136}$$

Here, the value used for the maximum input voltage is $2\sqrt{\mathrm{PAPR}\cdot Z_{\mathrm{O}}\cdot P_{\mathrm{tag}}}$, which is twice the magnitude of the impinging signal. The simulation graphs verify that the Dickson equation prediction for output voltage (2.0639 V) matches well with the simulated maximum output voltage 2.0144 V when the impinging signal has maximum voltage 0.8866 V.

It is evident in Figure 38 that voltage clipping occurs on the reflected signal during the charge time. The large current spikes occur during approximately 20% of the time period of the carrier sine waveform when the stage capacitors are charging up. Current is drawn out of the voltage source V_{A} and through the source resistor Z_{O} into the capacitors. The exact effect on the reflected waveform is found when equations (132) and (133) are rearranged to

solve for $V^-(t)$ in terms of $V^+(t)$:

$$V(t) = 2V^+(t) - Z_O I(t) \quad (137)$$

$$\Rightarrow V^-(t) = V^+(t) - Z_O I(t) \quad (138)$$

The impinging signal and input current have the same sign when current is providing charge to the capacitors. Therefore, any spike of the input current acts to diminish the reflected waveform. The amount of clipped voltage depends on the maximum value of the current spike. It is estimated from the simulation graph in Figure 38 that each current spike lasts for approximately 10% of the carrier sine waveform period. Therefore, the maximum current is estimated as five times the average input current during the charge time:

$$\max(I(t)) \approx 10\frac{Q_L}{T_{ch}}. \quad (139)$$

Multiplying this by the source resistance gives the magnitude of the voltage clip:

$$V_{clip} = 5\frac{Q_L}{T_{ch}} Z_O. \quad (140)$$

In the simulation in Figures 37 and 38, the average voltage clip across the charge time is 83.2 mV. The predicted voltage clip using equation (140) is 67.6 mV. This example shows a good agreement between the simulated voltage clipping and the prediction.

More signal conditioning is needed to estimate the range estimation bias that is added by the charge pump's nonlinear reflection. It is assumed that the tag receives the POW at high SNR such that noise is negligible, which is safe to assume since typical passive tag sensitivities lie between -20 and -10 dBm [2] producing SNRs in excess of 60 dB. The tag-received signal power P_{tag} is estimated from a link budget. An estimate of the reflected signal is made by creating a noiseless POW at signal power P_{tag} with the estimated voltage clip V_{clip} taken out of the charge time period. Figure 39a shows the voltage clipping applied to the 0 dBm, 15 MHz Gaussian POW used in the simulation. This wideband signal represents the empirical estimate of the reflected signal. The narrowband reader-receiver then filters this reflected signal as shown in Figure 39b.

Finally, the empirical estimate of the ranging bias is found by cross-correlating the baseband envelope of the clipped and filtered POW from Figure 39b with a clean POW.

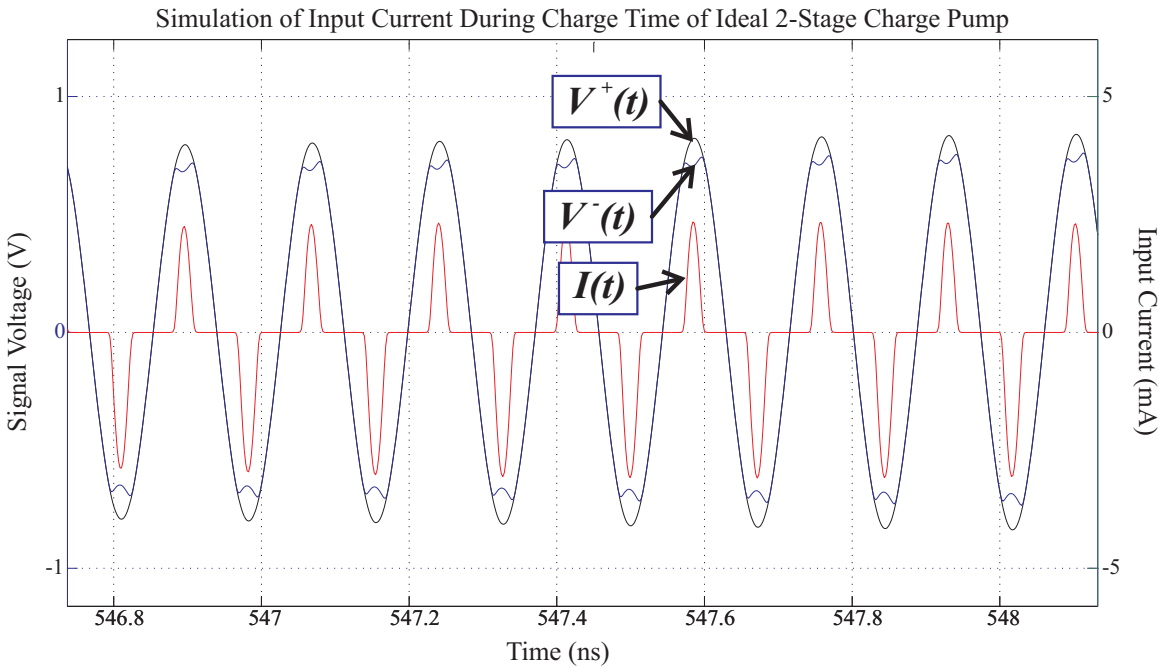

Figure 38: Voltage clipping during the charge time. High input current spiking causes the reflected signal to be clipped from the impinging signal.

The maximum of this cross-correlation occurs at the estimated time-delay bias. The ranging bias is computed using the distance formula:

$$\begin{aligned} r_{\text{bias}} &= v_{\text{p}} x \\ \text{where } x &= \arg\max_{x}(X_{\text{clip}}(x)). \end{aligned} \tag{141}$$

Here, v_{p} is the speed of light in the propagation medium, and $X_{\text{clip}}(x)$ is the cross-correlation of the clipped and filtered POW with the clean POW evaluted at time delay x. In the example from Figures 37, 38, and 39, the estimated ranging bias is 2.25 cm.

4.5.1 Effect of Tag-Received Power on Ranging Bias

Figure 40 is a plot of estimated ranging bias versus tag-received power for a Gaussian POW with 15 MHz RMS bandwidth and a PAPR of 15. Zero distortion is predicted when the charge pump receives less power than what is required to forward-bias a charge pump diode (-13.9 dBm in this case). The charge pump acts as an open-circuit reflector since the diodes do not conduct. At high tag-received power, the amount of voltage-clipping becomes less significant with respect to the magnitude of the input signal. The diode threshold

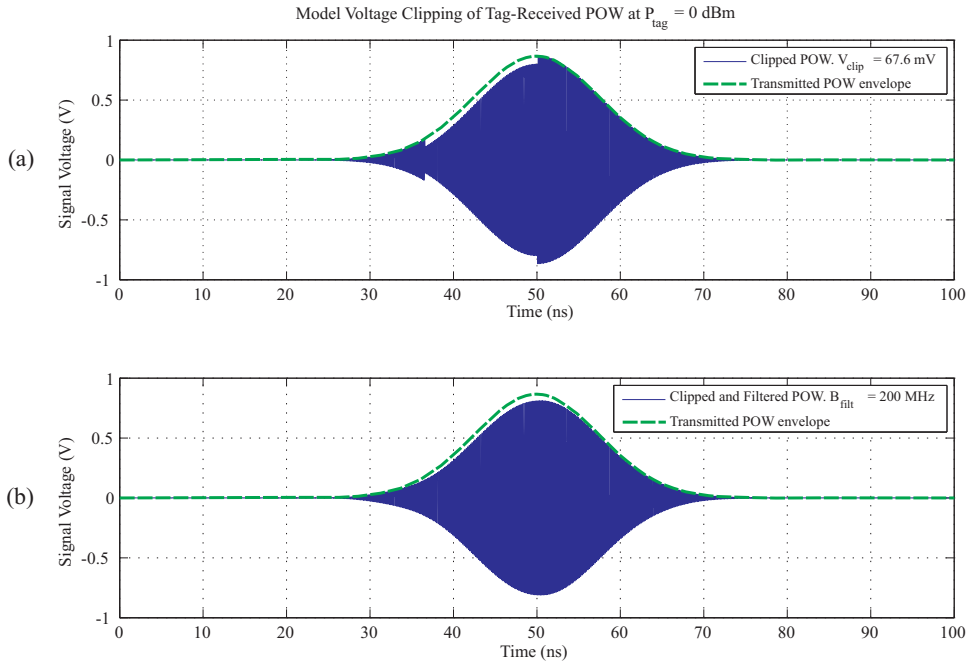

Figure 39: The bias-predicting model (a) clips a copy of the transmitted POW during the charge time and then (b) filters the clipped POW to the reader-receiver bandwidth.

becomes insignificant as the tag power increases as well. This small distortion relative to the magnitude of the POW produces smaller predicted bias as the tag power is increased.

Ranging bias is dependent on tag-received power. A tag that is close to the reader will experience a different ranging bias than a tag that is far away. Small-scale fading complicates the matter even further since deep fades can occur unpredictably within a small one-wavelength radius volume around a point in space [1]. The tag will not operate when the charge pump does not produce enough DC voltage. Therefore, ranging is impossible for tag-received power less than the tag's specified power sensitivity.

The curve in Figure is relatively flat for the range of possible tag-received power levels between -10 dBm and 40 dBm. The median value for predicted range bias is 2.03 cm in this range. Below -10 dBm, the charge pump does not produce enough DC voltage to power the 100 kΩ load at 3 V. Also, tag-received powers greater than 40 dBm are unrealistic when a 10 dBi reader antenna transmits 30 dBm of power.

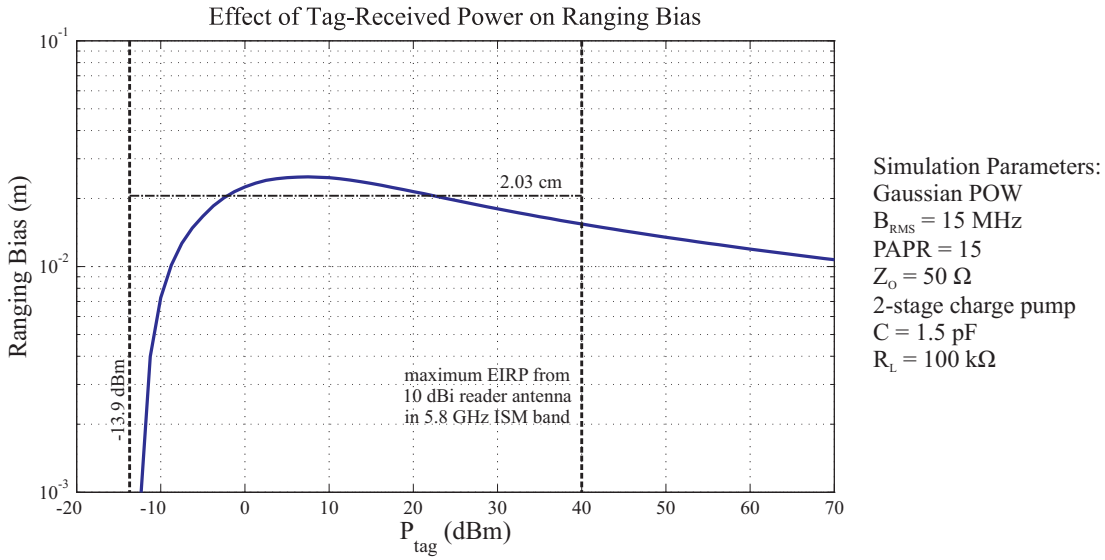

Figure 40: Ranging bias is always positive as predicted by the empirical model in equation (141). No bias is predicted for $P_{\text{tag}} < -13.9$ dBm when the charge pump diodes are not forward-biased by the voltage magnitude of the tag-received signal.

4.5.2 Effect of Charge Pump Parameters on Ranging Bias

A charge pump with high stage capacitance will absorb more charge than the same charge pump with small stage capacitance holding all other parameters constant and assuming the output voltage and impinging signal are the same. Thus, increasing stage capacitance increases the input current into the charge pump. Figure 41 shows that the model predicts higher distortions for larger stage capacitors on a 2-stage charge pump. The curves display a limiting behavior as stage capacitance increase. The curves for $C = 10$ pF to $C = 1000$ pF approximate the same upper bound curve.

The theoretical upper bound curve in Figure 41 for ranging bias predicted by the model is found by evaluating the limit as capacitance goes to infinity. The model described in equation (141) is then carried out with this value for maximum clipping voltage. The limit as stage capacitance approaches infinity evaluates to

$$\lim_{C\to\infty} V_{\text{clip}} = 5N\left(2\sqrt{\text{PAPR}\cdot Z_{\text{O}}\cdot P_{\text{tag}}} - V_{\text{t}}\right)\frac{T_{\text{st}}}{T_{\text{ch}}}\frac{Z_{\text{O}}}{R_{\text{L}}}. \tag{142}$$

A high number of stages N and rectified voltage $\left(2\sqrt{\text{PAPR}\cdot Z_{\text{O}}\cdot P_{\text{tag}}} - V_{\text{t}}\right)$ produces a large clipping voltage since the absorbed charge is proportional. Increasing the charge time T_{ch} while holding all else constant reduces the average input current, which reduces the

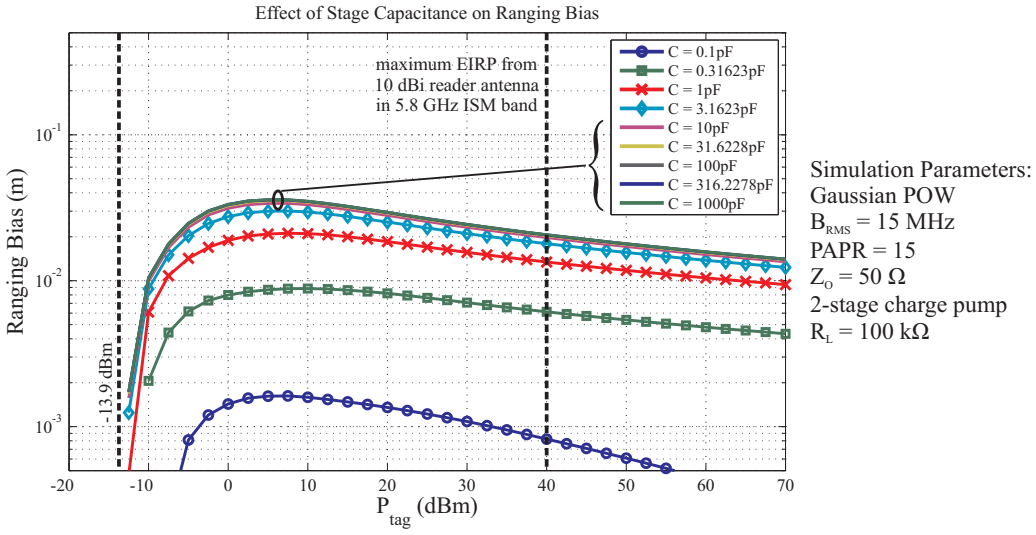

Figure 41: Ranging bias is larger for large stage capacitor values since they absorb more charge at the same output voltage.

value of the current spikes. Clipped voltage is inversely proportional to load resistance. A small load resistance R_{L} discharges the charge pump faster than a large load resistance. Thus, the input current spikes become larger in magnitude. The clipped voltage is capped by the magnitude of the tag-received POW. Voltage clipping cannot physically create a negative voltage on the reflected signal.

Load resistance affects ranging bias and behaves with a "sweet spot" (i.e. a 10 kΩ load resistance produces the largest ranging bias) as shown in Figure 42. Load resistances above and below 10 kΩ produce less ranging bias. An analytical solution of the load resistance that produces the maximum ranging bias according to this model is extremely complex and tedious. However, investigation into the simulations show that the resistance values below 10 kΩ put the charge pump into discontinuous operation, which occurs when the output decays faster than the POW time period. Thus, the output voltage rises from zero to its maximum voltage predicted by the Dickson equation (136) during the rise time of every POW pulse. This large voltage swing draws maximum current from the input source as compared to other load resistances. The model in Figure 42 predicts that the bias reduces in discontinuous operation from the maximum ranging bias. However, simulations show

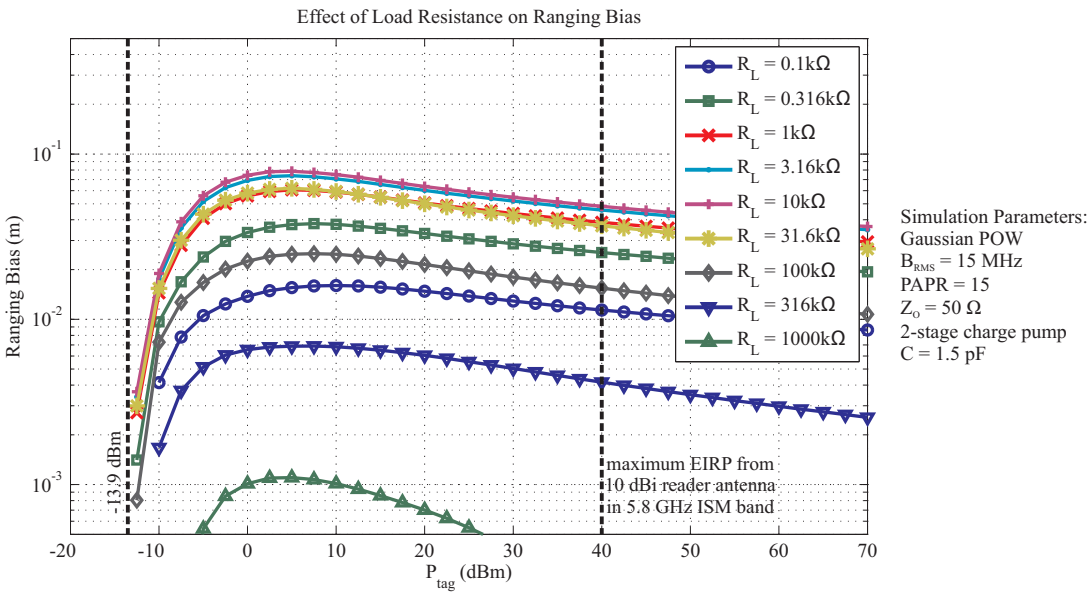

Figure 42: Increasing load resistance from 100 Ω to 1 MΩ shows that ranging bias increases to a maximum bias at 10 kΩ and then decreases to zero.

that ranging bias is nearly the same for load resistances less than 10 kΩ.

Ranging bias is sensitive to changes in the number of charge pump stages. The voltage clipping in equation (140) is linearly proportional to the number of stages N. Therefore, a high number of stages produces high distortion and severe ranging bias. Figure 43 shows this trend. There is a cap on the maximum ranging bias that is reached after $N = 30$ stages. The voltage clipping cannot be larger than the impinging POW magnitude. The model predicts a clipped, filtered, reflected signal that looks the same for any number of stages beyond $N = 30$. In this case, the maximum ranging bias depending on the number of stages is 51.8 cm. Existing passive sensors typically do not exceed a charge pump with 10 stages [27] for practical reasons; Designers choose the minimum number of stages to achieve a specified output voltage at the specified tag-received signal power. The ranging bias increases greatly for each stage added to the design as evidenced by Figure 43.

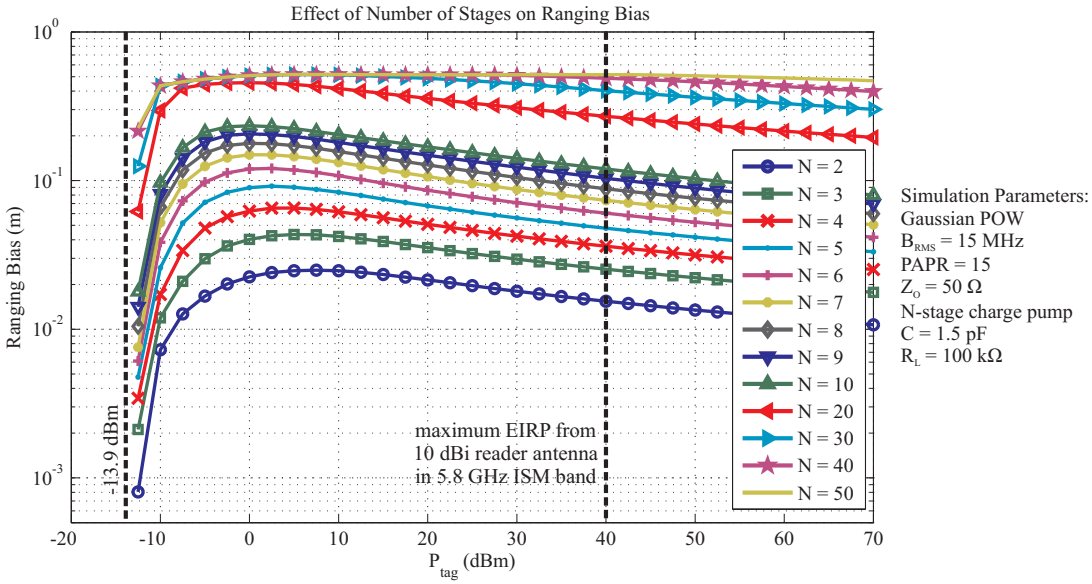

Figure 43: Charge pump stages have a significant effect on the ranging bias according to the model.

CHAPTER V

SIMULATIONS OF POW RANGING

The three phenomena addressed in these simulations that affect ranging performance are POW shape, environmental clutter, and nonlinear reflections. Each of the these three phenomena are tested independent of one another. First, the simulations on POW shape test across three values of RMS bandwidth and assume only noise in a free space environment (i.e. no environmental clutter or nonlinear reflection). Next, the simulations on nonlinear reflections vary the amount of input power into a charge pump reflection assuming no clutter. Two sets of simulations cover environmental clutter: frequency flat and frequency-selective environments. The frequency flat simulations vary the K-factor from -100 dB (Rayleigh fading) to 100 dB (free-space, no fading). The frequency selective simulations vary the mean radar cross section (RCS) from -30 to 10 dB(m^2).

Overall, the simulation results verify the theory from Chapter 4. The results found from these simulations show that maximum likelihood (ML) ranging with POWs adheres efficiently to the Cramer-Rao lower bound (CRLB) and is bounded above and below by the information limits. It is verified that ranging uncertainty is inversely proportional to the RMS bandwidth. Different POW shapes with the same RMS bandwidth perform equally well as range-estimation waveforms. It is evident from these results that a nonlinear reflection adds ranging bias. The model developed in Section 4.5 is accurate for a 2-stage charge pump with 1.5 pF capacitors and a 100 kΩ load resistor. The model is also accurate for charge pump parameters near these values, but the model becomes inaccurate when the number of stages increases or the charge pump operates in discontinuous mode. Typical simulated values for range estimation bias are between 0.5 and 10 cm. This is insignificant bias for systems with uncertainty specifications greater than 100 cm. It is found that frequency-flat clutter environments alter the uncertainty only slightly from the CRLB prediction when tested over the ensemble SNR of the received signal. Product-Rayleigh

Table 6: Set of POW shapes simulated. ($T_{\mathrm{POW}} = 100$ ns and $B_f = 150$ MHz for square-POWs)

Shape	Parameter	$B_{\mathrm{3dB,pls}}$	B_{RMS}	Shape	Parameter	$B_{\mathrm{3dB,pls}}$
Gaussian	$\sigma = 7.958$ ns	23.5 MHz	**10 MHz**	square	$D = 0.7858$	11.3 MHz
Gaussian	$\sigma = 5.305$ ns	35.3 MHz	**15 MHz**	square	$D = 0.3697$	24.0 MHz
Gaussian	$\sigma = 3.979$ ns	47.1 MHz	**20 MHz**	square	$D = 0.2150$	41.2 MHz

backscatter channels display slightly smaller uncertainty than the CRLB prediction, and product-Rician backscatter channels display slightly higher uncertainty. Frequency-selective clutter environments are found to add significant uncertainty and bias to the estimator. Stronger clutter adds more uncertainty and more bias than weaker clutter.

5.1 Simulations of Ranging With Various Power-Optimized Waveform Shape

Three Gaussian-POWs and three square-POWs are compared. Three values of RMS bandwidth are given to the POW shapes so they can be compared side-by-side: 10 MHz, 15 MHz, and 20 MHz. Table 6 shows the parameters of the simulated waveforms. All POWs simulated throughout this Chapter have a time period of 100 ns. The single-pulse 3-dB bandwidths for each POW are given as well. These listed square-POWs are more spectrally efficient than the Gaussian POWs for the RMS bandwidths shown. However, the PAPRs of the Gaussian POWs (10.0, 15.0, and 20.1 for $B_{\mathrm{RMS}} = 10$ MHz, 15 MHz, and 20 MHz respectively) are larger than the PAPRs of the equivalent square-POWs (2.5, 5.4, and 9.2) with the same RMS bandwidths. Thus, the Gaussian POWs listed provide more energy-harvesting POW gains than the listed square-POWs. There is only 150 MHz of allotted spectrum in the 5.8 GHz ISM band [18]. Thus, these simulated POWs are testing the limits of the spectral mask when considering the entire POW spectrum rather than just the 3-dB bandwidth.

5.1.1 Simulator Setup

The simulator setup is shown in Figure 44. The tag is randomly located uniformly between $0.05\lambda_{\mathrm{POW}}$ and $0.45\lambda_{\mathrm{POW}}$. These range limits are chosen to minimize the possibility of an

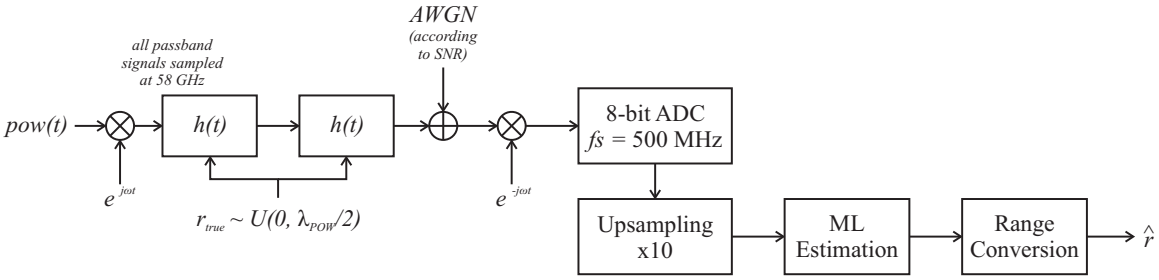

Figure 44: The POW shape simulation setup creates the POW and then adds a random delay and AWGN to simulate a noisy free-space channel.

ambiguity error, which occurs when the estimator loops around the estimated range by half the POW wavelength due to the estimation of an impossible range. For example, consider a tag located at a true range of $0.05\lambda_{\mathrm{POW}}$, and assume the reader receives the backscattered signal with -3 dB SNR. The high noise level may perturb the cross-correlation output such that the estimator measures a peak of the cross-correlation at a negative range of $-0.01\lambda_{\mathrm{POW}}$. A-priori knowledge states that a tag may only be located between 0 m and $0.5\lambda_{\mathrm{POW}}$; it cannot be located at a negative range. Therefore, the estimator deduces that the delay must be looped by half of the POW time period to a positive delay of $0.49\lambda_{\mathrm{POW}}$. This estimate has an extremely large ambiguity error (error $= r_{\mathrm{true}} - \hat{r} = -0.44\lambda_{\mathrm{POW}}$) that resulted from the tag's proximity to the edge of the possible ranges. Ambiguity errors are purposely minimized in the simulator to allow a good comparison of the estimator to the CRLB. The CRLB does not account for ambiguity errors, but the Ziv-Zakai lower bound [43] does take them into account.

The passband signals are represented in discrete time in the simulator and are sampled at 58 GHz, which is 10 times the center frequency of the passband at 5.8 GHz. This models the passband signals with 10 points per carrier time period. Additive white Gaussian noise (AWGN) is added with power according to the tested SNR value. The noisy passband signal is then downconverted to baseband where it is sampled at 500 MHz. An 8-bit analog-to-digital converter (ADC) is simulated as well to represent the sampling resolution of the oscilloscope used in the measurements in the next chapter. The simulator upsamples the sampled waveform from the ADC by a factor of 10 from 500 MHz to 5 GHz. The ML estimator is noncoherent, and it produces an estimate of delay, which is then converted to

a range estimate.

One thousand estimations are performed for each SNR value for every POW shape in Table 6. One thousand estimations per SNR value is a large enough sample set to provide consistently repeatable simulation results. The SNR test points are

$$\text{SNR} \quad \in \quad (-20, -15, \ldots, 40) \ \ \text{dB}. \tag{143}$$

A total of 78,000 estimations are performed in these simulations covering the six POW shapes in Table 6. The bias and uncertainty of the ML estimator are calculated from equations (58) and (60) in Chapter 4. The speed of light assumed for the estimator is that of a PTFE (teflon) substrate, which is the substrate material used in the 50 Ω SMA cables from the measurements in Section 6.1. The relative permitivitty is 2.1, which makes the speed of light $v_\text{p} = 2.0687 \cdot 10^8$ m/s.

5.1.2 Simulation Results

Figures 45, 46, and 47 show the simulation results for all three Gaussian POWs from Table 6, and Figures 48, 49, and 50 show the simulation results for all three square-POWs. The upper, middle, and lower information limits due to sampling and a-prior knowledge are:

$$\sigma_\text{up} = \sqrt{\text{Var}\left(\mathcal{U}\left(0, \frac{1}{2}v_\text{p}T_\text{POW}\right) - \mathcal{U}\left(0, \frac{1}{2}v_\text{p}T_\text{POW}\right)\right)} = \frac{v_\text{p}T_\text{POW}}{2\sqrt{6}} = 4.223 \text{ m} \tag{144}$$

$$\sigma_\text{mid} = \sqrt{\text{Var}\left(\mathcal{U}(0, \frac{1}{2}v_\text{p}T_\text{s})\right)} = \frac{v_\text{p}}{2\sqrt{12}f_\text{s}} = 5.97 \text{ cm} \tag{145}$$

$$\sigma_\text{low} = \sqrt{\text{Var}\left(\mathcal{U}\left(0, \frac{1}{2}v_\text{p}\frac{T_\text{s}}{10}\right)\right)} = \frac{v_\text{p}}{2\sqrt{12}(10f_\text{s})} = 0.597 \text{ cm} \tag{146}$$

Note that the upper information limit equation used here is different from the equation given in equation (110). Just as in the analysis leading to equation (110), the estimator effectively becomes a random range guesser at negative SNRs where noise dominates the signal. The time delay guesses are uniformly distributed between an upper limit of half the POW time period and lower limit of zero. However, this simulator picks the random tag ranges independently from a uniform distribution with nearly the same limits. Therefore,

the upper limit on estimator uncertainty is the standard deviation of the difference of two i.i.d. uniform random variables.

The limit on uncertainty provided by the noncoherent CRLB is (from equation (118))

$$\sqrt{\text{CRLB}} = \frac{v_\text{p}}{2\sqrt{f_\text{s} T_\text{POW}}(2\pi B_\text{RMS})\sqrt{\text{SNR}}} \tag{147}$$

This simulator has a sampling frequency of $f_\text{s} = 500$ MHz, time period $T_\text{POW} = 100$ ns, and speed of light in PTFE substrate $v_\text{p} = 2.0687 \cdot 10^8$ m/s.

Overall, the simulation results adhere strongly to the noncoherent CRLB and information bounds given in Section 4.3.4.

There is a strong adherence to the CRLB. The middle horizontal line (5.97 cm) represents the lower limit if the estimator operated at the ADC sampling rate of 500 MHz. The lowest information bound (0.597 cm) represents the absolute lowest limit of uncertainty of this estimator, which upsampled the analog-to-digital (ADC) sampling rate by a factor of 10.

The biases shown in the figures all converge to 0 m at high SNRs indicating perfect accuracy of the ML estimator. Some randomness of bias is observed for negative SNRs where the estimator receives little information from the received signal. This is expected since the ML estimator acts as a random range guesser at these low SNRs, but the simulated bias points deviate minutely around 0 m.

The quantization noise of the ADC has a negligible effect on the performance of the estimator. The signal-to-quantization-noise (SQNR) of a signal in an ADC sampling with Q bits of uncertainty is [49]

$$\text{SQNR} \approx 6.02Q \text{ dB} \tag{148}$$

This model assumes the signal spans the full range of the ADC signal limits. The SQNR is reduced by 6 dB assuming the received signal spans 1/2 of the full range of the simulator's 8-bit ADC. Under this condition, the SQNR of the simulator's 8-bit ADC is 42 dB. The highest simulated SNR is 40 dB, and the estimator reaches its lowest information limit between 20 dB and 30 dB (depending on the signal shape). Thus, the quantization noise has

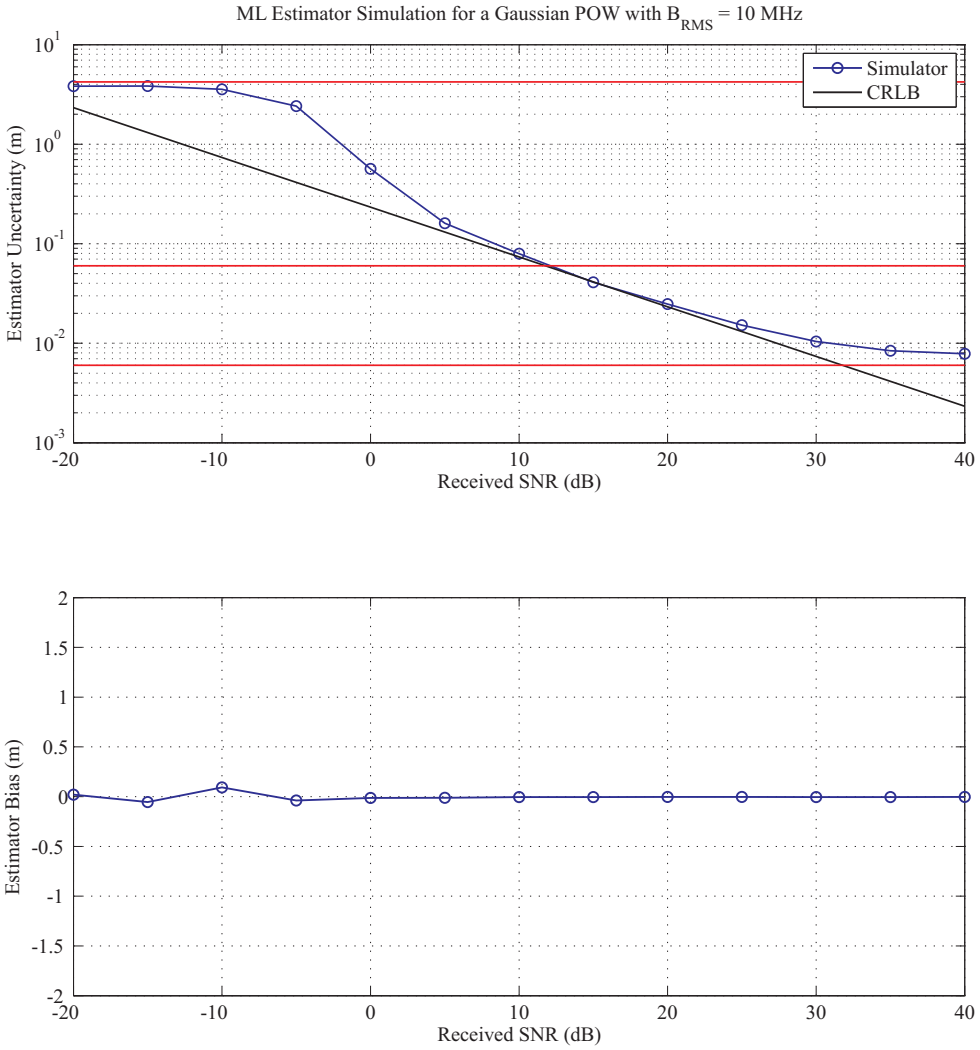

Figure 45: Simulated uncertainty and bias for a Gaussian POW with $B_{\text{RMS}} = 10$ MHz. Each data point represents the uncertainty or bias of the estimator after 1,000 trials at the specified SNR. The horizontal lines in the uncertainty graph are the information bounds.

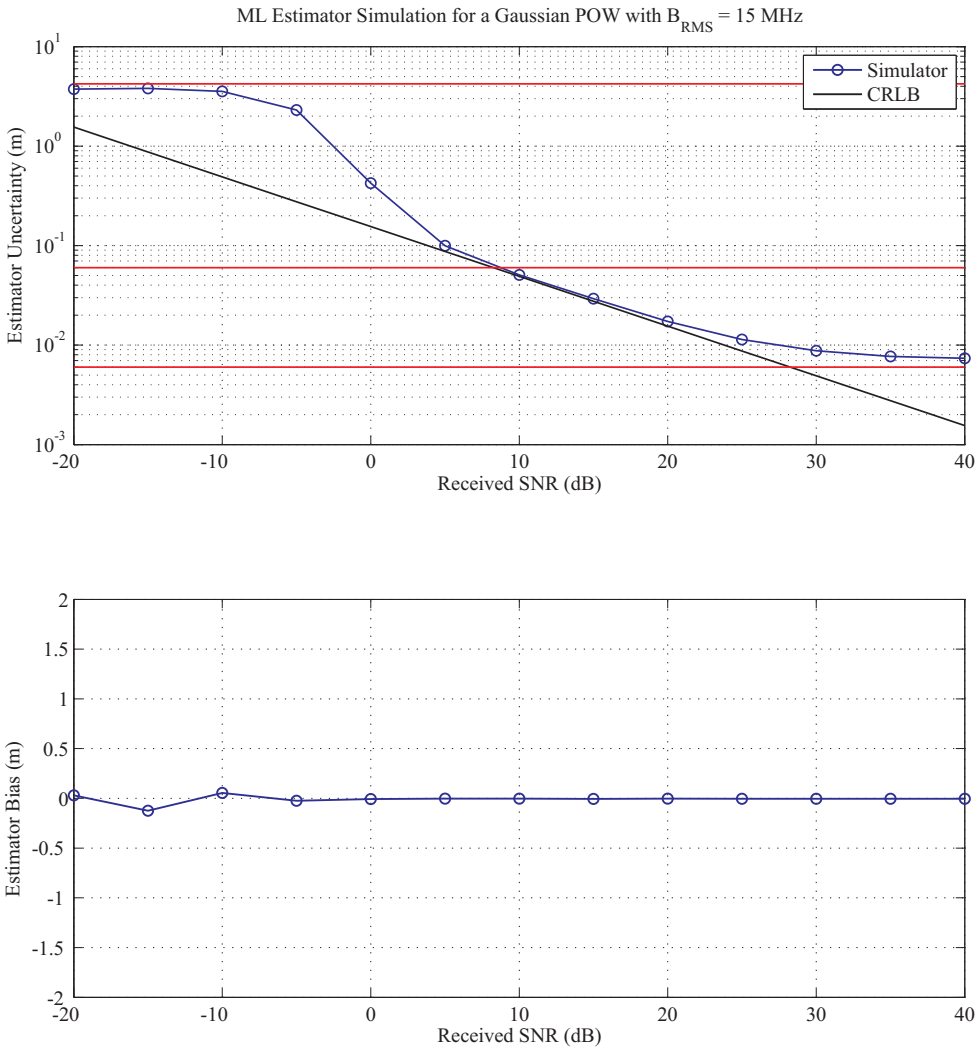

Figure 46: Simulated uncertainty and bias for a Gaussian POW with $B_{\mathrm{RMS}} = 15$ MHz. Each data point represents the uncertainty or bias of the estimator after 1,000 trials at the specified SNR.

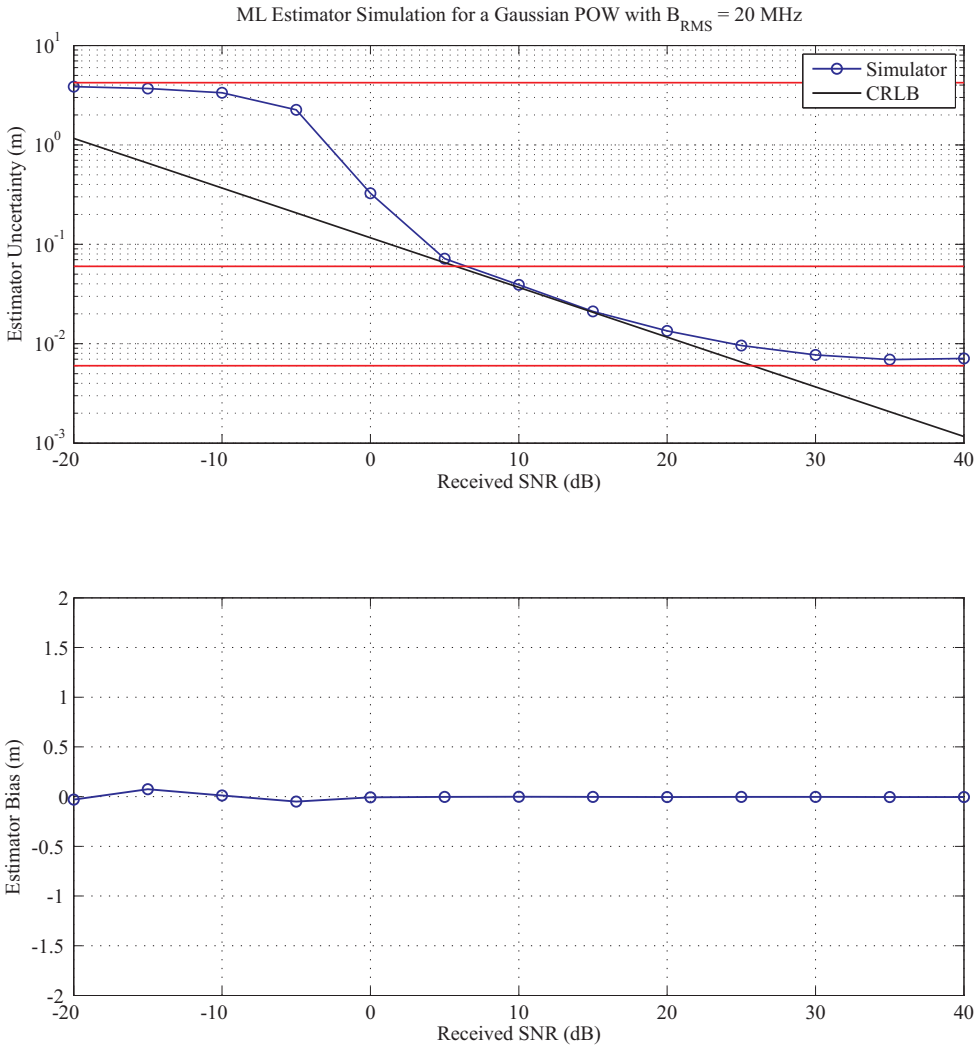

Figure 47: Simulated uncertainty and bias for a Gaussian POW with $B_{\mathrm{RMS}} = 20$ MHz. Each data point represents the uncertainty or bias of the estimator after 1,000 trials at the specified SNR.

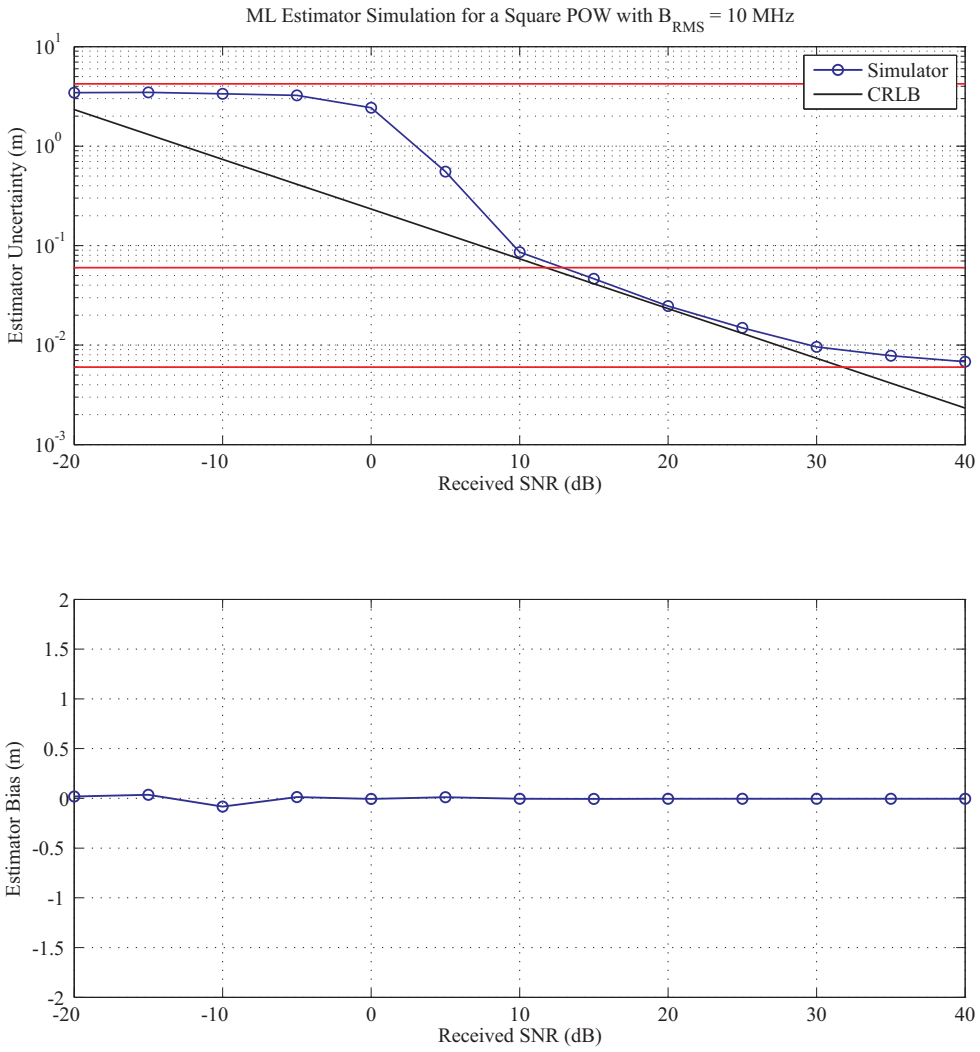

Figure 48: Simulated uncertainty and bias for a square-POW with $B_{\mathrm{RMS}} = 10$ MHz. Each data point represents the uncertainty or bias of the estimator after 1,000 trials at the specified SNR.

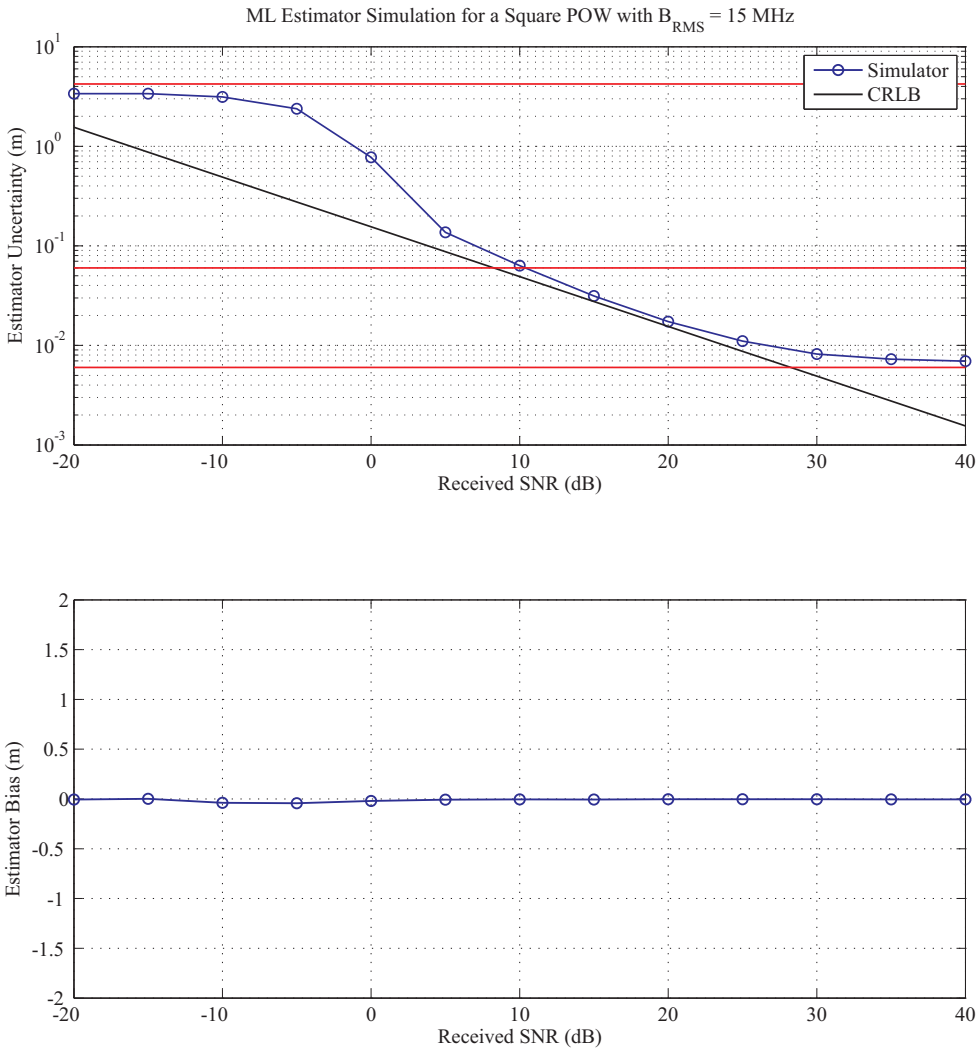

Figure 49: Simulated uncertainty and bias for a square-POW with $B_{\mathrm{RMS}} = 15$ MHz. Each data point represents the uncertainty or bias of the estimator after 1,000 trials at the specified SNR.

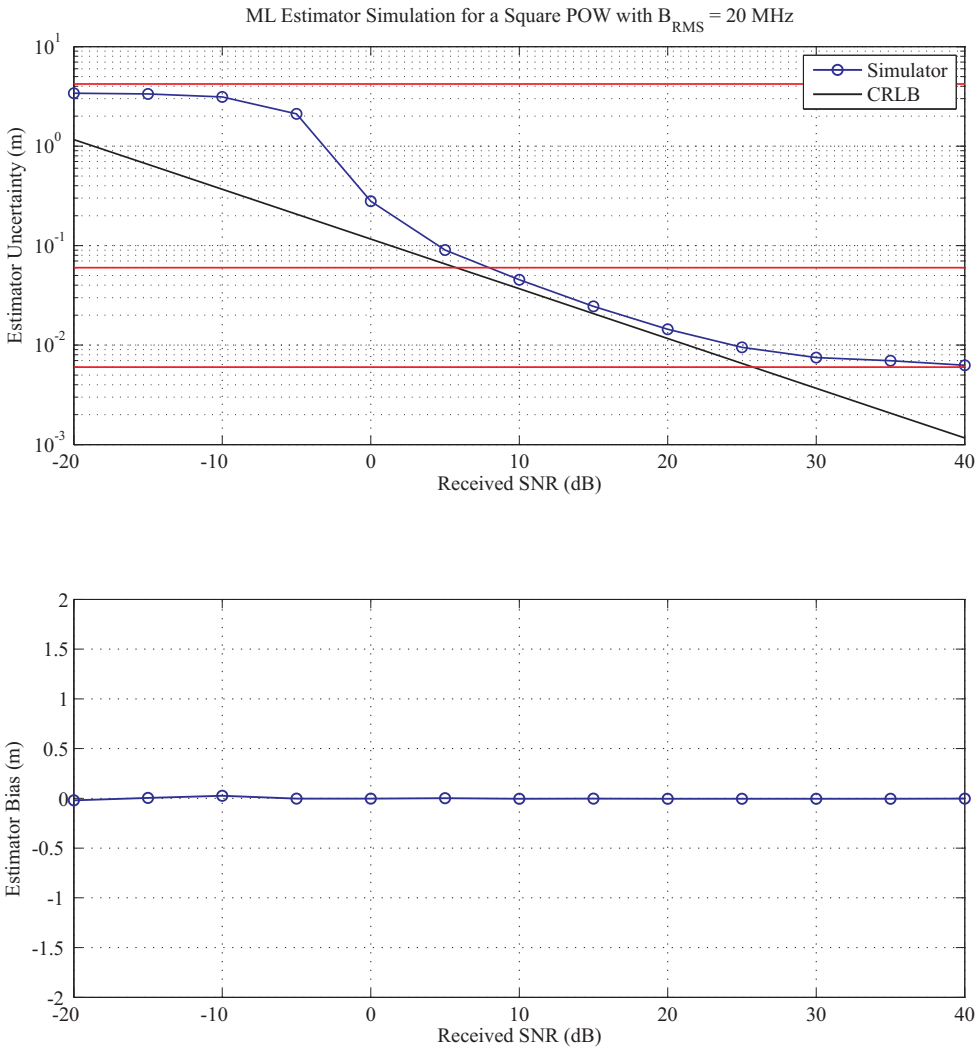

Figure 50: Simulated uncertainty and bias for a square-POW with $B_{\mathrm{RMS}} = 20$ MHz. Each data point represents the uncertainty or bias of the estimator after 1,000 trials at the specified SNR.

a negligible effect on the range estimations. This is verified by running the same simulations replacing the 8-bit ADC with a 16-bit ADC. No measurable difference in performance was found.

5.2 Simulations of Ranging Through Frequency-Flat Environments

Frequency-flat environments present a channel coefficient with a Rician-distributed envelope and uniformly distributed phase. It is shown that the variability of these two channel quantities do not alter the uncertainty of an estimator as the simulated uncertainties adhere to the CRLB. The simulated estimator is unbiased for all cases.

5.2.1 Simulator Setup

Figure 51 shows that the simulator setup is nearly identical to the POW shape simulation setup from Figure 44. The upconverted POW is normalized to a signal power of 0 dBm and then transmitted through two identical Rician channels to emulate a monostatic reader communicating with a single-antenna tag in a product-Rician backscatter channel. Noise is added with noise power

$$P_{\mathrm{N}}\ (\mathrm{dBm}) = 0\ \mathrm{dBm} - \mathrm{SNR}\ (\mathrm{dB}) \tag{149}$$

The test points varied in the simulations are

$$\begin{aligned} K &\in (-100, -10, 0, 10, 100)\ \ \mathrm{dB}, \\ \mathrm{SNR} &\in (-20, -15, \ldots, 40)\ \ \mathrm{dB}. \end{aligned} \tag{150}$$

For each value of the K-factor, the SNR is varied between -20 and 40 dB in 5-dB increments. One thousand ranging estimations are taken for each test point (K, SNR). Overall, 65,000 range estimations are taken over the test points described in the lists of (150). A new random Rician channel is created for each of the 65,000 range estimations. In these simulations, SNR represents the targeted ensemble average SNR of the received signal over the 1,000 estimations taken for each test point (K, SNR). A deep fade may occur, which gives a much lower SNR than what is set forth in the simulation plan. However, a large SNR is provided when there is constructive interference.

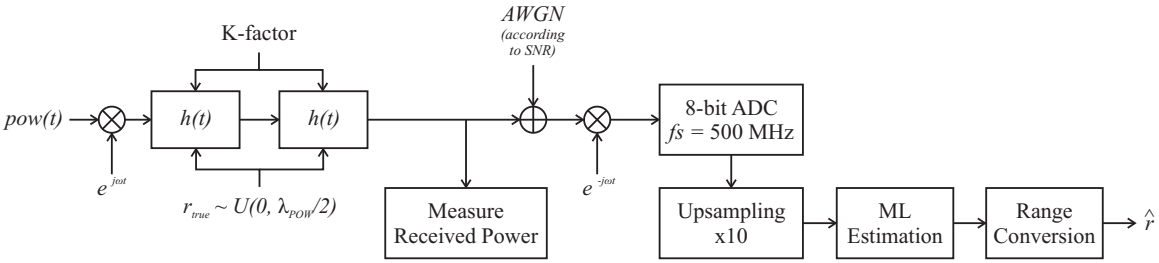

Figure 51: Ranging uncertainty and bias are simulated versus K-factor ∈ (-100, -10, 0, 10, 100) dB and SNR ∈ (-20, -15, ..., 40) dB. The case where K = 100 dB behaves like the noisy free-space simulations in Figure 46.

The received signal power of each iteration in the simulator is measured just before the AWGN is added as shown in Figure 51. This independent signal power measurement measures the ensemble average received SNR over all 1,000 iterations for each value of tested SNR. The simulated estimator uncertainty and bias results are adjusted to match the measured ensemble average SNR when there are any discrepancies.

5.2.2 Simulation Results

The results are plotted in Figure 52 for all values of tested K-factor. The uncertainty graph shows that all frequency-flat environments behave identically to free-space environments in terms of ranging performance. This behavior is expected based on the discussion from Section 4.4.1.

Table 7 shows the independently measured ensemble average of received SNR for all test points (K, SNR) in the simulation. Notice that the Rayleigh environment has a measured received ensemble average SNR that is 3.4 dB better than the targeted SNR. The environment with K = -10 dB has a measured ensemble average that is 2.0 dB better. This is an artifact of the simulator and could not be controlled. The estimator performance results in Figure 52 are adjusted for these SNR errors.

5.3 Simulations of Ranging Through Frequency-Selective Environments

These simulations classify an environment's clutter level by the average radar cross section μ_{RCS} of the random objects in the environment. This single-statistic classification based on average RCS is more descriptive of an environment's clutter than the coherence bandwidth

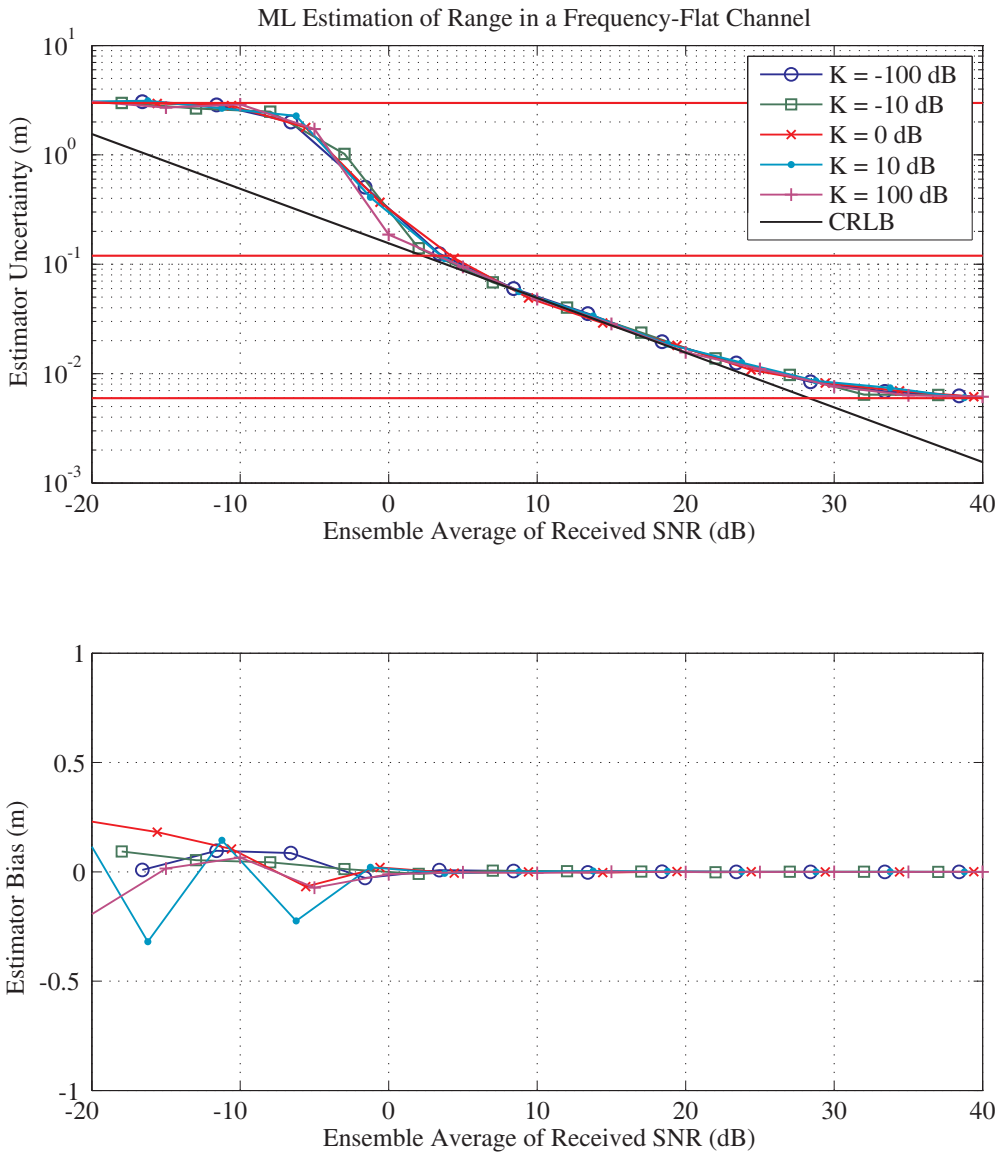

Figure 52: Simulated ranging performance for a ML estimator in a random flat-fading environment using a Gaussian POW with $B_{\mathrm{RMS}} = 15$ MHz.

Table 7: Independently Measured Ensemble Average Received SNR from Frequency-Flat Simulations

Targeted SNR	K = -100 dB	K = -10 dB	K = 0 dB	K = 10 dB	K = 100 dB
-20 dB	-16.6 dB	-18.0 dB	-20.6 dB	-21.2 dB	-20.0 dB
-15 dB	-11.6 dB	-13.0 dB	-15.6 dB	-16.2 dB	-15.0 dB
-10 dB	-6.6 dB	-8.0 dB	-10.6 dB	-11.2 dB	-10.0 dB
-5 dB	-1.6 dB	-3.0 dB	-5.6 dB	-6.2 dB	-5.0 dB
0 dB	3.4 dB	2.0 dB	-0.6 dB	-1.2 dB	0.0 dB
5 dB	8.4 dB	7.0 dB	4.4 dB	3.8 dB	5.0 dB
10 dB	13.4 dB	12.0 dB	9.4 dB	8.8 dB	10.0 dB
15 dB	18.4 dB	17.0 dB	14.4 dB	13.8 dB	15.0 dB
20 dB	23.4 dB	22.0 dB	19.4 dB	18.8 dB	20.0 dB
25 dB	28.4 dB	27.0 dB	24.4 dB	23.8 dB	25.0 dB
30 dB	33.4 dB	32.0 dB	29.4 dB	28.8 dB	30.0 dB
35 dB	38.4 dB	37.0 dB	34.4 dB	33.8 dB	35.0 dB
40 dB	43.4 dB	42.0 dB	39.4 dB	38.8 dB	40.0 dB
Difference	+3.4 dB	+2.0 dB	-0.6 dB	-1.2 dB	0.0 dB

as discussed in Section 4.4.2. The simulated estimator's ranging performance degrades significantly for high-clutter environments.

5.3.1 Simulator Setup

The simulator is modified slightly from the frequency-flat simulator as shown in Figure 53. Each of the 10 scatterers are placed randomly for each iteration of the simulator. One thousand iterations were carried out at each SNR value as before. This makes a total of 13,000 estimations for each value of mean RCS μ_{RCS}. The test points varied in the simulations are

$$\mu_{\text{RCS}} \in (-30, -20, -10, 0, 10) \text{ dB}(\text{m}^2), \tag{151}$$

$$\text{SNR} \in (-20, -15, \ldots, 40) \text{ dB}. \tag{152}$$

Each scatterer takes on a value of RCS from the log-normal distribution with a mean from the above list and standard deviation of 10 dB. The speed of light is assumed to be that of free-space: $c = 2.9979 \cdot 10^8$ m/s. The sampling frequency is 500 MHz, and the upsampling

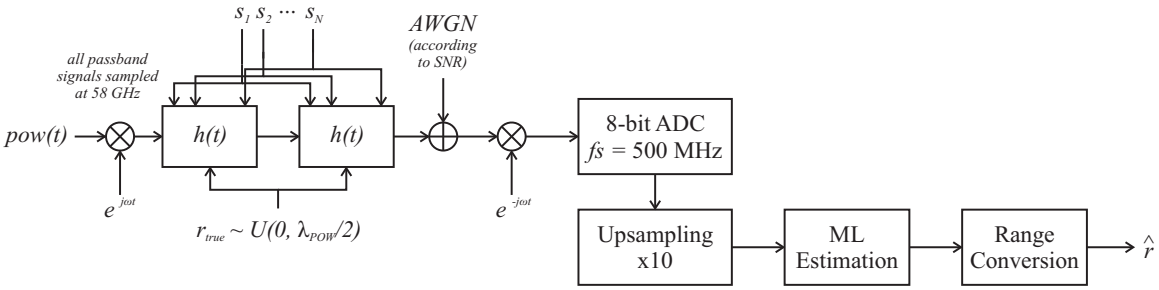

Figure 53: The frequency-selective channel is modeled with the LOS path from the reader to tag r_{true} and N random scatterers $s_1 \dots s_N$. Noise is added according to tested SNR.

frequency is 10 times faster just the same as previous simulations. The corresponding information limits are:

$$\sigma_{\text{up}} = \frac{cT_{\text{POW}}}{2\sqrt{12}} = 4.327 \text{ m} \quad (153)$$

$$\sigma_{\text{mid}} = \frac{c}{2\sqrt{12}f_{\text{s}}} = 8.65 \text{ cm} \quad (154)$$

$$\sigma_{\text{low}} = \frac{c}{2\sqrt{12}(10f_{\text{s}})} = 0.865 \text{ cm} \quad (155)$$

Thus, the path delays are calculated with the speed of light in free space, and the channel response is frequency-selective.

The simulator creates a two-dimensional environment as shown in Figure 54. Then, the channel response is computed based on the euclidian distances from the reader to the tag on paths involving one clutter object. Overall, there are 11 paths: The LOS path has the delay corresponding to the true range of the tag. Each of the other 10 paths involve only one of the 10 random objects and neglects paths containing two or more scatterers. The i^{th} path gain α_i is derived from equation (126) with the antenna gains assumed to have isotropic patterns ($G_r = G_t = 1$). The i^{th} path delay τ_i is computed with the Euclidian distance from the reader to the i^{th} object r_{ri} and the Euclidian distance from the object to the tag r_{rt}. The phase of each path is chosen uniformly between $-\pi$ and π. Also, the RCS

is chosen from the log-normal distribution:

$$\alpha_i = \frac{\lambda_c}{4\pi r_{ri} r_{ti}}, \tag{156}$$

$$\tau_i = \frac{r_{ri} + r_{ti}}{c}, \tag{157}$$

$$\phi_i \sim \mathcal{U}(-\pi, \pi), \tag{158}$$

$$\text{and } \log_{10} \sigma_i \sim \mathcal{N}(\mu_{\text{RCS}}, 10 \text{ dB}(\text{m}^2)) \tag{159}$$

The passband frequency is 5.8 GHz, which has a wavelength of 5.17 cm in free space. Each simulated iteration has a unique channel impulse response calculated by

$$h_{\text{sel}}(t) = \alpha_{\text{tag}} \delta\left(t - \frac{r_{\text{tag}}}{c}\right) e^{-jkr_{\text{tag}}} + \sum_{i=1}^{10} \sqrt{\sigma_i} \alpha_i \delta(t - \tau_i) e^{j\phi_i}. \tag{160}$$

The path gain of the LOS path is α_{tag}, which is computed using the randomly-chosen tag range. The tag's time delay is τ. The RMS delay spread and coherence bandwidth of the entire backscatter channel is calculated as well to show typical values simulated. These second-order statistics are calculated using: [56] [67]

$$\sigma^2_{\text{RMS,BS}} = 2\sigma^2_{\text{RMS}} \tag{161}$$

$$B_{\text{coh,BS}} = \frac{1}{5\sigma_{\text{RMS,BS}}} \tag{162}$$

$$\text{where } \sigma^2_{\text{RMS}} = \frac{\tau^2 \alpha^2_{\text{tag}} + \sum_{i=1}^{10} \tau_i^2 \sigma_i \alpha_i^2}{\alpha^2_{\text{tag}} + \sum_{i=1}^{10} \sigma_i \alpha_i^2} - \left(\frac{\tau \alpha^2_{\text{tag}} + \sum_{i=1}^{10} \tau_i \sigma_i \alpha_i^2}{\alpha^2_{\text{tag}} + \sum_{i=1}^{10} \sigma_i \alpha_i^2} \right)^2 \tag{163}$$

The RMS delay spread of the backscatter channel $\sigma^2_{\text{RMS,BS}}$ is twice the RMS delay spread of the one-way channel σ^2_{RMS} from the reader to the tag [67].

5.3.2 Simulation Results

Figure 55 shows the simulated estimator performance over the various clutter environments. The results indicate that ranging in low-clutter environments closely emulates ranging in free-space environments. The lowest simulated clutter environment (μ_{RCS} = -30 dBm^2) has the smallest uncertainty and operates near the CRLB at intermediate SNRs. However, this case performed with 9.4 dB more uncertainty than a free-space environment at high SNRs greater than 30 dB. The highest-clutter environment where $\mu_{\text{RCS}} = 10$ dBm^2 displays 24.4 dB more uncertainty than a free-space environment at these same high SNRs. On top

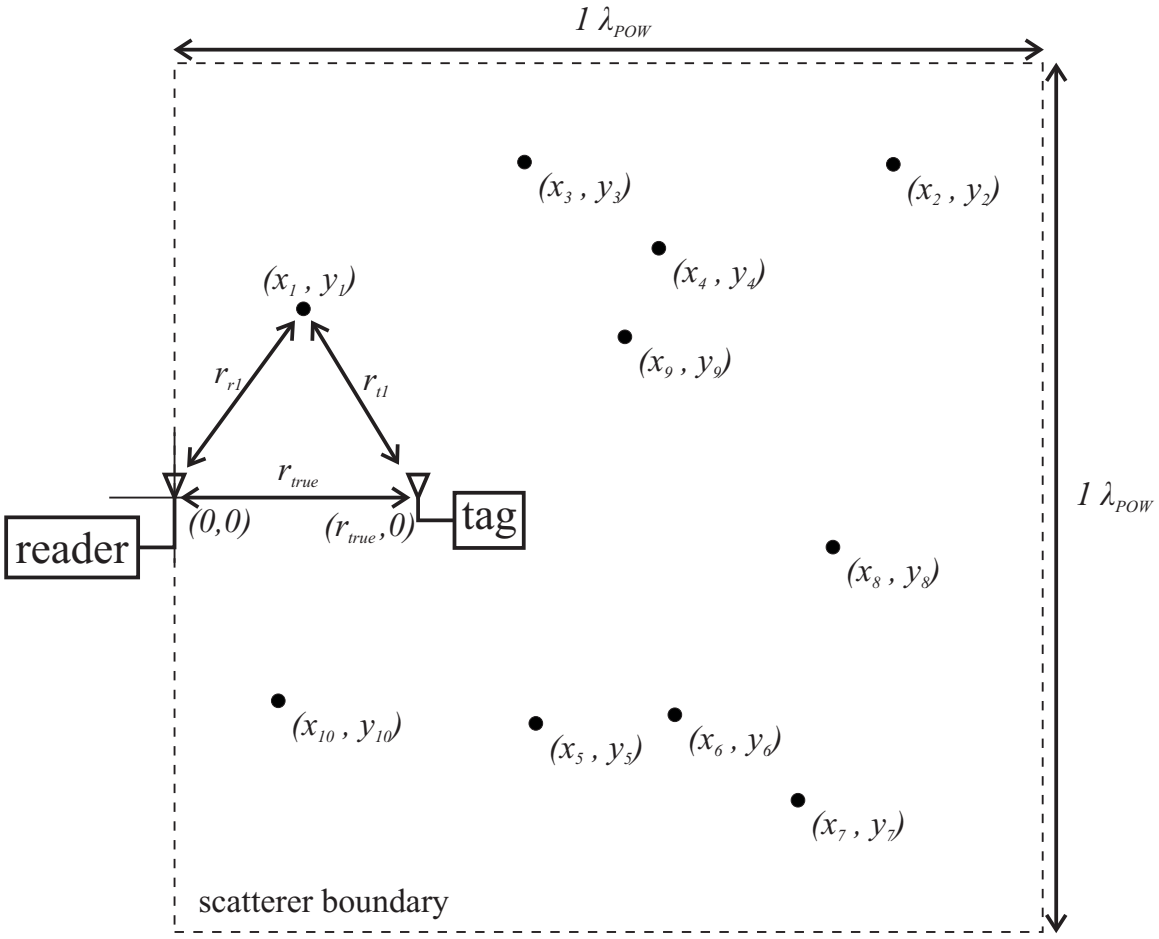

Figure 54: A simulated cluttered environment has 10 uniform-random scatterers placed within the boundaries $x \sim U(0, \lambda_{\mathrm{POW}})$ and $y \sim U(-\lambda_{\mathrm{POW}}, \lambda_{\mathrm{POW}})$. The tag is placed at a uniform-random range $r_{\mathrm{true}} \sim U(0.05\lambda_{\mathrm{POW}}, 0.45\lambda_{\mathrm{POW}})$, and the reader is located at the origin.

of this, the simulated biases show increasing bias with the level of clutter in the environment. The same ML range estimator performs with zero bias in a free-space environment.

The comparison with the free-space case is interesting, but it is not helpful for designers. At high SNRs, the free-space uncertainty is bounded from below by the range-bin uncertainty, which depends on the sampling frequency of the ADC (i.e. lower-information limit). The uncertainty of the estimator in a cluttered environment is more affected by the uncertainty in clutter rather than by range-bin uncertainty. The same simulations run with an upsampling factor of 20 instead of 10 showed no difference in performance. Thus, increasing the sampling frequency decreases the uncertainty for the free-space environment while keeping the uncertainty in a cluttered environment the same.

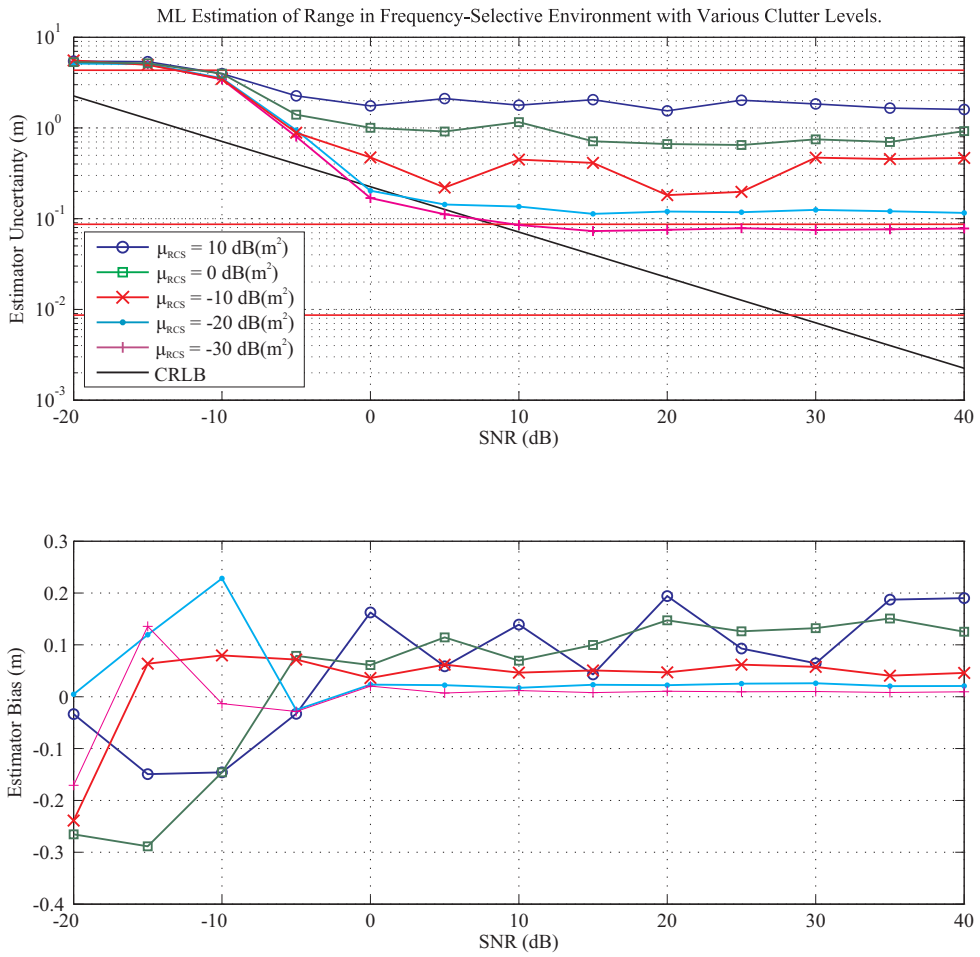

Figure 55: Estimator performance vs. SNR for random frequency-selective cluttered environments. The estimator's uncertainty and bias increase with the clutter level.

Table 8: Summary of Simulated Lower Bounds for Frequency-Selective Environments.

Environment	Smallest Simulated	Ranging	Average Simulated Statistics			
μ_{RCS}	Uncertainty	Bias	σ_{RMS}	B_{coh}	$\sigma_{\text{RMS,BS}}$	$B_{\text{coh,BS}}$
10 dB(m^2)	154.2 cm	14.7 cm	43.4 ns	4.61 MHz	61.4 ns	3.26 MHz
0 dB(m^2)	64.84 cm	13.6 cm	40.0 ns	5.00 MHz	56.6 ns	3.54 MHz
-10 dB(m^2)	18.20 cm	4.80 cm	41.4 ns	4.83 MHz	58.6 ns	3.42 MHz
-20 dB(m^2)	11.32 cm	2.23 cm	33.0 ns	6.06 MHz	46.7 ns	4.29 MHz
-30 dB(m^2)	7.297 cm	0.92 cm	32.8 ns	6.09 MHz	46.4 ns	4.31 MHz
Free-Space	0.865 cm	0.00 cm	0 ns	∞	0 ns	∞

The smallest simulated uncertainties for each cluttered environment including free space are shown in Table 8. The estimator bias for each simulated environment is shown in addition to the average coherence bandwidth for each environment. The values at the three highest tested SNRs (30, 35, and 40 dB) were averaged together for the calculations of simulated uncertainty and bias. The average coherence bandwidth was computed over all 13,000 unique environments created during the simulation for each value of mean RCS μ_{RCS}.

Frequency selective clutter is found to significantly increase estimator uncertainty, which must be compensated for in a design. It is desirable from a ranging-performance standpoint to reduce the 3-dB bandwidth of the POW below the coherence bandwidth of the channel. The frequency-flat clutter environments perform with less bias and less uncertainty overall as evidenced by comparing the simulation graphs in Figures 52 and 55.

There is no cost-effective method for filtering out the modulated multipath signal component without knowing the exact channel a-priori. Adaptive channel equalizers can be used to actively adjust the estimator to a changing environment [48]. In the absence of a channel equalizer, a designer must take the high uncertainty and bias as shown in these results into account. A designer should over-design the ranging uncertainty by a few orders-of-magnitude to compensate for the clutter. Also, integration of N_{POW} time periods in a single measurement reduces the uncertainty by a factor of $\sqrt{N_{\text{POW}}}$ (refer to Section 4.2.1).

As a simple example, an office building requires a passive wireless sensor network to track the location of its visitors whom are wearing visitor badges equipped with RFID. The specification calls for an estimator uncertainty of 50 cm. Assume the office environment is

frequency-selective with objects that have an average RCS of 0 dB(m^2) (e.g. computers, employees, swivel chairs, etc.). Readers are placed at regular intervals along the hallways and among the rooms. Within range of one reader, there are an average of 10 objects.

The energy-harvesting and data communications specifications call for a Gaussian POW with a PAPR of 12 and time period of 90 ns, which corresponds to an RMS bandwidth of 13.3 MHz and a 3-dB bandwidth of 31.3 MHz. As it happens, this 3-dB bandwidth is larger than all of the simulated values for coherence bandwidth. The simulated results from Table 8 indicate that the uncertainty will be about 65 cm if just one POW pulse is used for range estimation. Averaging together $N_{\mathrm{POW}} = 2$ time periods of the POW together in a single range measurement divides this uncertainty by a factor of $\sqrt{2}$, which makes the new uncertainty 46 cm.

It may be prudent to increase the number of integrated periods to a higher number than two. Each new range measurement will encounter a new frequency-selective channel if visitors are walking through the building. This way, the system can handle a higher variability of clutter. The system should be over-designed to meet the specifications.

These simulations are relevant and applicable when the clutter objects are expected to change orientation prior to each range measurement. This type of environment makes it very difficult to a design the communication link even for systems that do not use range measurements (e.g. WiFi, GSM, and Bluetooth). These simulated results do not apply to the situation where multiple range measurements are taken in a static frequency-selective environment where the clutter objects do not move between range measurements.

5.4 Simulations of Ranging on Nonlinear Reflections

The tag-received power and SNR are treated as independent variables in these simulations to cover all possibilities in real WSNs. Tag power and SNR are related by the range of the tag in real systems, but decoupling the two variables allows for the variability of antenna gains and receiver noise figures.

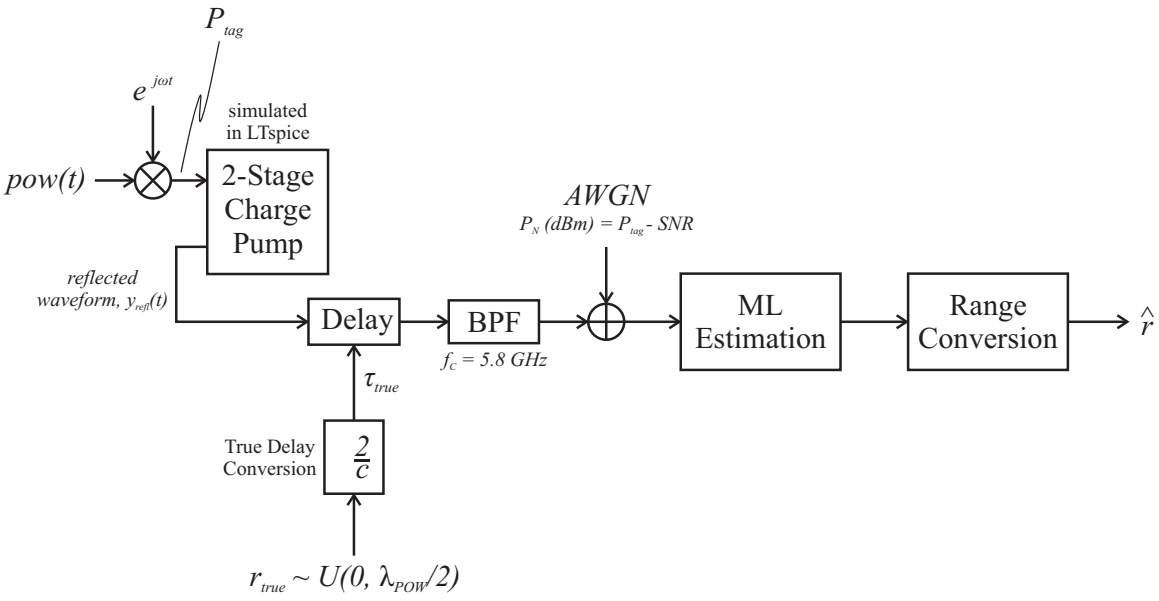

Figure 56: The amount of in-band distortion is dependent on tag-received power P_{tag}, which is tested across common values seen in passive WSNs. The simulator also tests across a wide range of SNR to allow comparison to the CRLB.

5.4.1 Simulator Setup

Figure 56 shows the simulation setup where the POW is upconverted to the passband and amplified to the tested tag-received power P_{tag}. This passband signal is imported into LTspice and connected to a two-stage charge pump, which is shown in Figure 57. The reflected waveform $y_{\text{refl}}(t)$ is simulated and imported back into the simulator where it is delayed according to twice the true range. Noise is added with noise power $P_{\text{N}} = P_{\text{refl}} - \text{SNR}$ (dB). The signal power used in the calculation of SNR is the power of the reflected signal. Then, the range is estimated in 1,000 trials for every test data point (P_{tag}, SNR). Tag-received power and SNR are varied across the values

$$P_{\text{tag}} \in (-10, 5, \ldots, 14) \text{ dBm} \tag{164}$$

$$\text{SNR} \in (-20, -15, \ldots, 40) \text{ dB}. \tag{165}$$

The tag-received power set spans a realistic range that can feasibly be received by passive RFID tags [27]. Also, these values for tag-received power are the same as in the measurements in Section 6.2.

The two-stage charge pump LTspice model in Figure 57 uses the complete circuit model

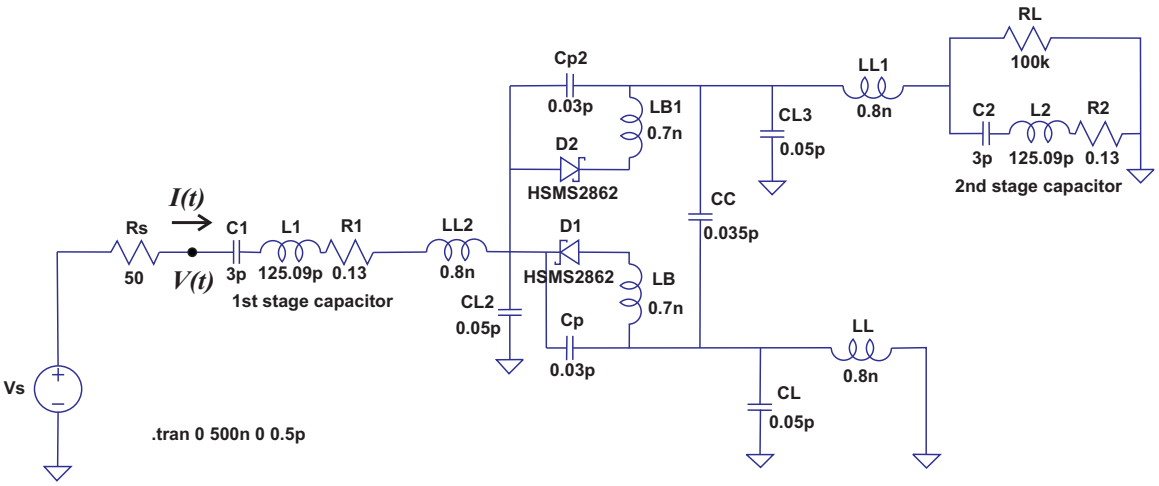

Figure 57: LTspice model of the tested two-stage charge pump with a 100 kΩ load resistance that models the passive tag DC load. The simulation computes the input waveform into the charge pump and the reflected waveform.

of the Avago HSMS-2862 diodes [39] to accurately model the diodes in the fabricated charge pump in the measurements presented in Section 6.2. The 50 Ω equivalent source models a 50 Ω tag feed structure. The input waveform to the tag (i.e. the waveform from which P_{tag} is calculated) and the reflected waveform are evaluated in the simulator as

$$y_{\text{tag}}(t) = \frac{1}{2}(V(t) + I(t)50\ (\Omega)) = \text{pow}(t)e^{j\omega t} \tag{166}$$

$$y_{\text{refl}}(t) = \frac{1}{2}(V(t) - I(t)50\ (\Omega)). \tag{167}$$

The source voltage pow(t) is created and imported into LTspice from the MATLAB simulator to target the tested charge pump input power P_{tag}. The resulting reflected waveform is then swept across the range of SNR to cover all test data points.

The simulations also test the effect of stage capacitance, load resistance, and number of stages. These charge pump parameters are swept across the following ranges:

$$\begin{aligned} C &\in (1, 1.5, 2, 2.5, 3)\ \text{pF} \\ R_{\text{L}} &\in (1, 10, 100, 1000)\ \text{k}\Omega \\ N &\in (2, 4, 6, 8)\ \text{stages.} \end{aligned} \tag{168}$$

The simulations for these typical and wide-ranging parameter values are compared to the bias model presented in Section 4.5. The RMS error, statistical correlation, and comparison

of the mean of the simulated biases with the predicted biases indicate the model's effectiveness. An RMS error less than half the mean simulated bias and a positive correlation greater than 0.5 indicates a good fit of the model to the simulations:

$$\frac{\mu_{\text{sim}}}{\sqrt{10}} < \mu_{\text{model}} < \sqrt{10}\mu_{\text{sim}} \tag{169}$$

$$\text{RMSE} < 0.5\mu_{\text{sim}} \tag{170}$$

$$\rho > 0.5. \tag{171}$$

The mean criterion was chosen to ensure the predictions of the model are within an order of magnitude of the simulated values. The model does not account for any parasitics, and a prediction approximate to the simulated value is considered satisfactory. The criterion for RMS error statistic is chosen to ensure the model predicted bias values close to the simulated bias values. The criterion for the correlation statistic was chosen to ensure the simulations closely follow the rising and falling trend of the predicted bias curve. Together, these statistics indicate how well the bias model fits the bias values from simulation.

5.4.2 Simulation Results

A simulation across the full range of SNR in (165) is carried out for each value of tag power tested. A graph of uncertainty and bias is made for each simulation point $(P_{\text{tag}}, \text{SNR})$ similar to the graphs in Figures 45 through 50. For example, Figure 58 shows the performance graphs for the simulation with $P_{\text{tag}} = 5$ dBm. The estimator uncertainty graph shows the same characteristic as the POW-shape simulations in the previous section. The CRLB and information limits bound the estimator uncertainty. All of the simulations on nonlinear reflections showed there is no difference in estimator uncertainty between a linear reflection and nonlinear reflection.

5.4.2.1 Bias vs. Tag Power

The bias graph of the estimator in Figure 58 shows a ranging bias of 3.26 cm. The model predicts a ranging bias of 2.48 cm using the same charge pump parameters, RMS bandwidth, and tag power. This simulated value and the predicted value for ranging bias are plotted in Figure 59 along with the simulated and predicted values under all values of tag power tested

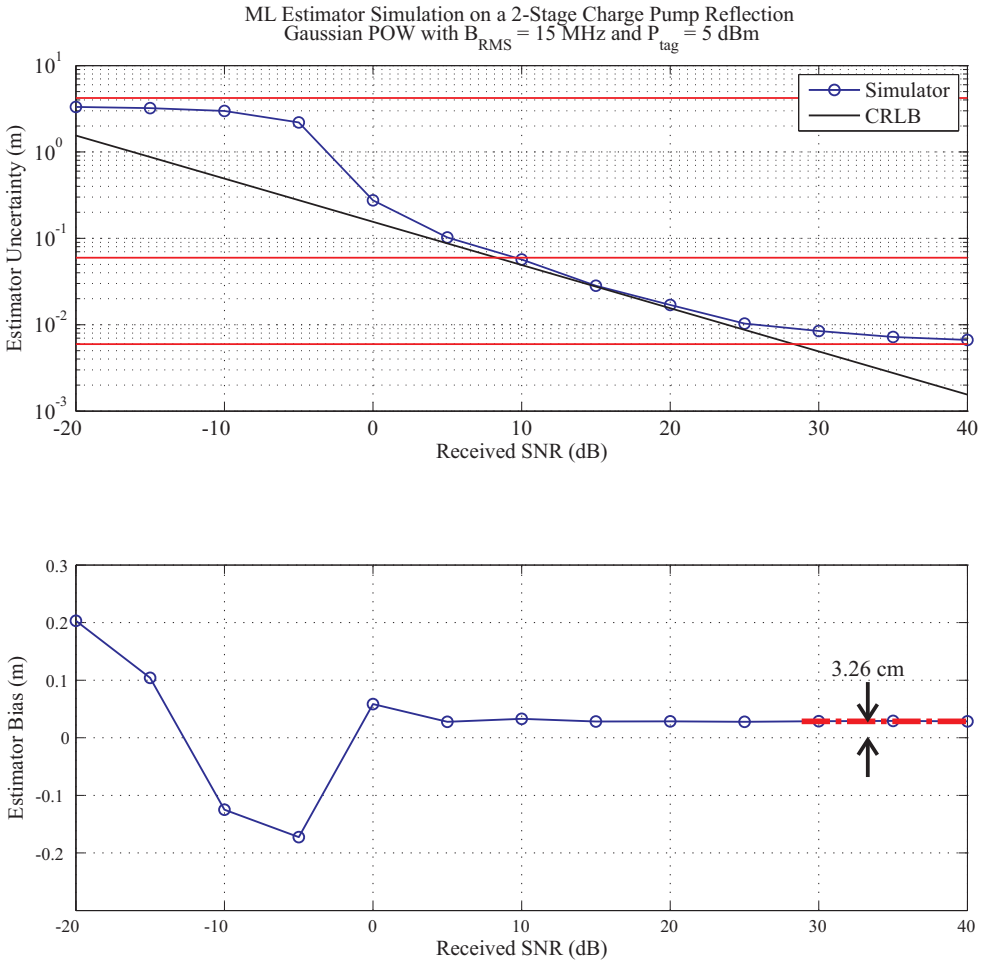

Figure 58: Typical simulated ranging performance on the 2-stage charge pump. The tag power is 5 dBm and the excitation is a Gaussian POW with $B_{\mathrm{RMS}} = 15$ MHz. The simulated ranging bias is 3.26 cm as shown.

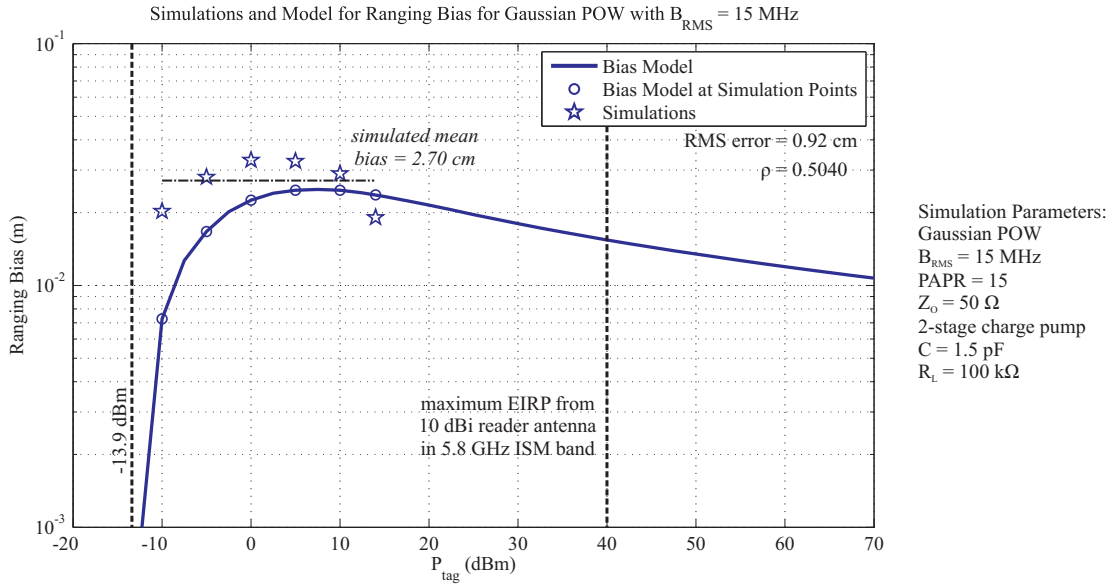

Figure 59: Simulated and predicted values for ranging bias with a 2-stage charge pump reflector. The model predicts the simulated values statistically well.

on the charge pump in Figure 57. The RMS error between the simulated and predicted biases is 0.92 cm, which is less than half of the mean of the simulated biases ($\mu = 2.70$ cm). Additionally, the correlation is 0.5040, and the mean of the simulated biases is within one order of magnitude of the predicted values. These statistics indicate a good fit of the model to the simulations.

5.4.2.2 Bias vs. Load Resistance

Figure 60 shows the simulated and predicted biases varied across charge pump load resistance. Each set of simulated and predicated biases are shown with the same color on the graph, and each has their own RMS error and correlation. Overall, the simulated data matches well with the model. Section 4.5.2 describes "sweet-spot" behavior where ranging bias is maximized for load resistance of nearly 10 kΩ. However, the simulations show that the 1 kΩ range estimation biases are nearly the same as the 10 kΩ biases. This behavior arises from discontinuous operation. In this mode, the charge pump output rises to the maximum output voltage from zero during the rise time of each POW pulse. Then, the

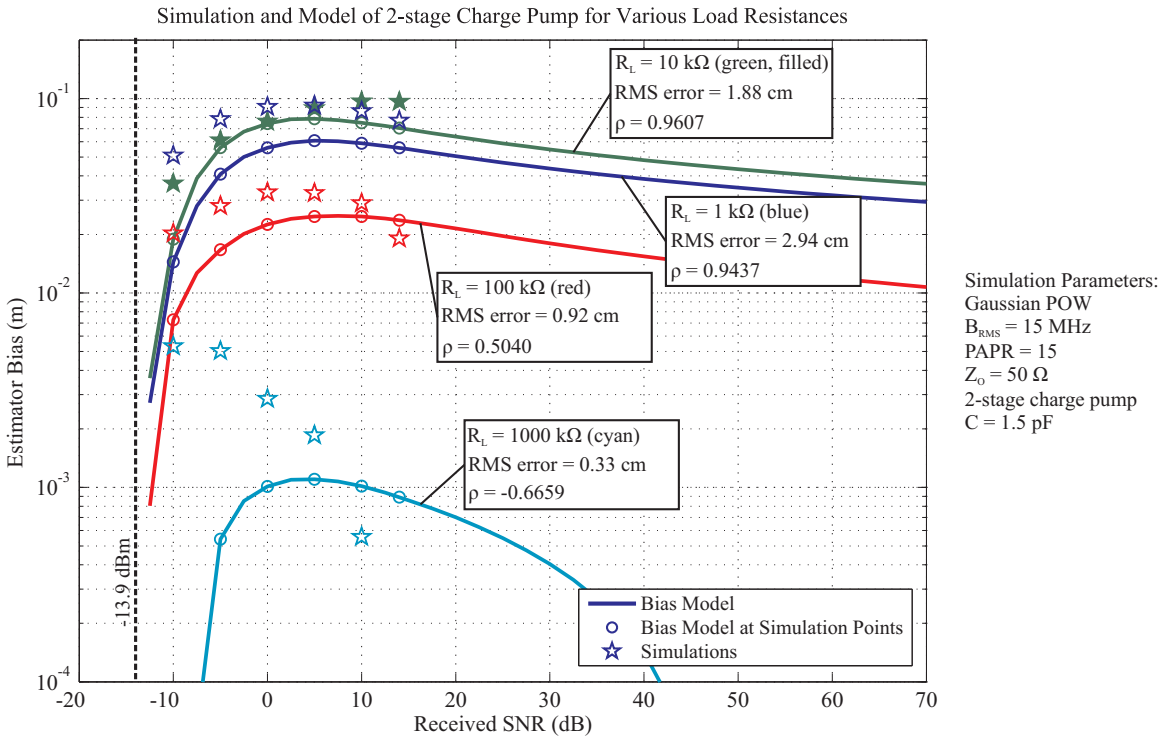

Figure 60: Simulated effect of load resistance on ranging bias. The model performs well for load resistances providing continuous steady-state operation of the charge pump.

charge pump output completely decays to zero during the starve time. Discontinuous operation draws the maximum possible current from the input source. Thus, the distortion is maximized. The model does not predict the discontinuous operation accurately.

The model accurately predicts the simulated ranging bias for the cases where $R_{\mathrm{L}} = 10$ kΩ and $R_{\mathrm{L}} = 100$ kΩ. The relevant first-order statistics for each of the load resistance simulations are:

1. $R_{\mathrm{L}} = 1$ kΩ: The average simulated ranging bias $\mu_{\mathrm{sim}} = 7.6$ cm, and the average predicted bias $\mu_{\mathrm{model}} = 4.77$ cm $= 0.63\mu_{\mathrm{sim}}$ is within the satisfactory range. The RMS error between the model and simulations is 2.94 cm, and the correlation is 0.9437. The model is accurate for this case according to the statistical criteria defined.

2. $R_{\mathrm{L}} = 10$ kΩ: The average simulated ranging bias $\mu_{\mathrm{sim}} = 7.92$ cm, and the average predicted bias $\mu_{\mathrm{model}} = 6.23$ cm $= 0.77\mu_{\mathrm{sim}}$ is within the satisfactory range. The RMS error between the model and simulations is 1.88 cm, and the correlation is 0.9607. The model predicts accurately for this case according to the statistical criteria defined.

3. $R_{\mathrm{L}} = 100$ kΩ: The average simulated ranging bias $\mu_{\mathrm{sim}} = 2.70$ cm, and the average predicted bias $\mu_{\mathrm{model}} = 1.99$ cm $= 0.74\mu_{\mathrm{sim}}$ is within the satisfactory range. The RMS error between the model and simulations is 0.92 cm, and the correlation is 0.5040. The model predicts accurate values for this case according to the statistical criteria defined.

4. $R_{\mathrm{L}} = 1000$ kΩ: The average simulated ranging bias $\mu_{\mathrm{sim}} = 2.40$ mm, and the average predicted bias $\mu_{\mathrm{model}} = 0.67$ mm $= 0.28\mu_{\mathrm{sim}}$ is within the satisfactory range. The RMS error between the model and simulations is 3.3 mm, and the correlation is -0.6659. These values are unsatisfactory. Therefore, the model is inaccurate in predicting the simulated values according to the statistical criteria defined.

The last test case where the load resistance is 1000 kΩ simulates a near-open-circuit load. Here, the discharging of the charge pump output capacitor due to parasitics is comparable to the discharging due to the load resistor. The charge lost due to parasitics is not accounted for in the model even though very little charge is lost during the starve time of the POW in this case. The model is inaccurate here, so a designer may choose to simulate the ranging bias manually in a circuit simulator.

5.4.2.3 Bias vs. Number of Charge Pump Stages

The model predicts the simulated biases well for a 2-stage charge pump. However, parasitics induce significant phase delay between the impinging and reflected waveforms that the model does not account for. Figure 60 shows the large disparity between the simulations and the model for charge pumps with 4, 6, and 8 stages. The first-order statistical evaluation of the model's accuracy indicates a poor fit of the model for the higher number of stages.

The model fails to predict the simulated biases accurately since the parasitics are not taken into account. In Section 4.5, the output voltage equation (136) neglects parasitic components and assumes that the charge pump behaves mostly as an open circuit. Thus, the input voltage to the charge pump is assumed to have twice the maximum voltage of the forward-propagating waveform $V^{+}(t)$. However, the parasitics of the charge pump modeled in Figure 57 present an imaginary impedance that perturbs the reflected signal out of phase with the impinging signal. Assuming a tag power of 10 dBm, the parasitics of

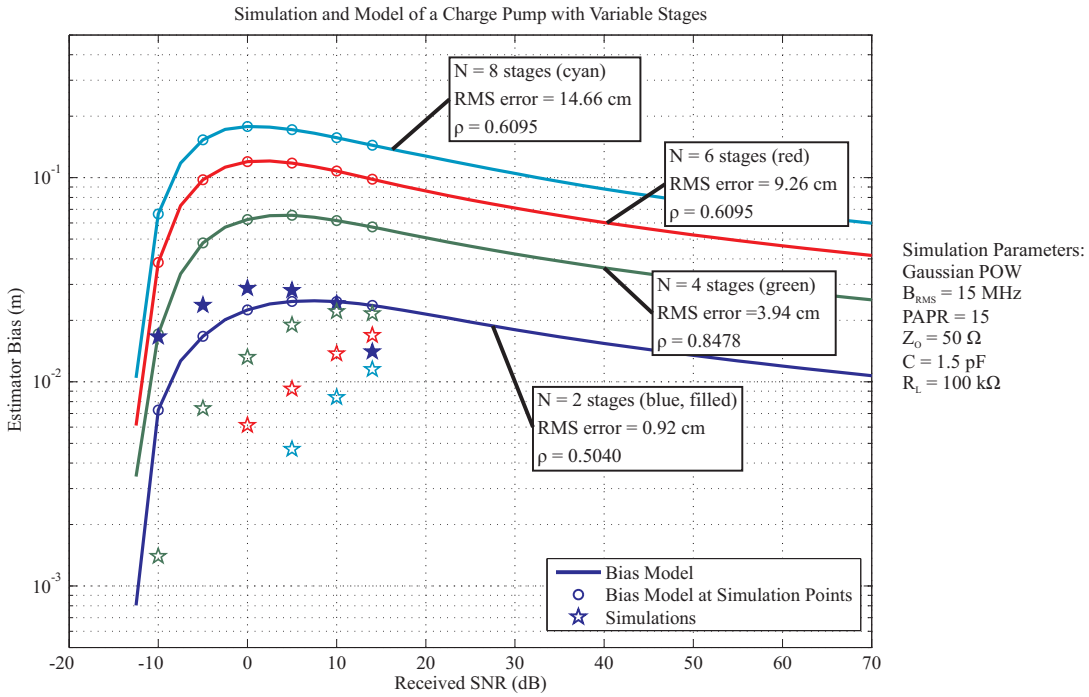

Figure 61: Simulated effect of the number of charge pump stages on ranging bias. Parasitics create a phase difference between the impinging and reflected waveforms, which lowers the input current and total distortion. This phase difference is not accounted for in the model.

the 2-stage charge pump in Figure 57 delays the reflected signal by approximately 79° from the impinging signal. Thus, the output equation overshoots the simulated output voltage. A 4-stage charge pump with the same parasitics on each stage delay the reflected signal by 122°. Both the 6-stage and 8-stage charge pumps presents a 166° delay. The 6-stage and 8-stage charge pumps present an approximate short-circuit to the impinging waveform. Simulations of a 10-stage charge pump show the delay is 167°. Adding stages increased the phase delay up to a maximum of 167°. A matching circuit could possibly bring this phase difference closer to zero and improve the accuracy of the model.

5.4.2.4 Bias vs. Stage Capacitance

The simulation results in Figure 62 show an increasing bias as stage capacitance is increased. The model predicts this relationship accurately but does not show a strong positive correlation with the simulated results in three of the five test cases in the figure. Each computed

RMS error is within 1/2 of the mean of the simulated results. Also, the mean of the predicted biases are within one order of magnitude of the simulated biases. The limiting behavior as capacitance increases is shown in these simulations. The simulationed biases for the cases where C =2, 2.5, and 3 pF are nearly the same, and the corresponding predicted biases are approaching the limit described in Section 4.5.2.

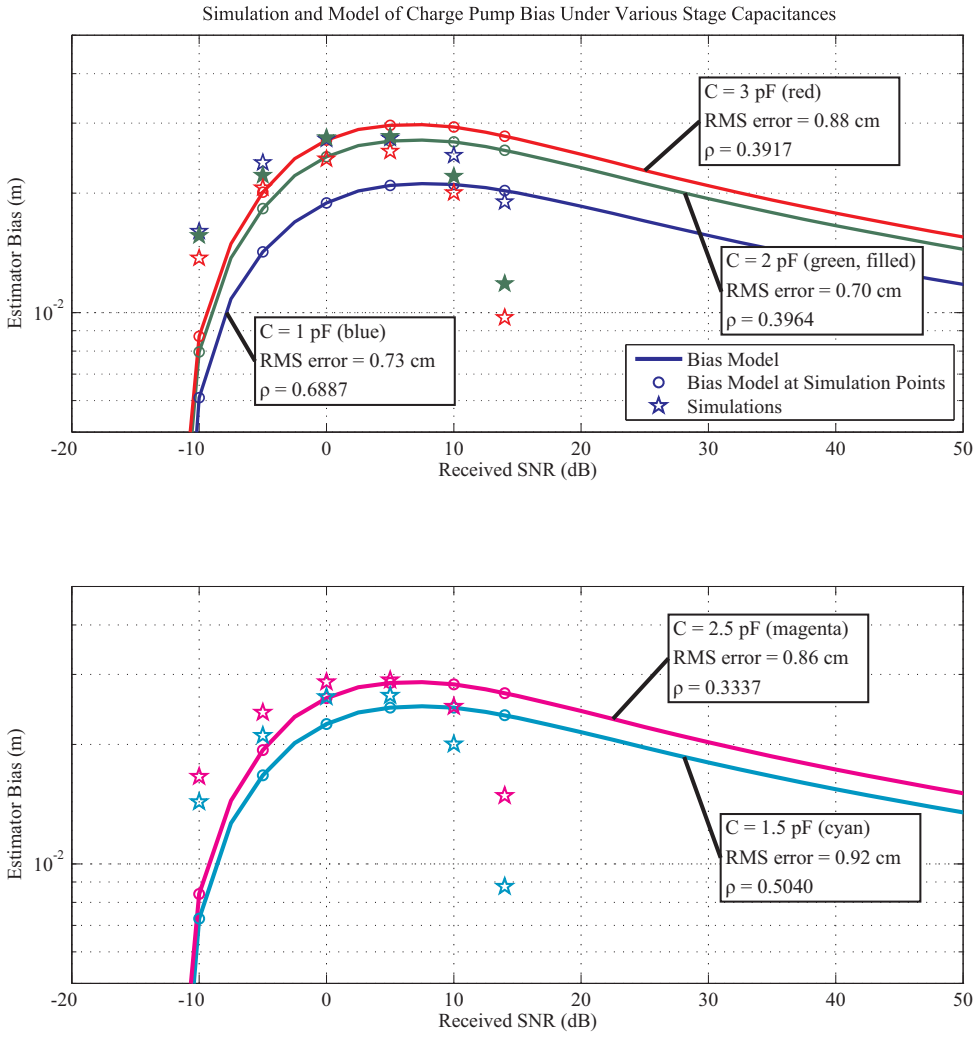

Figure 62: Simulated effect of the stage capacitance on ranging bias. Ranging bias increases with capacitance due to the extra charge required to fill the larger capacitors. The results are split into two figures for clarity.

CHAPTER VI

MEASUREMENTS OF POW RANGING

Two formal experiments measure the effects on range estimation performance of POW shape and nonlinear reflections. Appendix A describes the testbed in detail, and the following sections present the procedure and results for testing POW shape and nonlinear reflections. The last section presents a demonstration of ranging in two frequency-selective environments.

6.1 Test #1: Survey of Power Optimized Waveform Shapes

This experiment measures the effect of POW shape on ranging uncertainty and bias of a ML range estimator. The same POW shapes and parameters from Table 6 in Section 5.1 are tested in a transmission-line environment where the received SNR can be controlled. Clutter and nonlinear reflections are purposely eliminated from this experiment so that POW shape can be tested independently. A 50 Ω transmission line with SMA attachments is terminated with a short-circuit load. The physical length measured from one end of the teflon substrate (dielectric constant $\epsilon_{\mathrm{r}} = 2.1$) to the other end is $r_{\mathrm{true}} = 3.6576$ m (12 feet), and the velocity of propagation within the transmission line is $v_p = 2.0688 \cdot 10^8$ m/s. Thus, the true round-trip time delay is $\tau_{\mathrm{true}} = 35.360$ ns.

6.1.1 Experimental Setup

Figure 63 shows the experimental setup. The POW transceiver is connected to a variable attenuator and to the shorted transmission line environment. The variable attenuator is placed in-line with the receive chain of the POW transceiver to simulate the double path loss of a backscatter channel. The oscilloscope samples the received signal triggered by the function generator. Then, the received signal is upconverted by a factor of 10 from the original sampling frequency of 500 MHz. Refer to appendix A for a detailed description of the testbed and calibration procedure.

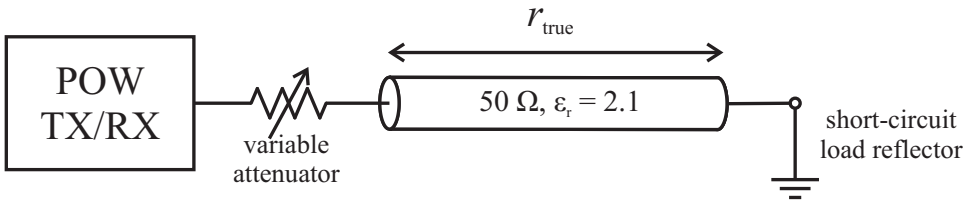

Figure 63: The experimental setup for testing ranging performance vs. POW shape. The POW is transmitted into a transmission-line environment through a variable attenuator, which controls the received SNR.

The attenuation is varied in 2.5 dB steps so that the received SNR is swept between -20 dB and 40 dB at in 5-dB steps. The highest measured received SNR varies with respect to the POW shape. One thousand range estimations are taken for each SNR value for each POW shape tested. One thousand estimations is a sufficient amount of estimations as evidenced by the similar simulation results in Section 5.1. The ranging uncertainty and bias are graphed vs. received SNR and compared to the CRLB.

6.1.2 Measurement Results

Figures 64, 65, and 66 show the measured ranging uncertainty and bias for the three tested Gaussian POWs. Figures 67, 68, and 69 show the results for the three tested Square POWs. Each of the measurement results are plotted with the CRLB and the information limits.

Please note the erroneous measurement in Figure 64 at a measured SNR of -1.2 dB. It is not known what exactly is the cause of this error. This measurement point (and each measurement point) takes approximately 30 minutes to measure. The received SNR is estimated when the experimentor is in the room at the start of each measurement. Then, the system is left to run autonomously. It is assumed that the experimental hardware was somehow disrupted without the experimenter's knowledge while measuring this particular data point. The measured uncertainty and bias at this point indicate that the true received SNR is -20 dB or less even though the estimated received SNR is -1.2 dB.

The upper, middle, and lower information limits derived in Section 4.3.4 are the same for each graph. The estimator has a-priori knowledge of the minimum and maximum limits for target range but does not receive any useful information from the received signal when the noise overpowers the signal. On the other hand, the estimator receives maximum

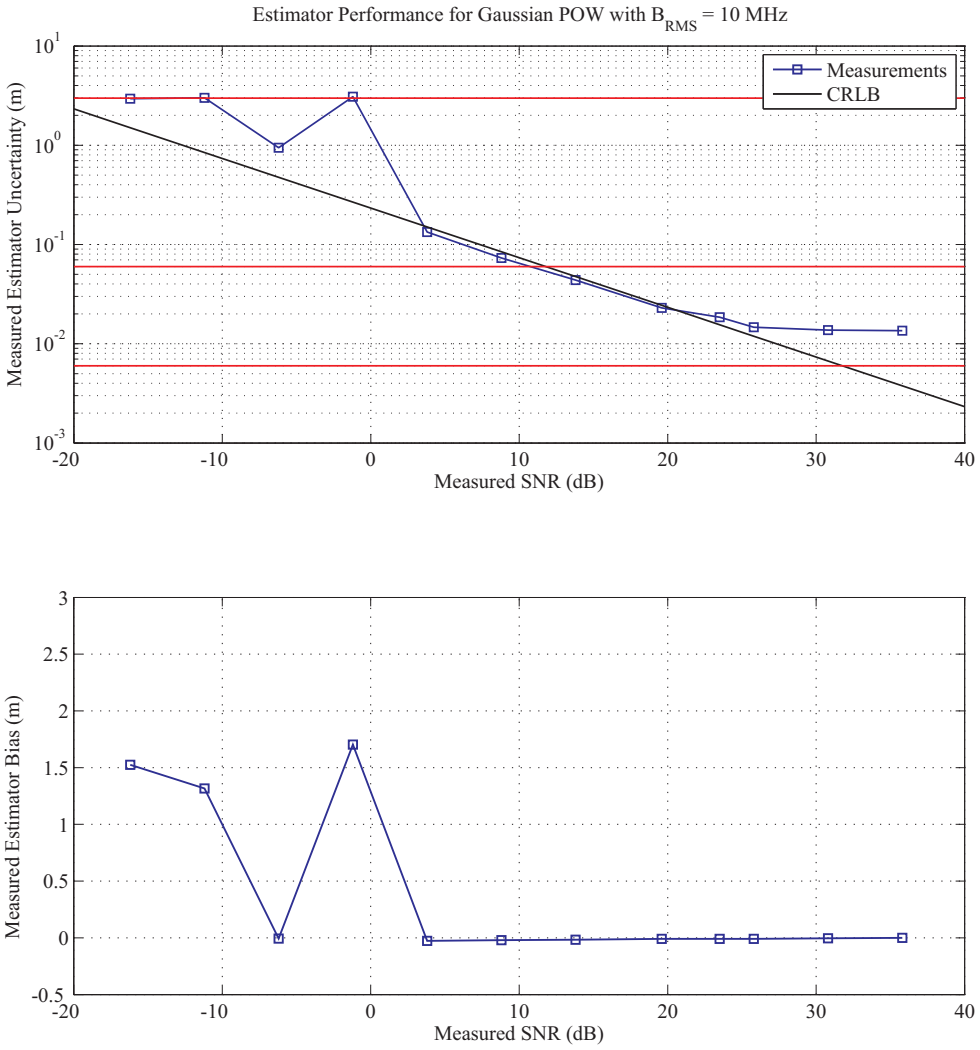

Figure 64: Measured performance of a maximum likelihood estimator using a Gaussian POW with $B_{\mathrm{RMS}} = 10$ MHz on a linear reflection. Uncertainty is limited by the upper and lower information bounds, and the bias plot shows the estimator is unbiased.

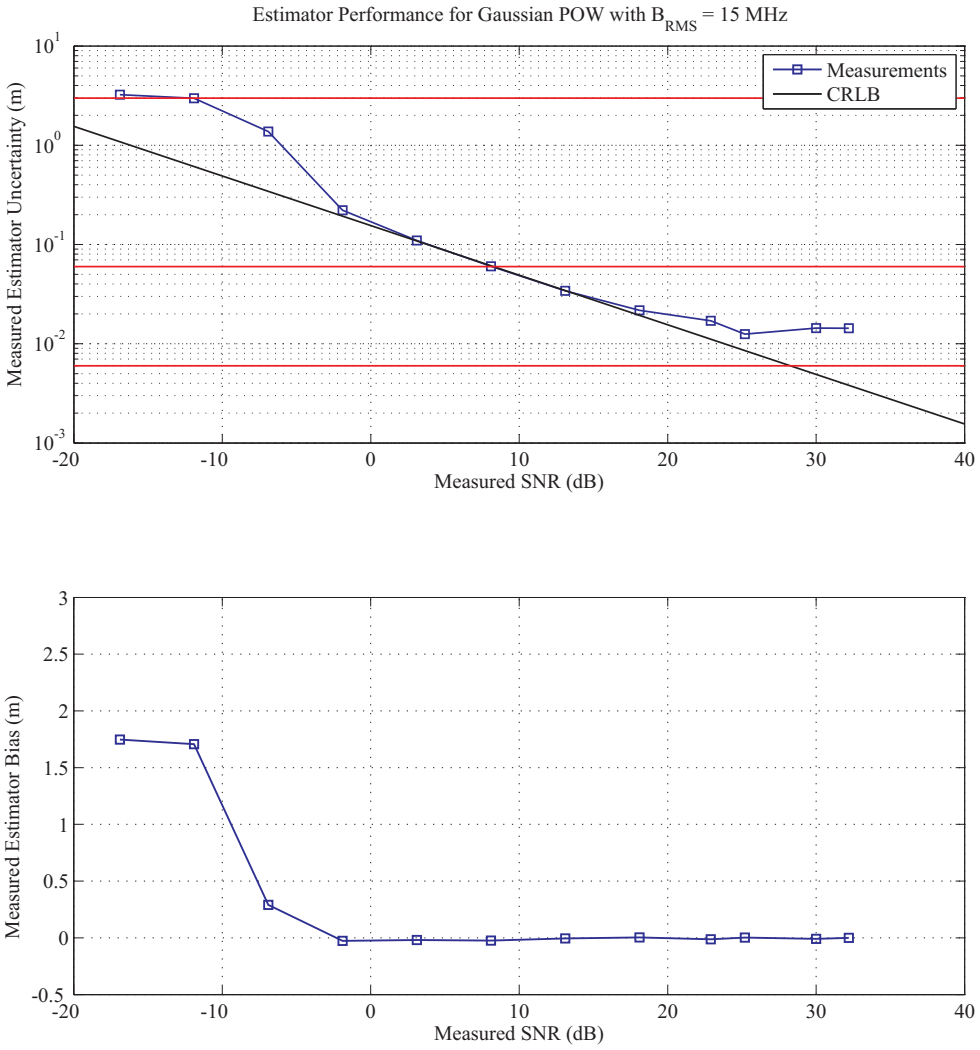

Figure 65: Measured performance of a maximum likelihood estimator using a Gaussian POW with $B_{\text{RMS}} = 15$ MHz on a linear reflection. Uncertainty is limited by the upper and lower information bounds, and the bias plot shows the estimator is unbiased.

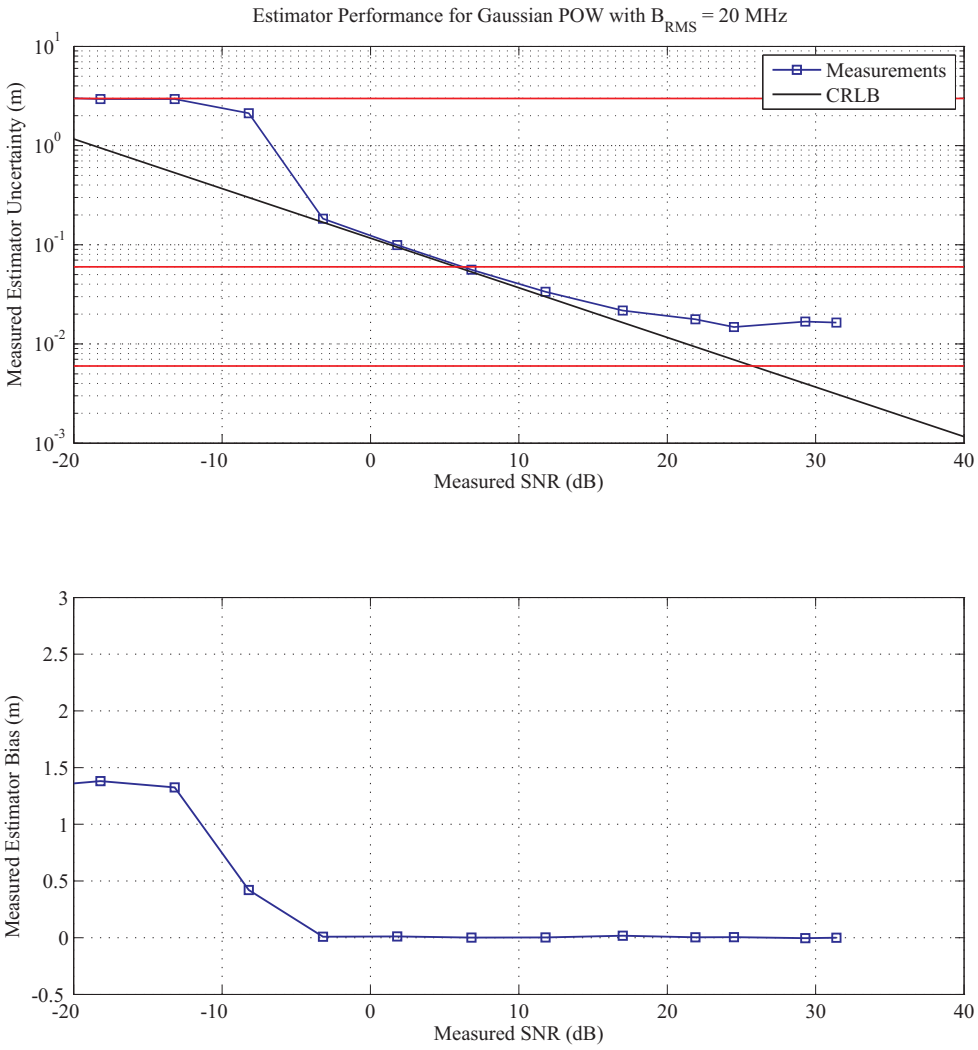

Figure 66: Measured performance of a maximum likelihood estimator using a Gaussian POW with $B_{\text{RMS}} = 20$ MHz on a linear reflection. Uncertainty is limited by the upper and lower information bounds, and the bias plot shows the estimator is unbiased.

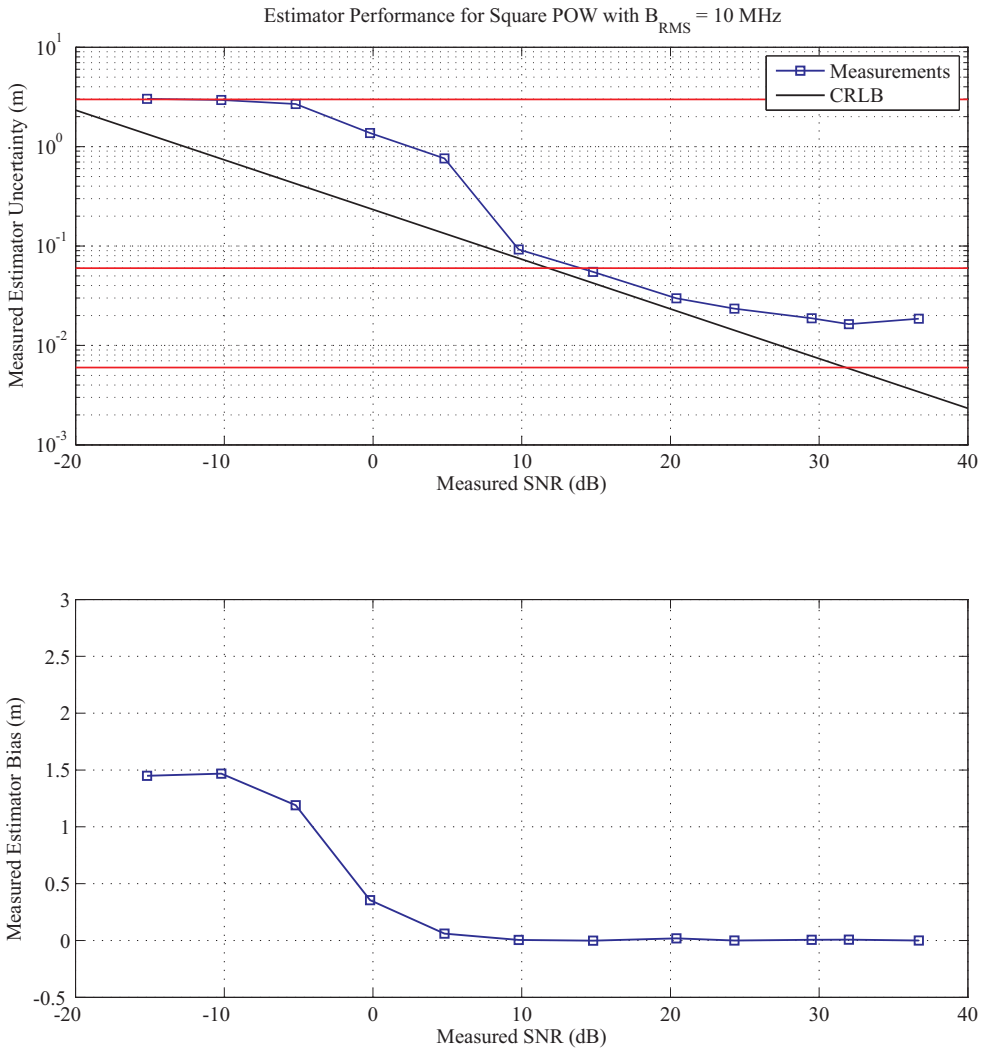

Figure 67: Measured performance of a maximum likelihood estimator using a Square POW with $B_{\text{RMS}} = 10$ MHz on a linear reflection. Uncertainty is limited by the upper and lower information bounds, and the bias plot shows the estimator is unbiased.

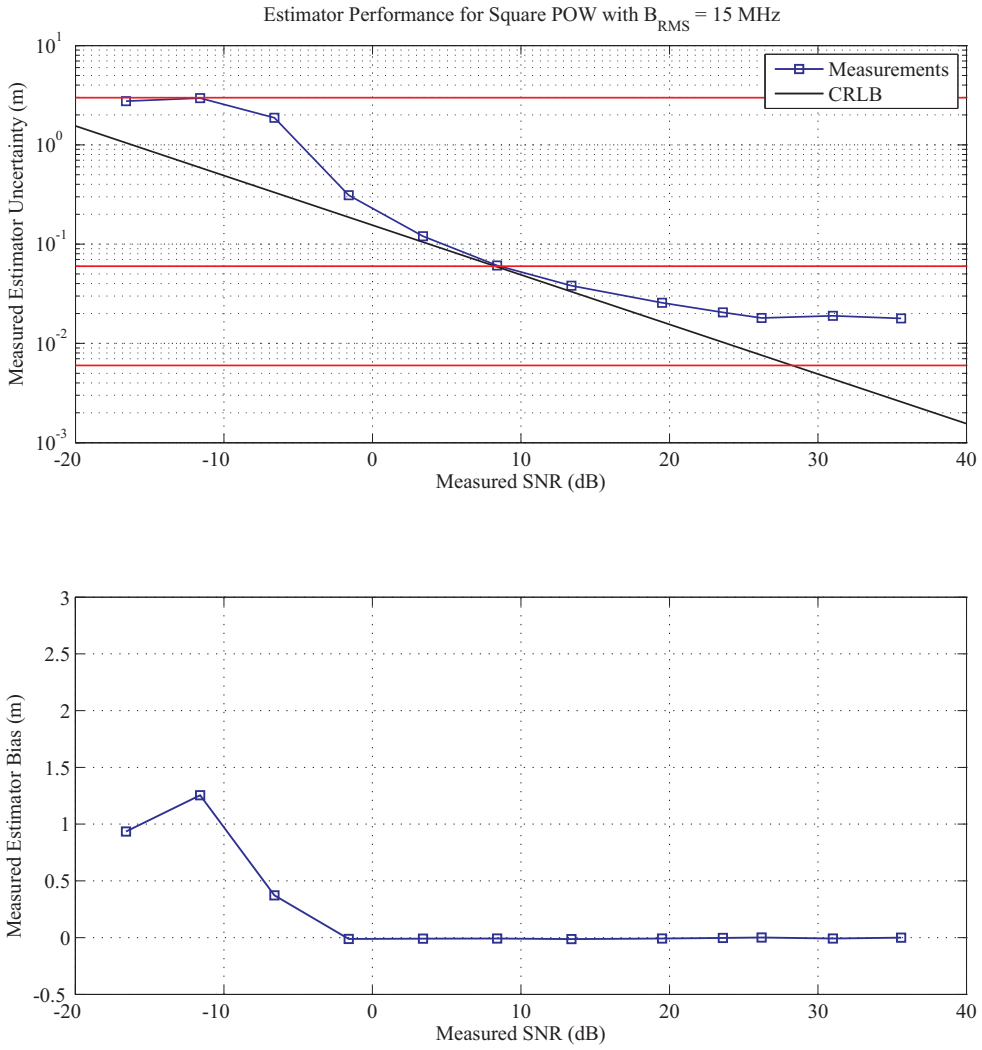

Figure 68: Measured performance of a maximum likelihood estimator using a Square POW with $B_{\text{RMS}} = 15$ MHz on a linear reflection. Uncertainty is limited by the upper and lower information bounds, and the bias plot shows the estimator is unbiased.

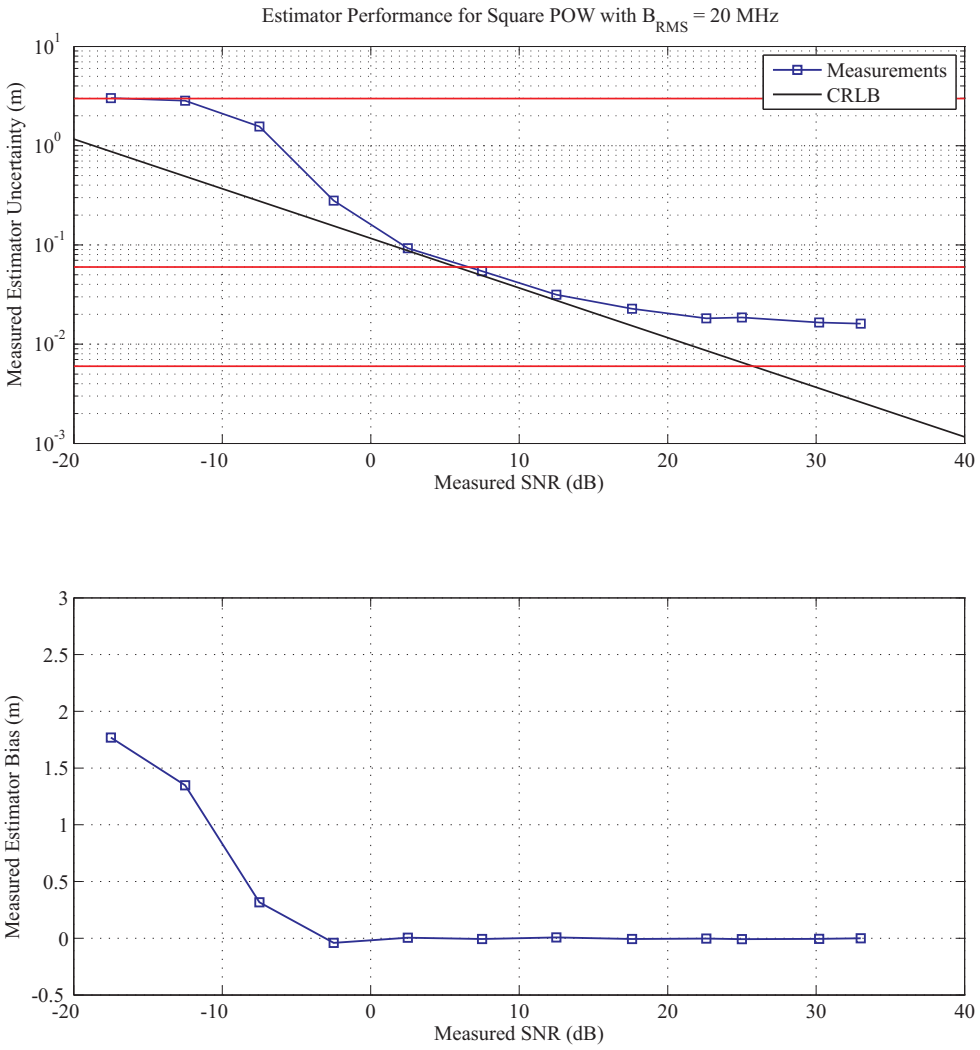

Figure 69: Measured performance of a maximum likelihood estimator using a Square POW with $B_{\text{RMS}} = 20$ MHz on a linear reflection. Uncertainty is limited by the upper and lower information bounds, and the bias plot shows the estimator is unbiased.

information when the signal significantly overpowers the noise at high SNRs. The estimator is then limited to range-bin uncertainty. The upper, middle, and lower information limits for each of these measurements are

$$\sigma_{\text{up}} = \sqrt{\text{Var}\left(\mathcal{U}\left(0, \frac{1}{2}v_{\text{p}}T_{\text{POW}}\right)\right)} = \frac{v_{\text{p}}T_{\text{POW}}}{2\sqrt{12}} = 2.986 \text{ m} \quad (172)$$

$$\sigma_{\text{mid}} = \sqrt{\text{Var}\left(\mathcal{U}(0, v_{\text{p}}T_{\text{s}})\right)} = \frac{v_{\text{p}}}{2\sqrt{12}f_{\text{s}}} = 5.97 \text{ cm} \quad (173)$$

$$\sigma_{\text{low}} = \sqrt{\text{Var}\left(\mathcal{U}(0, v_{\text{p}}T_{\text{s}})\right)} = \frac{v_{\text{p}}}{2\sqrt{12}(10f_{\text{s}})} = 0.597 \text{ cm} \quad (174)$$

These limits are plotted on the uncertainty graphs in Figures 64 through 69. The measured results adhere to the upper information limit but tail off slightly before the lower information limit is reached. This is likely due to the added uncertainty from the trigger, which is not simulated in Chapter 5.

The measured bias graphs show unbiased operation (i.e. perfect accuracy) at high SNRs. The estimator in each graph diverges to a bias between 1 and 3 m at negative SNRs. Here, the estimator randomly guesses range uniformly between 0 and $\lambda_{\text{POW}}/2$. Thus, the estimator's average estimate is $\lambda_{\text{POW}}/4$ or 5.172 m in the PTFE test cable when noise overpowers the signal. The true range is 3.6576 m, and the estimator should diverge to a bias of the difference between the estimator mean and the true range, or 1.514 m. Not enough measurement data was taken to confirm that the estimator diverged to 1.514 m at negative SNRs. However, all the graphs show a positive deviation from the true range in the area of 1.514 m.

6.2 Test #2: Ranging Performance vs. Charge Pump Reflections

Ranging performance on a charge pump reflector is tested against two independent variables: the amount of power impinging onto the charge pump, which represents the power received by a passive tag P_{tag}, and the received SNR after backscattering. These two parameters are independently controlled using separate variable attenuators in the transmitter chain and receive chain of the POW transceiver.

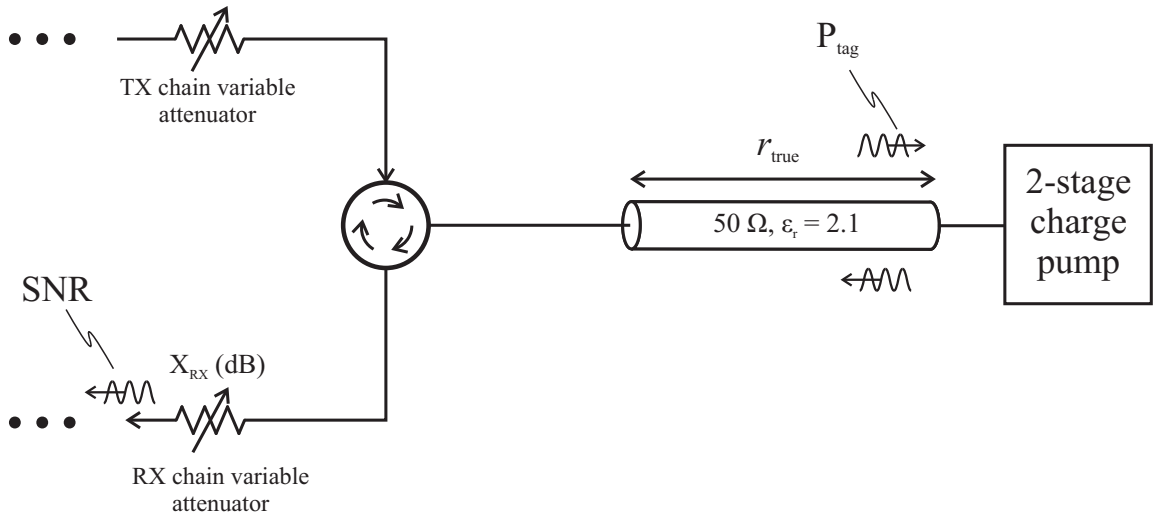

Figure 70: The experimental setup for testing ranging performance vs. nonlinear reflections. The incident power onto the 2-stage charge pump is controlled with the variable attenuator in the TX-chain, and the received SNR is controlled by the variable attenuator in the RX chain.

6.2.1 Experimental Setup

Figure 70 shows the experimental setup is similar to the POW shape experiments. The same 3.6576 m (12-foot) transmission line cable from the POW shape experiment is used.

The tag power and receive-chain attenuation are swept across the values

$$\begin{aligned} P_{\text{tag}} &\in \{-10, -5, 0, 5, 10, 14\} \text{ dBm}, \\ X_{\text{RX}} &\in \{0, 10, 20, \ldots, 70\} \text{ dB}. \end{aligned} \tag{175}$$

The first measurement point is ($P_{\text{tag}} = 14$ dBm, $X_{\text{RX}} = 0$ dB). From this measurement point, the receive-chain attenuation is iterated from 0 dB to 70 dB in 10 dB increments. Then, the tag power is attenuated down to the next value in the list. From here, the receive-chain attenuator is iterated through 0 dB to 70 dB again. The received SNR is greater than 10 dB for $X_{\text{RX}} = 0$ dB in all of the measurements. Therefore, received SNR can be accurately measured using the oscilloscope. The received SNR is measured with the oscilloscope for SNRs greater than 10 dB and dead-reckoned for SNRs less than 10 dB. More specifically, dead-reckoning decrements the received SNR by 10 dB from the previous received SNR value regardless of the current oscilloscope's SNR estimate.

A short-circuit load is measured along side the charge pump load for comparison. Any

ranging bias exhibited by the charge pump during range measurements will be evident when compared to the short-circuit range measurements. Figure 71 shows the circuits used for the measurements. The two-stage charge pump has a 50 Ω microstrip feed, 1.5 pF stage capacitors, a 100 kΩ load resistor, and Avago HSMS2862 Schottky diodes [39] with a threshold voltage of 0.35 V. The SMA connectors in the figure attach to the end of the 12-foot SMA cable. The microstrip leading from the SMA connectors to the load (either short, 50 Ω, or charge pump) adds an extra length of 1.25 cm, which corresponds to an extra roundtrip delay of 0.17 ns in the FR4 substrate ($\epsilon_{\mathrm{r}} = 4.2$). The microstrip appears to the estimator as 3.57 cm extra length in the PTFE substrate ($\epsilon_{\mathrm{r}} = 2.1$) of the cable. Thus, the 12.00 foot (3.658 m) cable used in the previous measurements of POW shape appears as a 12.12 foot (3.693 m) cable. This extra length was accounted for in the calculations of estimator bias.

Measured ranging bias is computed as the difference between the mean measured ranges from the short-circuit and the charge pump measurements at the two highest tested SNR values:

$$\begin{aligned} r_{\mathrm{bias}} &= \bar{r}_{\mathrm{CP}} - \bar{r}_{\mathrm{sh}} \\ \text{where } \bar{r}_{\mathrm{sh}} &= \frac{r_{\mathrm{sh}}(\mathrm{SNR}_1) + r_{\mathrm{sh}}(\mathrm{SNR}_2)}{2} \\ \text{where } \bar{r}_{\mathrm{CP}} &= \frac{r_{\mathrm{CP}}(\mathrm{SNR}_1) + r_{\mathrm{CP}}(\mathrm{SNR}_2)}{2} \end{aligned} \tag{176}$$

The averaging of 1,000 iterations at the two highest measured SNR values for each tested value of P_{tag} makes measurement noise negligible. Thus, only the nonlinear reflection effect will contribute to any range bias measured.

6.2.2 Measurement Results

The bias and uncertainty of the ML estimator are plotted in Figures 72 ($P_{\mathrm{tag}} = 14$ dBm) through 77 ($P_{\mathrm{tag}} = -10$ dBm). In the top graph, the measured estimation uncertainty is compared to the CRLB, upper information limit, and lower information limit. The bias is plotted versus received SNR in the bottom graph.

The measured results of uncertainty show a strong adherence to the CRLB for both

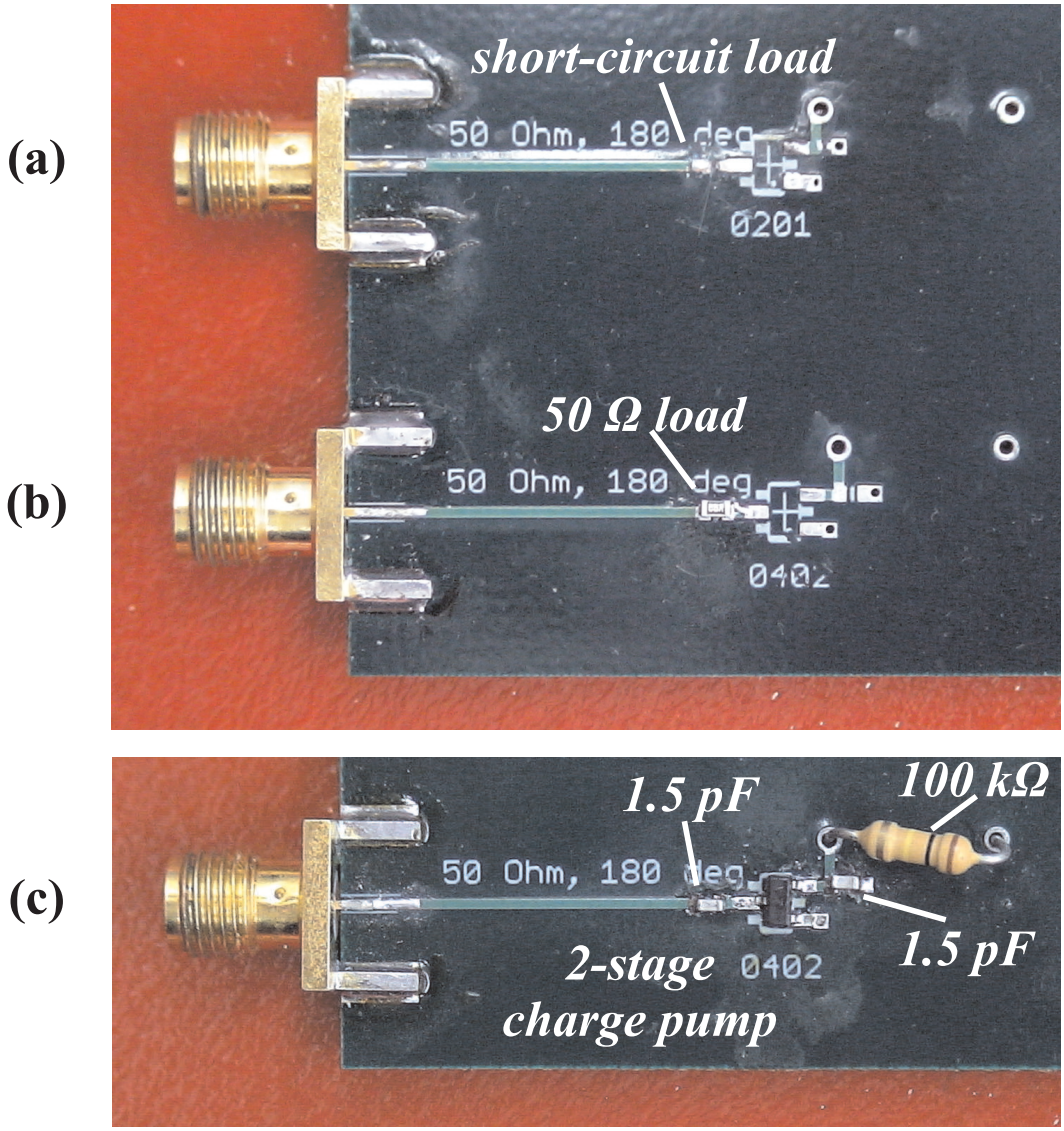

Figure 71: Test circuits used for ranging measurements: (a) The short-circuit load used as a linear reflector. (b) The 50 Ω load used for background measurements. (c) The two-stage charge pump load used as the nonlinear reflector.

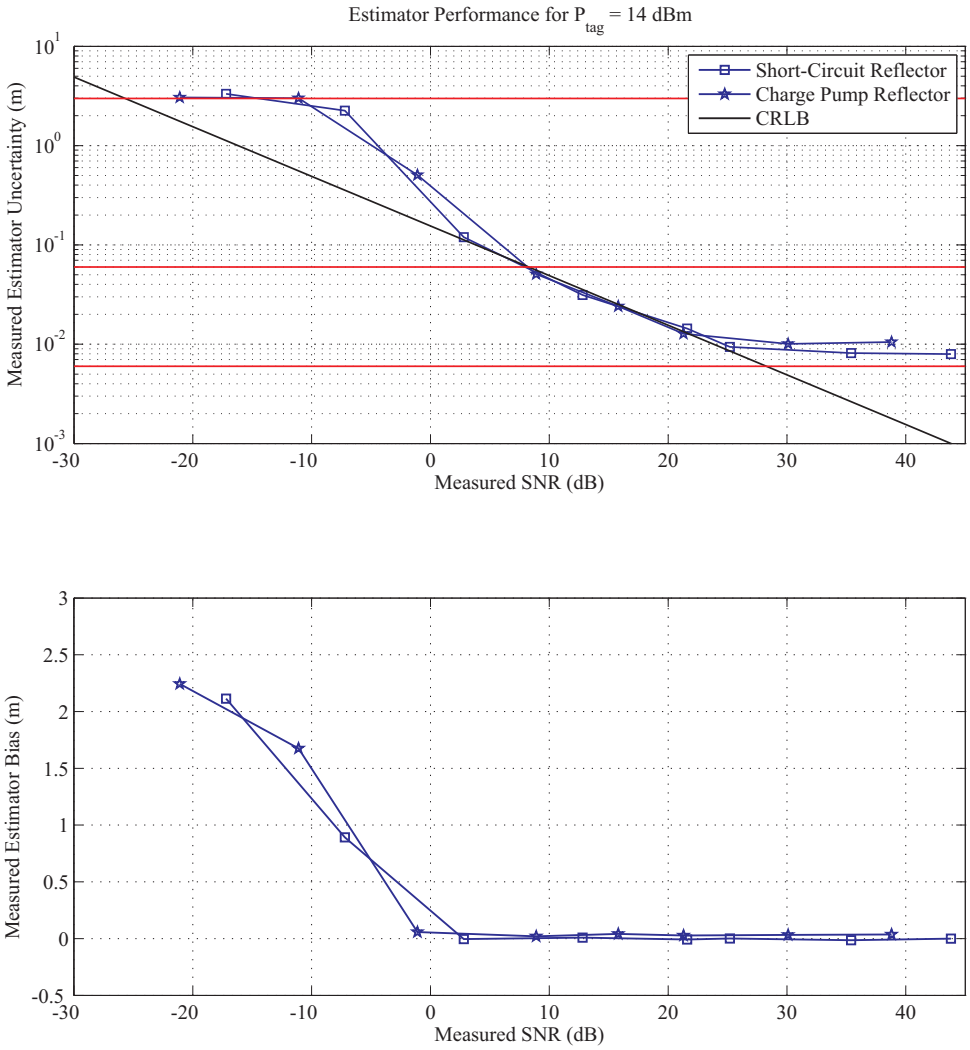

Figure 72: Measured performance of a maximum likelihood estimator using a Gaussian POW with $B_{\text{RMS}} = 15$ MHz on a 2-stage charge pump. The tag power is 14 dBm. The measured ranging bias added by the charge pump is 4.12 cm.

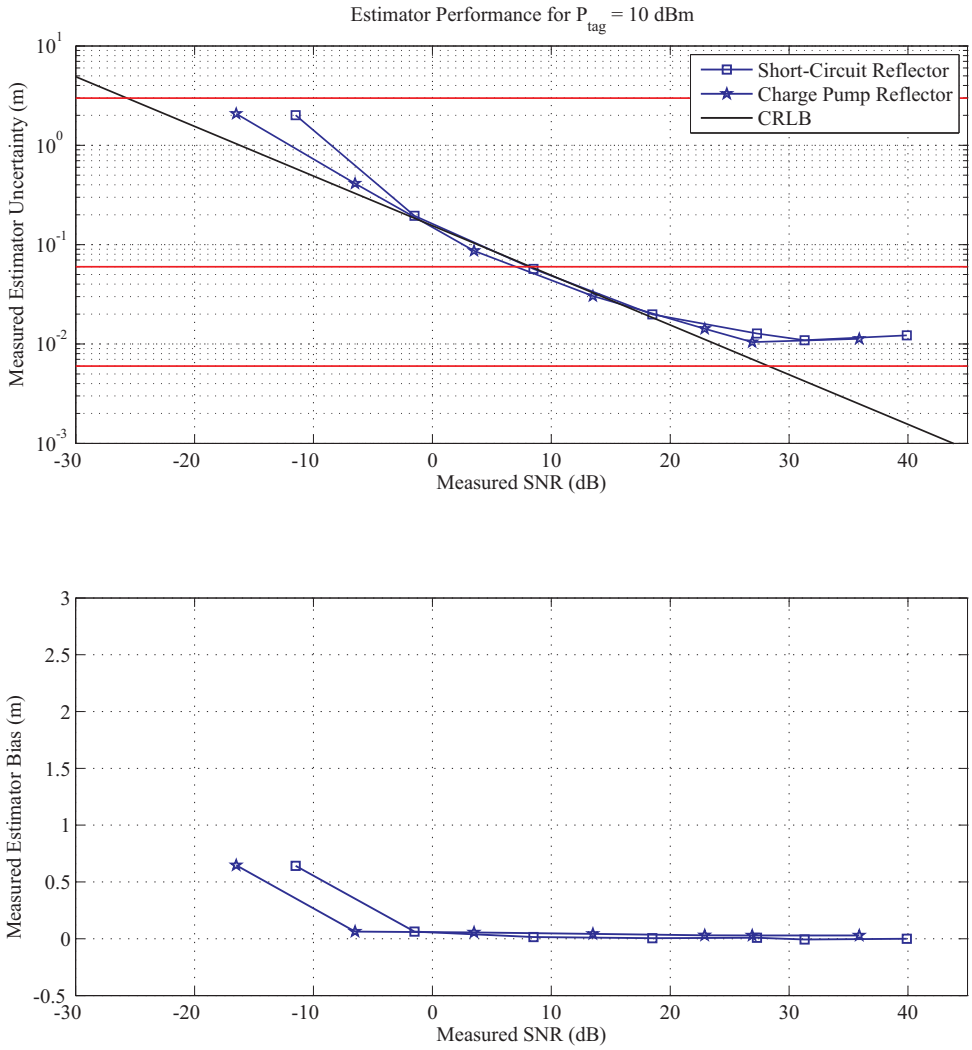

Figure 73: Measured performance of a maximum likelihood estimator using a Gaussian POW with $B_{\text{RMS}} = 15$ MHz on a 2-stage charge pump. The tag power is 10 dBm. The measured ranging bias added by the charge pump is 3.25 cm.

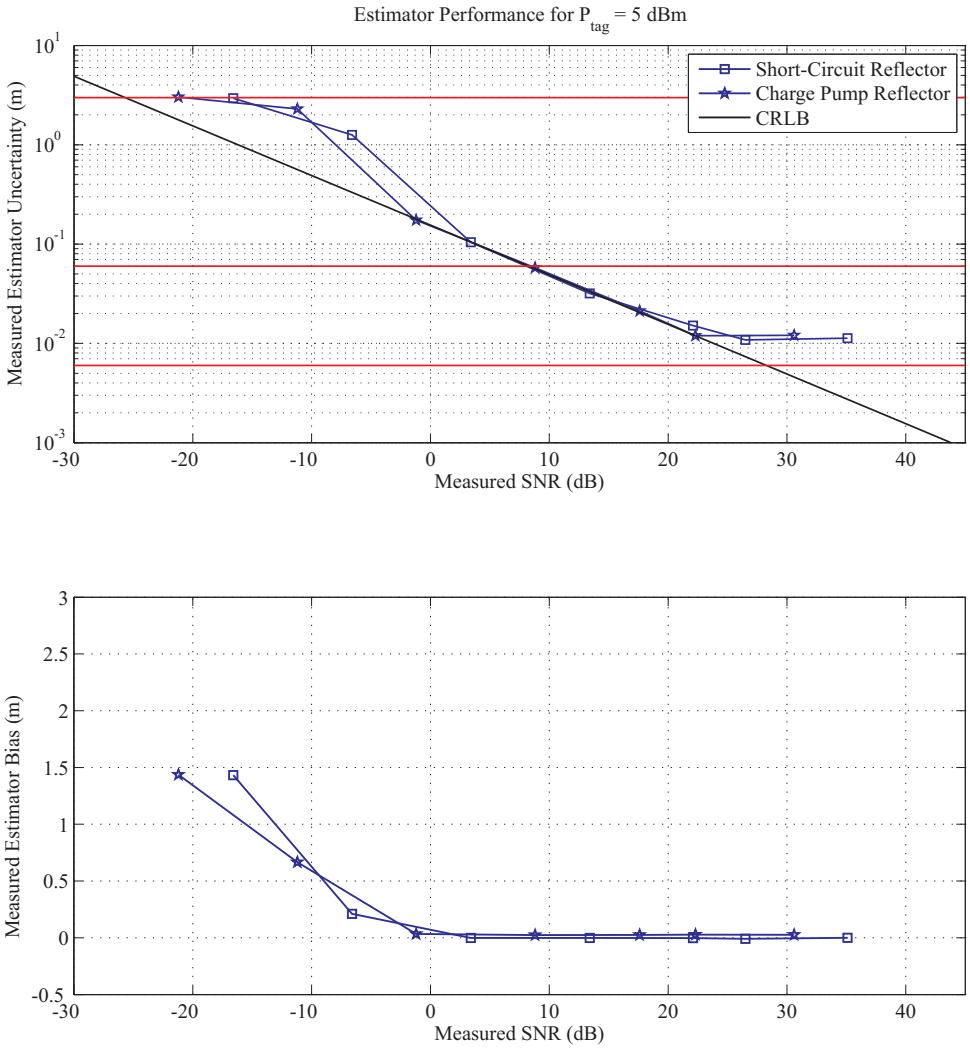

Figure 74: Measured performance of a maximum likelihood estimator using a Gaussian POW with $B_{\text{RMS}} = 15$ MHz on a 2-stage charge pump. The tag power is 5 dBm. The measured ranging bias added by the charge pump is 3.14 cm.

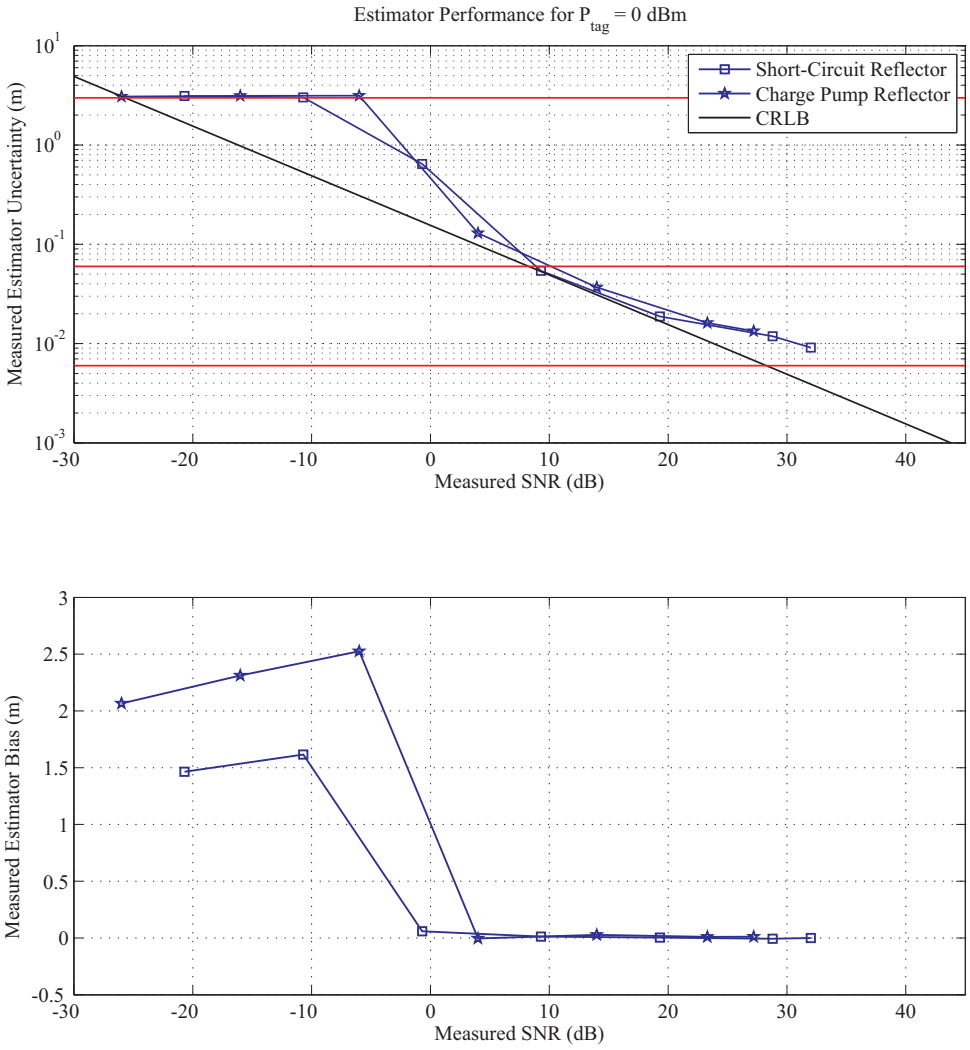

Figure 75: Measured performance of a maximum likelihood estimator using a Gaussian POW with $B_{\text{RMS}} = 15$ MHz on a 2-stage charge pump. The tag power is 0 dBm. The measured ranging bias added by the charge pump is 1.39 cm.

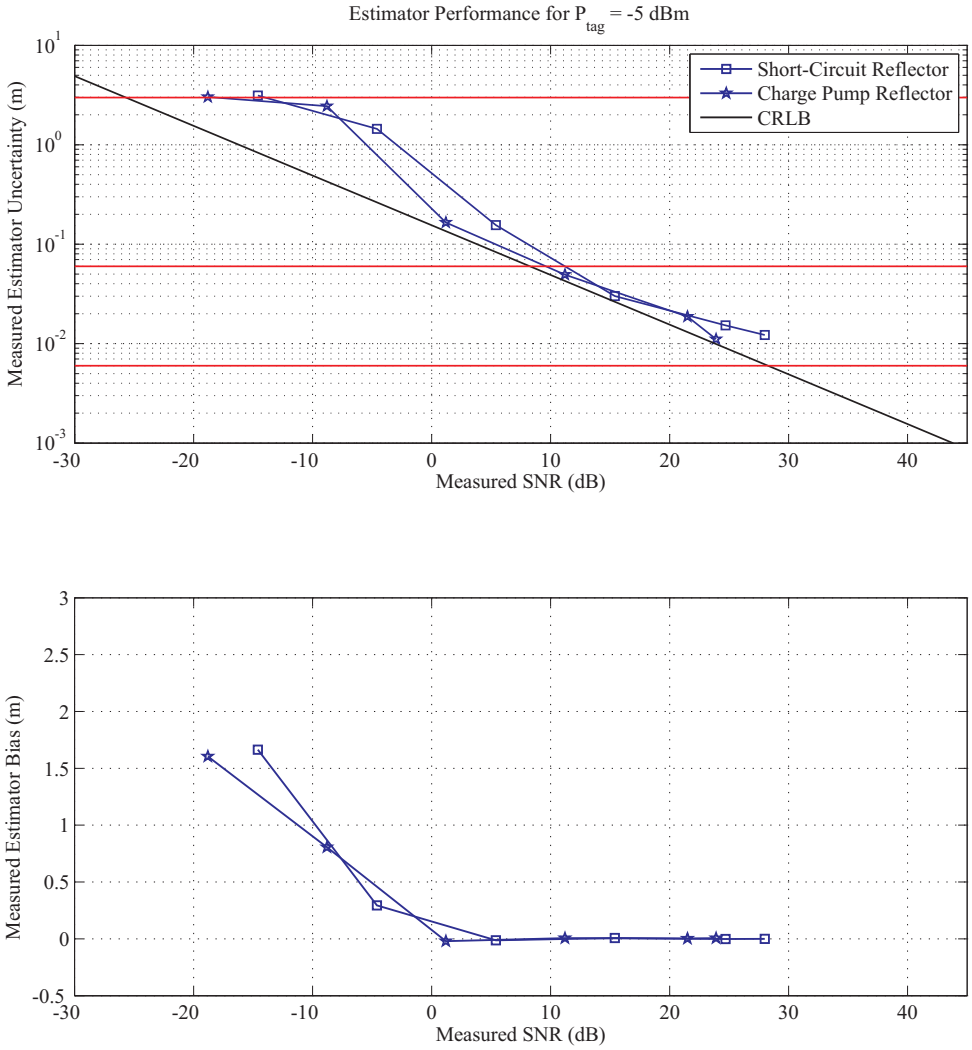

Figure 76: Measured performance of a maximum likelihood estimator using a Gaussian POW with $B_{\text{RMS}} = 15$ MHz on a 2-stage charge pump. The tag power is -5 dBm. The measured ranging bias added by the charge pump is 0.536 cm.

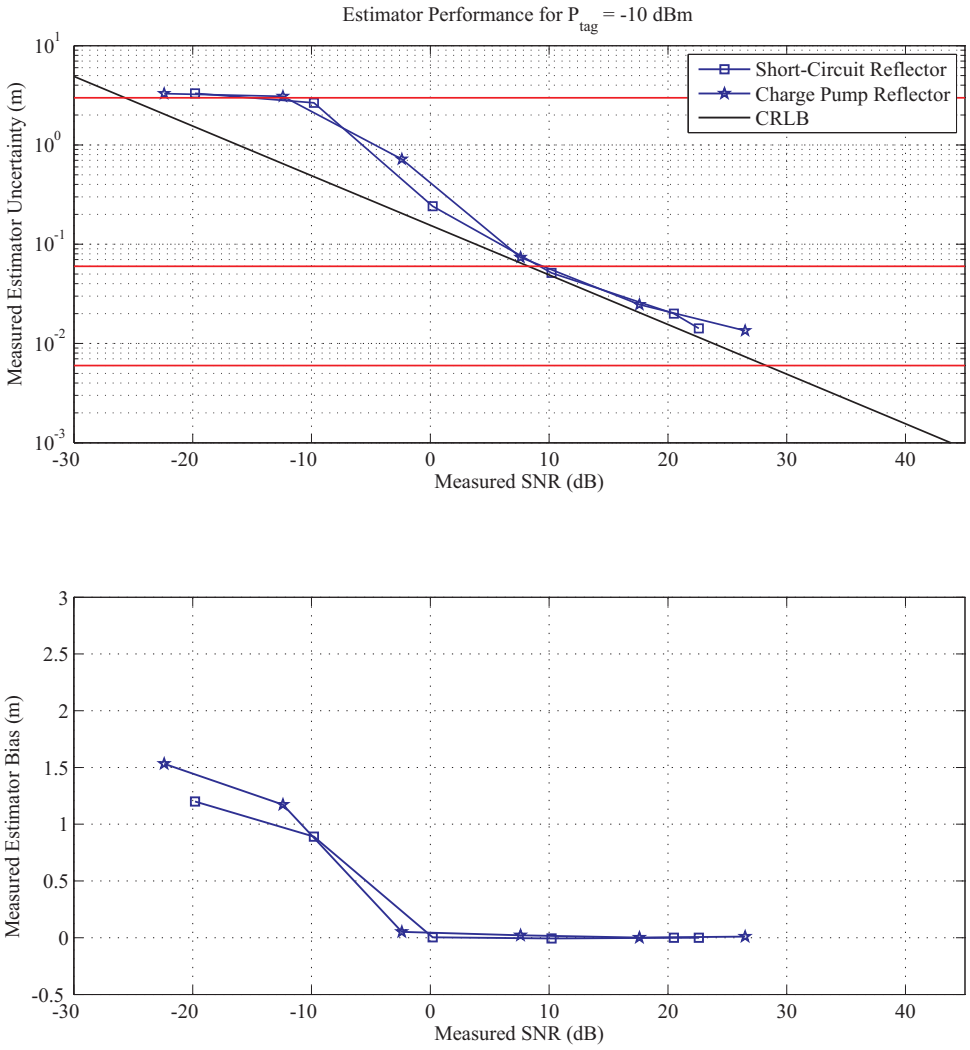

Figure 77: Measured performance of a maximum likelihood estimator using a Gaussian POW with $B_{\text{RMS}} = 15$ MHz on a 2-stage charge pump. The tag power is -10 dBm. The measured ranging bias added by the charge pump is 0.567 cm.

the charge pump reflector and short-circuit reflector. However, the estimator consistently produced range estimates with positive bias for the charge pump reflections as compared to the short-circuit reflections. The discrepancy between the mean range estimates of the two types of reflections is most clearly seen at high SNRs (>10 dB) for tag power cases 14, 10, and 5 dBm (Figures 72 through 74). The values for measured ranging bias for each value of tag power are listed here along with the predicted values from the model in equation (141):

- $P_{\text{tag}} = 14$ dBm. Measured $r_{\text{bias}} = 4.12$ cm. Predicted $r_{\text{bias}} = 2.37$ cm.
- $P_{\text{tag}} = 10$ dBm. Measured $r_{\text{bias}} = 3.25$ cm. Predicted $r_{\text{bias}} = 2.47$ cm.
- $P_{\text{tag}} = 5$ dBm. Measured $r_{\text{bias}} = 3.14$ cm. Predicted $r_{\text{bias}} = 2.48$ cm.
- $P_{\text{tag}} = 0$ dBm. Measured $r_{\text{bias}} = 1.39$ cm. Predicted $r_{\text{bias}} = 2.25$ cm.
- $P_{\text{tag}} = -5$ dBm. Measured $r_{\text{bias}} = 0.536$ cm. Predicted $r_{\text{bias}} = 1.67$ cm.
- $P_{\text{tag}} = -10$ dBm. Measured $r_{\text{bias}} = 0.567$ cm. Predicted $r_{\text{bias}} = 0.73$ cm.

These measured values are plotted along with the curve of predicted ranging bias versus tag power in Figure 78. Overall, the model predictions for bias are on the same order of magnitude as the measured values. The correlation between the six measured bias values and the six model values in the list above is 0.7715, which indicates a strong positive correlation. The RMS error is 1.01 cm, which is large compared to the average measured bias.

A designer has no control over the specific value of tag power that the tag receives when used in practice since tag range determines the tag power. The designer may choose a median value for ranging bias and include this value in calibrations. These measured results confirm that the charge pump itself does not add uncertainty to the estimator but does distort the waveform as explained by the model in Section 4.5.

6.3 Demonstrations of Range Estimation

Real range estimations in two different environments were taken to show the effects of frequency-flat environments. A laboratory environment represented a heavily cluttered

environment, and an empty hallway represented an environment with less clutter.

6.3.1 Demonstration Setup

The transceiver used in these demonstrations is slightly different from the transceiver used for the experiments in the previous two sections. This list summarizes the changes:

- Comb-filtering replaces the background measurement as the tool used for extracting the tag signal from the unmodulated multipath interferers.
- Oscilloscope averaging was turned on (256 averages) to reduce the noise floor by 24 dB.
- A high-power amplifier was added to the transmit chain to boost the average transmit power to 30 dBm.
- Two high gain patch antenna arrays were arranged in the bistatic reader configuration to reduce the self interference of the transceiver.
- For the hallway measurements, two 12-foot cables connect the transceiver output and input to the transmit and receive antennas, which increases the propagation delay of the transceiver to 115.2 ns.

Details of the demonstration transceiver are given in appendix B.

A Gaussian POW with an RMS bandwidth of 20 MHz, the same as in the simulations from the previous chapter, is used as the ranging waveform in the demonsrations. It performed with the lowest uncertainty of the simulated waveforms from Chapter 5.

The laboratory environment pictured in Figure 79 represents a medium-clutter environment full of reflective objects such as computers, measurement racks, desks, swivel chairs, and electrical measurement equipment. The room also has walls, a ceiling, and a floor. This environment can be simply characterized as a frequency-flat environment with a low K-factor. There will be a significant amount of indirect-path power reflecting off the surrounding clutter to the tag. The wavelength of the Gaussian POW used in these demonstrations is 100 ns, which has a wavelength in free space of 29.98 m. The room dimensions are measured as 4 m by 10 m. All of the clutter objects in the room are within one-half of the POW wavelength distance from the transceiving antennas.

The hallway environment pictured in Figure 80 represents a sparsely-populated medium-clutter environment with only walls, a ceiling, and a floor as the main clutter objects. This environment is assumed to be represented by a Rician channel with a higher K-factor than the laboratory. The surrounding clutter is not as imposing as in the laboratory environment. Therefore, less indirect-path power will arrive at the tag on average over the entire space of the environment. The length of the hallway from the antennas to the glass door is 12.1 m and the width of the hallway is 2.5 m. The reflections are all within a half-wavelength of the POW, but there are fewer clutter objects than the laboratory. The room dimensions are measured as 4 m by 10 m. All of the clutter objects in the room are within one-half of the POW wavelength distance from the transceiving antennas.

The coherence bandwidth was measured at ten different locations each in the laboratory and the hallway. These measurements were performed with an Agilent vector network analyzer using the transmit antenna from the transceiver and copy of the tag antenna. An example power delay profile is shown in Figure 81. The tag antenna is located 1.13 m away from the transmitter antenna in this measurement corresponding to the peak at the delay of 3.77 ns. The clutter of the environment contributes to the peaks following the initial LOS peak. Coherence bandwidth is measured for both environments using: [57]

$$\sigma^2_{\text{RMS}} = \frac{\int_0^\infty \tau^2 \left|h(\tau)\right|^2 d\tau}{\int_0^\infty \left|h(\tau)\right|^2 d\tau} - \left(\frac{\int_0^\infty \tau \left|h(\tau)\right|^2 d\tau}{\int_0^\infty \left|h(\tau)\right|^2 d\tau} \right)^2 \tag{177}$$

$$B_{\text{coh}} = \frac{1}{5\sigma_{\text{RMS}}} \tag{178}$$

The RMS delay spread σ^2_{RMS} is calculated first from the inverse Fourier transform of the measured channel frequency response $\tilde{H}(f)$ from the VNA. The Agilent E5071B network analyzer [3] used for these measurements has a measured noise floor of -80 dB. A cutoff threshold of -77 dB was used to prevent the noise of the network analyzer from affecting the coherence bandwidth measurements. The coherence bandwidth is found using the rule of thumb in equation (178). This particular channel has a measured coherence bandwidth of 192.3 MHz. The average coherence bandwidth of the laboratory is 171.8 MHz with a standard deviation of 75.0 MHz. For the hallway, the average coherence bandwidth is 222.9 MHz with a standard deviation of 84.7 MHz.

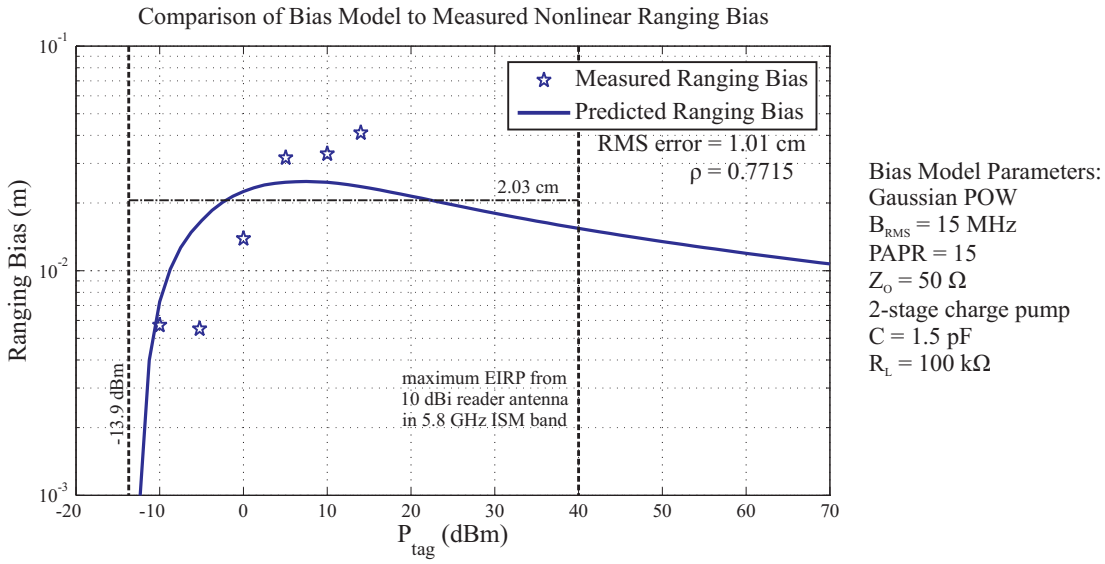

Figure 78: The measured values for ranging bias lie above and below the predicted bias curve. The RMS error is 1.01 cm, which is less than the mean measured bias of 2.17 cm. The correlation between predicted and measured bias values is 0.7715. This indicates that the bias model produced satisfactory predictions of ranging bias.

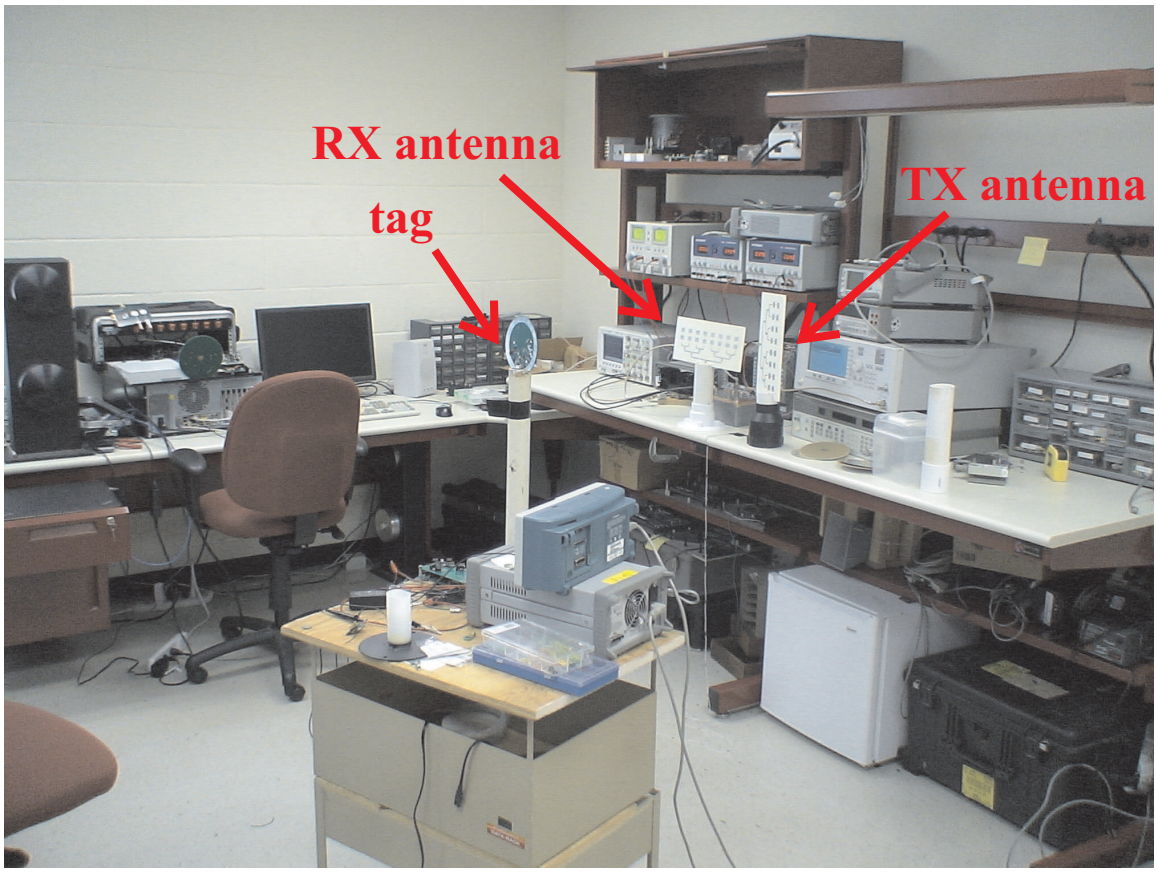

Figure 79: The laboratory environment used in the ranging demonstration contains many reflective objects.

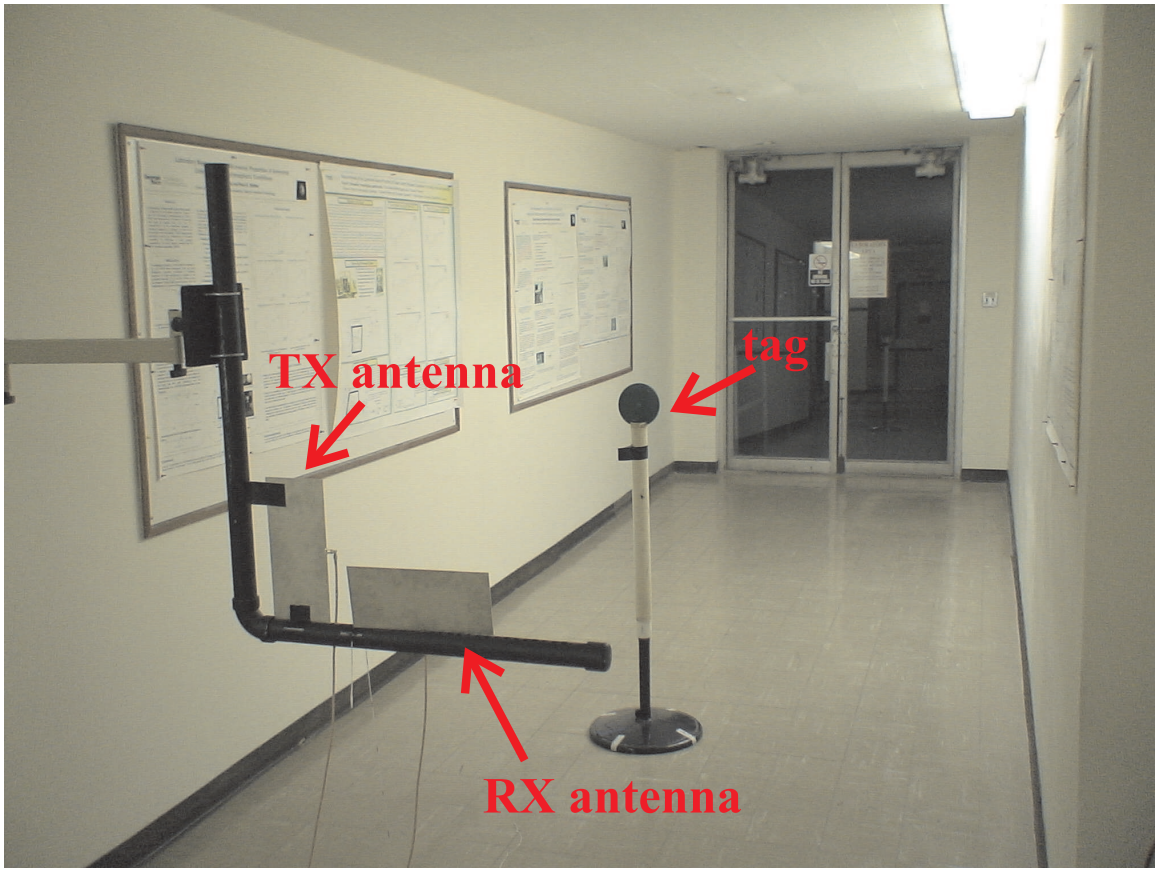

Figure 80: The hallway environment used in the ranging demonstration contains few reflective objects.

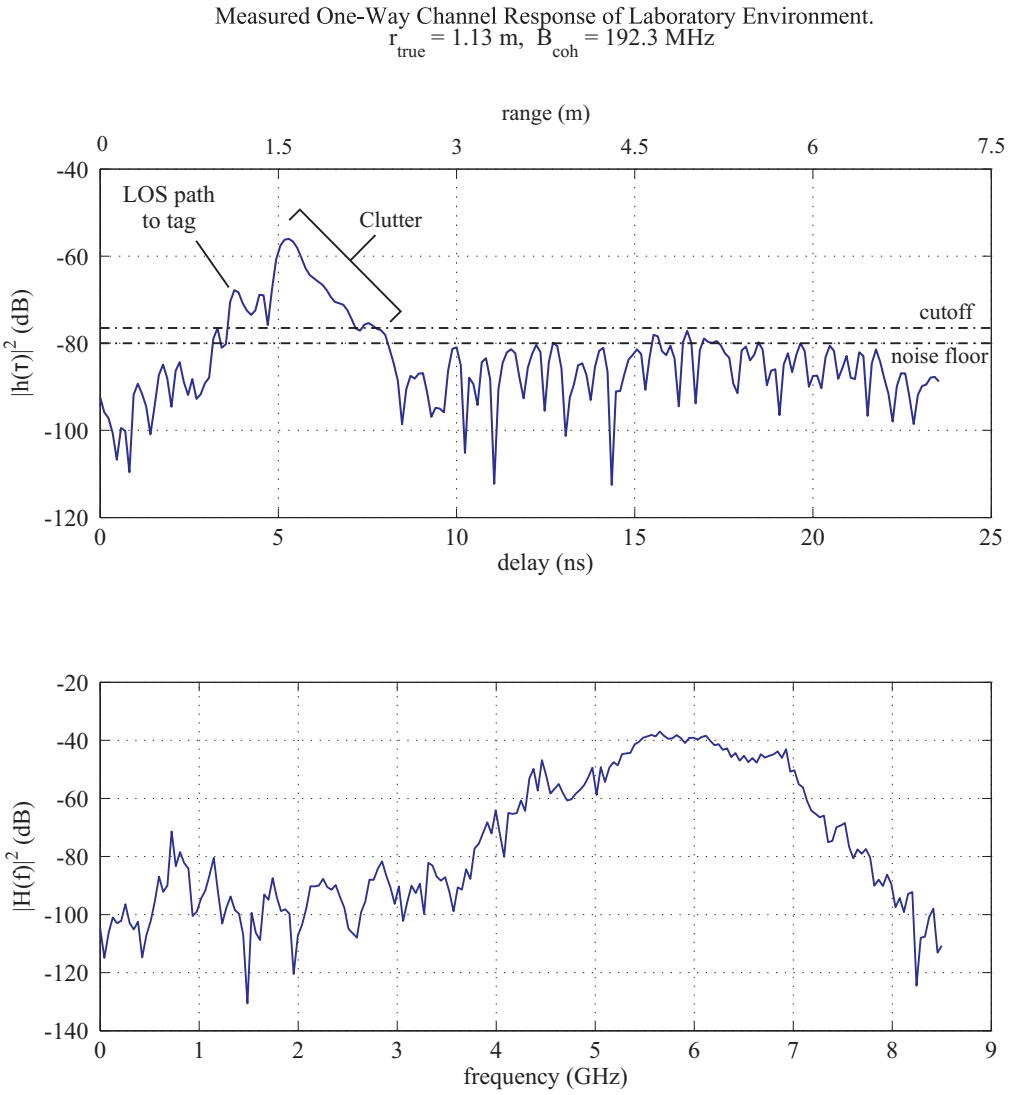

Figure 81: A high-resolution measurement of one power delay profile of the laboratory channel made with an Agilent E5071B network analyzer [3], which has a measured noise floor of -80 dB. The clutter contributes a peak that is 11.8 dB more powerful than the LOS path. The range axis on top shows most of the clutter have path lengths between 1.5 and 2.5 m.

Both of the measured coherence bandwidths are much larger than the 3-dB bandwidth of the Gaussian POW, which is given in Table 6 as 47.1 MHz. This indicates both environments are best represented by frequency-flat fading.

The procedure for taking range measurements starts by calibrating the transceiver. The transceiver propagation delay is 115.2 ns for the hallway environment since two 12-foot cables are used to connect the antennas to the transceiver. The transceiver propagation delay for the laboratory is 83.0 ns. After calibration, the tags are placed in the environment at a distance of 70 cm from the center of the pair of transceiving antennas. One thousand range estimations are taken at this distance before moving the tag between 2 and 10 cm farther away from the transceiving antennas (values around one wavelength of the 5.8 GHz carrier, $\lambda_c = 5.17$ cm). This process is repeated until 20 different ranges are estimated 1,000 times each.

The received SNR is estimated using the oscilloscope estimation method, which measures signal power from the raw received signal and extrapolates SNRs below 3 dB using the true tag range. For example, consider that the previous range estimate had a measured SNR of 2.00 (3 dB) at a tag range of 1.55 m, and the current tag range is moved back to 1.60 m. The SNR is extrapolated from the previous value as

$$\mathrm{SNR}_{1.6\ \mathrm{m}} = 2.00 \left(\frac{1.55\ \mathrm{m}}{1.60\ \mathrm{m}} \right)^4 = 1.76 \tag{179}$$

The path loss exponent value of 4 is the theoretical path loss exponent for free-space backscatter channels [68].

6.3.2 Measurement Results

The range estimations are plotted in Figure 82 versus received SNR. In some cases the estimations showed uncertainties near the CRLB, but most were well above. The frequency-selective nature of the environments is encapsulated in the uncertainty and bias results. The uncertainties vary widely above the CRLB, and the measured estimator bias is consistently positive.

There is an evident randomness about the uncertainty of the estimator depending on the received SNR. Ideally, the measured uncertainty should follow a well-behaved curve such

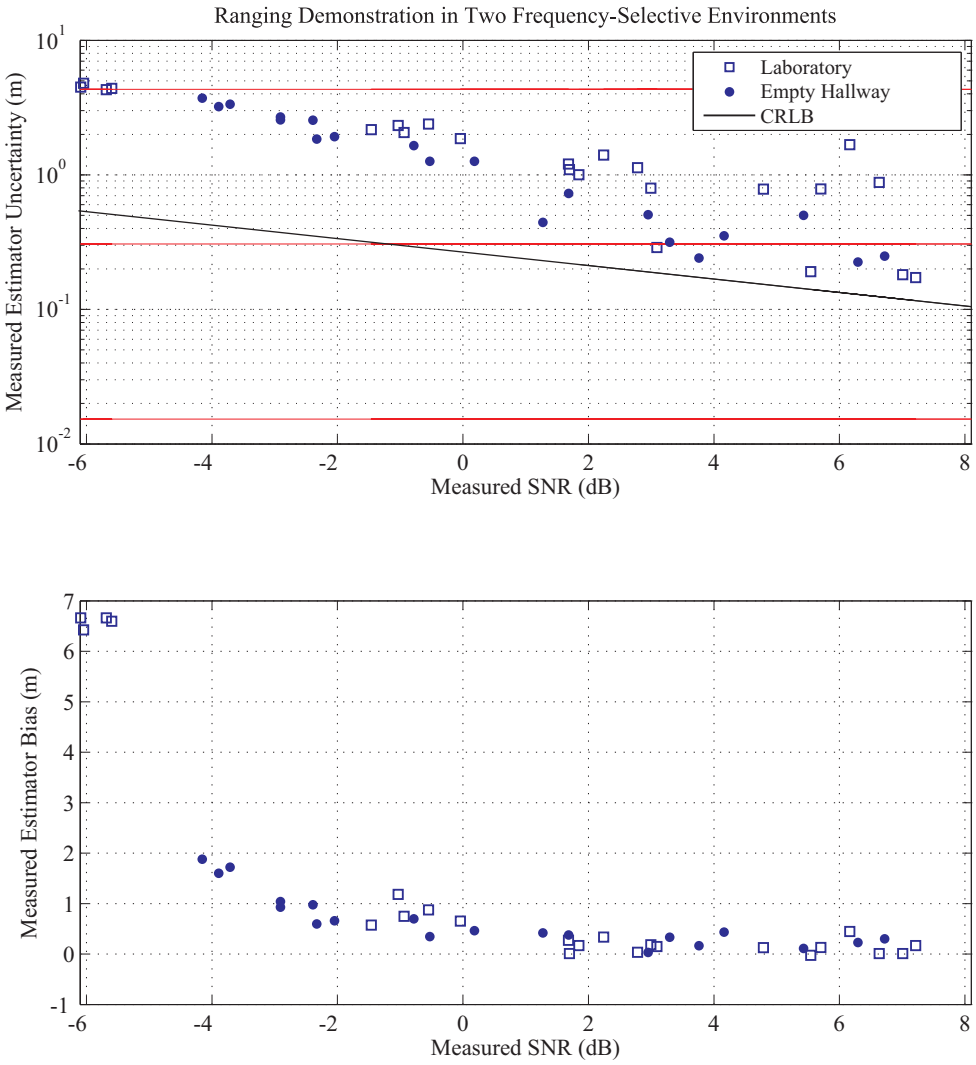

Figure 82: The ranging performance of the estimator shows added uncertainty from the randomness of the environment and positive bias from the frequency selectivity of the channel.

as the simulation results in Figure 47. This can be attributed to the environment changing between individual estimations. The system takes approximately 23 minutes to collect 1,000 range estimates. Elements in the environment outside the control of the experimentor changed positions during the 23-minute span. The rooms nearby the laboratory and near the hallway have people walking about. Chairs may have been moved. Tools may have been used and placed in different locations. The switching of power supplies and even the flicker of the flourescent lights may have had an effect on the randomness of the environment.

The uncertainty results are mostly well above the CRLB, which could indicate the range of SNRs measured is in the transition region between the upper information limit and the CRLB. The simulation results for a Gaussian POW with an RMS bandwidth of 20 MHz in Figure 47 show the transition region lies between SNR values of -10 and 5 dB. The received SNRs in the demonstration cover this range, but no received SNR higher than 7.2 dB could be measured.

The average RCS of the clutter in the laboratory is certainly higher than the average RCS of the hallway by visually comparing the two environments. However, this observation does not manifest itself in the measured uncertainties and biases. The average bias of the laboratory environment is 30.27 cm for received SNR values greater than 2 dB, and the standard deviation is 44.91 cm. The average bias for the hallway environment is 32.52 cm, and the standard deviation is 17.9 cm. The hallway gives more average bias, but the disparity is small. However, the hallway has a more consistent bias as evidenced by the smaller standard deviation of 17.9 cm. The mean biases can be calibrated out of the system if higher accuracy is needed.

CHAPTER VII

CONCLUSIONS

It was found that time-of-arrival ranging using an ML estimator is the most cost-effective and efficient method for measuring the range in a passive WSN that uses POWs for energy-harvesting improvements. Readers that are designed to transmit and receive POWs need only a software change to add the capability of measuring range. This research studied the three most critical contributers to ranging performance in passive WSNs. The over-arching research question was posed:

Assuming power-optimized waveforms are used for estimating range,
what are the effects of waveform shape, environmental clutter,
and nonlinear reflections on ranging performance?

It was found that the ranging uncertainty is most simply characterized by the Cramér-Rao lower bound and the information limits. The bias of a range estimator using POWs is zero in a free-space environment. Highly precise and perfectly accurate POW ranging systems are difficult to design because of the surrounding clutter in any real-world environment. Frequency-flat clutter environments were found to have a minor effect on ranging uncertainty, but frequency-selective environments imposed significant increases in the uncertainty and bias of an estimator. Nonlinear reflections added bias to range measurements on the order of a few centimeters, but no change in uncertainty was found.

7.1 Original Contributions

The following list summarizes the new and original work:

- POW: Multi-faceted invention for increasing the total range of passive wireless sensors and measuring the range to the tag
- Emprical model for predicting the range estimation bias of a reflection from a Dickson charge pump

- Cramér-Rao lower bound for use with POWs in a WSN
- Range measurement and calibration method
- Design methodology for POWs and charge pumps to meet energy-harvesting specifications
- Energy-harvesting and range-estimation statistics of a Gaussian POW, Square-POW, and M-POW.
- RMS bandwidth formula for a band-limited square-POW (i.e. square pulse)

7.2 Future Work

The measurements performed in the research verified all of the applicable theory. Ranging in passive WSNs with POWs are now characterized and understood. Further work in this area will delve into researching new techniques and methods for using POWs in passive WSNs and developing new POW shapes.

7.2.1 Power-Optimized Waveform Medium Access Control (POWMAC)

A WSN augmented with POW ranging may communicate with tags based on the true range of the tag. Consider an environment containing many tags spread out along a half-wavelength of the POW. The reader receives the backscattered signals from all of the tags simultaneously. The signal from a single tag can be filtered out from the rest based on the range of the tag. The reader can purposely cross-correlate the received signal at a delay corresponding to the desired range that the reader wants to access a tag.

For example, consider that there are tags located at 1 m, 3.5 m, and 9 m away from the reader, and the reader wants to receive the signal of the tag that is 3.5 m away. The reader will purposely cross-correlate the received signal from all tags at a delay of $2 \cdot 3.5 \text{ m}/c =$ 23.4 ns. Then, only the response from that targeted tag will pass through to the baseband demodulator. The issue of tag range resolution needs to be addressed: How close together may the tags be located before their backscattered signals mesh together at the reader-receiver?

7.2.2 Passive Tag-Based Frequency-Division Multiple Access

The spectrum of a POW has multiple carriers, which can be used individually to communicate simultaneously with multiple tags. Consider a 4-POW transmitted to eight tags within range of the reader. There are eight individual passband subcarriers presented by the 4-POW, and each of the eight tags may be designed to communicate on one of these subcarriers. However, each tag absorbs energy from all eight of the subcarriers.

The tags would need at least two antennas: One antenna is for energy-harvesting, and the other antenna is for communication. The energy-harvesting antenna has a matched bandwidth that is large enough to receive all eight subcarriers of the 4-POW. This allows the energy-harvesting efficiency improvments of the POW. The antenna used for communications has a matched bandwidth centered on one of the subcarriers and filters out all others. This way, many tags may communicate simultaneously with the reader.

7.2.3 Develop New POW Shapes

The three POW shapes presented in this research are the Gaussian POW, square POW, and M-POW. Descriptive parameters such as PAPR and RMS bandwidth quantify the ability of the POW to increase energy-harvesting efficiency. RMS bandwidth also quantifies the sharpness of the POW when used for range estimation. More POW shapes should be developed including, but not limited to:

- Raised-Cosine POW,
- Triangle POW,
- Sawtooth POW,
- Sinc POW,
- Sinc^2 POW, and
- Bessel POW.

7.2.4 More Measurements Over Current Research

All measurements and simulations in this research were performed for noncoherent estimators. The uncertainty of a coherent estimator decreases with the carrier frequency. Running the same simulations and measurements with a coherent estimator would completely verify or invalidate the corresponding theory.

More charge pump ranging bias measurements should be taken to characterize the effect of POW shape on the bias created from a nonlinear reflection. Square POWs, M-POWs, and other POW shapes should present different biases. The optimal POW for nonlinear reflections would be one that minimizes the bias over all possible POW shapes.

7.3 Publications and Presentations

The following sections list scholarly work including publications and conference presentations stemming from research performed for the author's M.S. thesis, Ph.D. dissertation, and other research projects.

7.3.1 Journal Articles

[1] M. S. Trotter, S. Hassig, and G. D. Durgin, G.D, "Extra Energy Harvesting Gains At 5.8 GHz With Power Optimized Waveforms." Submitted for publication to *IEEE Transactions on Microwave Theory and Techniques*. October 2010.

[2] C.R. Valenta, P. A. Graf, M. S. Trotter, G. A. Koo, G. D. Durgin, W. A. Daly, and B. J. Schafer, "High-Voltage Environment Backscatter Channel Measurements at 5.8 GHz." *IEEE Antennas and Propagation Magazine*, October 2011.

7.3.2 Conference Papers and Presentations

[1] C. R. Valenta, P. A. Graf, M. S. Trotter, G. A. Koo, G. D. Durgin, and B. J. Schafer, "Backscatter Channel Measurements at 5.8 GHz Across High-Voltage Corona." *IEEE Sensors Conference 2010*, p. 2400, 1-4 November 2010.

[2] C. R. Valenta, P. A. Graf, M. S. Trotter, G. A. Koo, G. D. Durgin, and B. J. Schafer,

"Transient Backscatter Channel Measurements at 5.8 GHz Across High-Voltage Insulation Gaps." *2010 Antenna Measurement Techniques Association Symposium*, October 2010.

[3] M. S. Trotter and G. D. Durgin, "Range Improvement Survey of Passive Tags Using Power Optimized Waveforms." *2010 IEEE International Conference on RFID*, 14-15 April 2010.

[4] M. S. Trotter, J. D. Griffin, and G. D. Durgin, "Power-optimized waveforms for improving the range and reliability of RFID systems," *2009 IEEE International Conference on RFID* , pp.80-87, 27-28 April 2009.

[5] M. S. Trotter, "Improved Range of WISP Tags Using Power Optimized Waveforms." presented at *the WISP Summit*. Berkeley, CA. November 2009.

[6] M. S. Trotter and G. D. Durgin, "Effect of DC to DC Converters on Organic Solar Cell Arrays for Powering DC Loads," Poster presented for *Center on Materials and Devices for Information Technology Research Retreat*. February 17, 2009.

[7] M. S. Trotter, W. J. Potscavage Jr., G. D. Durgin, and B. Kippelen, "A Charge Pump for Organic Solar Cells," Poster presented for *Center on Materials and Devices for Information Technology Research Retreat*. February 18, 2008.

7.3.3 Patent Applications

[1] M. S. Trotter and G. D. Durgin, "Systems and Methods for Providing a Power Optimized Waveform," U.S. PTO, 61/089,239, June 23, 2011.

[2] M. S. Trotter and G. D. Durgin, "Method for Wireless Range Measurement in Backscatter- and Reflected-Communications Systems." Invention Disclosure. Georgia Tech Research Corporation. January 25, 2011.

7.3.4 Invited Talks

[1] M. S. Trotter, "Power-Optimized Waveforms: Range Improvement and Range Finding," Talk given to Disney Research. Pittsburgh, Pennsylvania. August 22, 2011.

[2] M. S. Trotter, "Power-Optimized Waveforms: Range Improvement and Range Finding," Talk given to Johns Hopkins Applied Physics Laboratory. Laurel, Maryland. September 15, 2011.

[3] M. S. Trotter, "Power-Optimized Waveforms: Range Improvement and Range Finding," Talk given to HRL Labs. Malibu, California. October 11, 2011.

APPENDIX A

TRANSCEIVER TESTBED FOR MEASURING RANGE WITH POWER-OPTIMIZED WAVEFORMS

The testbed is a coherent monostatic transceiver as shown in Figure 83. The experiments in this research use a noncoherent estimator, but this testbed allows for coherent estimations if desired for future measurements. It cleanly produces POWs upconverted to 5.8 GHz at up to 17 dBm of average transmitted power. The maximum instantaneous power is 17 + PAPR_{dB} dBm depending on the PAPR of the POW shape. The transmitted signal is coupled to the tested environment through a circulator with 1 dB insertion loss in the forward path and 25 dB isolation in the reverse path.

The received signal is downconverted into I and Q signals using the direct-downconversion receiver developed recently for the work done by Griffin [1] and sampled with an Agilent DSO6104a oscilloscope. Channels 1 and 2 serve as the inputs for I and Q channels, respectively, and are both set to 50 Ω port impedances. This oscilloscope's vertical scaling can be as sensitive as 2 $^{\text{mV}}/_{\text{div}}$ and as large as 1 $^{\text{V}}/_{\text{div}}$. This oscilloscope takes 1,000 samples across the width of the screen per channel. The time division setting is set to 200 $^{\text{ns}}/_{\text{div}}$, and the vertical setting is set as low as possible to completely show the received signal without voltage clipping. This oscilloscope performs as an 8-bit ADC at a sampling rate of 500 MHz on both I and Q channels independently when operating at these settings.

The triggering is provided by the Agilent 33250A function generator, and the clocks are syncronized from the local oscillator source, which provides the passband center frequency 5.8 GHz to the transceiver. The function generator outputs a POW with a power of 3 dBm that is split equally into two signals: One branch feeds the transmitter chain and the other branch triggers the oscilloscope on channel 3. The trigger voltage is set to 225 mV regardless of the waveform shape used. This trigger voltage occurs at the positive, high-slope portion of the POW transmitted from the function generator.

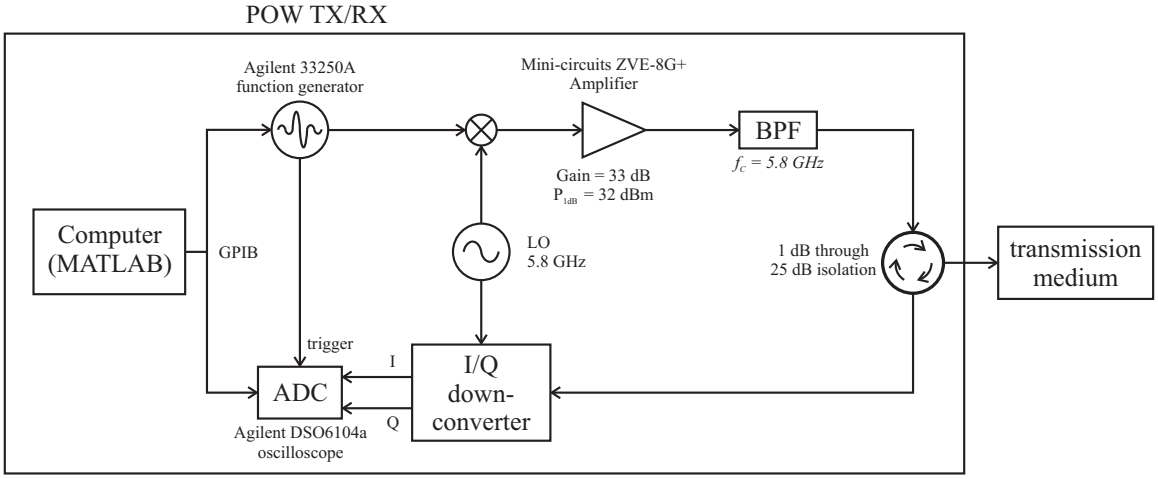

Figure 83: The POW transceiver is based on coherent RFID reader design. It uses a function generator as the POW source and an oscilloscope to quantize the received waveform. GPIB cables were used to communicate with the function generator and oscilloscope.

A.1 Calibration Procedure

In summary, the calibration procedure performs:

1. a noise floor measurement of the oscilloscope,

2. a highly precise measurement of the propagation delay within the transceiver, and

3. a background measurement of the environment without the target present.

The noise floor power is used in calculations of SNR.

The noise floor measurement involves three steps. First, a 50 Ω load is attached to the output port of the circulator. This measures the self-interference of the transceiver. Second, a low-power signal is measured with oscilloscope averaging turned on. Exactly 1,024 averages are taken to remove any noise. Third, the same signal is measured in a single-shot without averaging. The difference of the two signals is the noise signal, and its

signal power is computed in the discrete fashion:

$$\begin{aligned}
\vec{\tilde{y}}_{\text{self}} &= \begin{bmatrix} y_{\text{self,I}}[1] + jy_{\text{self,Q}}[1] \\ y_{\text{self,I}}[2] + jy_{\text{self,Q}}[2] \\ \vdots \\ y_{\text{self,I}}[1,000] + jy_{\text{self,Q}}[1,000] \end{bmatrix} \\
\vec{\tilde{n}} &= \vec{\tilde{y}}_{\text{self}} - \bar{\vec{\tilde{y}}}_{\text{self}} = \begin{bmatrix} \tilde{n}[1] \\ \tilde{n}[2] \\ \vdots \\ \tilde{n}[1,000] \end{bmatrix} \\
P_{\text{N}} &= 10\log\left(\frac{\sum_{k=1}^{1,000} \tilde{n}[k]\tilde{n}^*[k]\, T_{\text{S}}}{50}\right) + 30 \ \text{dBm}.
\end{aligned} \tag{180}$$

The over-bar notation $\bar{\vec{\tilde{y}}}_{\text{self}}$ represents the self-interference signal with oscilloscope averaging turned on while the complex vector notation $\vec{\tilde{y}}_{\text{self}}$ is the same signal sampled with a single-shot. The low-power signal measured is the self-interference signal of the transceiver. The circulator is terminated with a 50 Ω load so that only the isolated path from the transmitter to the receiver chain is the only path providing a signal to the receiver. All 1,000 points of the sampled noise waveform are used in the noise signal power computation. The sampling period T_{S} is 2 ns at the 500 MHz sampling rate of the oscilloscope. The noise is measured with a signal present to ensure that all amplifiers are operating within the system. The Agilent oscilloscope's noise floor varied depending on the vertical scaling used to display the received waveforms. Table 9 shows the noise floor for each level of the vertical scale.

The propagation time delay of the transceiver is measured by terminating the circulator with a short-circuit load. This way, the POW is immediately reflected at a distance of zero meters, and only the time delay of the transceiver is measured. The observed signal vector $\vec{\tilde{y}}_{\text{obs}}$ has high SNR on the oscilloscope and is averaged 1,024 times to eliminate noise. The self-interference signal is subtracted to obtain the reference POW to use in further range measurements. The magnitude is taken to simulate a noncoherent estimator:

$$\begin{aligned}
\vec{y}_{\text{ref}} &= \left|\bar{\vec{\tilde{y}}}_{\text{obs}} - \bar{\vec{\tilde{y}}}_{\text{self}}\right| \\
&= \overrightarrow{\text{pow}}_{\text{ref}}.
\end{aligned} \tag{181}$$

Table 9: Noise Floor Measurements of Agilent DSO6104A Oscilloscope With a 50 Ω Channel Impedance

Vertical Scale	Noise Floor
1 $^{\mathrm{V}}/_{\mathrm{div}}$	-16.4 dBm
500 $^{\mathrm{mV}}/_{\mathrm{div}}$	-18.4 dBm
200 $^{\mathrm{mV}}/_{\mathrm{div}}$	-29.7 dBm
100 $^{\mathrm{mV}}/_{\mathrm{div}}$	-32.6 dBm
50 $^{\mathrm{mV}}/_{\mathrm{div}}$	-32.9 dBm
20 $^{\mathrm{mV}}/_{\mathrm{div}}$	-34.0 dBm
10 $^{\mathrm{mV}}/_{\mathrm{div}}$	-34.3 dBm
5 $^{\mathrm{mV}}/_{\mathrm{div}}$	-50.5 dBm
2 $^{\mathrm{mV}}/_{\mathrm{div}}$	-51.5 dBm
Thermal Noise; $P_{\mathrm{N}} = kTB$ with $T = 297$ K and $B = 500$MHz	-86.9 dBm

This transceiver has a propagation time delay of 83.0 ns. The transceiver-delayed POW is designated as the reference POW vector $\overrightarrow{\mathrm{pow}}_{\mathrm{ref}}$, which is compared with a received signal vector in the cross-correlation during range measurements.

The final step in calibration is the background measurement, which is performed immediately prior to range measurements for every new environment presented to the circulator output port. The target is first removed from the environment. In a cable-ized environment, the short-circuit load of charge pump load is replaced with a 50 Ω load. Only the reflections from the permanent environment arive back at the receiver. The observed signal is averaged on the oscilloscope 1,024 times to remove noise. It is sampled at 500 MHz, and it consists of the background signal and the transceiver's self-interference. This averaged background signal vector, $\vec{\bar{y}}_{\mathrm{bgd}}$, consists of unmodulated multipath components (refer to Section 3.3) from the cable reflections and self-interference of the transceiver, which are assumed static (zero doppler effect) for the duration of the range measurements.

A.2 Taking a Range Measurement

The target (i.e. short-circuit reflector or charge pump) is connected to the end of the cable, and the oscilloscope takes a single-shot sampling of the received signals on the I and Q

channels. The observed signal vector consists of these components:

$$\vec{\tilde{y}}_{\text{obs}} = \overrightarrow{\text{pow}}_{\text{ref},\tau} e^{j2\pi f_c \tau} + \vec{\tilde{y}}_{\text{bgd}} + \vec{\tilde{n}}. \tag{182}$$

The background signal vector and noise are present as well as the backscattered signal vector $\overrightarrow{\text{pow}}_{\text{ref},\tau}$:

$$\overrightarrow{\text{pow}}_{\text{ref},\tau} = \begin{bmatrix} \text{pow}_{\text{ref}}(1T_s - \tau) \\ \text{pow}_{\text{ref}}(2T_s - \tau) \\ \vdots \\ \text{pow}_{\text{ref}}(1,000T_s - \tau) \end{bmatrix} \tag{183}$$

$$\tag{184}$$

The exponent $e^{j2\pi f_c \tau}$ is the received phasor referenced to the 5.8 GHz LO after I/Q down-conversion and is discarded once the magnitude is taken in this noncoherent estimator. The background signal is subtracted from the observed signal, and the magnitude is taken to get the input signal to the noncoherent estimator:

$$\begin{aligned} \vec{y}_{\text{est}} &= \left| \vec{\tilde{y}}_{\text{obs}} - \bar{\vec{\tilde{y}}}_{\text{bgd}} \right| \\ &= \left| \overrightarrow{\text{pow}}_{\text{ref},\tau} e^{j2\pi f_c \tau} + \vec{\tilde{n}} \right| \end{aligned} \tag{185}$$

This leaves the reference POW and the AWGN signal.

Prior to estimating range, the real-valued estimator signal $\vec{y}_{\text{est}}$ is upsampled by a factor of 10. To accomplish this upsampling cleanly, the estimator signal $\vec{y}_{\text{est}}$ is first truncated to the first samples that span a single time period of the POW. For example, the first 50 signal samples of 1,000 are taken to cover the first received POW time period. The sampling frequency is 500 MHz and the POW time period is 100 ns (i.e. $f_s T_{\text{POW}} = 50$ $^{\text{samples}}/_{\text{period}}$). Then, these 50 samples are replicated 50 times and upsampled by the upsampling factor 10 using sinc upsampling. Next, a single POW time period's worth of samples (i.e. $10 f_s T_{\text{POW}} = 500$ $^{\text{samples}}/_{\text{period}}$) is taken from the middle of the replicated, upsampled waveform. The replication is necessary to make the upsampling edge effects negligible.

A circular cross-correlation is then evaluated point-by-point with the estimator signal $\vec{y}_{\text{est}}$ and the reference POW $\overrightarrow{\text{pow}}_{\text{ref}}$, both of which have already been upsampled by a factor

of 10:

$$X_{\text{ref,est}}[x] = \sum_{k=1}^{500} \text{pow}_{\text{ref}}[k-x]\,|\tilde{y}_{\text{est}}[k]|. \tag{186}$$

The tested delay x is the same as in the analysis from Chapter 4. The tested delay is varied within the set of possible discrete delay bins ($x \in [0,\ {}^{T_s}/_{M},\ {}^{2T_s}/_{M}, \ldots,\ T_{\text{POW}}$) in steps of ${}^{T_s}/_{M}$). The delay estimate $\hat{\tau}$ is found with:

$$\hat{\tau} = \arg\max_{x} \left(X_{\text{ref,est}}[x]\right) \tag{187}$$

The range estimate is found by converting the delay estimate using the distance formula $\hat{r} = {}^{v_p\hat{\tau}}/_{2}$. The maximum of this cross-correlation function is found with a simple maximum-finding routine.

APPENDIX B

DEMONSTRATION TRANSCEIVER

The transceiver used in the ranging demonstration is based on the transceiver used in the experiments described in Appendix A. The changes from the experimental transceiver are:

- Comb-filtering replaces the background measurement as the tool used for extracting the tag signal from the unmodulated multipath interferers.
- Oscilloscope averaging was turned on (256 averages) to reduce the noise floor by 24 dB.
- A high-power amplifier was added to the transmit chain to boost the average transmit power to 30 dBm.
- Two high gain patch antenna arrays were arranged in the bistatic reader configuration to reduce the self interference of the transceiver.
- For the hallway measurements, two 12-foot cables connect the transceiver output and input to the transmit and receive antennas, which increases the propagation delay of the transceiver to 115.2 ns.

These changes are discussed in detail in the next few sections

B.1 Comb-Filtering

Comb-filtering is a method for removing the unmodulated multipath component of a POW received at the reader after backscattering has occured. A comb filter such as the one shown in Figure 84 deletes the spectral components of the received signal that are located at the transmitted POWs subcarrier frequencies. This method is much quicker and more efficient than performing a channel background measurement without the tag present. Background measurements suffer when the environment changes after calibration.

The received signal components that are modulated by the signal of the tag have spectral content on either side of each POW subcarrier as discussed in Section 3.3. Thus, only the

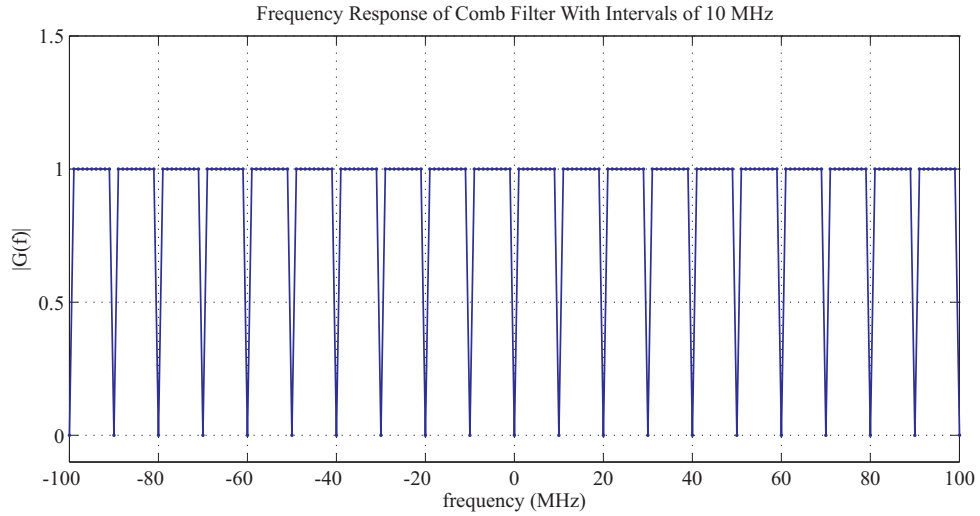

Figure 84: A comb filter that deletes spectral content located at POW subcarriers spaced in 10 MHz intervals.

tag's signal modulated on the POW and the measurement noise makes it past the comb filter.

B.2 Oscilloscope Averaging

The Agilent DSO6104a oscilloscope has a much higher noise floor than the typical backscatter radio. The noise floors of each voltage scaling setting is shown again in Table 10. Notice the thermal noise of a receiver at room temperature with a 500 MHz bandwidth is -86.9 dBm, which is more than 35 dB down from the best noise floor of the oscilloscope.

The noise power of each channel drops by a factor of 256 when averaging together 256 waveforms. The received SNR of the averaged signal is related to the received SNR of the single-shot signal by

$$\begin{aligned} \mathrm{SNR}_{\mathrm{avg}} &= \mathrm{SNR} + 10\log_{10}(256) \ \ (\mathrm{dB}) && (188) \\ &= \mathrm{SNR} + 24.1 \ (\mathrm{dB}) && (189) \end{aligned}$$

The tag signal is partially degraded as well since the tag and the clocks of the transceiver are not synchronized. Different amounts of averaging were tried (specifically 64, 128, 256, 512, 1024, and 2048 averages), but 256 averages provided the best received SNR of the tag signal. 64 averages provided too much noise, and 2048 averages diluted the tag signal too

Table 10: Noise Floor Measurements of Agilent DSO6104A Oscilloscope With a 50 Ω Channel Impedance

Vertical Scale	Noise Floor
1 $^{\mathrm{V}}/_{\mathrm{div}}$	-16.4 dBm
500 $^{\mathrm{mV}}/_{\mathrm{div}}$	-18.4 dBm
200 $^{\mathrm{mV}}/_{\mathrm{div}}$	-29.7 dBm
100 $^{\mathrm{mV}}/_{\mathrm{div}}$	-32.6 dBm
50 $^{\mathrm{mV}}/_{\mathrm{div}}$	-32.9 dBm
20 $^{\mathrm{mV}}/_{\mathrm{div}}$	-34.0 dBm
10 $^{\mathrm{mV}}/_{\mathrm{div}}$	-34.3 dBm
5 $^{\mathrm{mV}}/_{\mathrm{div}}$	-50.5 dBm
2 $^{\mathrm{mV}}/_{\mathrm{div}}$	-51.5 dBm
Thermal Noise $P_{\mathrm{N}} = kTB$ with $T = 297$ K and $B = 500$MHz	-86.9 dBm

much. The lowest noise floor of the oscilloscope with 256 averages drops from -51.5 dBm to -75.6 dBm.

B.3 High-Power Amplifier

The transmitted power was boosted to an average power of 30 dBm with bursts of maximum instantaneous power up to 30 + $\mathrm{PAPR}_{\mathrm{dB}}$ dBm. The amplifier is the Cree CGH55030F1 galium-nitride (GaN) high-electron mobility transistor (HEMT) amplifier, which is capable of transmitting up to 36 dBm of average power and up to 44.8 dBm of instantaneous power. This amplifier was placed after the Mini-Circuits ZVE-8G+ amplifier as shown in Figure 85. Higher values of received SNR were measured with this high-power amplifier.

B.4 Bistatic Configuration of High-Gain Patch Array Antennas

Two 16-element patch array antennas custom-built on a low-loss Rogers dielectric were configured in a bistatic reader configuration. Each antenna has a maximum gain of 17 dBi with a 25$^{\mathrm{o}}$ half-power beamwidth.

Figure 86 shows the antennas. Both antennas are linearly polarized as shown in the figure. The transmitting antenna is mounted horizontally where it is able to transmit vertically polarized radiation to the tag. The receiving antenna is mounted vertically where

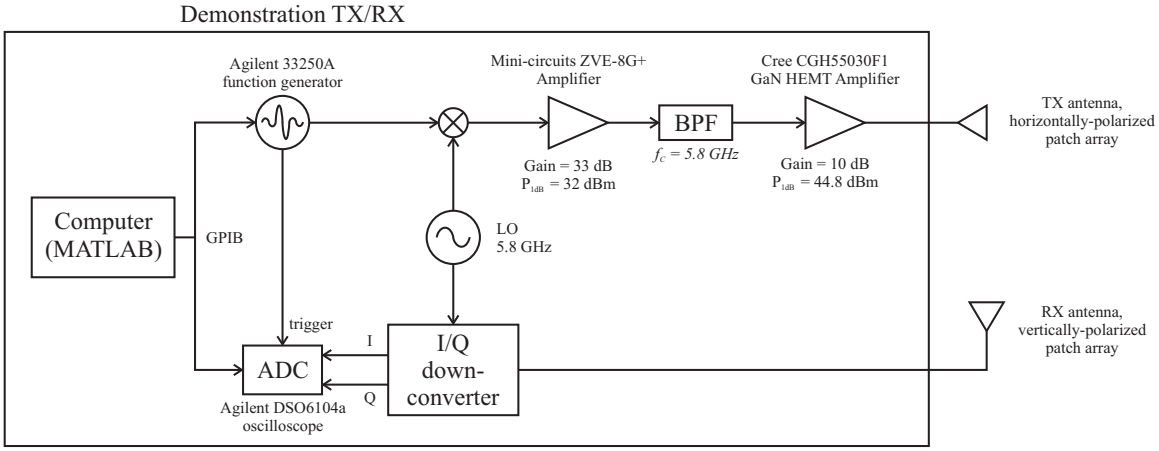

Figure 85: The POW transceiver is augmented to perform in the ranging demonstration. A high power amplifier from Cree boosts the average transmitted power to 30 dBm, and the bistatic configuration reduces the self interference of the transceiver.

it is able to receive horizontal polarization. These antennas display roughly 90 dB of isolation when mounted side-by-side in this configuration [69].

The SMA cables connecting the POW transceiver to the antennas in the picture are the same cables used in the experiments. Thus, the propagation delay of the transceiver is the same; 83.0 ns. However, the cables used in the hallway demonstration are both 12 foot cables, which added 32.2 ns to the propagation delay. The total delay for the hallway measurements was measured in calibration as 15.2 ns, but ambiguity says the delay must be located in the next POW time period since longer cables were used. Thus, 115.2 ns is the calibrated delay, which is $T_{\mathrm{POW}} = 100$ ns later.

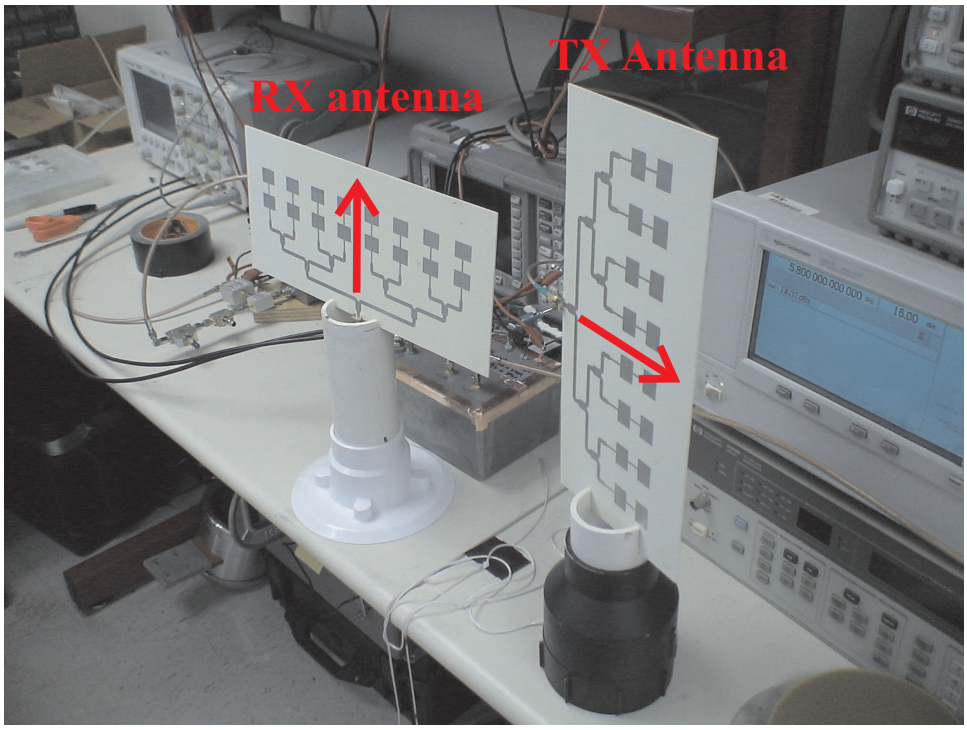

Figure 86: Two patch array antennas with maximum gain of 17 dBi are arranged in a bistatic configuration. The antennas are linearly polarized in the direction of the arrows.

REFERENCES

[1] J. D. Griffin, "High-frequency modulated-backscatter communication using multiple antennas," Ph.D. dissertation, Georgia Institute of Technology, March 2009.

[2] *ALN-9640 Squiggle Inlay*, Alien Technology, http://www.alientechnology.com/tags/index.php, March 2010.

[3] *Agilent ENA 2, 3 and 4 Port RF Network Analyzers; E5070B 300 kHz to 3 GHz; E5071B 300 kHz to 8.5 GHz*, Agilent Technologies, 2008.

[4] J. York and P. P.C., "Humancomputer interaction issues for mobile computing in a variable work context," *Int. J. Human-Computer Studies*, vol. 32, pp. 771 – 797, 2004.

[5] K. Nakamura, M. Kamio, T. Watanabe, S. Kobayashi, N. Koshizuka, and K. Sakamura, "Reliable ranging technique based on statistical RSSI analyses for an ad-hoc proximity detection system," in *IEEE International Conference on Pervasive Computing and Communications, 2009. PerCom 2009*, 2009, p. 1.

[6] J. Rencheng, P. Bo, M. Lisha, and G. Teng, "Research on Localization Method Based on RSSI Ranging-Error Compensation," in *5th International Conference on Wireless Communications, Networking and Mobile Computing, 2009. WiCom '09.*, 2009, p. 1.

[7] F. Bouchereau and D. . Brady, "Bounds on range-resolution degradation using RSSI measurements," in *2004 IEEE International Conference on Communications*, 2004, p. 3246.

[8] P. Nikitin, R. Martinez, S. Ramamurthy, H. Leland, G. Spiess, and K. Rao, "Phase based spatial identification of uhf rfid tags," in *2010 IEEE International Conference on RFID*, 2010, pp. 14 – 16.

[9] X. Wang, B. Moran, and M. Brazil, "Hyperbolic positioning using rips measurements for wireless sensor networks," in *15th IEEE International Conference on Networks, 2007.*, November 2007, pp. 425 –430.

[10] J. Friedman, A. Davitian, D. Torres, D. Cabric, and M. Srivastava, "Angle-of-arrival-assisted relative interferometric localization using software defined radios," in *IEEE Military Communications Conference*, October 2009, pp. 1 –8.

[11] V. P. Ipatov, *Spread Spectrum and CDMA, Principles and Applications*. John Wiley and Sons, 2005.

[12] J. S. Bergin, P. M. Techau, J. E. Don Carlos, and J. R. Guerci, "Radar waveform optimization for colored noise mitigation," in *Radar Conference, 2005 IEEE International*, May 2005, pp. 149 – 154.

[13] G. Gill, "Ultra-wideband radar using fourier synthesized waveforms," *Electromagnetic Compatibility, IEEE Transactions on*, vol. 39, no. 2, pp. 124 –131, May 1997.

[14] D. Garren, M. Osborn, A. Odom, J. Goldstein, S. Pillai, and J. Guerci, "Enhanced target detection and identification via optimised radar transmission pulse shape," *Radar, Sonar and Navigation, IEE Proceedings* -, vol. 148, no. 3, pp. 130 –138, jun 2001.

[15] M. S. Trotter, J. D. Griffin, and G. D. Durgin, "Power-optimized waveforms for improving the range and reliability of rfid systems," in *IEEE International Conference on RFID*, April 2009, pp. 80 – 87.

[16] M. S. Trotter and G. D. Durgin, "Survey of range improvement of commercial rfid tags with power optimized waveforms," in *IEEE International Conference on RFID*, April 2010, pp. 195 – 202.

[17] J. F. Dickson, "On-Chip High-Voltage Generation in MNOS Integrated Circuits Using an Improved Voltage Multiplier Technique," *IEEE Journal of Solid-State Circuits*, vol. SC-11, pp. 374 – 378, June 1976.

[18] *FCC Rules and Regulations Part 15 Section 247 (15.247), Operation within the bands 902 - 928 MHz, 2400 - 2483.5 MHz, and 5725 - 5850 MHz*, FCC.

[19] *European Telecommunications Standards Institute Radio Frequency Identification Equipment operating in the band 865 MHz to 868 MHz with power levels up to 2 W*, European Telecommunications Standards Institute, 2008.

[20] H. Stockman, "Communication by means of reflected power," *Proceedings of the IRE*, vol. 36, no. 10, pp. 1196 – 1204, October 1948.

[21] J. D. Cockcroft and E. T. S. Walton, "Experiments with High Velocity Positive Ions. (I) Further Developments in the Method of Obtaining High Velocity Positive Ions," *Proceedings of the Royal Society of London. Series A, Containing Papers of a Mathematical and Physical Character*, vol. 136, no. 830, pp. 619 – 630, 1932.

[22] P. Scherz, *Practical Electronics for Inventors*. McGraw-Hill, 2006.

[23] R. A. Oliver and C. J. Diorio, "Rfid tags with power rectifiers that have bias," U.S. Patent 7 561 866, September 26 2005.

[24] G. De Vita and G. Iannaccone, "Design Criteria For the RF Section of UHF And Microwave Passive RFID Transponders," *IEEE Transactions on Microwave Theory and Techniques*, pp. 2978 – 2990, September 2005.

[25] *Monza 4 Tag Chip Datasheet*, Impinj Inc., http://www.impinj.com/, June 2010.

[26] A. Sample, D. Yeager, and J. Smith, "A capacitive touch interface for passive rfid tags," in *IEEE International Conference on RFID*, April 2009, pp. 103 – 109.

[27] D. M. Dobkin, *The RF in RFID. Passive UHF RFID in Practice*. Elsevier, 2008.

[28] P. A. Hasan, A. and G. Durgin, "Reflected electro-material signatures for self-sensing passive RFID sensors ," in *2011 IEEE International Conference on RFID*, 2011, pp. 62 – 69.

[29] K. Along, Z. Chenrui, Z. Luo, L. Xiaozheng, and H. Tao, "Saw rfid enabled multifunctional sensors for food safety applications," in *2010 IEEE International Conference on RFID-Technology and Applications*, 2010, pp. 200 – 204.

[30] L. R. Lasser, G and S. A. L., "Broadband suppression properties of active leaking carrier cancellers," in *2009 IEEE International Conference on RFID*, 2009, pp. 208 – 212.

[31] C. Valenta, P. Graf, M. Trotter, G. Koo, G. Durgin, and B. Schafer, "Backscatter channel measurements at 5.8 ghz across high-voltage corona," in *IEEE Sensors Conference*, November 2010, p. 2400.

[32] H. Matsumoto and K. Takei, "An Experimental Study of Passive UHF RFID System with Longer Communication Range," in *Proceedings of Asia-Pacific Microwave Conference*, 2007, pp. 1 – 4.

[33] J. S. Park, J. J. W., S. Y. Ahn, H. H. Roh, H. R. Oh, Y. R. Seong, L. Y. D., and K. Choi, "Extending the Interrogation Range of a Passive UHF RFID System With an External Continuous Wave Transmitter," *IEEE Transactions on Instrumentation and Measurement, accepted for future publication*, November 2009.

[34] E. Stade, *Fourier Analysis*. Wiley-Interscience, 2005.

[35] C. K. Chui, *Wavelets: A Mathematical Tool For Signal Processing*. SIAM, 1997.

[36] EPCglobal, *EPC (TM) Radio-Frequency Identity Protocols Class-1 Generation-2 UHF RFID Protocol for Communications at 860 MHz - 960 MHz Version 1.2.0*, October 2008.

[37] T. Tanzawa and T. Tanaka, "A dynamic analysis of the dickson charge pump circuit," *IEEE Journal of Solid-State Circuits*, vol. 32, no. 8, pp. 1231–1240, August 1997.

[38] M. S. Trotter, "Effect of dc to dc converters on organic solar cell arrays for powering dc loads," Master's thesis, Georgia Institute of Technology, January 2009.

[39] *HSMS-280x, Surface Mount RF Schottky Barrier Diodes*, Avago Technologies, http://www.avagotech.com/, April 2010.

[40] R. Prasad, *OFDM for wireless communications systems*. Artech House, 2004.

[41] G. Gonzalez, *Microwave Transistor Amplifiers*. Prentice-Hall, Inc., 1997.

[42] H. Urkowitz, *Signal Theory and Random Processes*. Artech House Inc., 1983.

[43] A. Weiss and E. Weinstein, "Fundamental limitations in passive time delay estimation–part i: Narrow-band systems," *Acoustics, Speech and Signal Processing, IEEE Transactions on*, vol. 31, no. 2, pp. 472 – 486, April 1983.

[44] A. Bensky, *Wireless Positioning Technologies and Applications*. Artech House, Incorporated, 2007.

[45] J. Zhu, "Indoor/outdoor location of cellular handsets based on received signal strength," Master's thesis, Georgia Institute of Technology, May 2006.

[46] J. Zhu and G. Durgin, "Indoor/outdoor location of cellular handsets based on received signal strength," in *IEEE 61st Vehicular Technology Conference*, vol. 1, June 2005, pp. 92 – 96.

[47] X. Li, Y. Zhang, and M. G. Amin, "Multifrequency-based range estimation of rfid tags," in *IEEE International Conference on RFID*, April 2009, pp. 147 – 154.

[48] J. Choi, *Adaptive and Iterative Signal Processing in Communications*. Cambridge University Press, 2006.

[49] J. G. Proakis, *Digital Communications, 4th Edition*. McGraw-Hill, 2000.

[50] J. Soubielle, I. Fijalkow, P. Duvaut, and A. Bibaut, "GPS positioning in a multipath environment," *IEEE Transactions on Signal Processing*, vol. 50, no. 1, pp. 141 – 150, January 2002.

[51] A. Slavìk, *Product Integration, Its History and Applications*. Matfyzpress, 2007.

[52] M. A. Richards, *Fundamentals of Radar Signal Processing*. McGraw-Hill, 2005.

[53] M. Al-Nuaimi and A. Siamarou, "Coherence bandwidth characterisation and estimation for indoor rician multipath wireless channels using measurements at 62.4ghz," *IEE Proceedings - Microwaves, Antennas and Propagation*, vol. 149, no. 3, pp. 181 – 187, June 2002.

[54] G. Janssen, P. Stigter, and R. . Prasad, "Wideband indoor channel measurements and ber analysis of frequency selective multipath channels at 2.4, 4.75, and 11.5 ghz," *IEEE Transactions on Communications*, vol. 44, no. 10, pp. 1272 – 1288, October 1996.

[55] N. Moraitis and P. Constantinou, "Measurements and characterization of wideband indoor radio channel at 60 ghz," *IEEE Transactions on Wireless Communications*, vol. 5, no. 4, pp. 880 – 889, April 2006.

[56] T. S. Rappaport, *Wireless Communications - Principles And Practice, 2nd Edition*. Pearson Education, 2009.

[57] G. D. Durgin, *Space-Time Wireless Channels*. Prentice Hall Professional, 2003.

[58] D. Kim, M. A. Ingram, and W. W. Smith Jr., "Measurements of Small-Scale Fading and Path Loss for Long Range RF Tags," *IEEE Antennas and Propagation Magazine*, vol. 51, no. 8, pp. 1740 – 1749, August 2003.

[59] *Communication Channel Estimation and Waveform Design: Time Delay Estimation on Parallel, Flat Fading Channels*, Army Research Laboratory, http://www.dtic.mil/dtic/, February 2010.

[60] M. Skolnik, *Introduction to radar systems*. McGraw-Hill, 1980.

[61] G. E. Bottomley, *Channel Equalization for Wireless Communications: From Concepts to Detailed Mathematics*. John Wiley and Sons, 2011.

[62] F. Crowne and C. Fazi, "Nonlinear radar signatures from metal surfaces," in *IEEE International Radar Conference - Surveillance for a Safer World*, March 2009, pp. 1 – 6.

[63] E. Powers, J. Hong, and Y. Kim, "Cross sections and radar equation for nonlinear scatterers," *IEEE Transactions on Aerospace and Electronic Systems*, vol. AES-17, pp. 602 – 605, July 1981.

[64] R. O. Harger, "Harmonic radar systems for near-ground in-foliage nonlinear scatterers," *IEEE Transactions on Aerospace and Electronic Systems*, vol. AES-12, pp. 230 – 245, March 1976.

[65] J. Obregon and F. Farzaneh, "Definition of nonlinear reflection coefficient of a microwave device using describing function formalism," *IEEE Transactions on Microwave Theory and Techniques*, vol. 32, no. 4, pp. 452 – 455, April 1984.

[66] A. Peterson and G. Durgin, *Transient Signals on Transmission Lines: An Introduction to Non-Ideal Effects and Signal Integrity Issues in Electrical Systems*. Morgan and Claypool, 2008.

[67] D. Arnitz, U. Muehlmann, and K. Witrisal, "Wideband characterization of backscatter channels: Derivations and theoretical background," *Antennas and Propagation, IEEE Transactions on*, vol. PP, no. 99, p. 1, September 2011.

[68] K. Finkenzeller, *RFID Handbook: Fundamentals and Applications in Contactless Smart Cards and Identification*. John Wiley and Sons, 2003.

[69] G. Durgin and A. Rohatgi, "Multi-antenna rf tag measurement system using backscattered spread spectrum," in *2008 IEEE International Conference on RFID*, April 2008, pp. 1 –8.